

UNIVERSITA' DEGLI STUDI DI NAPOLI "FEDERICO II"



DIPARTIMENTO DI FARMACIA

Dottorato di ricerca in Scienza del Farmaco

XXX ciclo

*“Synthesis, structural and biological characterization of modified
aptamers and of azocompound derivatives having potential
pharmacological activity”*

Dott.ssa Elisa Riviaccio

Tutor: Prof.ssa Michela Varra

Coordinatore: Prof.ssa Maria Valeria D’Auria

Index

| | |
|-----------------------|----------|
| Abstract | 1 |
|-----------------------|----------|

Part I

| | |
|--|-----------|
| 1. Introduction | 3 |
| 1.1. Aptamers and SELEX | 3 |
| 1.2. G-quadruplex | 4 |
| 2. DNA Aptamers as potential antiproliferative agents..... | 10 |
| 2.1. Site specific replacements of a single loop nucleoside with a dibenzyl linker may switch the activity of TBA from anticoagulant to antiproliferative | 10 |
| 2.2. Results | 13 |
| 2.3. Discussion..... | 29 |
| 2.4. Conclusion..... | 34 |
| 2.5. Experimental section | 35 |
| 3. DNA aptamers as potential anti-HIV agents | 41 |
| 3.1. Structural Studies and biological evaluation of T30695 variants modified with single chiral glycerol-T reveal the importance of LEDGF/p75 for the aptamer Anti-HIV-Integrase activities | 41 |
| 3.2. Results and discussion..... | 44 |
| 3.3. Conclusion..... | 66 |
| 3.4. Experimental section | 67 |
| <i>Bibliography</i> | 71 |

Part II

| | |
|---|------------|
| 1. Introduction | 77 |
| 1.1. Azobenzenes as molecular photoswitchers | 77 |
| 1.2. Modulating Azobenzenes photoisomerization for <i>in vivo</i> use | 81 |
| 2. Azobenzene Photoswitchers as anti-cancer tools | 82 |
| 2.1. Photo-control of cancer cell growth by N-substituted pyrrol azo-derivatives | 82 |
| 2.2. Results..... | 83 |
| 2.3. Experimental section | 100 |
| 3. Incorporation of a 4-(dimethylamino)azobenzene moiety into G-quadruplex aptamers..... | 122 |
| 3.1. Introduction | 122 |

| | |
|----------------------------------|------------|
| 3.2. Results and discussion..... | 124 |
| 3.3. Conclusion..... | 147 |
| 3.4. Experimental section | 149 |
| <i>Bibliography</i> | <i>155</i> |

Abstract

Single-stranded RNA and DNA aptamers have been developed in order to selectively inhibit specific biological targets. The tridimensional structural arrangement of aptamers guarantees their selective and specific binding to the target. A large number of G-rich aptamers are able to form G-quadruplex (G-4) structures. The high polymorphism of G-4 structure provides for a range of stable structures having specific recognition sites on the corresponding target. Several aptamers based on the G-4 structures are attractive tools for the detection and treatment of vascular, cancer and viral diseases, many of which are currently being tested in preclinical and clinical trials.

Often, in order to increase the *in vivo* nuclease aptamer resistance and/or to elucidate the aptamer-target structure-activity relationships, the initial aptamers, obtained by SELEX (Systematic Evolution of LIgands by EXponential enrichment), are subjected to chemical modifications. In this context, a piece of my research activity has been centred on the synthesis of modified G-quadruplex forming aptamers endowed with potential pharmacological activities.

In order to explore the potential of the TBA G-quadruplex as antiproliferative agent, I searched for that TBA single residue modification capable both to turn off the antithrombin activity and to preserve the aptamer antiproliferative action. I reached this goal modifying the TBA with a particular biphenyl linker that was used instead of T residue at position 3, 4, 7, 9, 12 or 13. Each of six TBA variants was studied from structural point of view by CD, CD melting, 1 and 2D NMR techniques. The acquired data demonstrated that almost all the sequences were able to fold into monomolecular “chair-like” G-Quadruplex structure, strongly similar to that of TBA. On the other hand, the results of biological studies showed that two TBA variants, containing the modification at T4 or T13, lacked of the TBA antithrombin activity but preserved the TBA antiproliferative activity on He-La cells. Results concerning this research are discussed in the chapter 2, part I.

Another G-quadruplex forming aptamer, named T30695 was been chemically modified at T-loop residues. T30695 has been selected as HIV-Integrase (HIV-In) inhibitor and its biological action is today still ambiguous. In fact, the T30695 virus inhibition is also connected with the binding to Gp120. The formation of T30695-Gp120 complex impairs the host-viral interaction and thus reduces the infectivity of HIV. Furthermore, in view of the results of recent studies on the G-quadruplex T30695 typology, such previously reported T30695-HIV-In structure-activity relationships require to be revised. A part of my studies has been performed to acquire new information about T30695 anti-HIV-In activity. In particular, I synthesised a new set of modified T30695 aptamers in which single T residue at position 4, 8 or 12 was modified as R or S glycerol T. Structural studies on modified aptamers, performed using CD, CD melting, EMSA, HRMS and ¹H NMR, highlighted that almost all modified sequences were able to form the same G-Quadruplex typology of that of T30695. LEDGF-p75 dependent and independent integration assays provided information about the biological behaviour of the modified aptamers. The results of these studies are described in the chapter 3, part I.

During the third year of my PhD course I have focused my studies on the synthesis of azobenzene photowitchers useful both as antiproliferative agents and as modifying units of conjugated aptamers. Some newly synthesized chiral azo-heteroarenes showed promising photo-regulated antiproliferative activity on HCT116-p53^{-/-} cancer cells. Results concerning the synthesis, the structural characterization and the biological behaviours of these new molecules are described in the chapter 2, part II.

Finally, I carried out the synthesis of 1-(4-dimethylaminobenzyl)-2-(4'-(R-2,3-dihydroxypropoxy))diazobenzene as phosphoramidite building block useful to obtain 5'-conjugated oligonucleotides. I performed the conjugation of the synthesized building block at 5'-end of the TBA and of the T30695 aptamers. Preliminary spectroscopic studies concerning the behaviour of conjugated aptamers under photo-illumination are reported in chapter 3, part II.

Part I

1. Introduction

1.1. Aptamers and SELEX

Aptamers (from the Latin “aptus” meaning “to fit”) are short, single-stranded DNA or RNA oligonucleotides, that, through specific three dimensional structures, bind with high affinity and specificity to a large variety of molecular targets [1][2]. Most of aptamer-target complexes show dissociation constants in the picomolar to nanomolar range. Several chemical and biological properties make aptamers suitable for a growing number of therapeutic and diagnostic applications [3][4]. Notably, the use of aptamers instead of antibodies have many important advantages, such as:

- High thermal stability, most of discovered aptamers preserve their tertiary structure over many cycles of denaturation/renaturation;
- Low immunogenicity, oligonucleotides are not identified by the human immune system as foreign agents;
- Aptamers can be synthesized with high reproducibility and low production costs. Moreover, they can be easily subjected to different types of post-synthetic modification, in order to increase their *in vivo* life time;
- The low molecular weight makes aptamers capable to penetrate the tissue barriers better than antibodies.

Aptamers are isolated from 10^{12} – 10^{15} combinatorial oligonucleotide libraries through a technique known as SELEX (*Systematic Evolution of Ligands by EXponential enrichment*)[1][2]. The SELEX process relies on three steps (Figure 1): in the initial stage (*library generation*) a large library of single-stranded oligonucleotide templates, consisting of random sequence regions, usually 30–40 mers, is obtained from integrated DNA Technologies. The 5’-and 3’- terminal sequences are fixed for the primer binding. In the second stage (*binding and separation*) firstly the sequences of the library are exposed to the target-ligand, than the unbound components are removed using a

partitioning method. At last, in the third stage (*amplification*) the target-bound sequences are eluted and amplified by PCR in order to be used for the next rounds of incubation, separation, and amplification. The complete SELEX process generally comprises of 7-15 rounds of selection discovering a small number of aptamers having high affinity and specificity toward the target (Figure 1)[5].

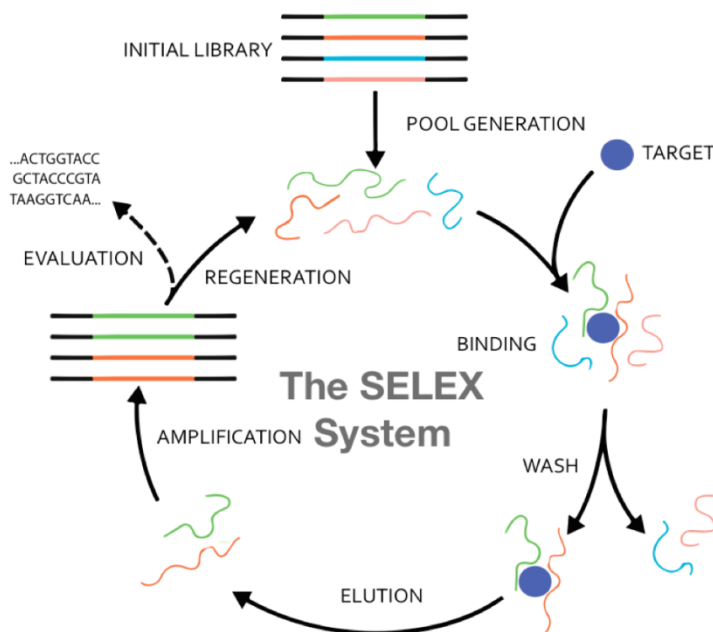


Figure 1. SELEX (Systematic Evolution of Ligands by EXponential enrichment).

1.2. G-quadruplex

G-rich DNA or RNA aptamers are able to adopt such particular spatial arrangements called G-quadruplex (G-Q) structures, arising from the stacking of a certain number of G-quartets. Each G-quartet consists of four guanine bases cyclically connected to each other through Hoogsteen hydrogen bonding (Figure 2) [6].

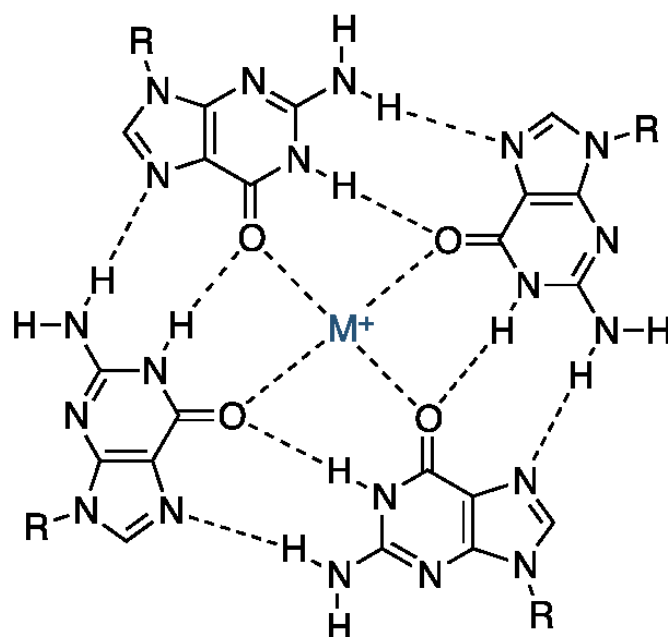


Figure 2. Hydrogen-bonding between bases and metal ion coordination in a G-quartet.

A large number of GQ typologies have been structurally characterized by means of NMR or X-Ray techniques, thus evidencing a high structural GQ polymorphism [7][8]. Particularly, GQs can arise from one, two or four single stranded oligonucleotides and, consequently can be unimolecular (intramolecular), bimolecular (dimeric) and tetramolecular (tetrameric). Generally, a potential unimolecular GQ has the following sequence:



m represents the number of G residues forming the G-tracts, while X_n , X_o and X_p are the residues being part of the loops.

Almost all bimolecular structurally characterized GQs involve the association of two identical sequences $X_n G_m X_o G_m X_p$, in which n and p , namely, the number of residues separating the G-tracts (G_m), may or may not be zero. Four $X_n G_m X_o$ or $G_m X_n G_m$ strands can associate to form tetramolecular GQs.

Furthermore, into monomolecular and bimolecular GQs, the phosphate backbone polarity of G-tracts can be parallel or anti-parallel thus originating parallel or antiparallel GQs and affecting the relative orientations and the localizations of the *loops*. Some examples are shown in the figure 3. In

a parallel bimolecular GQs (Figure 3a), the loops, that connect two G-tracts, in each single stranded oligonucleotides, should link the bottom G-tetrad with the top one, leading to a particular spatial arrangement called propeller-type (double-chain-reversal loop). Into the anti-parallel bimolecular GQs the two G-tracts of each strand can be linked either by diagonal or lateral (edgewise) loops (Figure 3b and 3c).

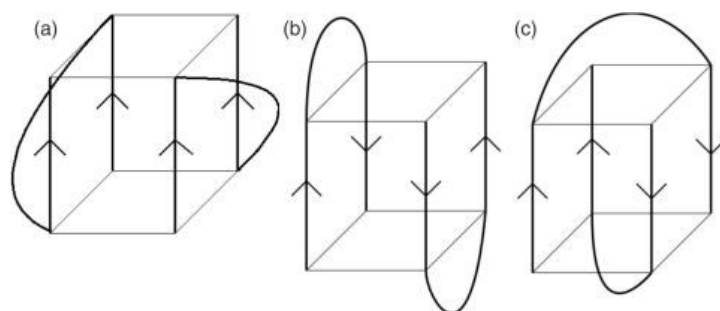


Figure 3. Schematic diagrams of the (a) parallel, (b) lateral and (c) diagonal loop of dimeric GQs.

Additionally, the GQ lateral loops can be classified as head-to-head or head-to-tail. In the first type, loops are located on the same GQ face; conversely, in the latter type they are located on the opposite GQ faces. Further important GQ features are related to the glycosidic torsion angles assumed by the guanine residues forming the GQ core (Figure 4); guanine residues forming parallel GQs are preferentially in the conformation *anti*, while they alternatively assume the *syn* and *anti* conformations in the case of anti-parallel GQs (Figure 4).

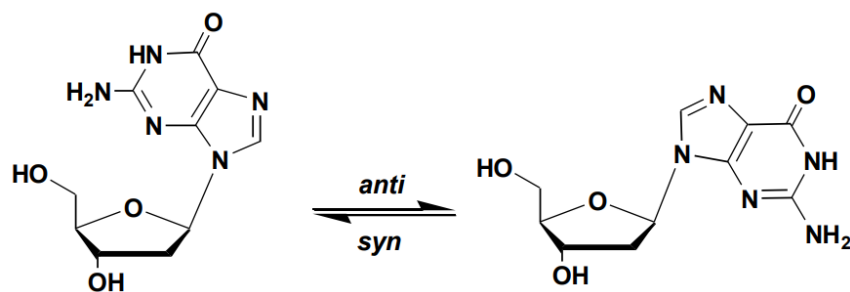


Figure 4. Guanine glycosidic angles in *syn* and *anti* conformations.

Most importantly, the overall GQ structure is stabilized by different type of cations, especially potassium cations. Generally, the monovalent cations occupy the negative charged central cavities of the G-quadruplex core coordinating the guanine O6 oxygen atoms and thus reducing the strong negative electrostatic potential of the inner cavity of the GQ core [7-10] (Figure 5). Inner the GQ-core, the relative location of the cations respect to the stacked G-quartets depends on the nature of the ion; the small Na^+ ions preferentially coordinate the four O-6 of the same G-quartet, occupying the inner cavity of each G-quartet; being their radius more higher than that of Na^+ , K^+ ions are centred between two G-quartets, coordinating the eight O-6 atoms of the two G-quartets in a symmetric tetragonal bipyramidal configuration [11] (Figure 5).

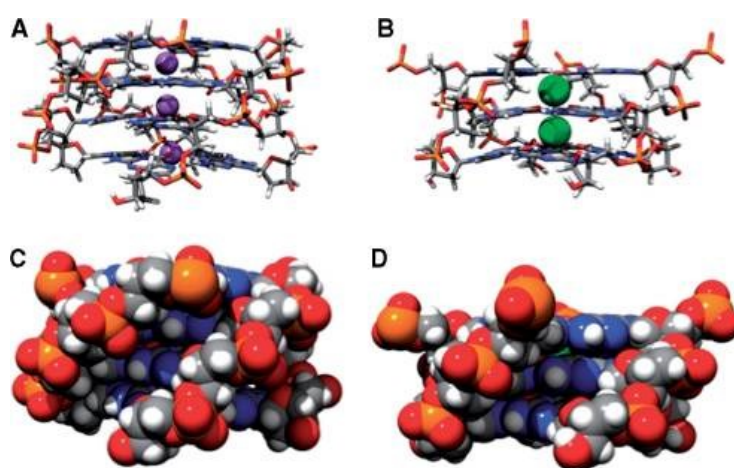


Figure 5. Location of the cations respect to the stacked G-quartets. (A) Parallel stacked quartets with Na^+ stabilization (purple spheres) from $(\text{d}(\text{TGGGGT})_4)$, (B) parallel stacked quartets with K^+ stabilization (green spheres) from $(\text{dA}(\text{GGGTTA})_3\text{GGG})$, (C) $\text{d}(\text{TGGGGT})_4$ stacking in space filling representation, (D) $\text{dA}(\text{GGGTTA})_3\text{GGG}$ stacking in space filling representation [from *Nucleic Acids Res.*, vol. 36, no. 17, pp. 5482–5515, 2008].

The majority of the studies have been centred on the evaluation of the influence of Na^+ or K^+ on the GQ structure stability and typology; however, several other monovalent and divalent ions are able to influence the G-Q structure futures, including the monovalent cations Rb^+ , Cs^+ , NH_4^+ , and Tl^+ and divalent cations Sr^{2+} , Ba^{2+} , and Pb^{2+} [9].

Cations play a critical role in stabilizing G-quadruplex structures in the following order: $K^+ > Ca^{2+} > Na^+ > Mg^{2+} > Li^+$ and $K^+ > Rb^+ > Cs^+$ [12]. In addition, the GQ typology and/or GQ conformations can also depend on the type of cations used in the solution. Although some general trends are evident (i.e. potassium can promote parallel conformations)[13], the prediction of the possible GQ typologies, raised from a certain sequence, is not obvious, and it requires to be characterized empirically under different folding conditions.

Guanine-rich sequences spread along the genome of most organisms, especially at the ends of chromosomes, named telomeres [14]. They consist of such simple motifs repeated in tandem. Human telomeres consist of the hexanucleotide d(TTAGGG)_n 5–10 kb length, that terminate in a single-stranded 3'-overhang of 35–600 bases. This motif was found also in other regulatory regions, specifically in the immunoglobulin switch regions and in the promoter of the c-myc oncogenes [15]. After 20–40 replication cycles telomeres are progressively shortened until cells death is induced. This mechanism is closely related to the cellular immortality; indeed, immortalized cells preserve the length of their telomeres during an unlimited number of cell cycles. In this frame, an RNA-dependent DNA polymerase enzyme, named telomerase, acts to preserve telomere length and integrity, thus playing an important role in tumorigenesis. Several studies suggested that the folding of telomeric DNA into GQs can decrease the enzymatic activity of telomerase, thus reducing cancer cell survival [16]. In this context, notable efforts are now performing in order to discover new anticancer drugs able to bind and to stabilize telomeric GQs. Some discovered GQ targeting drugs are reported in figure 6 [17-22].

Actually the G-quadruplex-targeting drug, quarfloxacin® (CX-3543, Cylene Pharmaceuticals in San Diego, CA, USA) (Figure 6a) has showed an excellent *in vivo* activity in various solid tumors and is ongoing the Phase II clinical trials. Quarfloxin arises from the design of G-quadruplex-interactive fluoroquinolones [23], a class of duplex DNA-gyrase or DNA-topoisomerase II complexes targeting drugs. Quarfloxin targets selectively GQs in rDNA-respect to duplex or single-stranded DNA and it is also selectively internalized into the nucleolus of cancer cells [23][24].

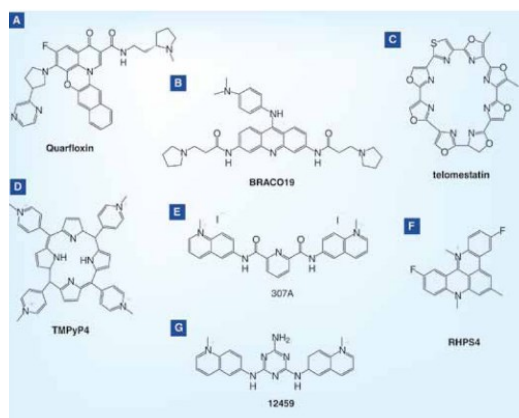


Figure 6. G-quadruplex-targeting drugs [from *Futur. Med. Chem.*, vol. 2, no. 4, pp. 619–646, 2010].

In order to explore new potential GQ-based cancer therapy, the researchers are now focused on the discovered of new ligands for GQs, but also on the physical and biological characterization of different GQ-forming aptamers that have shown very interesting anticancer properties. The first part of my research activity was centred on the latter field and has been developed through the synthesis and the structural characterization of new TBA analogues useful as antiproliferative agents. The background and the results of this activity will be discussed in the next chapter.

2. DNA Aptamers as potential antiproliferative agents

2.1. Site specific replacements of a single loop nucleoside with a dibenzyl linker may switch the activity of TBA from anticoagulant to antiproliferative

Currently cancer is the leading cause of death all over the world. Although the therapies now available increase the life expectancy, on the other hand, significantly produce serious side effect arising from the lack of selectivity towards cancer cells. Importantly, a right prognosis corresponds with shorter detection and diagnosis timelines, for this reason the discovery of new biomarkers that are specific to particular cancers is crucial in the field of cancer biology. Clearly there is an urgent need for further cancer therapies to improve efficacy and selectivity against cancer cells, and disease-specific biomarkers for the recognition of proteins, or other biological molecules that distinguish between normal and malignant cells. In this context nucleic acid aptamers have been identified as very promising therapeutic and diagnostic agents, drawing the attention in the cancer research. The ability of aptamers to fold into secondary and tertiary structures allow to bind selectively a wide range of targets through a shape-specific recognition.

Many G-rich oligonucleotides (GROs), forming G-quadruplex structures, have shown the ability to inhibit the cancer cells growth, among them the most advanced in preclinical and clinical studies is a 26-mer sequence (5'-GGTGGTGGTGGTTGTGGTGGTGGTGG), formerly developed by Aptamera as AGRO100, then as AS1411 after acquisition by Antisoma in 2005, and currently in Phase II clinical trials. AS1411 was developed from observations based on antiproliferative properties on cancer cells of some G-rich oligonucleotides. The antiproliferative activity of these GROs (such as the 29-mer GRO29A; 5'-TTTGGTGGTGGTGGTTGTGGTGGTGGTGG-3' with a 3' aminoalkyl modification) was associated with their ability to form stable G-quadruplex [25][26] and their biological activity was correlated with binding to a specific protein, known as nucleolin [25]. Additional studies showed that some analogues, including an unmodified DNA phosphodiester oligonucleotide (GRO29A-OH), were stable in serum-containing medium and thus

resistant to nuclease degradation [27], consequently AS1411 arose from the considerations that the 3'-modification was not required for either nuclease resistance or activity [27] and that the 5'-terminus "tail" (5'-TTT) of GRO29A was not essential for activity [28][29].

AS1411 displayed antiproliferative activity in huge number of cancer cell lines, proving such a tumor-selectivity [29][30].

AS1411 growth-inhibitory was dependent on the time course [28]; specifically when AS1411 was added to cells, cell division was inhibited and the induction of cell death occurred only after prolonged exposure (2–4 days, depending on the cell line).

Actually, AS1411 proceeds through Phase II clinical trials, but many questions about the activity and mechanism of action of GROs remain incomplete. In early studies the biological activities of GROs seemed to be depending on quadruplex formation and a specific GRO-protein binding [31]. The GROs molecular target was considered to be nucleolin, a multifunctional protein involving in many cellular processes, such as ribosome biogenesis, DNA replication, transcription, translation, chromatin remodelling, apoptosis, cytokinesis, protein trafficking and telomere maintenance [27][32]. Although nucleolin was considered mainly a nucleolar protein, its functions as a cell surface receptor and as a shuttling protein between cytoplasm and nucleus were reported [33]; furthermore it was found overexpressed in cytoplasm and on the cell surface of many cancer cells [30]. According to the ability of nucleolin to play a role in the endocytosis of many ligands, nucleolin-mediated cellular uptake mechanism for AS1411 was initially proposed. Further studies showed that the initial uptake of AS1411 occurs through macropinocytosis and that a subsequent abnormal nucleolin stimulated macropinocytosis (24–72 h after addition) led to the additional cancer-selective uptake of the aptamer [34].

Additionally, AS1411 has been found to inhibit many functions involving the nucleolin [28][35], but the exact role of nucleolin and the real mechanism of action of AS1411 haven't been clarified. After all in further studies the antiproliferative activity of GROs seemed to be attributed to the cytotoxicity of their guanosine-based degradation products [36].

While it is reasonable to suppose that GROs can target cancer cells through different pathways, poor information, if any, about the structure-activity relationships (SARs) between G-quadruplex typologies and protein interactions are available. Indeed, almost all anticancer GROs are characterized by a high grade of structural polymorphism [37][38]. They form in solution several G4 structures differing for the molecularity and/or loop arrangement [39]. Therefore, the possibility to fully understand the SAR of each oligodeoxynucleotide (ODN) is definitely subject to the availability of biologically active sequences forming single and well-defined G-quadruplex structures.

Interestingly, a cell-based screening of several GROs demonstrated that the GT-rich 15-mer ODN, TBA (thrombin binding aptamer $G_2T_2G_2TGTG_2T_2G_2$, an ODN binding and inhibiting thrombin) [40-42], possesses a significant antiproliferative activity [43]. Moreover, an electrophoretic mobility shift assay showed that TBA, like AS1411, is able to bind to a nucleolar protein, thought to be nucleolin [43]. A powerful correlation between the stability of the TBA tertiary structure and the two related functional effects has been shown as well. Both the anticoagulant [44] and the antiproliferative efficiencies [43] of TBA are enhanced in the presence of K^+ ions, which are known to promote and stabilize the structuration of TBA into a monomolecular chair-type antiparallel G-quadruplex.

Additionally, recently reported data suggested that antiparallel G-quadruplex forming ONs, including TBA, accumulate into mitochondria of CL1-0 living cells [45]. Into this cellular district, G4 structures could occur to regulate some essential events [46][47]. In particular, it has been shown that NOA1, a large GTP binding protein [48], binds some parallel and antiparallel G-quadruplex forming ONs [49]. Unfortunately, the potential of the TBA G4 as a molecular tool in cancer research is strongly limited by its high affinity to thrombin and to most of the thrombin precursors [50]. Still, since no connection between anticoagulant and antiproliferative activities is apparent, different TBA regions and/or different binding mode with its biological targets are most

likely involved, thus giving the opportunity to perform SAR studies of the two biological effects separately.

2.2. Results

In the quest for new TBA analogues endowed with increased antiproliferative activity, it is not unreasonable to start investigating chemical modifications of TBA sequence that, safeguarding the G4 tertiary structure, selectively quench its anti-thrombin activity. In the light of this reasoning and of the literature data concerning the TBA/thrombin interaction [41][42] and the related SARs, [51-53] we have synthesized a pool of seven new 15-mer TBA analogues (TBA-bs) (Table 1), each of them containing a dibenzyl linker replacing one nucleoside in the loop regions. The new TBA analogues were investigated for their structural and biological properties. CD and NMR measurements indicated that most of the new analogues were able to fold into monomolecular 'chair-like' G4s very similar to that adopted by the TBA. Biological results obtained by performing the fibrinogen, prothrombin time (PT) and Methylthiazol Tetrazolium (MTT) tests, indicated that two out of the seven derivatives (TBA-bs4 and TBA-bs13) lost the antithrombin and anticoagulant activities but preserved (TBA-bs4) or enhanced (TBA-bs13) the antiproliferative activity with respect to the TBA. The NMR based molecular model of the G4 formed by TBA-bs13 suggested that the dibenzyl linker could obstruct the binding of TBA-bs13 to thrombin, by steric hindrance in the inner region delimited by the TT loops, thus determining the exclusive switch of the biological activity toward the antiproliferative one.

Table 1. TBA-based sequences (TBA-bs) containing 2,2-dibenzylpropane-1,3- diol (**X**) at the indicated position

| ON | Sequence |
|----------|---|
| TBA | G ₁ G ₂ T ₃ T ₄ G ₅ G ₆ T ₇ G ₈ T ₉ G ₁₀ G ₁₁ T ₁₂ T ₁₃ G ₁₄ G ₁₅ |
| TBA-bs3 | G ₁ G ₂ X ₃ T ₄ G ₅ G ₆ T ₇ G ₈ T ₉ G ₁₀ G ₁₁ T ₁₂ T ₁₃ G ₁₄ G ₁₅ |
| TBA-bs4 | G ₁ G ₂ T ₃ X ₄ G ₅ G ₆ T ₇ G ₈ T ₉ G ₁₀ G ₁₁ T ₁₂ T ₁₃ G ₁₄ G ₁₅ |
| TBA-bs7 | G ₁ G ₂ T ₃ T ₄ G ₅ G ₆ X ₇ G ₈ T ₉ G ₁₀ G ₁₁ T ₁₂ T ₁₃ G ₁₄ G ₁₅ |
| TBA-bs8 | G ₁ G ₂ T ₃ T ₄ G ₅ G ₆ T ₇ X ₈ T ₉ G ₁₀ G ₁₁ T ₁₂ T ₁₃ G ₁₄ G ₁₅ |
| TBA-bs9 | G ₁ G ₂ T ₃ T ₄ G ₅ G ₆ T ₇ G ₈ X ₉ G ₁₀ G ₁₁ T ₁₂ T ₁₃ G ₁₄ G ₁₅ |
| TBA-bs12 | G ₁ G ₂ T ₃ T ₄ G ₅ G ₆ T ₇ G ₈ T ₉ G ₁₀ G ₁₁ X ₁₂ T ₁₃ G ₁₄ G ₁₅ |
| TBA-bs13 | G ₁ G ₂ T ₃ T ₄ G ₅ G ₆ T ₇ G ₈ T ₉ G ₁₀ G ₁₁ T ₁₂ X ₁₃ G ₁₄ G ₁₅ |

X = 2,2-dibenzylpropane-1,3-diol.

Synthesis of ONs

The synthesis of derivative **3** (Figure 7) started from the commercially available 2,2-dibenzylpropane-1,3-diol **1**, that was subjected to the standard protection of one alcoholic function with 4,4'-dimethoxytrityl group. The protected product **2** was then reacted with β -cyanoethyl-N,N'-diisopropyl-chloro-phosphoramidite to obtain **3**. This monomer was used to automatically synthesize the modified ONs reported in Table 1 using the standard phosphoramidite protocol [54]. The length of the coupling cycle using the new monomer **3** was extended from 2 min to 10 min. The yields of coupling were similar to those obtained using the standard phosphoramidite building blocks.

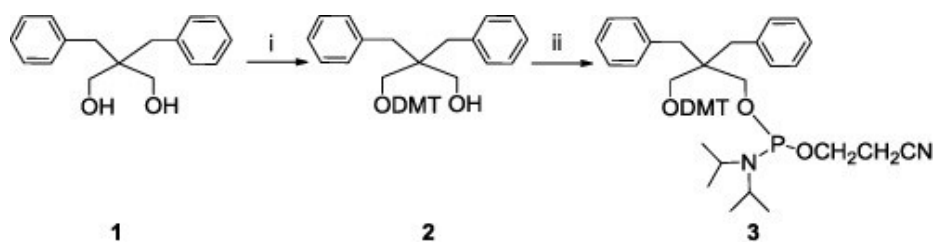


Figure 7. Synthesis of phosphoramidite building block. i) 2,2-dibenzylpropane-1,3-diol 1 (2.0 g, 7.8 mmol), 4,4-dimethoxytrityl chloride (1.32 g, 3.9 mmol), 4-dimethylaminopyridine (2.0×10^{-2} g, 0.16 mmol) dry Py (5.0 ml), 2.5 h, yields 40%; ii) 2 (1.0 g, 1.8 mmol), β-cyanoethyl-N,N'-diisopropyl-chloro-phosphoramidite (0.450 ml, 1.8 mmol), DIPEA (0.350 ml, 3.6 mmol), dry DCM (3.5 ml), 1.0 h, 85%.

CD and CD melting

The folding of TBA into the monomolecular antiparallel chair-like G-quadruplex structure causes a well-known CD profile characterized by three positive bands at 212, 247 and 295 nm and a negative band around 270 nm [55]. Indeed, CD spectroscopy is commonly used to quickly evaluate the effects of sequence modifications on the general feature of TBA G-quadruplex [56]. To this purpose we performed CD analyses both in PBS (Figure 8) and K^+ buffer. From collected data it appears that almost all new ONs in both used buffers fold into structures that display a CD profile very close to that of TBA. However, in some cases slight differences in the profile or in the intensity of bands were revealed. To analyse these effects as a function of the position occupied by dibenzyl linker along the sequence, the collected data were divided into two sets.

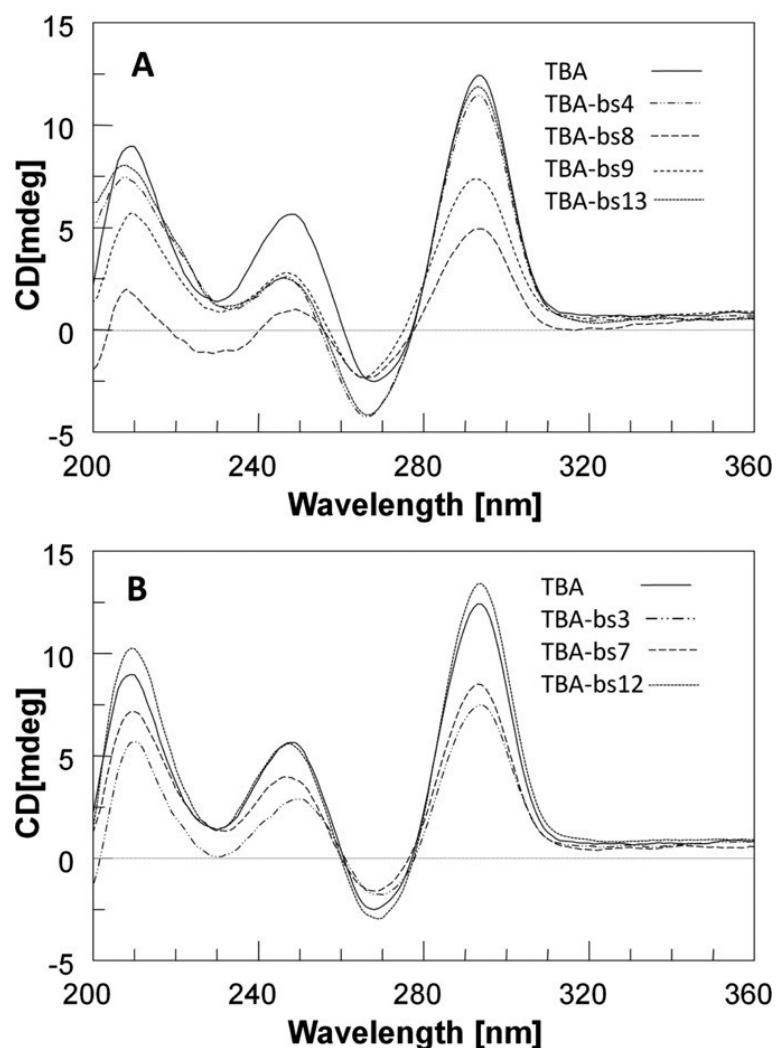


Figure 8. CD profile of TBA and TBA-based sequences. Spectra were collected at 10°C, using [ON] of 2.0×10^{-5} M in PBS buffer.

According to NMR and X-ray data, that designate the residues at position 4, 8, 9 and 13 as essential for the topology and the stability of the G4 structure, we grouped the CD profiles of the corresponding TBA-bs variants in figure 8, panel A. Notably, the CD spectra of TBA-bs8 and TBA-bs9 showed a significant decreasing in the intensity of the CD band at 292 nm, compared to that of TBA. Furthermore, the spectra of the variants (Figure 8a) containing the linker **1** at position 4 or 9 or 13 were strongly similar to each other and slightly differed from that of TBA by a more negative CD signal in the range 230–270 nm.

The CD spectra of TBA-bs modified at position 3 or 7 or 12 are shown in figure 8, panel B. All the variants in this group preserved almost unchanged the CD profile of TBA. The only difference we observed was a slight decrease in the intensity of the positive CD bands for TBA-bs3 and TBA-bs7. To evaluate the thermal stability of the folded G-quadruplexes we performed CD melting experiments. The melting curves were registered monitoring the change of the intensity of the band at 295 nm increasing the temperature from 10°C to 90°C (Figure 9). The derived apparent melting temperatures (Table 2) indicated that the thermal stability of TBA-bs4 and TBA-bs13 G4s was slightly higher than that measured for TBA ($\Delta T_m \sim 3\text{--}4^\circ\text{C}$ in both PBS and K^+ buffer) whereas that of TBA-bs3, TBA-bs7 and TBA-bs12 was almost unchanged. In contrast, TBA-bs8 and, especially, TBA-bs9 folded into G4s considerably less stable than that of TBA in both K^+ buffer ($\Delta T_m -4.3$ and -15.5°C , respectively) and PBS. Furthermore, in the case of TBA-bs9, as a result of the poor structure stability in PBS, it was not possible to calculate the melting temperature from the corresponding melting curve.

Finally, to probe the molecularity of the G-quadruplexes, all the CD melting experiments in K^+ buffer were also performed on samples at the two additional strand concentrations of 1.0×10^{-4} and 8.3×10^{-6} M (12-fold relative dilution). For all TBAs, we did not observe significant differences between the two sets of melting profiles thus suggesting that the modified ONs preserve the ability of TBA to fold into monomolecular G4s [57].

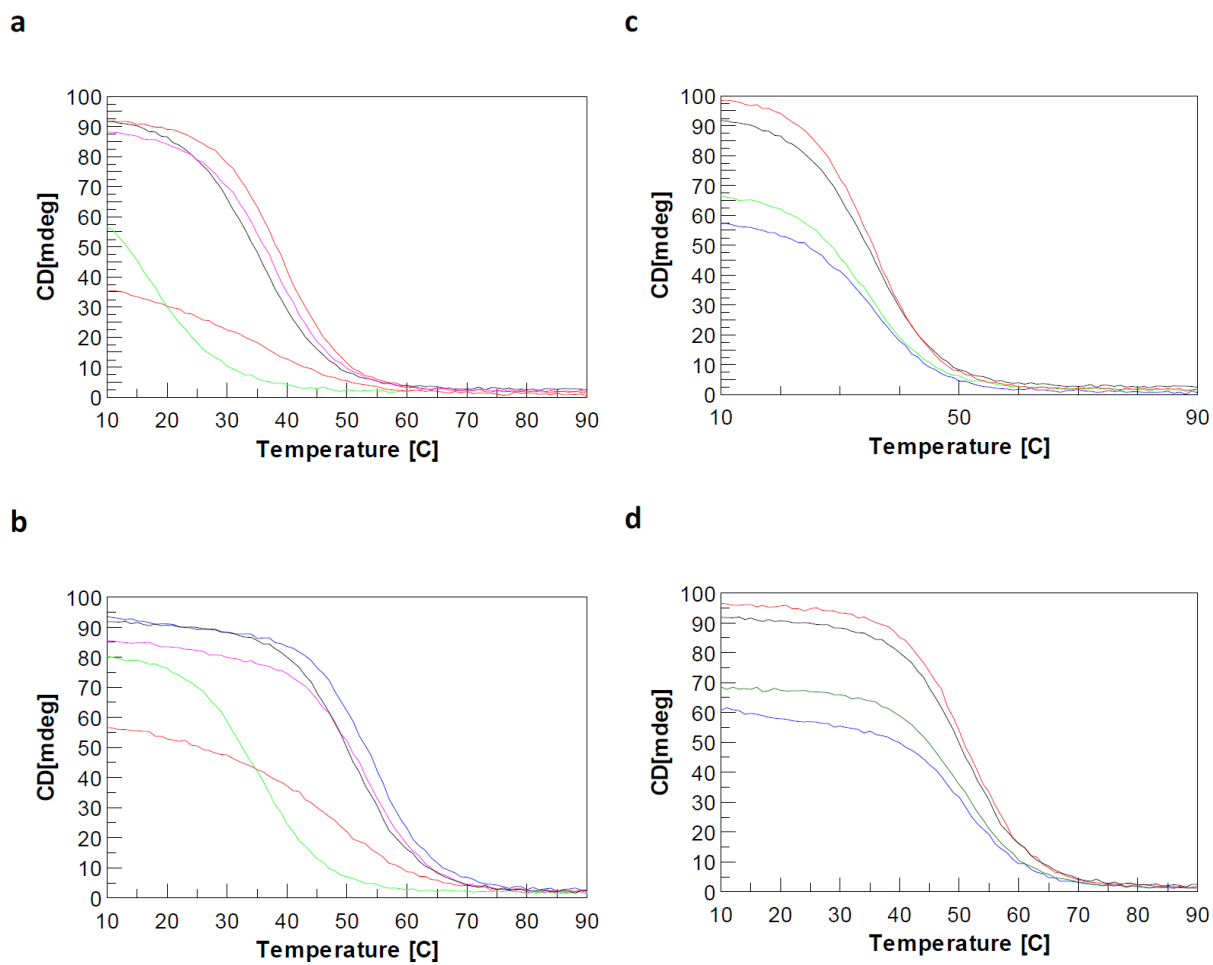


Figure 9. CD melting profiles of TBA and TBA-based sequences. Fixed wavelength 295 nm, [ON] of 2.0×10^{-5} M. Cell length 0.5 cm. Temperature scan speed 0.5 °C/min. **a.** PBS. **b.** K⁺ buffer. Lines: black TBA; red TBA-bs8; green TBA-bs9; fuchsia TBA-bs4; blue TBA-bs13. **c.** PBS. **d.** K⁺ buffer. Lines: black TBA; blue TBA-bs3; green TBA-bs7; red TBA-bs12.

Table 2. Thermal stability and biological properties of TBA and TBA-based sequences. The apparent melting temperatures (°C) were measured as minimum in the first derivative of CD melting profiles.

| <i>Name</i> | ^a <i>T_m</i> (K) | ^b ΔT_m | ^c <i>T_m</i> (PBS) | ^b ΔT_m | ^d <i>w/o</i> ± ^e SD 10 μ M | ^f <i>PT</i> ± ^g SE 20 μ M |
|-----------------|---------------------------------------|---------------------------|---|---------------------------|--|---|
| TBA | 50.7 | 0 | 35.1 | 0 | 0.669±0.054 | 49.8 ± 1.28 |
| TBA-Bs3 | 50.0 | -0.7 | 35.4 | +0.3 | 0.996±0.045 | 43.6 ± 2.15 |
| TBA-Bs4 | 51.9 | +1.2 | 37.2 | +2.1 | 0.700±0.093 | 14.1 ± 0.25 |
| TBA-Bs7 | 50.0 | -0.7 | 34.5 | -0.6 | 0.400±0.103 | 56.3 ± 0.97 |
| TBA-Bs8 | 46.4 | -4.3 | 34.4 | -0.7 | 0.811±0.047 | 25.8 ± 0.30 |
| TBA-Bs9 | 35.3 | -15.4 | ^h n.d. | ^h n.d. | 1.087±0.1059 | 24.8 ± 0.80 |
| TBA-Bs12 | 51.1 | +0.4 | 35.4 | +0.3 | 0.739±0.031 | 52.0 ± 1.73 |
| TBA-Bs13 | 53.3 | +2.6 | 38.9 | +3.8 | 0.498±0.103 | 12.5 ± 0.55 |

^aAnnealing buffer: 90 mM KCl, 10 mM potassium phosphate, pH 7.4.

^bCalculated respect to TBA melting temperature.

^cAnnealing buffer: PBS, pH 7.4.

^dRatio between measured absorbance in MTT test in presence and in absence of ONs.

^eStandard Deviation.

^fMeasured Prothrombin Time in human plasma.

^gStandard Error.

^hnot determinable.

NMR structural characterization

The ability of all the here reported TBA-bs to fold into a TBA-like antiparallel quadruplex was also assessed by NMR spectrometry. The ¹H NMR spectrum of TBA annealed in Na⁺ or K⁺ containing buffer is characterized by the presence of eight well resolved signals in the 11.5–12.5 ppm region, attributable to the exchange protected imino protons involved in the formation of two G tetrads, and by fifteen aromatic proton signals (6.8–8.5 ppm) attributable to H8 and H6 protons of guanine and thymine bases, respectively. Moreover, two peculiar upfield-shifted methyl signals of mutually H-bonded T4 and T13 are seen at around 1.0 ppm. Finally, the alternating *syn-anti-syn-anti* glycosidic bond conformation within the two stacked G-tetrads, typical of most antiparallel quadruplexes, is

observed. As for the TBA, the quadruplex diagnostic imino signals were observed in the water suppressed ^1H NMR spectra of the here reported TBA-bs, with the noticeable exception of TBA-bs8 (Figure 10). Hence, the replacement of a single T residue in one of the three loops for the dibenzyl linker did not impede the quadruplex formation, whereas the replacement of G8, the only guanosine in the sequence not engaged in the two G-tetrads, did it. In particular, as we already observed in our previous papers [53][58], the replacement of T3 or T4 in the TBA sequence with acyclic nucleoside analogues induces changes in the resulting NMR profiles that are very similar to those induced when the replacement occurs at T12 or T13, respectively. It is interesting to note that the similarity observed between members of each TBA-bs3/TBA-bs12 or TBA-bs4/TBA-bs13 couple was also observed by CD and by fibrinogen or prothrombin time assays (vide infra). According to the biological results, we undertook a detailed structural study of the G-quadruplexes formed by TBA-bs12 and TBA-bs13 by using the NMR-refined molecular mechanics approach [40], based on the analyses of NOE connectivities and TOCSY spectra.

NOE connectivities in the G-quadruplex structures arise from the glycosidic bonds within the G-tetrad, in particular between the H8/6 proton of the base and the H1' proton of the sugar, and also between the H8/6 proton of the base and H1' proton of the next base sugar, observable in a *syn* to *anti* conformation. Furthermore, specific NOE connectivities can elucidate the G-quadruplex folding topology. The cyclic NOE connectivities between the imino (H1) proton of a guanine and the H8 proton of the next guanine are used to assess the G-tetrad alignment. Moreover, NOEs between imino protons of adjacent guanines can also be detected, but in many cases these cross-peaks are not distinctly observable.

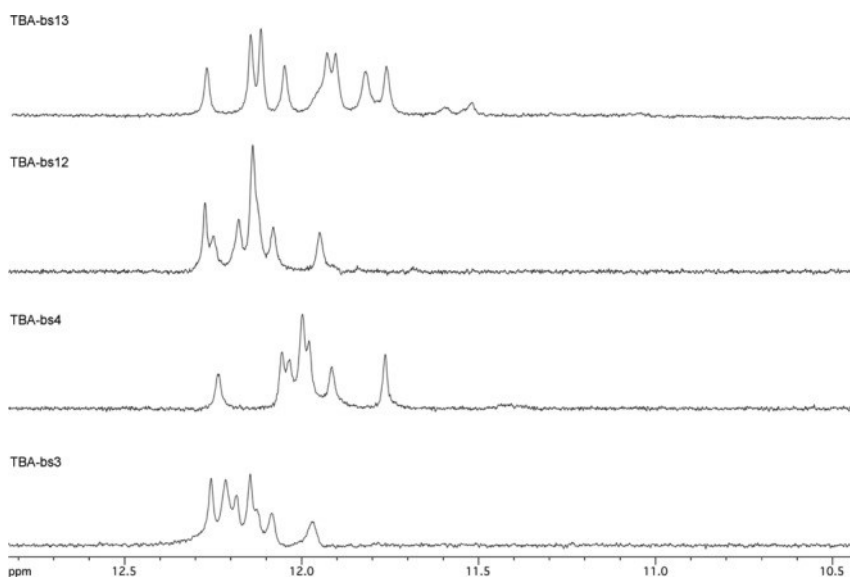


Figure 10. Representative ^1H NMR imino proton regions of TBA-bs incorporating the 2,2-dibenzylpropane-1,3-diol at the indicated position (25°C; PBS buffer, $\text{H}_2\text{O}/\text{D}_2\text{O}$ 9:1).

Structural investigation of TBA-bs12

The ^1H NMR spectrum of TBA-bs12 recorded at 25°C (Figure 10) was characterized by the presence of eight partially overlapped signals in the 11.9–12.3 ppm region attributable to the exchange-protected imino protons involved in the formation of Hoogsteen hydrogen bonds of two G-tetrads, in close analogy with previous observations on the antiparallel quadruplex formed by the unmodified TBA [40]. Because of the presence of the two benzene rings in the linker at position 12, the aromatic portion of the ^1H spectrum (6.8–8.5 ppm) was populated by more than the 14 signals belonging to the protons of guanines and thymine of the G4 structure. In addition, other weaker signals belonging to one or more minor conformations likely including the unfolded form were observed in this region. With the aim of minimizing the exchange between the G-quadruplex and the unfolded form, we recorded the ^1H NMR spectrum of TBA-bs12 also at 10°C (Figure 11, panel A). As expected, a general simplification of the NMR spectrum was observed. In particular, at 10°C most of the weaker signals disappeared and an improved dispersion of the signals was obtained. The combined analysis of 2D NOESY and TOCSY spectra (700 MHz, 10°C) allowed us to get the nearly complete assignment of exchangeable and non-exchangeable protons using the

standard procedure. The TOCSY data are not shown here, but they were used to confirm the assignments based on the NOESY data. The overall analysis of NOE connectivities and the evaluation of the $\Delta\delta$ between TBA-bs12 and TBA confirmed that TBA-bs12 adopts a three-dimensional structure that is very similar to the TBA chair-like antiparallel quadruplex. In particular, the analysis of the intranucleotide and internucleotides H8/H6 to H1' NOE connectivities (Figure 11, panel B) confirmed that four out of the eight guanosines involved in the two G-tetrads adopt the syn glycosidic bond conformation, as seen for TBA. The NOE connectivities between the methyl signal of T9 and four imino protons confirmed that T9 is stacked above the G1-G15-G10-G6 G-tetrad (synGs are underlined) (Figure 11, panel C). Finally, the very low $\Delta\delta$ observed for the methyl signal of T4 (δ 1.07 ppm; $\Delta\delta$ 0.04 ppm) disclosed that the substitution of T12 with the linker **1** did not interfere with the tertiary structure adopted by TBA-bs12, even in the close proximity of the substitution site, and suggested that the two benzene rings could not occupy the cleft delimited by the two TT loops. The latter observation is noteworthy, considering that most of the X-ray diffraction data of TBA-thrombin complexes have shown that the TBA recognizes the thrombin anion-binding exosite I (ABE I; also known as the fibrinogen exosite) by using the T3-T4 and T12-T13 loops. To get insights about the orientation of the benzene rings of **1** with respect to the quadruplex scaffold, and to rationalize the effects on the antiproliferative and antithrombin activities shown by TBA-bs12, we performed a NMR-restrained molecular mechanics study. As we expected, among the 109 NMR inter proton distances used in the calculations only a few involved close contacts with the atoms of the linker **1**, and the resulting averaged structure confirmed in full (Figure 12) that in the G4 structure formed by TBA-bs12, the two benzene rings are positioned aside from the G4 core, thus allowing its recognition by the thrombin ABE I.

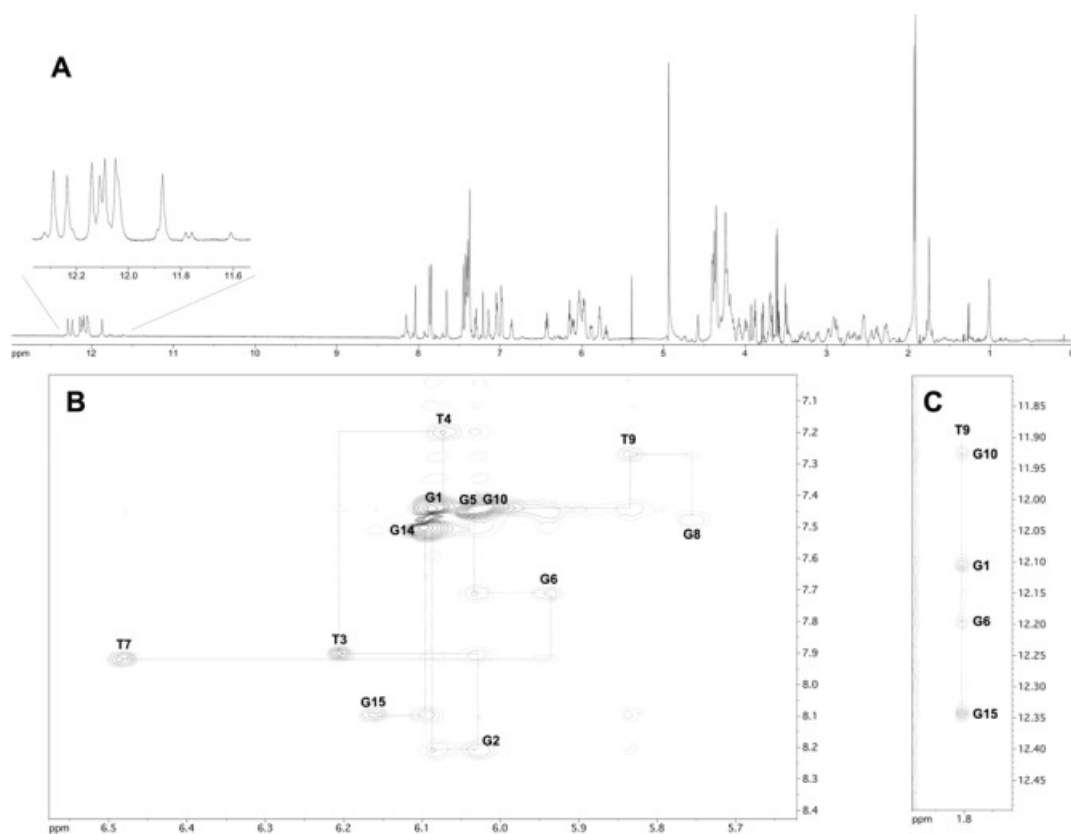


Figure 11. NMR study of TBA-bs12 annealed in PBS/D₂O 9:1 (10°C, 700 MHz). (A) ¹H NMR spectrum. The expansion of the imino proton region is shown in the inset. (B, C) Expansions of the 2D NOESY (200 ms mixing time) spectrum. The sequential H1'-H8 or H1'-H6 connectivities and the self-peaks involving H1' protons have been drawn in B using dotted lines and labels, respectively. NOE correlations between T9 methyl protons and H8 protons of the G10-G1-G6-G15 tetrad are shown in C.

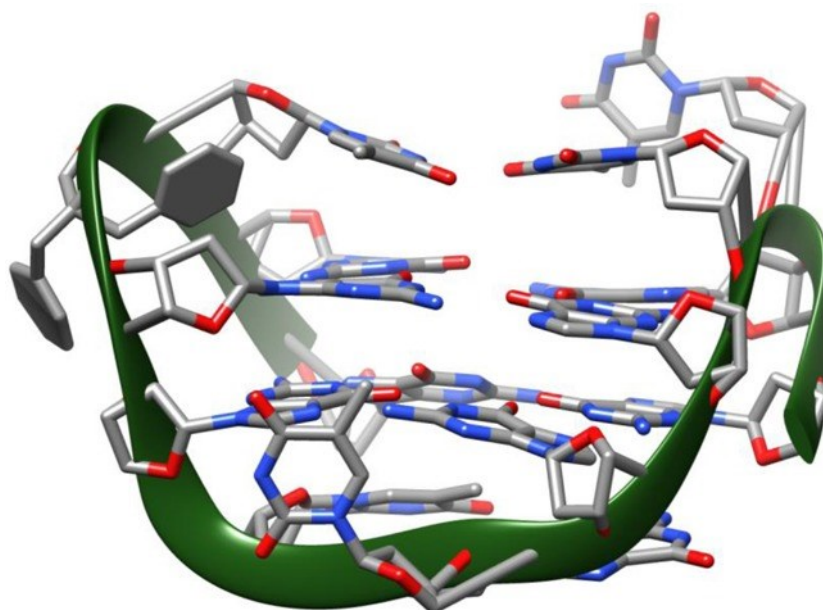


Figure 12. 3D average structure of TBA-bs12 obtained by NMR-restrained molecular mechanics. Nucleotides are shown as sticks, the 2,2-dibenzylpropan-1,3-diol linker as sticks and filled rings and the phosphate backbone as a green solid ribbon.

Structural investigation of TBA-bs13

The NMR structural elucidation of the G4 formed by TBA-bs13 in PBS buffer was performed as described above for TBA-bs12. The NMR characterization confirmed the formation of a stable antiparallel chair-like G4 stabilized by two G-tetrads (8 well resolved imino proton signals; Figure 13, panel A) connected by the T3-T4, T12-X13 and T7-G8-T9 loops. Intra- and inter-nucleotide NOE connectivities confirmed that the methyl group of T9 is stacked above the G1-G15-G10-G6 tetrad (Figure 13, panel C) and that the two G-tetrads are made up of alternating *syn* and *anti* Gs (Figure 13, panel B). All together, the analysis of the ^1H chemical shifts and $\Delta\delta$ between the NMR signals of TBA-bs13 and TBA indicated that the incorporation of the dibenzyl linker at position 13 of TBA does not induce major distortions in the resulting G4 scaffold. However, differently from TBA-bs12, we observed a significant up-field shifting for the imino protons of G5, G6, G10, G11, G14 and G15, and a down-field shifting for the methyl signals of T4 and T12. These NMR evidence suggested that the two benzene rings of the linker were not projected aside the G4 core as found for TBA-bs12. Accordingly, among the 75 NOE distance restraints included in the calculations, 8 involved NOE contacts between the atoms of the linker and those of nucleosides G11, T12 and G14. The resulting minimized average structure of TBA-bs13 obtained by the NMR-refined molecular mechanics calculations is shown in Figure 14. According to the simulated structure, the two benzene rings of X13 are located in the pocket delimited by the two TT loops. In particular, the ring coloured in red in Figure 14 is stacked exactly above the 6-membered ring of G11, whereas the blue ring is turned away the G2-G5-G11-G14 tetrad pointing at the T3-T4 loop. These findings are in agreement with the observed $\Delta\delta$ caused by the strong benzene rings current.

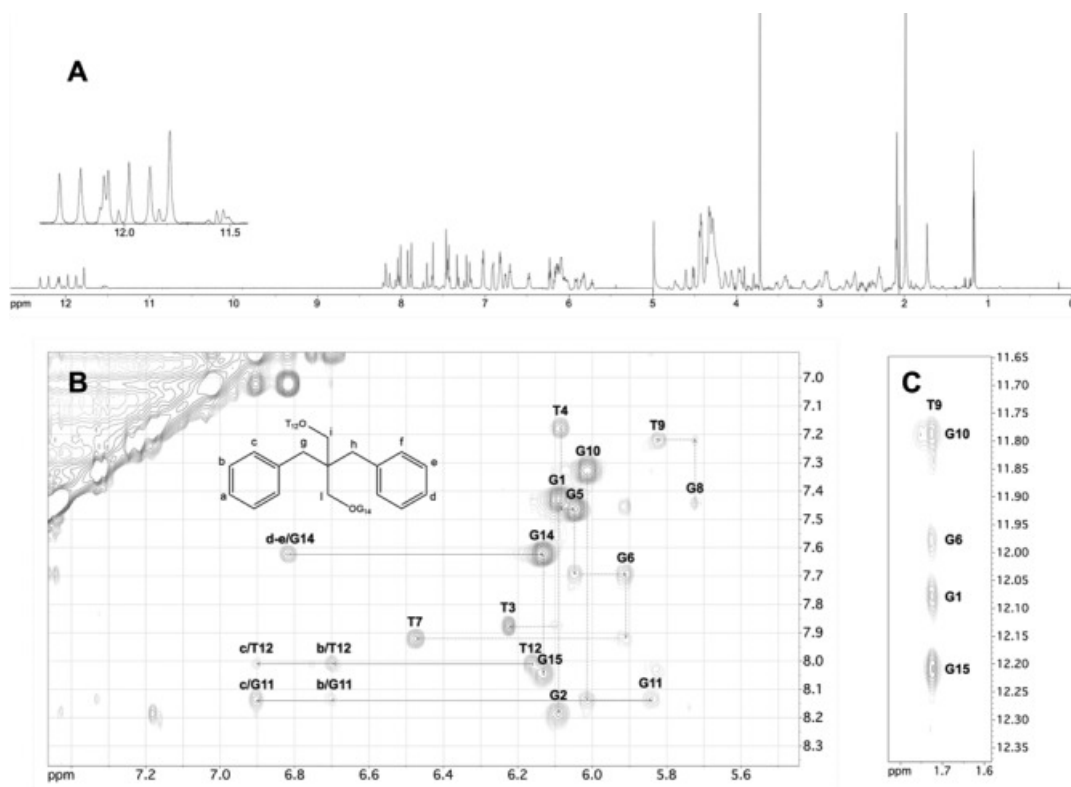


Figure 13. NMR study of TBA-bs13 annealed in PBS/D₂O 9:1 (10°C, 700 MHz). (A) ¹H NMR spectrum. The expansion of the imino proton region is shown in the inset. (B,C) Expansions of the 2D NOESY (200 ms mixing time) spectrum. The NOE connectivities between atoms of X13 and nucleotides atoms are traced and labelled in panel B. The sequential H1'-H8 or H1'-H6 connectivities and the self-peaks involving H1' protons have been drawn in B using dotted lines and labels, respectively. NOE correlations between T9 methyl protons and H8 protons of the G10-G1-G6-G15 tetrad are shown in C.

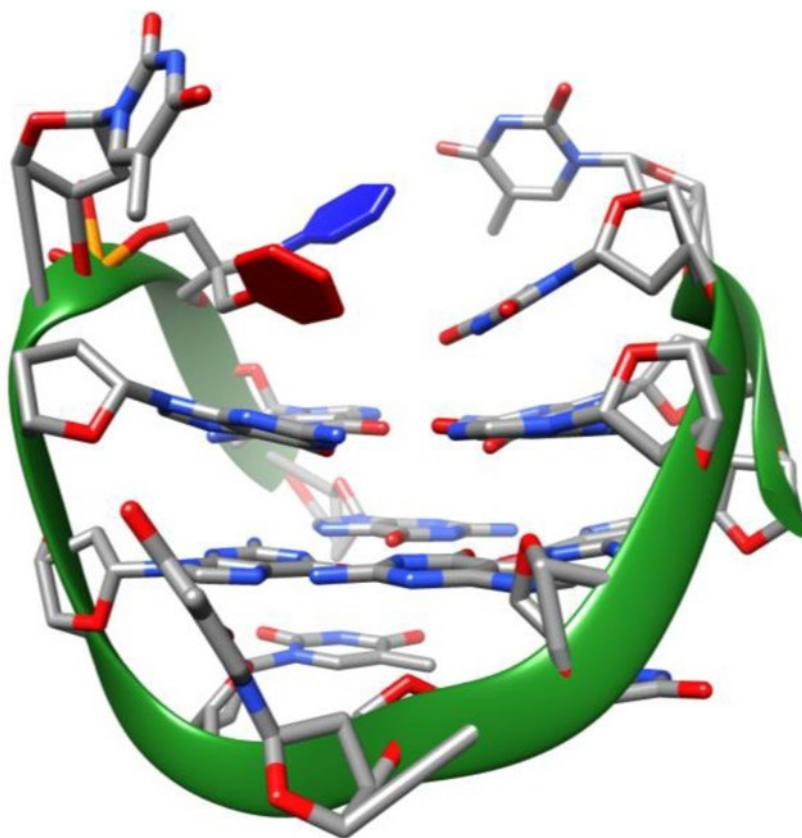


Figure 14. 3D average structure of TBA-bs13 obtained by NMR-restrained molecular mechanics. Nucleotides are shown as sticks, the 2,2-dibenzylpropan-1,3-diol linker as sticks and red and blue filled rings and the phosphate backbone as a green solid ribbon.

Fibrinogen assay

In order to assess the effect on the enzymatic activity of thrombin and to correlate the biological effects with the structural data, the modified ONs were tested in the fibrinogen clotting assay. The thrombin-induced clotting of fibrinogen was measured spectrophotometrically, following the increase in absorbance at 380 nm as a function of time [59]. The assay was performed using 2 mg per ml of fibrinogen, 1 NIH of thrombin and various concentrations of each aptamer (20, 50 and 100 nM). The comparison of resulting data (Figure 15) evidenced marked differences among the modified TBA-bs in their ability to inhibit the fibrinogen clotting formation. TBA-bs12 showed an increased inhibitory effect relative to the unmodified sequence, at all explored concentrations. TBA, TBA-bs3 and TBA-bs7 prolonged the fibrinogen clotting time at almost the same extent. TBA-bs9 and, especially, TBA-bs8 showed a significant decreased inhibitory effect relatively to TBA. Most

significantly, at all explored concentrations, TBA-bs4 and TBA-bs13 resulted totally unable to compete with fibrinogen for the binding to the enzyme.

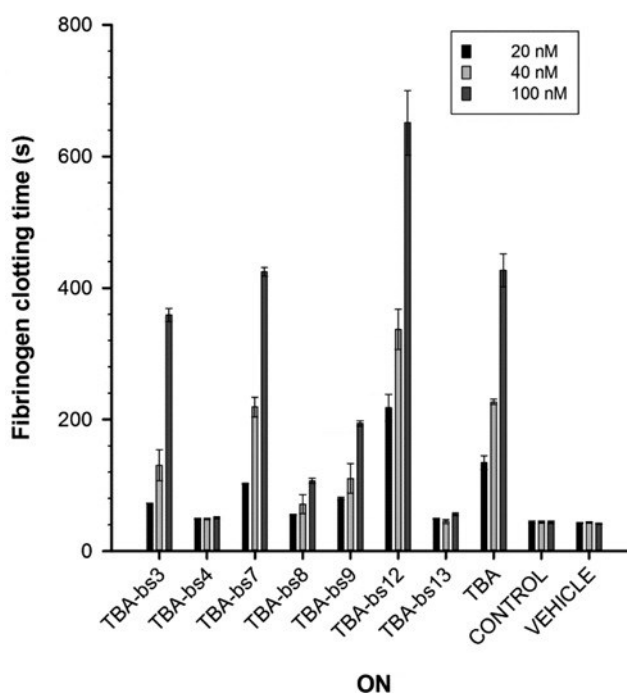


Figure 15. Fibrinogen clotting time (sec) in presence of each ON measured at three different concentrations (20, 40 and 100 nM). The bars of control and vehicle represent the fibrinogen clotting time values of the system in absence of any ONs and diluted with the buffer alone, respectively.

PT assay

To validate the results obtained from the fibrinogen clotting assay, we performed PT tests on human plasma (PT assay). As shown in figure 16, the PT values pointed to a trend of the anticoagulant activities that was almost in agreement with the antithrombin activities measured in the fibrinogen assay. Major difference resulted in the behaviour of TBA-bs12, which showed in fibrinogen assay, but not in PT test, a significant increasing in the antithrombin efficiency with respect to TBA. Herein, among the tested ONs, TBA-bs7 proceeded as the best anticoagulant one. The PT values measured in presence of TBA-bs4 or TBA-bs13 confirmed that these modified sequences were wholly unable to inhibit thrombin.

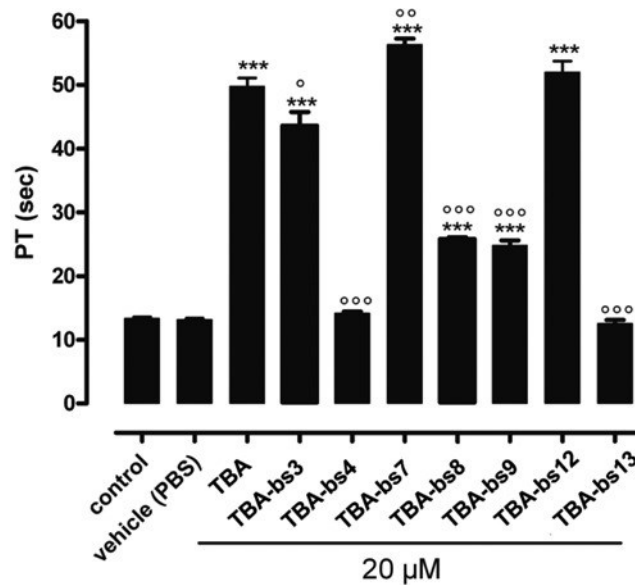


Figure 16. PT values obtained following 15 min of ON incubation with human plasma at concentration of 20 μM [ON]. Each measurement has been performed in triplicate and it was shown as mean \pm SEM. PT values are expressed in seconds. The basal PT time is 13.4 ± 0.2 s. ***= $P < 0.001$ vs. vehicle; °, °°, °°°= $P < 0.05, < 0.01, < 0.001$ versus TBA.

MTT test

On the basis of literature data [43], all modified sequences and TBA were examined for their antiproliferative activities against He-La cervical carcinoma cell line at three different concentrations, 1 (Figure 17, panel A), 5 and 10 μM (Figure 17, panel B). As a result, all but TBA-bs9 were judged to be active against this tumor cell line. Specifically, TBA-bs7 and TBA-bs13 had the greatest effect on the cell growth, at all tested concentrations. Notably, TBA-bs4 and TBA-bs13 preserved the antiproliferative activity of TBA against He-La cells, but, according to fibrinogen and PT data, lacked in thrombin affinity. To better explore the antiproliferative effect of TBA-bs13, dose-response experiments at concentrations between 1.0×10^{-3} and 50 μM were performed. The obtained clear dose-response curves indicated a 5-fold increased cell growth inhibition for TBA-bs13 with respect to TBA (Figure 18).

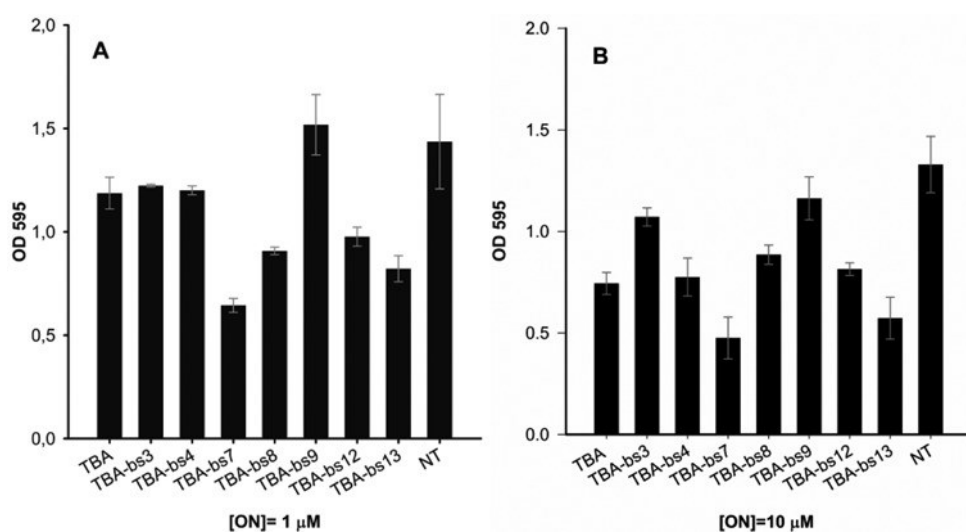


Figure 17. Antiproliferative activity on He-La cervical carcinoma. Cells were treated with two different doses of ON, 1 (A) and 10 (B) μM , annealed in K^+ buffer (see experimental section). The bar NT (Not Treated) reports the cell viability in absence of ON. Cell viability was assayed seven days after addition of ON using the MTT assay. A pool of three different sets of experiments (each repeated in triplicate) was performed, and each value expressed as mean \pm Standard Deviation.

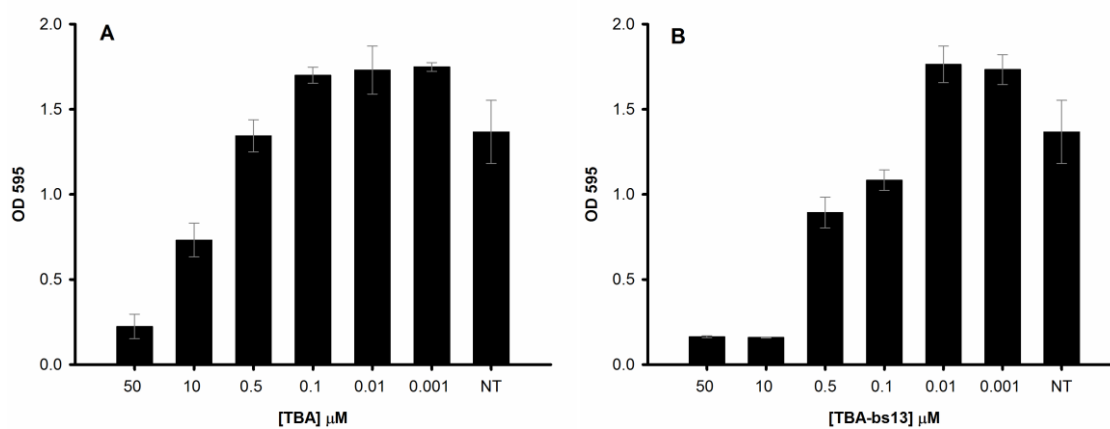


Figure 18. Concentration-dependent response in MTT assay for TBA (A) and TBA-bs13 (B). Cell viability was assayed seven days after addition of ON using the MTT assay. A pool of three different sets of experiments (each repeated in triplicate) was performed, and each value expressed as mean \pm Standard Deviation.

2.3. Discussion

The findings that specific modifications of TT loops of TBA negatively interfere with its thrombin affinity without affecting the G-quadruplex stability [58][60], and that the antiproliferative activity is a general property of GT-rich ON strands [35] make ready the perspectives of modified TBAs as

selective antiproliferative ONs provided with the notable advantage to fold into well-defined G-quadruplex structures. Aimed by this idea, we selected, among the commercially available acyclic diols, the unusual dibenzyl-linker **1** (Figure 7) as the modifying agent for the obtainment of a series of new TBA-based sequences (see Table 1) in which **1** (indicated as X in Table1) replaced one at the time the loop nucleotides of TBA. Indeed, the linker **1** provided for: (i) two hydroxyls, to make the required phosphoramidite building block **3**; (ii) an aromatic portion, to mimic the aptitude of some loop residues in the TBA G-quadruplex to stack on the adjacent G-quartet [41][42]; (iii) a moderate bulky portion, to cause steric clash between the TBA G4 and thrombin [58]. Finally, as the requirements were fulfilled into symmetrical molecules, it was also ensured that the insertion of the linker did not give rise to diastereomeric nucleic acid sequences [60].

CD and ¹H NMR studies performed on the new synthesized TBA-bs suggested that the resulting G4 structures strongly resembled that of the TBA (Figures 8-10). Indeed, all CD profiles showed the stronger positive band around 295 nm and a weak negative band around 270 nm, that are generally accepted as distinctive for antiparallel G4s structures [55][56]. According to the CD data, the G4 diagnostic imino signals were observed in the 11.5–12.5 ppm region of the ¹H NMR spectra of the new derivatives (for some examples see Figure 10), as for the TBA, with the exception of TBA-bs8. Furthermore, in line with previous structural data which arranged the nucleobases 3, 12 and 7 outside the G-quadruplex core, the apparent CD melting temperatures of the G4 TBA-bs3, TBA-bs12 and TBA-bs7 were similar to that of TBA (Figure 9 and table 2). Differently, substantial destabilization of the G4 structure occurred when the linker **1** occupied the position 8 or 9 of the TGT loop ($\Delta T_m = -4.3$ and -15.5°C , respectively, compared to that of TBA in K^+ buffer; (Figure 9 and Table2). Given that T8 and G9 stack on the G1-G15-G10-G6 quartet, thus stabilizing the TBA G-quadruplex core, the obtained T_m values suggested that neither of the two benzene rings of the linker **1** efficiently mimic the role of the replaced nucleobase in the G4 structure formed by TBA-bs8 and TBA-bs9.

Interestingly, stable antiparallel G4s were obtained from the folding of TBA-bs4 and TBA-bs13 ($T_m = 51.9$ and 53.3°C , respectively, in K^+ buffer; 37.2 and 38.9°C in PBS; Table 2), thus suggesting that the aromatic moieties at position 4 or 13 could provide for the stacking interactions with the nucleobase on the adjacent quartet (G2-G5-G11-G14).

The results from PT and fibrinogen assays (Figures 15-16) allowed us to assess the involvement of the linker **1** in the formation of TBA-thrombin complex, while those from the MTT assay (Figures 17-18) the influence of **1** on the TBA cytotoxicity. By modifying the TGT loop, it resulted that TBA-bs8 and TBA-bs9, that folded into the least stable G4 structures, still affected, although with reduced efficiency, the coagulation time measured in both the fibrinogen and PT assays (Figures 15-16) and showed the lowest antiproliferative effects in the MTT test on He-la carcinoma cell line (Figures 17-18). On the other hand, both the anticoagulant activity and the cytotoxic effect of TBA-bs7 resulted increased. These results could reflect a tighter correlation between the structural stability of G4s and the antiproliferative activity [26][35], than that observed with the antithrombin efficiency [60][58]. Indeed, among these three ONs, the best-structured TBA variant (TBA-bs7) was also the strongest growth-inhibitor agent and *viceversa* (TBA-bs9). However, none of these ONs showed a selective action with respect to the two functional effects. Consequently, their G4 structures were not further investigated. The most relevant outcomes emerged from TBA variants modified at one residue of the TT loops. In fact, although the corresponding G4s had T_m values very similar to each other ($\Delta T < 3.3^\circ\text{C}$; Table 2), their biological properties were significantly different. In the MTT assay (Figures 17-18), TBA-bs4 and TBA-bs13, which resulted totally unable to act as anticoagulant agents (Figures 15-16; Table 2), showed significant cytotoxic effects on He-La cells, and TBA-bs13 was a better inhibitor of cell growth than TBA. Contrarily, TBA-bs3 and TBA-bs12 afforded to a good correlation between structure stability, antithrombin and antiproliferative activities (Figures 15-18, Table 2).

The biological properties of the last two sequences were almost comparable to that of TBA. Nevertheless, it was also observed that the increased antithrombin activity of TBA-bs12 with respect to TBA, measured in fibrinogen assay (Figure 15), was not observed in the PT test (Figure 16, Table 2). Such incoherence between the fibrinogen and PT data was previously observed by us and others for other TBA variants, and supports the hypothesis that the clotting inhibitory activity of some modified TBAs could not wholly depend on the ability of the aptamers to compete with fibrinogen for thrombin ABE I. In fact, the presence in the plasma medium of other thrombin effectors and/or precursors, and the thrombin allostery, which regulates the complex thrombin action during homeostasis, could also play an important role in determining the anticoagulant effect of such type of TBA derivatives. However, the overall results evidenced that, despite the TBA G-quadruplex well sustained the replacement of one T with the linker 1 at any position of the TT loops, the TBA-thrombin complex did not tolerate such modification at T4 or T13. Furthermore, the results were consistent with the TBA tertiary structure, which leads residues T3 and T12, as well as T4 and T13, to occupy equivalent positions with respect to the G quartets. Nevertheless, TBA-bs12 and TBA-bs13 are slightly more potent inhibitors of cell growth than TBA-bs3 and TBA-bs4, respectively (Figures 17-18). At the best of our knowledge, this is the first evidence that loop structure is a further parameter capable to affect the antiproliferative efficiency of the TBA G-quadruplex in addition to G4 stability.

To better understand the requirements to discriminate between the antiproliferative and antithrombin effects, we undertook an extensive 2D NMR study of the G4s formed by TBA-bs12 and TBA-bs13 in PBS buffer. The inspection of the NMR-restrained molecular mechanics average G4 structure of TBA-bs12 (Figures 11-12) confirmed that the two benzene rings of 1 are projected outside the G4 core. In contrast, in the corresponding average structure obtained for TBA-bs13, the benzene ring coloured in red in figure 14 stacked exactly above the 6-membered ring of G11, whereas the blue ring turned away the G2-G5-G11-G14 tetrad pointing at the T3-T4 loop. These

findings agree in full with the anticoagulant activities showed by TBA-bs12 and TBA-bs13. In fact, a lot of structure-activity relationships and the analysis of several X-ray TBA-Thrombin complexes [42], showed that the TBA G-quadruplex interacts with thrombin mainly through the TT loops region. Particularly, essential polar interactions between the nucleobases T4, T13 and G5 of the tertiary structure and the side chains of Arg 77, Arg 75 and Tyr 76 located in the ABE I of the thrombin take place, whereas T3 and T12 are essentially involved into hydrophobic contacts. Given that the dibenzyl linker was positioned outside the TT loops, the modification at T12 did not provoke substantial alteration in the TT loops region of the resulting G4, and almost all the above mentioned contacts between TBA and thrombin could occur. As opposite to this, the G-quadruplex bioactive conformation could be significantly affected by the replacement of T13 with the dibenzyl linker¹, seeing that the two benzene rings occupied the region between the TT loops. Consequently, despite the overall topology of the G4 formed by TBA-bs13 strongly resembled that of TBA, the formation of a stable TBA-thrombin complex was completely prevented.

Finally, the cytotoxic effect of TBA-bs13 on the He-La cell line was studied in comparison with that of TBA by means of MTT dose response experiments at concentrations in the range of 0.001–50 μM (Figures 17-18). Inhibition of cell growth by TBA-bs13 started at 0.1 μM and reached the maximum effect at 10 μM , whereas TBA produced the same effects at concentration in the range of 1–50 μM . Consequently, TBA-bs13 was significantly more potent than TBA in the inhibition of He-La cell line growth.

Interestingly, it has been ascertained that some G4s bind NOA1 [49], a large GTP binding protein involved in important mitochondrial functions such as the synthesis of specific proteins, cellular respiration and apoptosis [48][61]. In particular, both parallel and antiparallel DNA G4s are able to bind NOA1, but only the antiparallel ones also cause an increasing of about 4–5 folds of the NOA1 GTP-ase activity [49]. The GTP dependent allosteric regulation has also been established for other GTP binding proteins involved in cancer development, survival and resistance [61][62]. In light of the ability of TBA (antiparallel G-quadruplex) to accumulate into mitochondria [45], it will be of

interest to verify the existence of such connection between the antiproliferative activities of new TBAs on He-La cells and the NOA1 functionality into mitochondria and/or in other cellular districts.

2.4. Conclusion

In conclusion, we showed that artful modifications in the TBA could provide cytotoxic GROs which are able to fold into the well-known TBA G-quadruplex topology but avoiding the TBA anticoagulant action. In particular, the replacement of the residue 4 or 13 with the dibenzyl linker¹ afforded two TBA variants, specifically TBA-bs4 and TBA-bs13, which resulted unable to inhibit thrombin but showed significant antiproliferative activity against the He-La cell line. TBA-bs13 showed a 5-fold increased cell growth inhibition relative to the TBA as determined by the MTT dose response assay. The data concerning the other modified TBAs showed that none of them had a selective action relative to either the biological properties of TBA. It is noteworthy that TBA-bs9, which folded into the least stable G4, showed the lowest antiproliferative activity at all the explored concentrations. A good correlation between the structure stability and the antiproliferative action on He-La cells was also observed for the other two TBA-bs modified at one residue of the TGT loop, TBA-bs7 and TBA-bs8. Among the here reported new analogues, TBA-bs7 showed to be the best inhibitor of He-La cell line growth. Nevertheless, the presented data also demonstrated that more complex phenomena than the G-quadruplex stability control the difference in the antiproliferative effects of the TBA-bs obtained by replacing one of the residues in the TT loops of the TBA with the dibenzyl linker **1**.

Although further deepened studies on these new TBA variants are certainly necessary, we herein described a potential route to obtain helpful G-quadruplex tools for the understanding of the molecular factors that contribute to the cytotoxicity of quadruplex-forming GROs.

2.5. Experimental section

Chemicals and anhydrous solvents were purchased from Fluka-Sigma-Aldrich. TLCs were run on Merck silica gel 60 F254 plates. Silica gel chromatography was performed using Merck silica gel 60 (0.063–0.200 mm). The API 2000 (Applied Biosystems) mass spectrometer was used to perform the analyses of the intermediates and the monomer. NMR data were collected on Varian Mercury Plus400 and ^{UNITY} INOVA 500 MHz spectrometers equipped with a broadband inverse probe with z-field gradient, and on a Varian^{UNITY} INOVA 700 MHz spectrometer equipped with a triple resonance cryoprobe. The data were processed using the Varian VNMR and the iNMR (<http://www.inmr.net>) software packages. Reagents and phosphoramidites for DNA syntheses were purchased from Glenn Research. ON syntheses were performed on a PerSeptive Biosystem Expedite DNA synthesizer. HPLC purifications and analyses were carried out using a JASCO PU-2089 Plus HPLC pump equipped with a JASCO BS-997–01 UV detector. CD experiments were performed on a JASCO 715 spectropolarimeter equipped with a PTC-348 temperature controller. The fibrinogen assay was performed using a JASCO 530 UV spectrophotometer equipped with the PTC-348 temperature controller.

Synthesis of monomer phosphoramidite building block 3

Compound 2. 2,2-dibenzylpropane-1,3-diol (1.0 g, 4.1 mmol), 4,4'-dimethoxytrityl chloride (696.0 mg, 2.0 mmol) and 4-dimethylaminopyridine (25 mg, 0.21 mmol) were dissolved in dry pyridine (20 ml) and dry CH₃CN (10 ml). The resulting solution was stirred at room temperature (r.t.) under argon for 1.5 h. Dry methanol (200 μl) was then added to quench the reaction. After 30 min under stirring, the solution was concentrated under reduced pressure and the residue purified by column chromatography on silica gel (eluted with 90:10:0.1 DCM/MeOH/Et₃N) to give monodimethoxytritylated **2** as a clear white solid (40% yield from **1**; R_f 0.7 in DCM/MeOH 90:10 v/v).

^1H NMR (400 MHz, CDCl_3) δ ppm 7.26–7.00 (19H); 6.90 (4H); 3.78 (s, 6H); 3.72 (s, 2H); 3.45 (s, 2H); 2.89 (s, 2H); 2.47 (s, 2H).

^{13}C NMR (100 MHz, CDCl_3) δ ppm 156.1; 145.5; 139.9; 137.2; 130.0; 129.8; 129.2; 128.2; 127.4; 127.0; 126.6; 126.4; 124.2; 113.9; 89.1; 69.9; 60.7; 55.8; 40.5; 39.4.

ESI mass (positive mode) calculated 558.28; found 559.3 $[\text{M} + \text{H}]^+$, 581.3 $[\text{M} + \text{Na}]^+$.

Compound 3. 2 (425 mg, 0.76 mmol) was dried in vacuo overnight before being dissolved in anhydrous DCM (8 ml) and diisopropylethylamine (530 μl , 3.0 mmol) under argon. 268 μl of β -cyanoethyl diisopropylchlorophosphoramidite was then added (1.2 mmol). After 40 min, the reaction was diluted with ethyl acetate (15 ml), and finally washed with 10% sodium carbonate solution (15 ml) and brine (15 ml). The organic layer was dried on magnesium sulphate and concentrated *in vacuo*. The residue was purified by silica gel chromatography eluted with DCM, ethyl acetate and triethylamine (80:10:10). The fractions containing the product were collected and concentrated under vacuum, yielding **3** as white foam (85% yield; R_f 0.65 in $\text{CHCl}_3/\text{MeOH}/\text{Et}_3\text{N}$ 97:3:0.05 v/v/v).

^1H NMR (400 MHz, CDCl_3) δ 7.90–6.85 (23H); 3.90 (2H); 3.76 (6H); 3.65 (2H); 3.60 (2H); 3.45 (2H); 3.39–3.02 (2H); 2.60–2.45 (4H); 1.09 (6H); 1.04 (6H).

^{13}C NMR (175 MHz, DMSO-d_6) δ 158.6; 151.6; 147.3; 139.4; 135.1; 130.3; 129.1; 127.8; 127.7; 127.1; 126.4; 126.1; 124.2; 113.1, 90.5; 71.2; 64.4; 60.4; 55.2; 47.3; 33.6; 29.7; 27.6; 20.9; 19.3; 17.3.

ESI mass (positive mode) calculated 758.3; found 759.9 $[\text{M} + \text{H}]^+$, 781.9 $[\text{M} + \text{Na}]^+$.

Synthesis of oligomers

TBA and TBA-bs were synthesized using standard solid phase DNA chemistry on a controlled pore glass (CPG) support following the β -cyanoethyl phosphoramidite method [54]. The coupling time for the modified monomer was prolonged from 2 min to 10 min. The oligomers were detached from

the solid support and deprotected by treatment with an aqueous ammonia solution (33%) at 55°C overnight. The combined filtrates and washings were concentrated *in vacuo*, dissolved in H₂O, and purified by HPLC using an anionic exchange column eluted with a linear gradient (from 0% to 100% B in 30 min) of phosphate buffer at pH 7.0 (A: 20 mM NaH₂PO₄ aqueous solution containing 20% CH₃CN; B: 1.0 M NaCl, 20 mM NaH₂PO₄ aqueous solution containing 20% CH₃CN, elution time 18.9 min). The oligomers were successively desalted by molecular exclusion chromatography on Biogel P-2 Fine. The purity (95%) was checked on HPLC using an analytical reverse phase column (Phenomenex, Clarity Oligo-RP, 3 μm, 2 × 10 mm) eluted with a gradient of CH₃CN in triethylamine acetate (pH = 7.4, CH₃CN from 0% to 100% in 40 min). The concentrations of the samples used in CD and UV experiments were determined by measuring the absorbance at 260 nm at 80°C and using the open access program available at <http://basic.northwestern.edu/biotools/OligoCalc.html>[64].

CD experiments

To perform the CD experiments on modified TBA sequences, each ON was dissolved in K⁺ buffer (90 mM KCl, 10 mM KH₂PO₄, pH 7.4) or PBS (Phosphate Buffered Saline) at the final ON concentration of 2.0×10^{-5} M and submitted to the annealing procedure (heating at 90°C for 5 min and slowly cooling at r.t.). Before each experiment the samples were equilibrated at 10°C for 30 min. CD spectra were recorded from 200 nm to 400 nm at 100 nm min⁻¹ scanning rate, 16 s response, 2.0 nm bandwidth, cell length 0.1 cm, vol. 400 μl. Each CD profile was obtained by taking the average of three scans. CD melting curves were obtained by monitoring the variation of absorbance at 295 nm from 10°C to 90°C, cell length 1 cm, vol 1400 μl, temperature scan speeds of 0.1 and 0.5°C min⁻¹.

Furthermore, the CD melting experiments in K⁺ buffer were also performed at ON concentrations of 1.0×10^{-4} and 8.3×10^{-6} M. These samples were obtained by diluting a 1.0×10^{-3} M sample, properly annealed in K⁺ buffer. The samples at 1.0×10^{-4} M were subjected to the melting-annealing

experiments (cell length 0.1 cm, vol 400 μ l), whereas those at 8.3×10^{-6} M to the annealing-melting experiments (cell length 0.5 cm, vol 1200 μ l). The temperature scan speed was fixed at $0.2^\circ\text{C min}^{-1}$.

Fibrinogen clotting assay

The fibrinogen clotting times were measured spectrophotometrically following the procedure previously described [59] ONs were incubated for 1 min at 37°C in 1.0 ml of PBS containing 2.0 mg/ml of fibrinogen (fibrinogen from human plasma, F 3879, Sigma-Aldrich) in a PMMA cuvette (vol 1.5 ml, cell length 1 cm, Brand). 100 μ l of human thrombin (10 NIH per ml; Sigma-Aldrich, T8885, human thrombin suitable for the thrombin time test) was then added to the solution containing the fibrinogen and the ON. For each ON, three sets of experiments at concentration of 20, 50, 100 nM were performed. The time required for fibrin polymerization was determined from the UV scattering curve, registered, as a function of time (wavelength fixed at 380 nm), in triplicate for each ON concentration. The clotting time value reported as mean \pm SE was derived as the maximum of the second derivative of each scattering curve. The basal clotting time (25.6 ± 1.5 s) was referred to the clotting time value determined in absence of any ONs.

NMR experiments

NMR samples were prepared in PBS/D₂O (90:10, v/v) at a single strand concentration of about 5 mM. One-dimensional NMR spectra were acquired as 16384 data points with a recycle delay of 1.0 s at 25°C . Data sets were zero filled to 32768 points prior to Fourier transformation and apodized with a shifted sine bell squared window function. Two-dimensional NMR spectra of TBA-bs12 and TBA-bs13 were acquired at 10°C using a recycle delay of 1.2 s. NOESY spectra were acquired with mixing times of 100, 200 and 300 ms. TOCSY spectra were recorded with the standard MLEV-17 spin-lock sequence and a mixing time of 80 ms. Water suppression was achieved by including a double pulsed-field gradient spin-echo (DPFGSE) module in the pulse sequence prior to acquisition. In all 2D experiments, the time domain data consisted of 2048 complex points in t₂ and 400 fids in t₁ dimension. The sequence-specific resonance assignment of all proton signals of TBA-

bs12 and TBA-bs13 was obtained using NOESY and TOCSY spectra following the standard procedure.

Molecular modelling

The initial structure of TBA-bs12 and TBA-bs13 was built using as the starting point the coordinates of the NMR solution structure of TBA quadruplex (PDB id. 148D). The nucleoside T12 or T13, respectively, was replaced with the linker **1** (Figure7) by using the builder module of the Insight II (2005) software package (Accelrys). The obtained molecules were parameterized according the AMBER force field and the atom of the linker **1** were selectively minimized using the steepest descent and conjugate gradient minimization methods until convergence to a RMS gradient of 0.001 Kcal mol⁻¹ was reached. The structures were then neutralized by adding 14 sodium counterions and solvated in a square TIP3P water box (38 × 38 × 38 Å). Water molecules were minimized (RMS ≤ 0.1 Kcal mol⁻¹) and the systems were subjected to NMR-restrained energy minimization (steepest descent and conjugate gradient methods until convergence to a RMS gradient of 0.001 Kcal mol⁻¹) as described below. The systems were first minimized using the following restraints: 109 or 75 quadratic interproton distances (fixed-length; 30 Kcal mol⁻¹force constant) for TBA-bs12 or TBA-bs13, respectively; 32 flat-bottomed hydrogen bond constraints (16 hydrogen/acceptor 1.7–2.0 Å and 16 donor/acceptor 2.7–3.0 Å; 100 Kcal mol⁻¹); 5 glycosidic torsion angles constrained to a range of -160°/-70° (flat bottomed; 200 Kcal mol⁻¹) as required for*anti*Gs; 4 glycosidic torsion angles constrained to a range of 10°/100° (flat bottomed; 200 Kcal mol⁻¹) as required for*syn*Gs. Next, the distance restraints were removed and the systems were subjected to a second minimization. Finally, all restraints were removed and a final energy minimization was performed. All calculations were repeated 10 times on each system until convergence at the RMS gradient ≤0.001 Kcal mol⁻¹ was reached. For each system the average minimized structure was then obtained by using the analysis module of the Insight II 2005 software package. The average RMSD value was 0.988 Å for TBA-bs12 and 0.983 Å for TBA-bs13.

Prothrombin (PT) Time

PT time was measured by using a Koagulab MJ Coagulation System with a specific kit RecombiPlas Tin HemosIL (Instrumentation Laboratories, Lexington, MA, USA). The procedure was performed according to the manufacturer's instructions. In our experimental protocol a time course (up to 15 min) of each ON or vehicle with 100 μ l of plasma at 37°C was performed. In details, 2.0 μ l of the corresponding ON solution (1.0×10^{-3} M in PBS) or vehicle (PBS) was added in the apposite microtube, to achieve the final concentration of 20 μ M. Similarly, to reach the final concentration of 2 μ M, 2.0 μ l of 1.0×10^{-4} M ON solution was added to 100 μ l of plasma at 37°C. Next, 200 μ l of the kit solution containing Recombiplastin was added with consequent activation of the extrinsic pathway. The PT measurement was produced in triplicate, and the average and its standard error values were calculated. The basal clotting time was determined by measuring the clotting time in the absence of any ON (13.4 ± 0.2 s). The incubation with PBS did not modify the PT measurement.

MTT test

He-La cervical carcinoma cells were seeded in a 96-well plate at a density of 250 cells/well in Dulbecco's modified Eagle's medium supplemented with 10% fetal bovine serum. Briefly, 24 h after being cultured, cells were treated with the different ONs for 7 days and afterward 20 μ l of MTT solution (5 mg/ml, Sigma-Aldrich) was added into each well and incubated for 4 h. The growth medium was then removed and replaced with 4 mM HCl, 0.1% Nondet P-40 (NP40) in isopropanol (150 μ l/well) in order to dissolve the blue-purple crystals of formazan. The absorbance was then measured using a Microplate Reader at 595 nm. Cell viability of triplicate cultures was assessed and graphed together with the corresponding standard deviation.

This work was published on: *Nucleic Acids Res.* 2015 Sep 18; 43(16): 7702–7716.

3. DNA aptamers as potential anti-HIV agents

3.1. Structural Studies and biological evaluation of T30695 variants modified with single chiral glycerol-T reveal the importance of LEDGF/p75 for the aptamer Anti-HIV-Integrase activities

Currently, HIV-1 infection treatment guidelines adopted in USA and EU provide for the simultaneous administration of 3 antiretroviral drugs (HAART “*Highly Active Anti-Retroviral Therapy*”) in severely compromised patients [65][66]. Coupling at least two different mechanisms of action, (i.e. nucleoside reverse transcriptase inhibitors (NRTIs) plus either a non-nucleoside reverse transcriptase inhibitor (NNRTI) or a protease inhibitor) this therapeutic approach interferes at different stages of the viral life cycle and efficiently suppresses the viral replication, both reducing the risks of disease-related morbidities and increasing the life expectancy. Nevertheless, significant side effects associated with poor drug tolerability compromises the long-term treatments with HAART. Indeed, recent data show that an increasing number of patients stop HAART mainly for the persistence of severe side effects. These behaviors in turn trigger the evolution of drug resistant viral phenotypes which pose the major clinical problem.

The other issues pointed out by non-profit world-wide organizations [67] include the increased HIV spread among young people. Contrarily to the common perception, these problems are not confined to the African populations but are present worldwide. To defeat AIDS/HIV risks and infectious, at least two crucial intervention policies are challenged. The first one has to guarantee an efficient world-wide prevention campaign turned to young people. The latter has to support researches on HIV resistance and survival mechanisms including alternative anti-HIV drug discovery.

Several aptamers have been developed against infective agents with special attention on HIV [68] [69]. Indeed, GQ forming DNA aptamers are selected against the envelope glycoprotein gp120, or the HIV-Integrase, or the HIV reverse transcriptase, etc. Thus, each of these aptamers should inhibit the viral life cycle (Figure 19) at different stage [68].

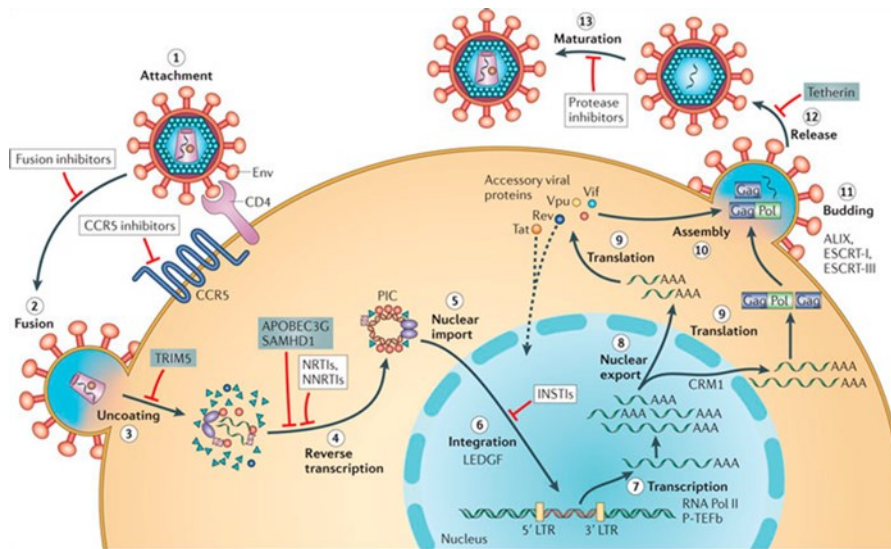


Figure 19. Schematic representation of the viral life cycle [from *Nat.Rev.Microbiol.*, vol. 10, no. 4, pp. 279–290, 2009]. The glycoprotein gp120, exposed on the surface of the HIV envelope (Env), recognizes and binds the receptor CD4 and co-receptor CCR5 (step 1), leading to the fusion and to the entrance of the viral particles into the cell (step 2). The uncoating of the viral capsid (step 3) leads to the release of the viral genomic nucleic acid and to the reverse transcription (step 4), providing the pre-integration complex (PIC). After the entrance into the cell nucleus (step 5), PIC-associated integrase turns into the integrated provirus, aided by the host chromatin-binding protein lens epithelium-derived growth factor (LEDGF) (step 6). Proviral transcription (step 7), mediated by host RNA polymerase II (RNA Pol II), produces different viral mRNAs, which require energy-dependent export to leave the nucleus via host protein CRM1 (Chromosomal Region Maintenance 1 protein, also known as Exportin 1) (step 8). mRNAs are used as templates for protein production (step 9), and genome-length RNA is incorporated into viral particles with protein components (step 10). Viral-particle budding (step 11) and release (step 12) from the cell is mediated by ESCRT (endosomal sorting complex required for transport) complexes and ALIX (ALG-2-interacting protein X) and is accompanied or soon followed by protease-mediated maturation (step 13) to create an infectious viral particle.

As an example, the 17-base oligonucleotide (ON) named T30177 (5'-GGTGTGGGTGGGTGGGT-3', Figure 20a) inhibits HIV-1 integrase at nanomolar concentrations [70]. A sub-sequent reevaluation of pharmacological properties of T30177 also showed that it binds to the viral envelope protein gp120, impairing the host-viral CD4-gp120 interaction [71]. Phase I clinical trials of Zintevir, an analog of T30177 containing phosphorotioate groups at specific positions, demonstrated its potent antiviral activity on humans; however, excluding some specie-specific toxicity at high drug dose, Phase II was discontinued.

Additional studies showed that the T30177 variant, named T30695 (5'-GGGTGGGTGGGTGGGT-3') in which the depletion of the T residue at position 3 produces a continuous 5'-end G₃ tract, had increased antiretroviral activity with respect to the parent variant. Similarly, to T30177, T30695 also binds to HIV-Integrase, inhibiting the enzymatic activity at 3'-end processing stage. Structure-activity studies established a tight correlation between the GQ stabilities and the integrase inhibitory efficiencies of these two aptamers [72][73]. Recently, Phan and coworkers have solved both the T30177 and T30695 GQ structures in buffered solution using NMR techniques (Figure 20a-b)[74][75]. Elegantly overcoming the difficulties related to the symmetry of these GQ typologies, they have shown that parallel-stranded monomers of both T30177 and T30695-GQs stack at 5'-ends to form very stable GQ dimers (Figure 20a-b).

However, dissecting the exact binding mode of T30695 to IN has remained elusive due to the biological complexity of the viral integration machinery, which includes the ability of IN to adopt various multimeric forms [76][77]. Sgobba et al. built a molecular model for (HIV-IN)₄-93del complex [78] and suggested that T30695 could interact with HIV-1 IN in a similar manner. Indeed, 93-del is a 16-mer ON (5'-GGGGTGGGAGGAGGGT-3'), firstly reported as an inhibitor of the RNase H activity, that also exerts HIV-IN inhibition at nanomolar concentration [79]. It adopts a dimeric GQ structure, (Figure 20c) named interlocked, comprising two parallel-stranded GQ subunits, which are singularly engaged with each other through the G-base at the 5'-end (Figure 20c) [80]. In the proposed (HIV-IN)₄-aptamer complex models, T30695 or 93-del GQ occupy the positively charged cavity of HIV-1 IN tetramer. The aptamers bind to an IN tetramer, principally, through their phosphate groups, interacting with basic residues and amide backbones mainly localized at the base of the IN tetramer cavity. Further interactions could involve T bases in the loops of the GQs. Because of their six and two single T loops, T30695 and 93-del GQs could exhibit different binding energy interactions with HIV-1 IN tetramer, with more favorable free energy variation values obtained for the formation of (HIV-IN)₄-T30695 complex [78].

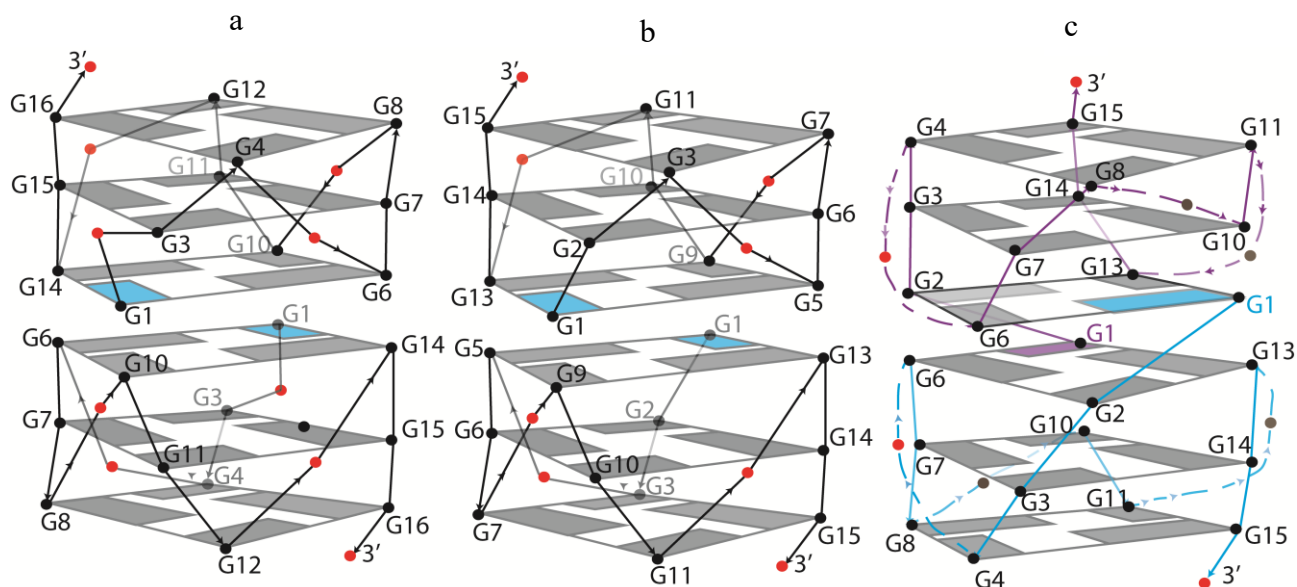


Figure 20. Schematic representation of dimeric G-quadruplexes of T30177 (a), T30695 (b), and 93-del (c). Continuous and dashed lines represent phosphate backbones connecting G residues and T loops (a and b) or G residues and T or A loops (c).

Despite the two models for the HIV-1 IN-aptamer complexes appeared to be comparable, disintegration assays revealed that 93-del inhibited C- or N-terminally truncated enzyme at the same extent, [79] whereas, T30695 required N-terminal domain (NTD) of the enzyme to exert its integrase inhibitory activity [81].

These observations suggest that the two aptamers differently interact with the NTD, and the proposed molecular model of the (HIV-1 IN)₄/T30695 complex needs to be further refined.

3.2. Results and discussion

To gain additional information on the mechanism of action of T30695 and its analogues we have extended structure-activity relationships (SARs) studies through the development of new derivatives of T30695. In particular, for the reasons given above, modifications at the loop residues were targeted as they could influence the binding ability of T30695 GQ to HIV-1. We synthesized T30695 variants, in which the *R* or *S* chiral acyclic nucleoside 1, named glycerol T, (Figure 21) singly replaced the thymine residues at the T30695 loops. Because of its impact on both phosphate

backbone and/or spatial orientation of nucleobase, *R* and *S* glycerol T are good candidates as T analogues to modify T30695 GQ loops. The rational basis of this approach lays in a previous study [58] which demonstrated that, in the folded thrombin binding aptamer G-quadruplex (TBA-GQ), the two phosphate backbones adjacent to the *R* and *S* modified monomers can reach the same conformation, while the corresponding T nucleobase projected at opposite side. As a consequence of the nucleobase orientation, the two TBA-GQs containing either the *R* or the *S* glycerol nucleoside at specific positions also showed opposite trends in their antithrombin activity [58]. These results prompted us to examine the influence of T loop replacement with either *R* or *S* glycerol T on thermal stability and on biological activity of T30695-GQ. Circular dichroism (CD) melting, electrophoretic mobility shift assay (EMSA), and high resolution mass spectrometry (HRMS) experiments provided information about the thermal stability and the stoichiometry of T30695-GQ variants, whereas CD and ^1H NMR studies were performed to evaluate the effect of the modification on T30695-GQ typology. Furthermore, LEDGF/ p75 dependent and independent integration assay were carried out to evaluate the impact of T loop modification on T30695-GQ biological activities.

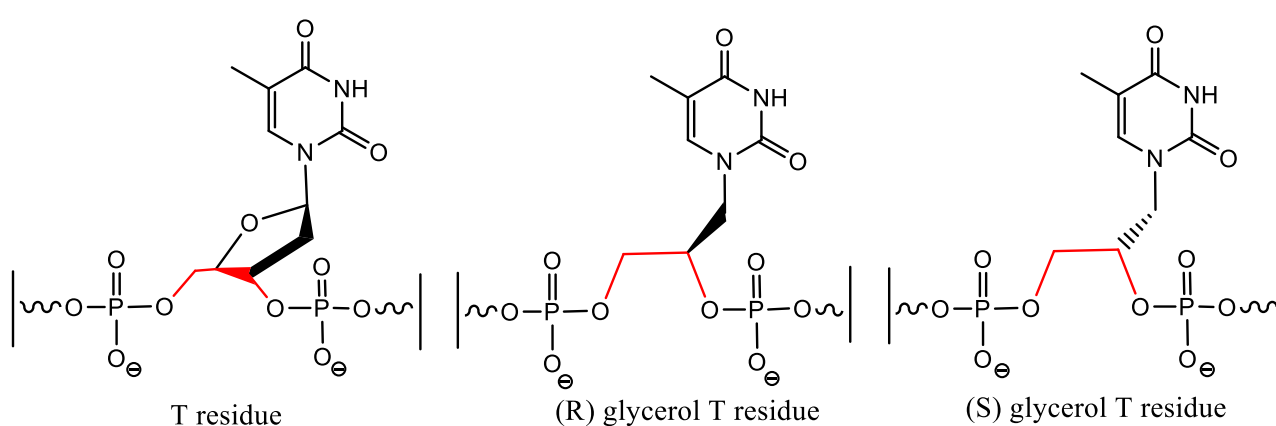
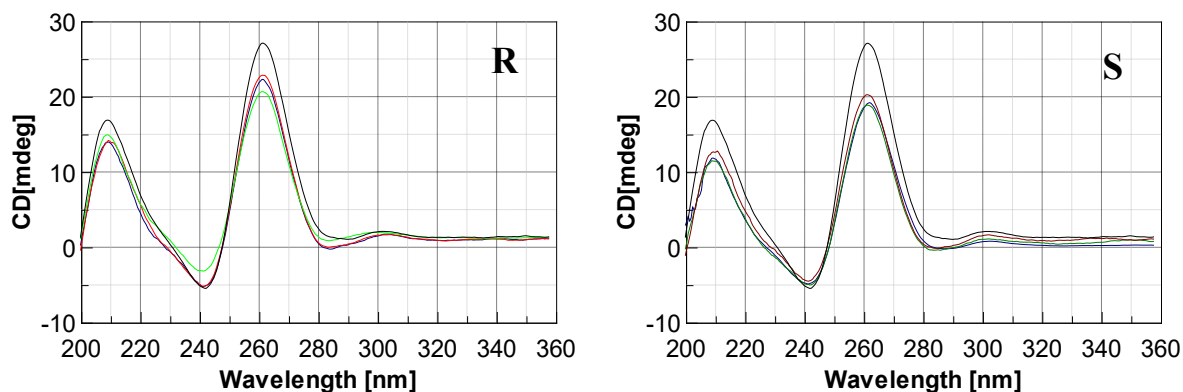


Figure 21. Glycerol T instead of T residue reduces by one bond the phosphate backbone (colored in red).

CD and CD-based melting experiments reveal that the *R* or *S* chirality of one glycerol T loop differently affects the stability of T30695-GQ, largely in presence of Na⁺

CD studies on folded GQs of T30695 and its analogues were performed using three different buffer solutions: K buffer (10 mM potassium phosphate buffer, 10 mM KCl, pH=7,4), PBS (Sigma-Aldrich), and Na buffer (10 mM sodium phosphate buffer, 60 mM NaCl, pH=7,4). As shown in figure 22, T30695 and its derivatives showed similar CD profiles in all the examined salt conditions. Particularly, three positive CD bands at about 209, 262 and 303 nm and one negative CD band at 242 nm were present [55][56][73][74][82]. The CD band at 262 nm always had the highest absolute intensity. These data suggested that the G4 structures formed by the new modified sequences strongly resembled that formed by T30695 [74].

Panel A



Panel B

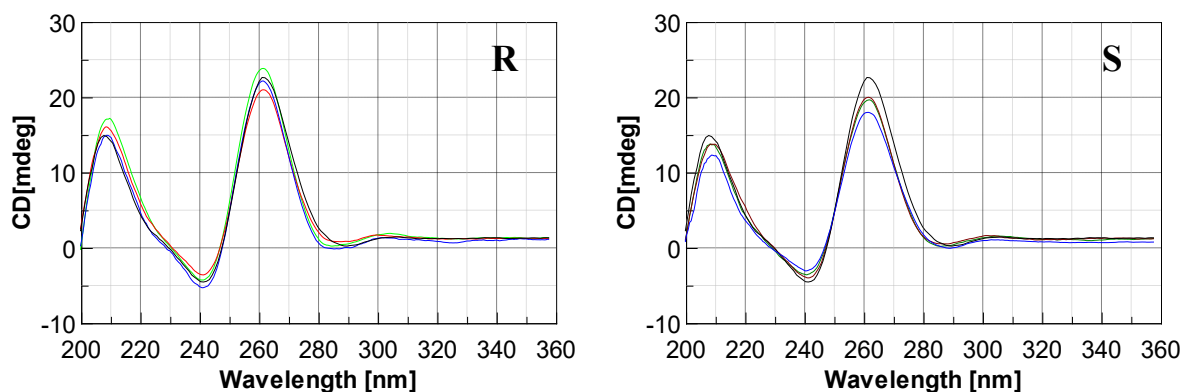


Figure 22. Panel A and B. CD spectra of T30695 and its analogues in K (10 mM potassium phosphate buffer, 10 mM KCl, pH=7,4) and Na Buffer (10 mM phosphate buffer, 60 mM NaCl, pH 7,4), respectively. CD profiles of variants containing the *R* or *S* acyclic T residue are shown in the corresponding R or S picture T30695 (black), T30695-r4 and T30695-s4, (blue), T30695-r8 and T30695-s8 (red), T30695-r12 and T30695-s12 (green). Each aptamer is used at final concentration of 20 μ M. Cuvette o.l. 0.1 cm.

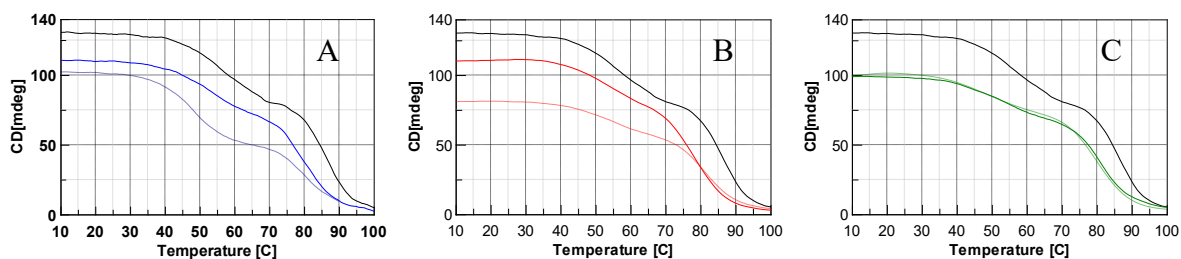


Figure 23. CD melting experiments in K buffer. In all panels, the black line refers to the CD melting profile of T30695, whereas continuous or dotted blue, red and green lines are referred to modified T30695 containing the *R* or *S* acyclic T residue at position 4 (Panel A) or 8 (Panel B) or 12 (Panel C). Cuvette o.l. 0.5 cm.

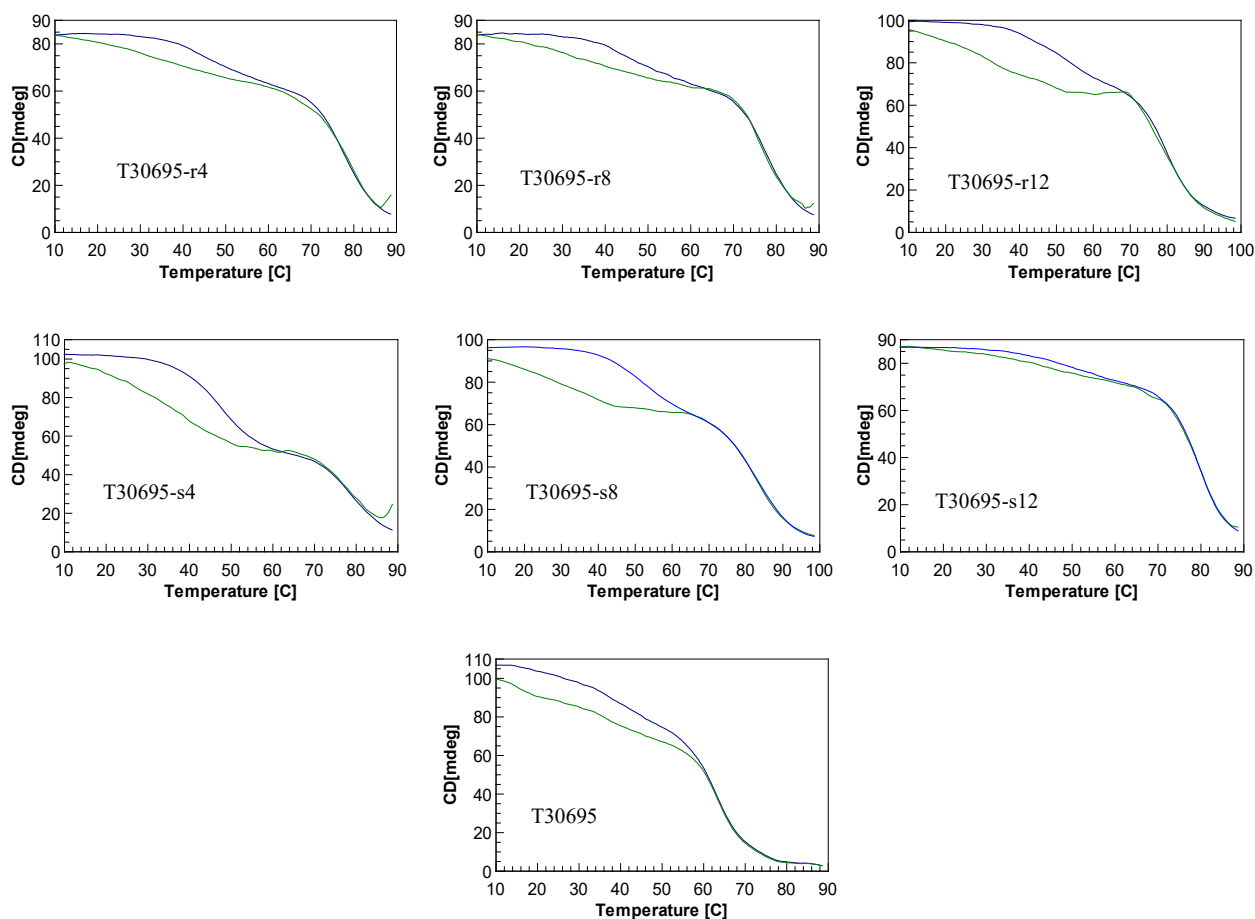


Figure 24. CD heating (blue) and cooling (green) profiles of T30695 and T30695 variants. Fixed wavelength 263 nm, [ON] of 2.0×10^{-5} M. Cell length 0.5 cm. Temperature scan speed 0.2 °C/min. K buffer (10 mM KCl, 10 mM potassium phosphate buffer, pH 7.4).

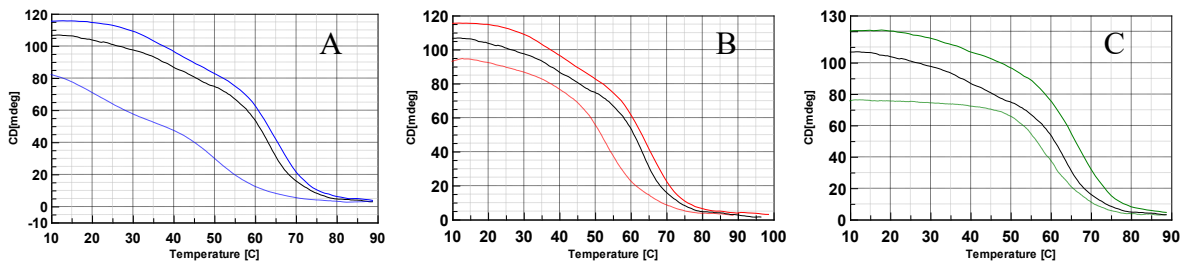


Figure 25. CD melting experiments in Na buffer. In all panels, the black line is referred to the CD melting profile of T30695, whereas continuous or dotted blue, red and green lines are referred to modified T30695 containing the *R* or *S* acyclic T residue at position 4 (Panel A) or 8 (Panel B) or 12 (Panel C). Cuvette o.l. 0.5 cm.

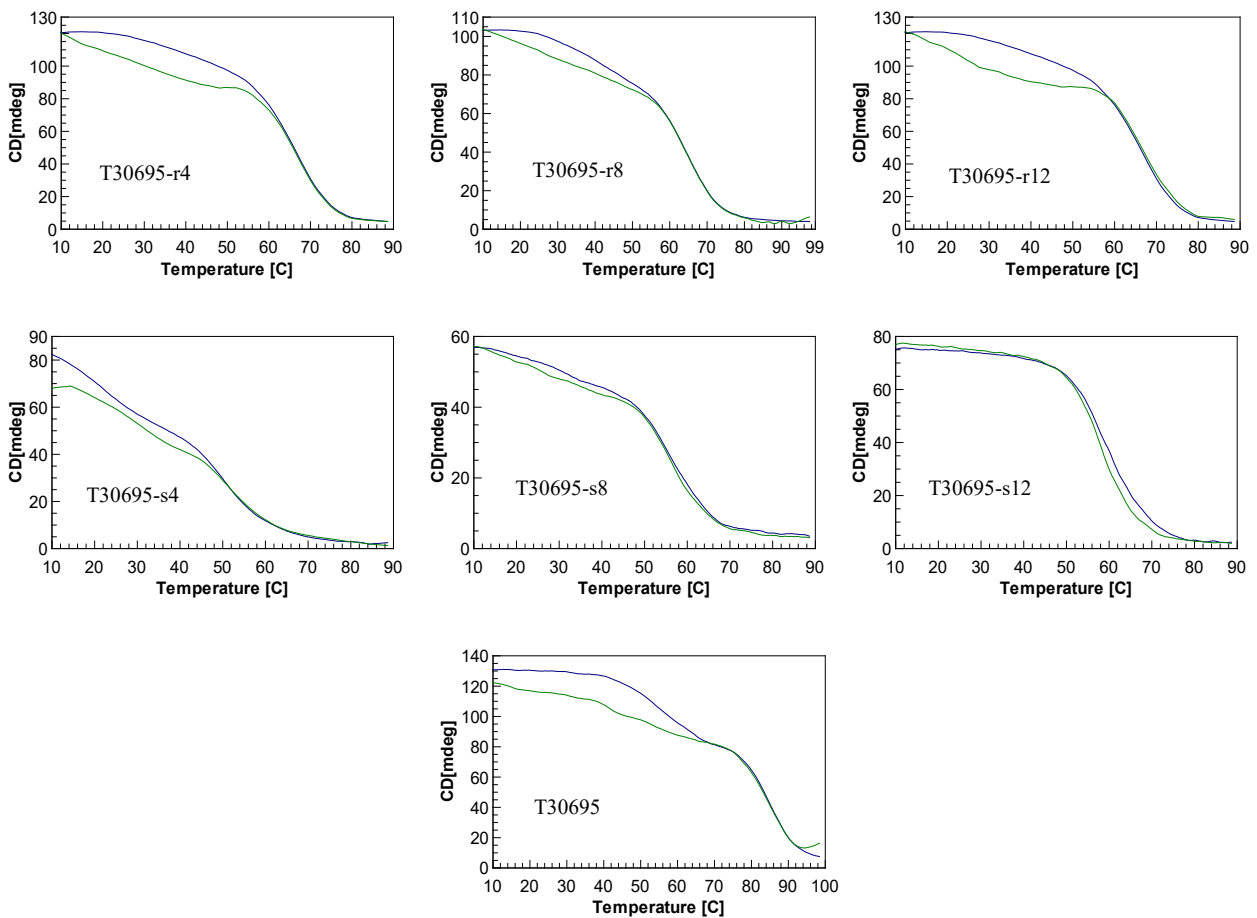


Figure 26. CD heating (blue) and cooling (green) profiles of T30695 and T30695 variants. Fixed wavelength 263 nm. [ON] of 2.0×10^{-5} M. Cell length 0.5 cm. Temperature scan speed 0.2 °C/min. Na buffer (10 mM sodium phosphate buffer, 60 mM NaCl, pH=7,4).

On the basis of previously reported NMR structural data [74][75][83]. T30695 folds into a dimeric G4 structure, formed by 5'-5' end-to-end stacking of two monomolecular G4s, each of them containing four parallel strands and three reversed T loops. Assuming that the new aptamers are able to fold into similar G4s, the acyclic T residue must arrange one T loop of each monomeric G4. In order to evaluate the effects of the T loop modification on GQs stabilities, we performed CD-

based heating and heating/cooling experiments using the three above mentioned buffered conditions (Figures 23-26, table 3). In presence of Na⁺ or K⁺ ions almost all the acquired CD heating/cooling curves showed two inflection points, suggesting that two different events, dimeric GQs→GQs monomers→single strands, occurred in the solutions [11][84]. In presence of K⁺ ions, the CD heating-cooling curves showed thermal hysteresis between 10 and 55-60 °C, whereas they were almost the same in the range of 55-90 °C (Figure 24). These behaviors suggested that, in most of examined cases, the used rate of heating or cooling (0.2°C min⁻¹) was faster than the rate of the interconversion 5'-5' end-to-end stacked dimeric GQs→GQs monomers. However, the monomolecular folding/unfolding processes should occur at equilibrium (Figure 24). Accordingly, T_{1/2} for the event dimers→ monomers (i.e. the temperature at which 50% of the initial stacked GQ-dimers still existed in the solution) and T_m (i.e. the melting temperature of GQ-monomers), were achieved from each CD heating curve (Figures 23-24 and table 3).

In view of the ascertained ability of K⁺ ions to stabilize GQ structures better than NH₄⁺ or Na⁺ ions, in K⁺ containing buffer [9][85], all the CD heating/cooling curves (Figures 23-24) showed the occurrence of the two unfolding events at higher temperatures than in all the other explored conditions. However, in presence of the K⁺ ions the replacement of a T residue at position 4, 8 or 12 with either *R* or *S* acyclic T always negatively affected the thermal stability of T30695 G4 structure (Table 3).

The trend in the GQ thermal stabilities was almost unchanged also using PBS buffer (in addition to Na⁺, this buffer also contains small quantities of K⁺) (Table 3) ,or ammonium acetate buffer (Figures 32-33), with all T_m values being lower than those observed in the K⁺ containing buffer.

Finally, in the Na⁺ containing buffer T30695-*r*4, T30695-*r*8 and T30695-*r*12, GQs had similar thermal stability than that of T30695 (Figures 25-26 and table 3). CD heating/cooling curves showed a less pronounced first inflection point than in the presence of K⁺ ions (Figure 24). Most importantly, the *R* or *S* chirality of the acyclic T significantly affected the monomolecular T30695-

GQ stability (Table 3 and Figure 26). Indeed, T_m of T30695-*r*4, T30695-*r*8 and of T30695-*r*12 GQs were, respectively, of 16, 11 and 10 °C higher than that of T30695-*s*4, T30695-*s*8 and T30695-*s*12.

| ON | K buffer | | | PBS | | | Na buffer | | | |
|---------------------|-----------|-----------|----------------|-----------|-----------|----------------|-------------|-----------|----------------|--------------------|
| | $T_{1/2}$ | T_m | $^a\Delta T_m$ | $T_{1/2}$ | T_m | $^a\Delta T_m$ | $T_{1/2}$ | T_m | $^a\Delta T_m$ | R,S $^b\Delta T_m$ |
| T30695 | 56 | 86 | — | 55 | 78 | — | N.D. | 64 | — | — |
| T30695- <i>r</i> 4 | 54 | 80 | -6 | 50 | 72 | -6 | 40 | 67 | +3 | 16 |
| T30695- <i>s</i> 4 | 49 | 79 | -7 | ND | 70 | -8 | 22 | 51 | -13 | |
| T30695- <i>r</i> 8 | 55 | 77 | -9 | 50 | 72 | -6 | N.D. | 65 | +1 | 11 |
| T30695- <i>s</i> 8 | 55 | 81 | -5 | 50. | 70 | -8 | N.D. | 54 | -10 | |
| T30695- <i>r</i> 12 | 50 | 81 | -5 | 50. | 72 | -6 | N.D. | 67 | +3 | 10 |
| T30695- <i>s</i> 12 | 50 | 80 | -6 | 50. | 72 | -6 | N.D. | 57 | -7 | |

Table 3. $T_{1/2}$ and T_m of T30695-GQ and of its variants annealed in different buffer solutions. $^a\Delta T_m$ is the difference between the T_m of each variant and that of T30695 in each reported buffer. $^b\Delta T_m$ is the differences between the T_m of the two variants containing the acyclic T as R and S stereomer in Na⁺ containing buffer.

Despite the chirality of the glycerol T in one T30695 loop could affect the GQ thermal stabilities in different manners and could imply the involvement of different phenomena, (i.e changes in loop hydrations and length could result in increasing the loop conformational flexibility) the trend of the thermal stabilities of T30695-*r* and-*s* GQ variants in different buffer conditions could be partially related to slight differences between Na⁺ and K⁺ GQ cores [42][86]. Indeed, NMR [86] and X-Ray [42] studies on GQs showed that potassium ions due to their relatively large radii reside between the G-quartet planes, coordinating the eight O atoms of G bases of two successive G-quartets. Conversely, the small Na⁺ ions can occupy a range of different positions inside the GQ core, including the G-quartet in-plane site. As a consequence of the ion mobility, the compactness of the GQ core is smaller in the presence of Na⁺ than K⁺. Therefore, the constrains related to the G-quartet distances and/or to the requisite coplanarity in each G-quartet could decrease with Na⁺ ions, thus allowing to similar stability of T30695-GQ and its *r* variants.

Conversely, the opposite orientation of the nucleobase in the S-glycerol T significantly affected the thermal stability of T30695-s GQs, in contrast with our previous results obtained from studies on TBA-GQs variants [58]. Most probably, changes in parameters characterizing the GQ loops, such as the number of residues forming it, its spatial arrangement with respect to the GQ core, including its involvement in coordinating ions and/or water molecules, accounted for the characteristic behavior of T30695-s4, -s8 or -s12 GQ variants in presence of Na⁺.

Results from gel electrophoresis assays reveal that all T30695 variants form GQ dimers in Na⁺ buffer.

In order to verify the ability of T30695-r and -s variants to fold into 5'-5' end-to-end stacked GQs in the presence of Na⁺, non-denaturing gel electrophoresis mobility shift assay was performed. Figure 27 shows the mobilities of T30695 (lane 2), of the T30695 variants (lanes 3-8), of TBA (lane 9) and of 5'-TT-T30695 (lane 1), on non-denaturing gel containing 50 mM of NaCl at r.t. (Panel A) and 5°C (Panel B). TBA and 5'-TT-T30695 were used as internal reference for monomolecular GQs. The migrations of TBA and that of 5'-TT-T30695 [74][75] were faster than that of T30695, thus corroborating the hypothesis that folding of T30695 gives rise to dimeric GQ. T30695-r4 (lane 8), T30695-r8 (lane 6) and T30695-s12 (lane 3) migrated at the same extent of T30695, suggesting that these three variants preserved almost unchanged the ability of T30695 to form dimeric GQs. Smearing of T30695-r12 (lane 4), T30695-s8 (lane 5) and T30695-s4 (lane 7) occurred. This phenomenon was already observed and attributed to the formation of other dimer types such as, 3'-3' end-to-end stacked GQ dimers [74][75]. T30695-s4 also showed a higher quantity of the fastest migrating band, that migrated similarly to 5'-TT-T30695, than the other species. According to CD results, these data suggested that, all the T30695 new variants were able to form, at least in part, GQ dimers.

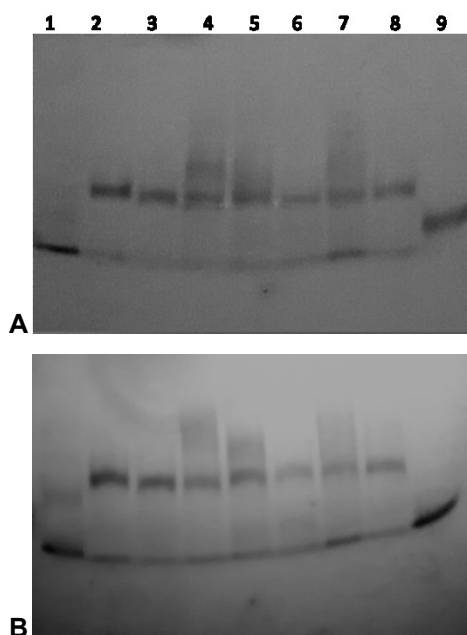


Figure 27. Gel electrophoresis of oligonucleotides in 12% non-denaturing gel containing 50 mM NaCl at 25 (panel A) and 5°C (Panel B). 5'-TT-T30695 lane 1, T30695 lane 2, T30695-s12 lane 3, T30695-r12 lane 4, T30695-s8 lane 5, T30695-r8 lane 6, T30695-s4 lane 7, T30695-r4 lane 8, TBA lane 9.

Almost all T30695 GQ variants give rise to the same pattern of resonances in ^1H NMR experiments with K^+ or Na^+ ions.

The folding of nucleic acids into GQs can be qualitatively established by simple ^1H NMR spectroscopy, because of the presence of characteristic imino ($\sim 10.0\text{-}13.0$ ppm) and aromatic ($\sim 6.8\text{-}8.0$ ppm) proton resonances in the spectra [87]. Commonly, the number of imino and aromatic signals correlate with the folded GQ typologies, whereas the ratio between the intensity of imino and aromatic signals should correlate with the percentage of the nucleic acid sequence structured into GQs. Unfortunately, in the ^1H NMR spectrum of T30695 GQ an extensive overlapping of both imino and aromatic proton signals appeared [74][75][88]. As a consequence, T30695 GQ characterization by NMR studies was previously performed introducing an Inosine residue instead of a G at a specific position [74][89]. This modification most probably causing the disruption of the structural symmetry, provoked the resolution of the proton signals in the spectra. Herein, each T30695 GQ variant contains a single modification at T loop, which leaved unaffected the shape and

the position of the T30695 GQ proton resonances (Figure 28). Despite this, the fact that the imino and aromatic regions of all ^1H NMR spectra were almost identical for all the variants, with the only exception of the T30695-s4 GQ, suggested that almost all the new variants should keep unchanged the T30695 ability to fold into 5'-5' end-to-end stacked dimers of parallel GQ. Notably, the imino proton resonance signals of the T30695-s4 variant were particularly crowded and extensively overlapped, that, could result from the presence of different species in the solution.

In view of the ambiguous profiles of the CD-based heating/cooling curves obtained for some T30695 variants in the presence of Na^+ , that, partially or totally lacked the first inflection point, we selected the couple of T30695-r and -s12 GQs to acquire, in this saline buffered conditions, the ^1H NMR spectra (Figure 29) at different temperatures (25-65°C). At 25 °C, the imino and the aromatic regions of the spectra showed almost the same patterns of proton resonance signals than that obtained in presence of K^+ ions (Figure 28). Increasing the temperature from 25 to 65°C, the imino proton resonance intensities slowly decreased whereas the aromatic region of the spectra became more crowded. At temperatures higher than 45°C neither in T30695-r12 nor in T30695-s12, the shape and the position of the imino proton signals significantly changed, whereas new proton signals appeared only in aromatic region, thus suggesting that unfolded species were slowly forming in the solutions. Consistently with the absence of a clearly visible inflection point for T30695-s12 dimers in the CD heating/cooling curves, the two GQ events, dimers→monomers→unfolded appeared almost overlapped also in the ^1H NMR heating experiments. This hypothesis was corroborated by our EMSA assays, (Figure 27) in which both aptamers showed the main band that migrated at the same extent of the T30695.

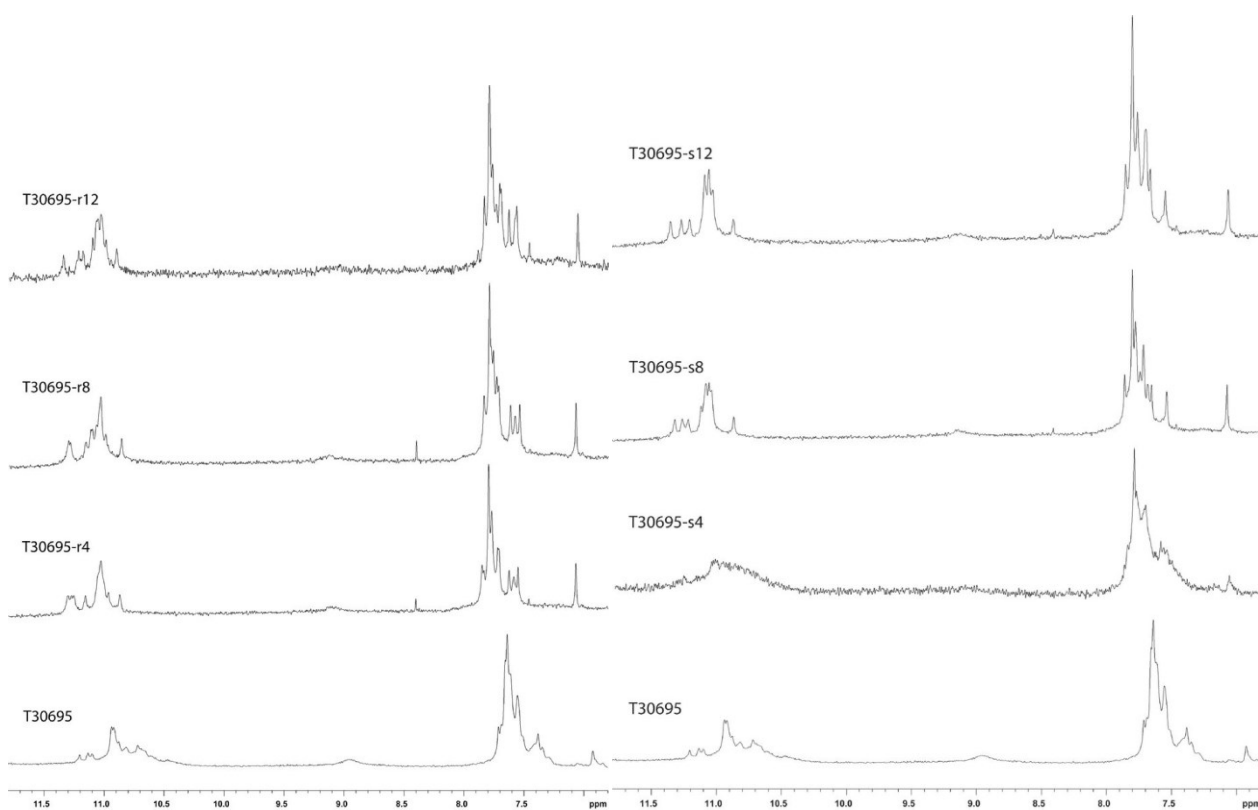


Figure 28. ¹H NMR spectra in the range of 7.0-12.5 ppm of T30695 and its variants in K buffer (10 mM potassium phosphate, 10 mM KCl, pH= 7.4).

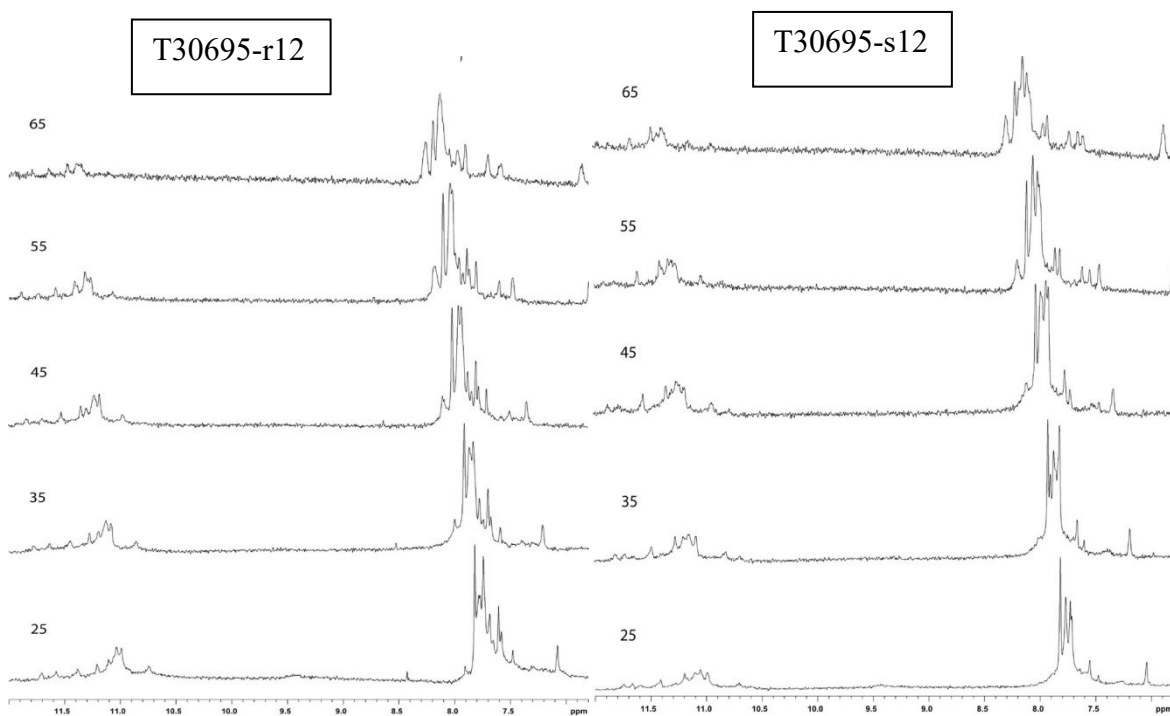


Figure 29. ¹H NMR spectra at different temperatures (25-65°C) in phosphate buffer solution (20 mM) containing 70 mM of NaCl.

Mass spectrometry of aptamers confirm the ability of T30695 variants to form GQ dimers

Molecularity of GQs can be studied by Electrospray Ionization Mass Spectrometry (ESI-MS) [90][91]. Indeed, ESI technique can preserve in gas phase GQs and/or GQ complexes formed in solution [92]. Generally, in order to analyze the GQs by ESI-MS, the ON samples are annealed in buffered solution containing ammonium ions. This because NH_4^+ , similarly to monovalent ions such as Na^+ and K^+ , stabilizes the GQ core, by balancing the negative electrostatic forces generated by the oxygen atoms of the guanine bases arranged in G-quartets[93]. Most importantly, in the gas phase, the GQ should retain metallic cations both in the core and on the phosphate groups, whereas the ammonium ions are kept only in the GQ core. As a consequence of this specific inclusion, MS data can be related to the number (n) of G-quartets forming the GQ, according to the relationship $n \text{ NH}_4^+ \rightarrow (n+1) \text{ G-quartets}$ [9][94].

In view of the poor resolution of proton resonances in the ^1H NMR spectra, we used HRMS to corroborate the attribution of bands having slow electrophoretic mobility shifts to the end-to-end stacked dimers of GQ monomers. Firstly, T30695 at 10 μM was annealed in buffer solution containing four different ammonium acetate (AA) concentrations, namely 25, 50, 75 and 100 mM. The MS experiments were performed by increasing the temperature of the capillary during the sample injection from 100 $^\circ\text{C}$ to 300 $^\circ\text{C}$. The analyses of the obtained spectra showed that while for the 100 and 75 mM AA solutions a heavy background noise hampered a clear interpretation of the full scan HRMS spectrum including assignment of elemental formula to each of the detected ions, at 25 and 50 mM AA solutions, much evidence could be obtained on the presence in gas phase of either the unfolded, the monomeric or the dimeric forms. (Figure 30, Table 4).

Table 4. Ion assignment of ions contained in full scan HRMS of T30695.

| Form | <i>m/z</i> | Ion | Elemental Composition | RDB | Δ ppm |
|----------|------------|---------------------------|--|-------|--------------|
| DIMER | | | | | |
| | 1469.1158 | $[2M+5NH_4-12H]^{7-}$ | $C_{320}H_{402}O_{196}N_{141}P_{30}$ | 205.5 | 1.124 |
| | 1472.2533 | $[2M+5NH_4+Na-13H]^{7-}$ | $C_{320}H_{401}O_{196}N_{141}NaP_{30}$ | 205.5 | -0.765 |
| | 1475.3956 | $[2M+5NH_4+2Na-14H]^{7-}$ | $C_{320}H_{400}O_{196}N_{141}Na_2P_{30}$ | 205.5 | 0.607 |
| | 1714.1347 | $[2M+5NH_4-11H]^{6-}$ | $C_{320}H_{403}O_{196}N_{141}P_{30}$ | 205 | 0.183 |
| | 1717.7994 | $[2M+5NH_4+Na-12H]^{6-}$ | $C_{320}H_{402}O_{196}N_{141}NaP_{30}$ | 205 | 0.790 |
| | 1721.4623 | $[2M+5NH_4+2Na-13H]^{6-}$ | $C_{320}H_{401}O_{196}N_{141}Na_2P_{30}$ | 205 | 0.348 |
| MONOMER | | | | | |
| | 1026.3758 | $[M-7H+2NH_4]^{5-}$ | $C_{160}H_{198}O_{98}N_{70}P_{15}$ | 104.5 | 0.715 |
| | 1030.7726 | $[M+Na-8H+2NH_4]^{5-}$ | $C_{160}H_{197}O_{98}N_{70}NaP_{15}$ | 104.5 | 1.111 |
| | 1022.96934 | $[M-6H+NH_4]^{5-}$ | $C_{160}H_{195}O_{98}N_{69}P_{15}$ | 105.5 | -0.446 |
| UNFOLDED | | | | | |
| | 1019.5655 | $[M-5H]^{5-}$ | $C_{160}H_{192}O_{98}N_{68}P_{15}$ | 106.5 | 1.033 |
| | 1023.9614 | $[M-6H+Na]^{5-}$ | $C_{160}H_{191}O_{98}N_{68}NaP_{15}$ | 106.5 | 0.551 |
| | 1274.7086 | $[M-4H]^{4-}$ | $C_{160}H_{193}O_{98}N_{68}P_{15}$ | 106 | 0.959 |
| | 1280.20341 | $[M+Na-5H]^{4-}$ | $C_{160}H_{192}O_{98}N_{68}NaP_{15}$ | 106 | 0.427 |
| | 1285.6988 | $[M+2Na-6H]^{4-}$ | $C_{160}H_{191}O_{98}N_{68}Na_2P_{15}$ | 106 | 0.350 |
| | 1699.9473 | $[M-3H]^{3-}$ | $C_{160}H_{194}O_{98}N_{68}P_{15}$ | 105.5 | 1.003 |
| | 1707.2739 | $[M+Na-4H]^{3-}$ | $C_{160}H_{193}O_{98}N_{68}NaP_{15}$ | 105.5 | 0.580 |

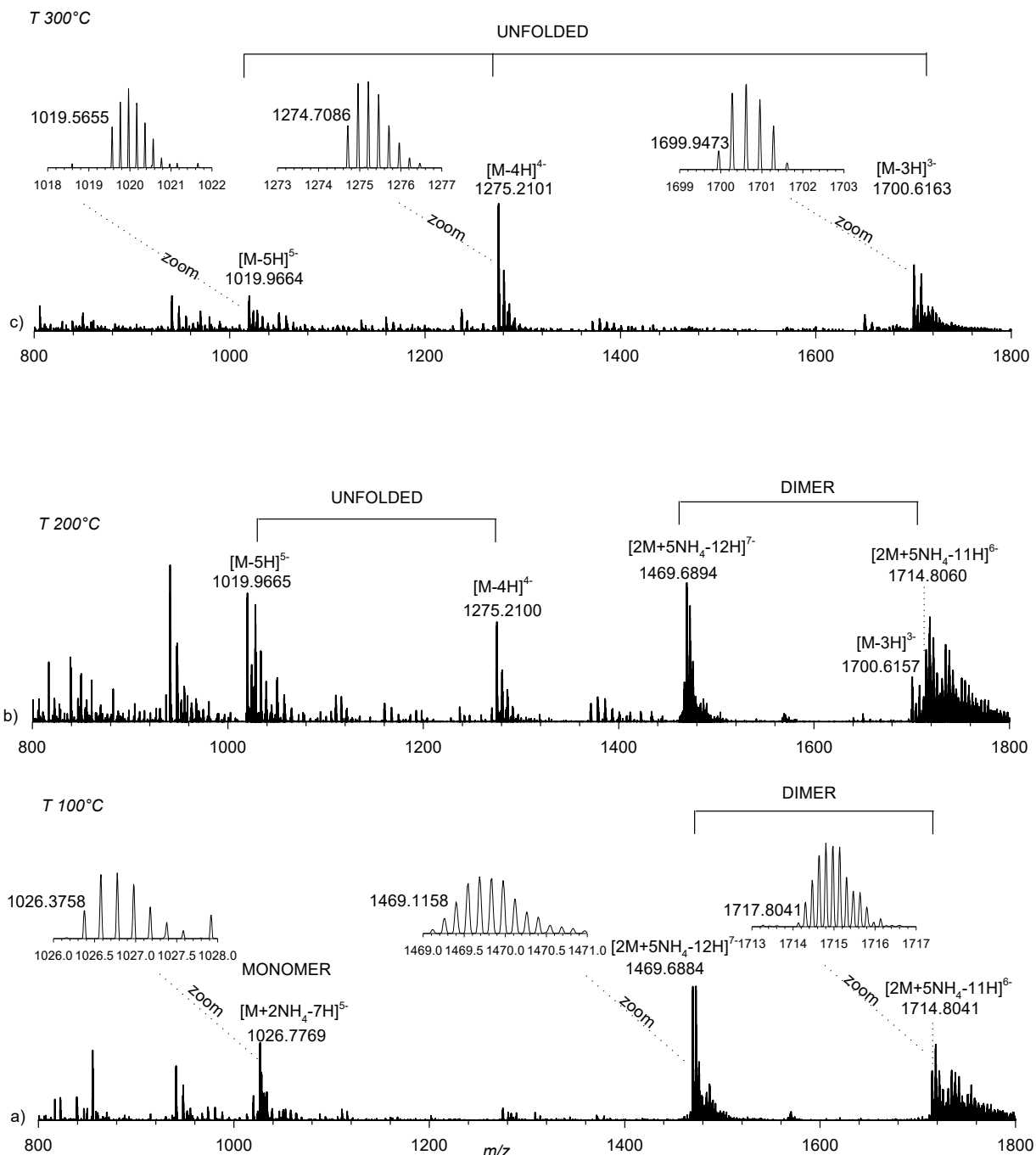


Figure 30. Full HRMS spectrum of T30695 acquired at a capillary Temperature of a) 100°C, b) 200 °C and c) 300 °C. Ion assignments of unfolded, monomeric and dimeric ions are reported in Table 4.

Indeed, the number of ammonium ions (either 2 or 5) associated with each ion peaks could be directly related to the presence of either the monomeric or the dimeric GQs, respectively (Figure 30). Noteworthy, in MS spectra performed using 5'TT-T30695, which is known not to form GQ dimers, [77] only the mass peak patterns including 2 NH_4^+ ions appeared (Figure 31 and table 5).

Interestingly, T30695 at the minimum temperature (100°C) formed ions due to the monomeric forms $[M+2\text{NH}_4-7\text{H}]^{5-}$ and $[M+\text{NH}_4-6\text{H}]^{5-}$ in the region m/z 1000-1050 and ions due to the dimeric forms $[2M+5\text{NH}_4-12\text{H}]^{7-}$ and $[2M+5\text{NH}_4-11\text{H}]^{6-}$ in the region m/z 1400-1800 (Figure 30a). As the

temperature increased (200°C), the presence of ions due to the unfolded forms $[M-nH]^{n-}$ (n=3-5) arouse throughout the spectrum with the dimeric forms still present (Figure 30b). At the highest temperature (300 °C) only the unfolded forms were detected in the spectrum (Figure 30c).

Table 5. Ion assignment of ions contained in full scan HRMS of 5'TT-T30695.

| Form | <i>m/z</i> | Ion | Elemental Composition | RDB | Δ ppm | |
|------------|------------|--------------------------|---|---------------------------------------|--------------|--------|
| MONOMER | 1147.9932 | $[M+2NH_4-7H]^{5-}$ | $C_{180}H_{224}O_{112}N_{74}P_{17}$ | 114.5 | -0.245 | |
| | 1152.1833 | $[M+2NH_4+Na-8H]^{5-}$ | $C_{180}H_{223}O_{112}N_{74}NaP_{17}$ | 114.5 | 1.151 | |
| | 1156.7857 | $[M+2NH_4+2Na-9H]^{5-}$ | $C_{180}H_{222}O_{112}N_{74}Na_2P_{17}$ | 114.5 | -0.483 | |
| | 1161.1815 | $[M+2NH_4+3Na-10H]^{5-}$ | $C_{180}H_{221}O_{112}N_{74}Na_3P_{17}$ | 114.5 | -0.989 | |
| | 1435.2425 | $[M+2NH_4-6H]^4+$ | $C_{180}H_{225}O_{112}N_{74}P_{17}$ | 114 | -0.816 | |
| | 1440.73664 | $[M+2NH_4+Na-7H]^4+$ | $C_{180}H_{224}O_{112}N_{74}NaP_{17}$ | 114 | -1.747 | |
| | 1446.23481 | $[M+2NH_4+2Na-8H]^4+$ | $C_{180}H_{223}O_{112}N_{74}Na_2P_{17}$ | 114 | 0.116 | |
| | 1451.72898 | $[M+2NH_4+3Na-9H]^4+$ | $C_{180}H_{222}O_{112}N_{74}Na_3P_{17}$ | 114 | -0.791 | |
| | UNFOLDED | 1141.1825 | $[M-5H]^{5-}$ | $C_{180}H_{218}O_{112}N_{72}P_{17}$ | 116.5 | -0.317 |
| | | 1145.57984 | $[M+Na-6H]^{5-}$ | $C_{180}H_{217}O_{112}N_{72}NaP_{17}$ | 116.5 | 0.515 |
| 1149.97636 | | $[M+2Na-7H]^{5-}$ | $C_{180}H_{216}O_{112}N_{72}Na_2P_{17}$ | 116.5 | 0.627 | |
| 1426.73458 | | $[M-4H]^4+$ | $C_{180}H_{219}O_{112}N_{72}P_{17}$ | 116 | 2.933 | |
| 1432.22805 | | $[M+Na-5H]^4+$ | $C_{180}H_{218}O_{112}N_{72}NaP_{17}$ | 116 | 1.514 | |
| 1437.72271 | | $[M+2Na-6H]^4+$ | $C_{180}H_{217}O_{112}N_{72}Na_2P_{17}$ | 116 | 0.933 | |

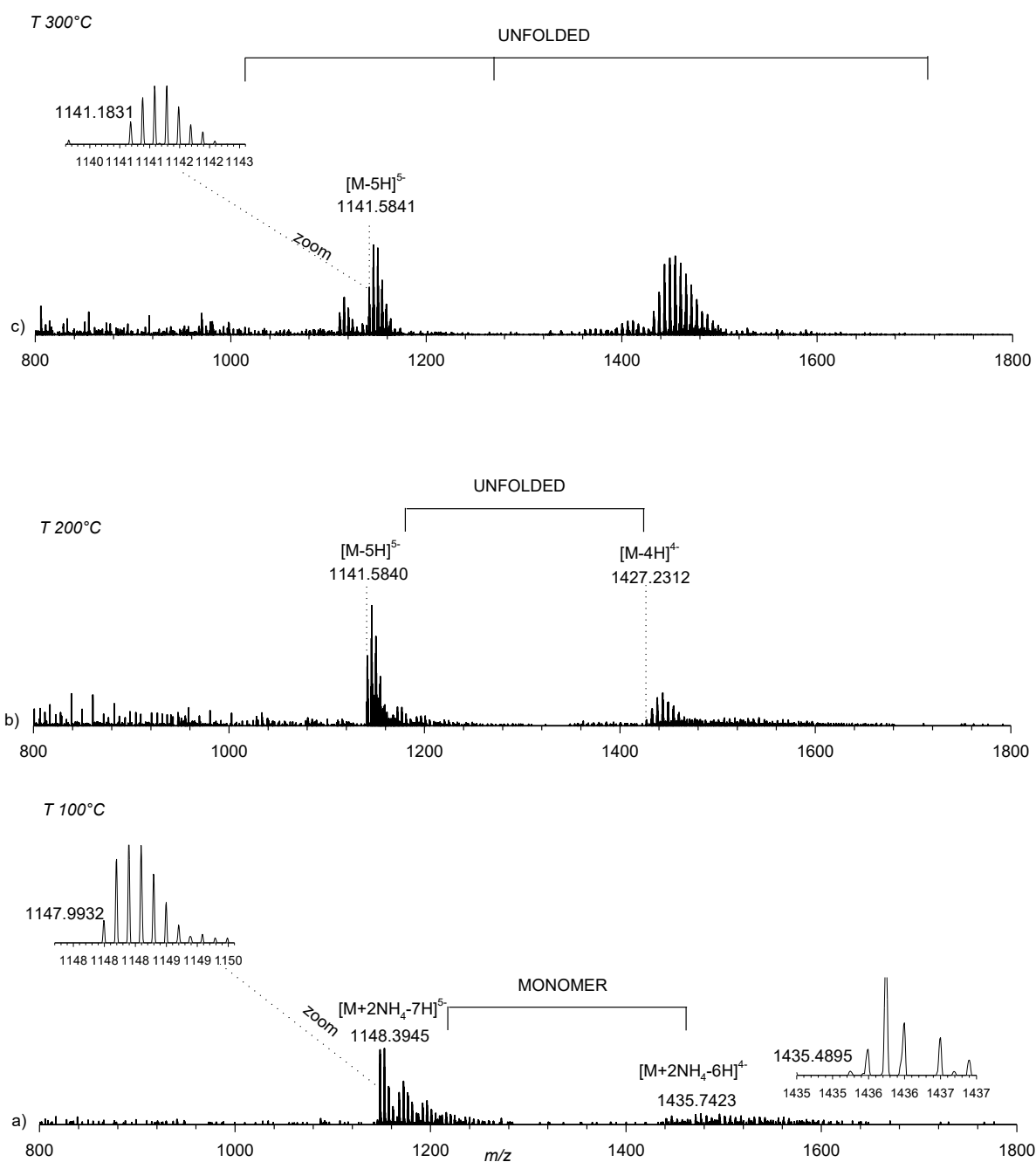


Figure 31. Full HRMS spectrum of 5' TT-T30695 acquired at a capillary Temperature of a) 100°C, b) 200 °C and c) 300 °C. Ion assignments of unfolded, monomeric and dimeric ions are reported in Table 5.

Despite the trend of the peak pattern intensities as a function of the capillary temperature was only qualitative, the persistence of the dimeric GQ peak patterns over that of the monomeric ones at high temperatures, could be indicative of the robustness of the 5'-5' stacking interaction between the two T30695 GQ monomers, which appeared to strongly stabilize the whole GQ structure in the gas phase.

Finally, considering that the ammonium concentration used in the solution was almost unrelated to the relative intensity of the monomeric and dimeric GQs peaks (data not shown), 10 μ M solutions of each T30695 variant were annealed in 75 mM AA and then diluted 1:3 with water.

In order to provide evidence that ammonium ions did not significantly affect the T30695 GQ typology, the same MS samples were also analyzed by CD and CD melting experiments. As expected, the CD profiles of T30695 and its variants (Figure 32) resulted very similar to those obtained in presence of monovalent cations K^+ or Na^+ , whereas the CD melting temperatures were in the range of 57-61 $^{\circ}C$ (Figure 33).

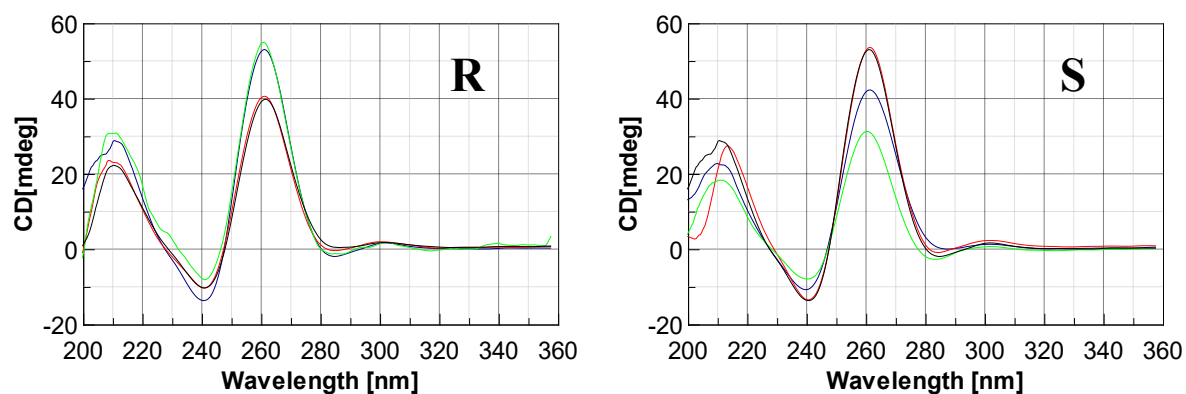


Figure 32. CD spectra of T30695 and its variants annealed at 10 μ M in 75 mM of acetate buffer and then diluted 1:3 with water. The CD profiles of GQ variants containing the *R* or *S* acyclic T residue are shown in the corresponding panel R or S. T30695 (black), T30695_{r-4} and T30695_{s-4}, (blue), T30695_{r-8} and T30695_{s-8} (red), T30695_{r-12} and T30695_{s-12} (green). Cuvette o.l. 0.5 cm.

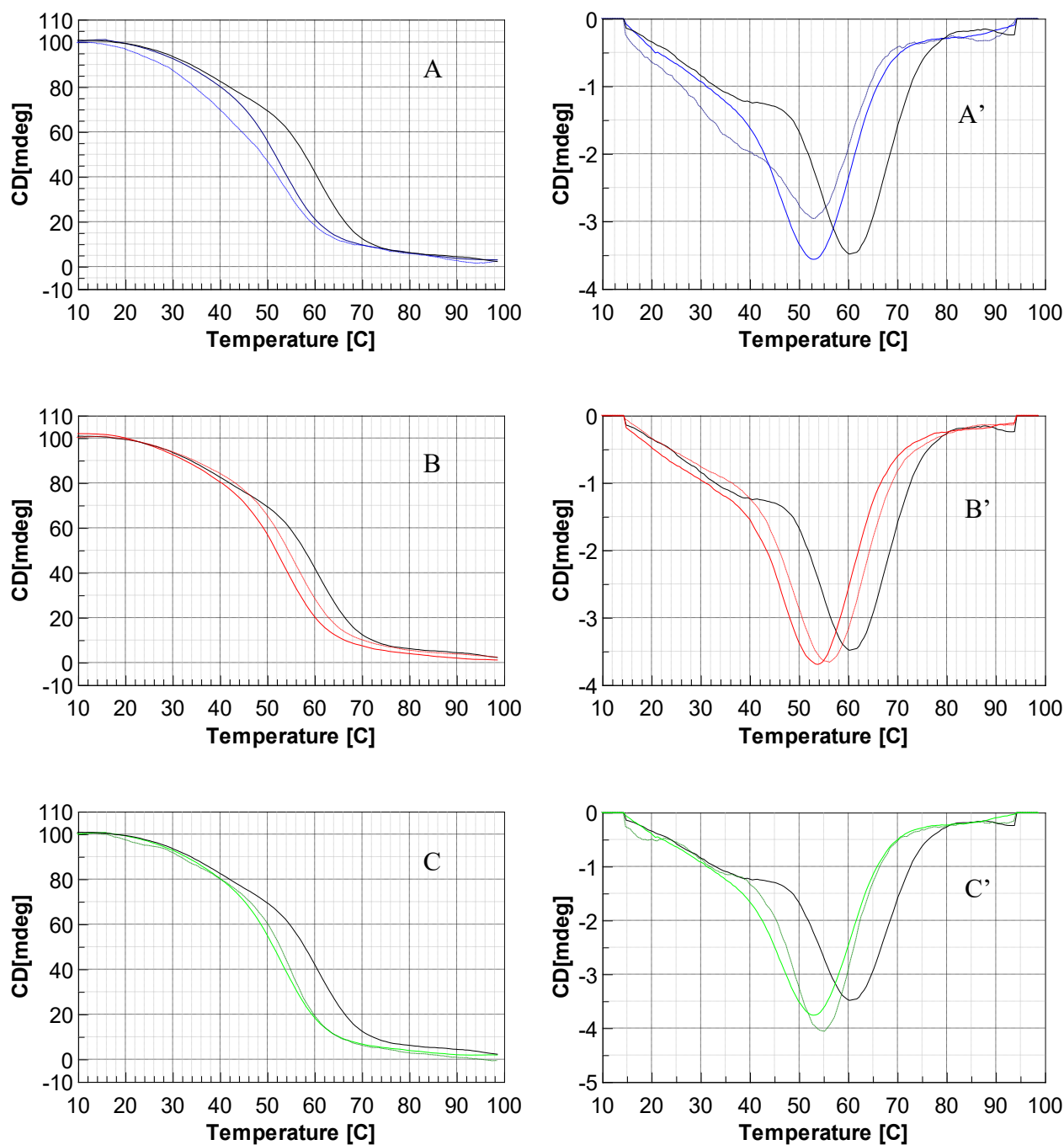


Figure 33. 0-100 mdeg normalized CD melting experiments in ammonium acetate buffer. In all panels, black line is referred to the CD melting profile of T30695, whereas continuous or dotted blue line are referred to modified T30695 containing one *R* or *S* acyclic T residue at position 4 (Panel A) or 8 (Panel B) or 12 (Panel C). The first derivatives of each melting curves were also reported in panels A', B' and C'.

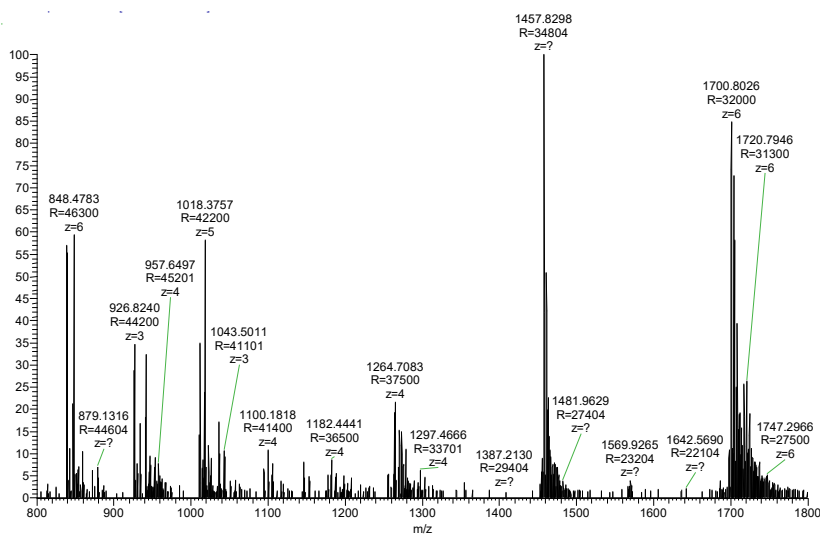
Full HRMS spectra of the T30695 *R* and *S* variants strongly resembled that of T30695 in distributions of ion forms (monomeric, dimeric and unfolded) at the different temperatures and relative ion ratios (Figure 34 and table 6). In more detail, for all the variants, with increasing capillary temperatures the unfolded species became gradually the dominant ion species. Despite the

MS data cannot account for the specific GQ typology, the overall acquired data strongly suggested that the introduction of one R or S acyclic T in place of T in the T30695 sequence did not significantly affect the ability of the resulting variants to form dimeric GQ by end-to-end staking of the monomers.

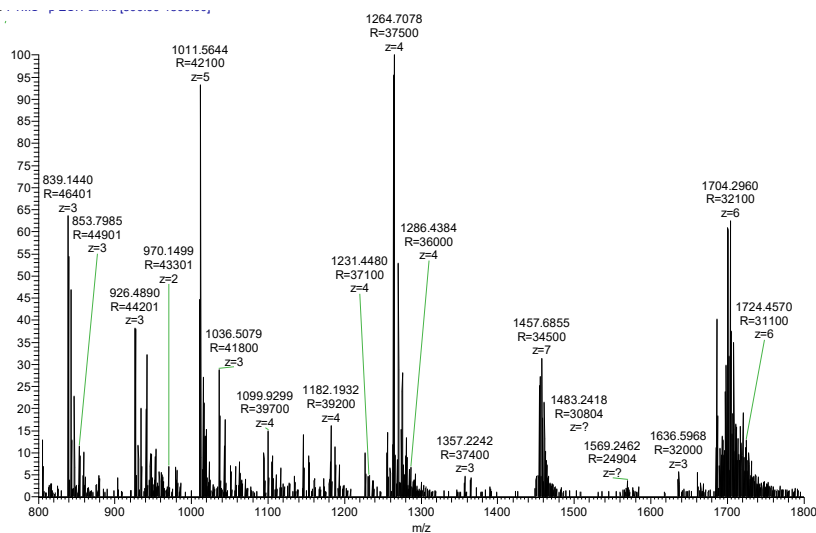
Table 6. Ion assignment of ions contained in full scan HRMS of T30695-r8.

| Form | <i>m/z</i> | Ion | Elemental Composition | RDB | Δ ppm |
|-----------------|-------------------|---|---|------------|--------------------------------|
| DIMER | | | | | |
| | 1457.1123 | [2M+5NH ₄ -12H] ⁷⁻ | C ₃₁₆ H ₃₉₈ O ₁₉₄ N ₁₄₁ P ₃₀ | 203.5 | 1.555 |
| | 1460.2473 | [2M+5NH ₄ +Na-13H] ⁷⁻ | C ₃₁₆ H ₃₉₇ O ₁₉₄ N ₁₄₁ NaP ₃₀ | 203.5 | -2.062 |
| | 1700.1327 | [2M+5NH ₄ -11H] ⁶⁻ | C ₃₁₆ H ₃₉₉ O ₁₉₄ N ₁₄₁ P ₃₀ | 203.0 | 1.725 |
| | 1703.7941 | [2M+5NH ₄ +Na-12H] ⁶⁻ | C ₃₁₆ H ₃₉₈ O ₁₉₄ N ₁₄₁ NaP ₃₀ | 203.0 | -0.396 |
| MONOMER | | | | | |
| | 1017.9744 | [M-7H+2NH ₄] ⁵⁻ | C ₁₅₈ H ₁₉₆ O ₉₇ N ₇₀ P ₁₅ | 103.5 | 2.499 |
| | 1022.3704 | [M+Na-8H+2NH ₄] ⁵⁻ | C ₁₅₈ H ₁₉₅ O ₉₇ N ₇₀ NaP ₁₅ | 103.5 | 2.107 |
| UNFOLDED | | | | | |
| | 1011.1626 | [M-5H] ⁵⁻ | C ₁₅₈ H ₁₉₀ O ₉₇ N ₆₈ P ₁₅ | 105.5 | 1.348 |
| | 1015.5596 | [M-6H+Na] ⁵⁻ | C ₁₅₈ H ₁₈₉ O ₉₇ N ₆₈ NaP ₁₅ | 105.5 | 1.944 |
| | 1264.2066 | [M-4H] ⁴⁻ | C ₁₅₈ H ₁₉₁ O ₉₇ N ₆₈ P ₁₅ | 105.0 | 2.342 |
| | 1269.7020 | [M+Na-5H] ⁴⁻ | C ₁₅₈ H ₁₉₀ O ₉₇ N ₆₈ NaP ₁₅ | 105.0 | 2.264 |
| | 1685.9443 | [M-3H] ³⁻ | C ₁₅₈ H ₁₉₂ O ₉₇ N ₆₈ P ₁₅ | 104.5 | 1.971 |

A) T=100°C



B) T=200°C



C) T=300°C

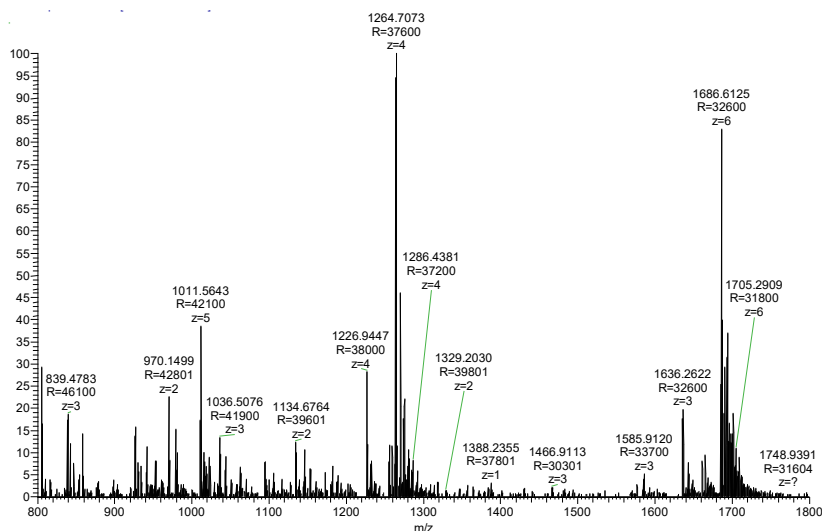


Figure 34. Full HRMS spectrum of the T30695 variant r8 acquired at a capillary Temperature of a) 100°C, b) 200 °C and c) 300 °C.

Ion assignments of unfolded, monomeric and dimeric ions are reported in table 6.

LEDGF/p75 adversely affects the Integrase inhibitory efficiency of T30695 and its variants.

With the aim to analyze how substantial differences between the T_m values of the T30695-GQs variants in the presence of Na^+ ions could affect the aptamer anti-integrase activities, we performed LEDGF/p75 dependent and independent integration assays [95] under respective conditions (Table 7). In the presence of LEDGF/p75 the IC_{50} value for T30695 was 146 nM (Table 7), whereas that of T30695 variants were in the range of 224-106 nM. The most favorable value (106 ± 7.3) was obtained for T30695-s8. Two variants, T30695-r4 and T30695-s12, exhibited increased IC_{50} values compared with their unmodified counterparts, whereas the other variants and T30695 showed similar integrase inhibitory efficiencies. Comparisons of the CD melting temperature (Table 3) and the IC_{50} (Table 7) values for modified aptamers containing the R or S acyclic T at position 4 or 8 suggest the lack of correlation between GQ thermal stabilities and the integrase inhibitory activities. In fact, T30695-s4 and T30695-s8 GQs, which exhibited significantly decreased T_m values compared to the unmodified structure (ΔT_m of -13 and -10 °C respectively, table 3), showed higher inhibitory potency (IC_{50} 151 ± 6.8 and 106 ± 7.3 nM, respectively, table 4) than the corresponding T30695-r4 and T30695-r8 GQs (IC_{50} 224 ± 14 and 158 ± 6.2 nM, respectively). Only in the case of the aptamers modified at T12 the loss of T30695-s12 GQ stability ($\Delta T_m = -7$ °C, calculated with respect to T30695) could account for the increased IC_{50} (220 ± 9.6 nM) value.

It is noteworthy that our measured IC_{50} value of T30695 was about 10-fold higher than that reported in literature [72][73][96], for this reason we performed also LEDGF/p75 independent integration assay; in the absence of LEDGF/p75 the inhibitory potencies of all aptamers significantly increased. Analyses of the IC_{50} values revealed that in all cases the aptamers modified with the S acyclic nucleotides showed slightly higher inhibitory activity than the corresponding R isomers. In addition, without LEDGF/p75 in the assay, the modifications at T8 with the R or S acyclic T had slightly improved the T30695 integrase inhibitory activity, whereas opposite trend was observed for T30695-r12 and T30695-s12. Overall these findings argue against positive correlation between the aptamer GQ stabilities and GQ integrase inhibitory efficiencies.

Finally, comparative analyses of ratios between the IC₅₀ values measured for each aptamer with the two different assays, with or without LEDGF (+LEDGF IC₅₀/-LEDGF IC₅₀, table 7), as well as ratios between the IC₅₀ values measured for each variant and that of T30695, in the presence or absence of LEDGF/p75 (-LEDGF, IC₅₀variant/IC₅₀T30695, +LEDGF, IC₅₀variant/IC₅₀T30695, table 7) also showed that LEDGF/p75 differentially affected the inhibitory potencies of aptamers, which varied depending on the position of modified nucleoside (4 or 8 or 12) and the chirality of modified nucleoside (R or S). Indeed, the ratio of IC₅₀ values for each aptamer in the experimental conditions shifted from 5,0 (T30695-r12) to 11,0 (T30695-r8), whereas the IC₅₀ values of new variants were from 0.7- up to 1,9-fold than that of T30695.

Previous studies revealed that HIV-1 IN forms tetramers having distinct conformations depending on the presence of viral DNA or LEDGF/p75 in the solution and that the binding of LEDGF/p75 modulates the structure of free IN and of IN/DNA complex [97][98][99]. Our findings suggest that the ability of LEDGF/p75 to stabilize specific HIV-1 IN tetramers also adversely affects the binding of T30695 and its variants and that the interactions between the three T loops of the GQs and HIV-1 IN could be differently affected by the LEDGF/p75 binding to the HIV-1 IN.

Table 7. IC₅₀ values of T30695 and its variants measured in presence or in absence of LEDGF/p75.

| ON | IC ₅₀ LEDGF Independent (nM) | IC ₅₀ LEDGF Dependent (nM) | +LEDGFIC ₅₀ / -LEDGFIC ₅₀ | -LEDGF IC ₅₀ variant/ IC ₅₀ T30695 | +LEDGF IC ₅₀ variant/ IC ₅₀ T30695 |
|---------------|--|--|--|--|--|
| T30695 | 16.68±2.62 | 146±6 | 9 | | |
| T30695-r4 | 30.15±3 | 224±14 | 7 | 1.8 | 1.5 |
| T30695-s4 | 24.49±4.1 | 151±6.8 | 6 | 1.5 | 1 |
| T30695-r8 | 13.9±1.9 | 158±6.2 | 11 | 0.8 | 1.1 |
| T30695-s8 | 11.75±3.75 | 106±7.3 | 9 | 0.7 | 0.7 |
| T30695-r12 | 31.52±1.74 | 151±8.1 | 5 | 1.9 | 1 |
| T30695-s12 | 27.79±6.32 | 220±9.6 | 8 | 1.7 | 1.5 |

3.3. Conclusion

In this study, six new T30695 variants were synthesized with the acyclic R or S glycerol linker instead of deoxyribose unit at 4, 8 or 12 T residue. Based on our previous studies on TBA-GQ, this type of modification should provoke local changes in GQ conformations in the final T30695-GQ variants, that without affecting the structural stabilities could still potentially influence biological activities of aptamers.

Our CD, ¹H NMR, EMSA and HRMS studies showed that the new synthesized T30695 variants are able to fold in dimeric GQ structures that resemble that of T30695. Based on the number of ammonium ions incorporated into the GQ structure, the ability to form dimers for all T30695 GQ variants was confirmed by HRMS results carried out in the presence of ammonium acetate ions. In addition, in presence of Na⁺ ions, all T30695-GQ variants also had the same electrophoretic mobility as T30695-GQ, which in turn presented a lower electrophoretic mobility than 5'-TT-T30695-GQ and TBA-GQ, which are known to form monomolecular GQ.

CD heating and heating/cooling experiments also showed that the T_m values were always much higher in the presence of K⁺ ions than Na⁺ ions and that significant differences between the T_m values of T30695-r4, -r8, or -r12 and the corresponding T30695-s4, or -s8, or -s12 GQs were noticeable mainly in the presence of Na⁺. Finally, the HIV-1 IN inhibitory activities of T30695 variants, annealed in the presence of Na⁺ ions, were evaluated using LEDGF/p75 dependent and independent assays. Our data support the hypothesis that LEDGF/p75 is able to negatively modulate the binding of T30695 and its variants to HIV-1 IN tetramers. Indeed, the obtained results showed that: i) the stability of T30695-GQ variants only marginally affects their ability to inhibit HIV-1 IN activity; iii) addition of LEDGF/p75 in the assay substantially reduced (about 10-fold) the ability of T30695 to inhibit HIV-1 IN; iv) LEDGF/p75 also affected the inhibitory efficiencies of T30695 variants, but the extent of this effect depended on the position and the chirality (R or S) of glycerol T loop in the GQ; iv) T30695-s8 consistently exhibited better inhibitory efficiency than T30695. Despite more in depth studies should be performed to clarify the role of LEDGF/p75 in

determining the T30695 inhibitory efficiency against HIV-1 IN, our results are relevant for the assessment of the molecular factors that contribute to the true effectiveness of G-quadruplex forming aptamers as inhibitors of HIV-1 IN.

3.4. Experimental section

Chemicals and anhydrous solvents were purchased from Fluka-Sigma-Aldrich. TLCs were run on Merck silica gel 60 F254 plates. Silica gel chromatography was performed using Merck silica gel 60 (0.063–0.200 mm). Reagents and phosphoramidites for DNA syntheses were purchased from Sigma-Aldrich. ON syntheses were performed on a PerSeptive Biosystem Expedite DNA synthesizer. HPLC purifications and analyses were carried out using a JASCO PU-2089 Plus HPLC pump equipped with a JASCO BS-997-01 UV detector. CD experiments were performed on a JASCO 715 spectropolarimeter equipped with a PTC-348 temperature controller. NMR data were collected on Varian ^{UNITY}INOVA 500 MHz spectrometers equipped with a broadband inverse probe with z-field gradient and on a Varian ^{UNITY}INOVA 700 MHz spectrometer equipped with a triple resonance cryoprobe. The data were processed using the Varian VNMR and the NMR (<http://www.inmr.net>) software packages. Mass spectrometry data were collected on a hybrid linear ion trap LTQ Orbitrap XL™ Fourier Transform MS (FTMS) equipped with an ESI ION MAX™ source (Thermo-Fisher; San José, CA, USA).

Synthesis of oligomers

T30695 and its variants were synthesized using standard solid phase DNA chemistry on a controlled pore glass (CPG) support 3'-bounded to the first nucleotide of the sequence, following the β -cyanoethyl phosphoramidite method[54]. Modified phosphoramidite building block was obtained as previously described[58]. The coupling time of modified monomer was prolonged from 2 to 15 min. The oligomers were detached from the solid support and deprotected by treatment with an aqueous ammonia solution (33%) at 55 °C overnight. The combined filtrates and washings were concentrated under reduced pressure, dissolved in H₂O, and purified by HPLC using an anionic

exchange column eluted with a linear gradient (from 0% to 100% B in 30 min) of phosphate buffer at pH 7.4 (A:20 mM NaH₂PO₄ aqueous solution containing 20% CH₃CN; B: 1.0 M NaCl, 20 mM NaH₂PO₄ aqueous solution containing 20% CH₃CN, elution time 19 min). The oligomers were successively desalted by molecular exclusion chromatography on Biogel P-2 Fine. The purity (95%) was checked by ¹H NMR spectra acquired in D₂O. The concentrations of the samples used in CD and UV experiments were determined by measuring the absorbance at 260 nm at 80 °C and using the open access program available on <http://basic.northwestern.edu/biotools/OligoCalc.html> [64].

CD, CD heating and heating/cooling experiments

To perform the CD experiments, each ON was dissolved in K buffer (10 mM KCl, 10 mM potassium phosphate buffer, pH 7.4), PBS (Sigma-10 mM phosphate buffer, NaCl 138 mM; KCl 2.7 mM, pH 7.4), Na buffer (10 mM sodium phosphate buffer, 60 mM NaCl, pH=7,4) or ammonium acetate buffer (75 mM, NH₄CH₃COO) at the final ON concentration of 2.0×10^{-5} M and submitted to the annealing procedure (heating at 90 °C for 5 min and slowly cooling at r.t.). Before each experiment, the samples were equilibrated at 10 °C for 15 min. In ammonium acetate buffer (75 mM), the ON concentration was of 34 μM. After annealing, the samples were diluted with water to reach about 11 μM of ON and 25 mM of ammonium acetate.

CD spectra were recorded from 200 to 400 nm at 100 nm min⁻¹ scanning rate, 16 s response, 2.0 nm bandwidth, cell length 0,1 cm, V=400 μL. Each CD profile was obtained by taking the average of three scans.

CD heating and heating/cooling curves were obtained by monitoring the variation of absorbance at 263 nm from 10 to 90 (or 100) °C [ON] = 2.0×10^{-5} M, cell length 0.5 cm, V=1400 μL, temperature scan rate 0.2 °C min⁻¹. The resulting curves were processed using the adaptive smoothing (convolution width 25). Each heating/cooling curve was acquired in triplicate. For each T30695 variants, T_{1/2} and T_m values were calculated from the two minima of the first derivatives of the heating curves. The average of three values and the Standard Error were reported in Table 3.

¹H NMR experiments

NMR samples were prepared in the same K or Na buffer used for CD experiments, containing 10 % (v/v) /D₂O at a single strand concentration of about 4 mM. At each showed temperature, the ¹H NMR spectra were acquired as 16,384 data points with a recycle delay of 1.2 s. All spectra were recorded using pulsed-field gradient DPGSE for H₂O suppression. Data sets were zero filled to 32,768 points prior to Fourier transformation and apodized with a shifted sine bell squared window function.

Electrophoresis gel shift assay

ONs were annealed in Na buffer. The samples, with a total strand concentration of 0,2 O.D.x μL (100 μL), were heated to 90°C, gently cooled at r.t., than incubated at 20°C for two days. 2 μL of each solution were diluted with 4 μL of loading buffer (50% glycerol, 50% Na buffer,v:v) and loaded and ran on 12% non-denaturing polyacrylamide gels in 1XTBE buffer containing 50 mM of NaCl. The electrophoresis were ran at 5°C or 25 °C for 4 h at 120 V. The gel was visualized by UV lamp.

High Resolution Mass Spectrometry experiments

Oligonucleotides were annealed in 100, 75, 50, and 25 mM ammonium acetate buffer with a total strand concentration of 3 O.D. x mL (1 mL). The samples were directly infused into the HRMS instrument at 5 mL/min. The oligonucleotides annealed in 75 mM ammonium acetate buffer was further diluted with distilled water to a total strand concentration of 1 O.D. x mL (1 mL). Full scan HR MS experiments were acquired in negative ion mode in the mass range m/z 800-1800 at a resolving power of 60,000 (FWHM at m/z 400). The following source settings were used: a spray voltage of 3 kV, a capillary temperature in the range 100-300°C, a capillary voltage of -90 V, a sheath gas and an auxiliary gas flow of 40 and 1 (arbitrary units), respectively. The tube lens voltage was set at -150 V. Calculation of elemental formula was performed on the mono-isotopic peak of each ion cluster using Xcalibur software version 2.0.7 with a mass tolerance of 3 to 5 ppm.

The isotopic pattern of each ion cluster was taken into consideration in the assignment of molecular formula.

LEDGF/p75 dependent and independent integration assays

Previously developed homogenous time-resolved fluorescence (HTRF) technique [97] was used to determine IC₅₀ values of aptamers for both LEDGF/p75 dependent and independent integration activities. The ONs (lyophilized powders) were dissolved in phosphate buffer solution containing 70 mM of Na⁺ ions at pH=7 (at final ON concentration of 5 mM). The solutions were then annealed by heating at 95° C for 5 minutes and slowly (7-8 hrs) cooled down to room temperature. The ON solutions were serially diluted with buffer. For each ON, the highest stock concentration tested was 1mM which gave the final concentration of 20uM in the assay. 100 nM IN was incubated with varying concentrations of aptamers for 1 hour at room temperature in the reaction buffer containing 20mM HEPES (pH 7.5), 1mM DTT, 10 mM MgCl₂, 10% glycerol, 0.05% Brij-35, and 0.1 mg/mL BSA. Then integration reactions were initiated by addition of 50 nM 5'-Cy5 labelled 21-mer viral DNA and 10 nM 3'-Biotinylated target DNA and incubated for 3 hours at 37°C. For LEDGF/p75 dependent assay also 100 nM LEDGF/p75 was added to the reaction. For detection of the reaction products 2nM Eu-SA antibody in the detection buffer (20 mM EDTA, 0.05% Brij-35, 1mg/mL BSA and 1M NaCl) was added to the reaction mixture at the 1:1 ratio and incubated overnight at 4°C. The HTRF signal was recorded by PerkinElmer EnSpire multimode plate reader.

This work has been submitted for publication.

Bibliography

- [1] C. Tuerk and L. Gold, "Systematic evolution of ligands by exponential enrichment: RNA ligands to bacteriophage T4 DNA polymerase.," *Science*, vol. 249, no. 4968, pp. 505–510, 1990.
- [2] A. D. Scheludko *et al.*, "© 19 90 Nature Publishing Group," *J. Colloid Interface Sci.*, vol. 245, no. 1, pp. 118–143, 1998.
- [3] K. M. Song, S. Lee, and C. Ban, "Aptamers and their biological applications," *Sensors*, vol. 12, no. 1, pp. 612–631, 2012.
- [4] B. Santosh, and P. K. Yadava, "Nucleic Acid Aptamers: Research Tools in Disease Diagnostics and Therapeutics" *BioMed Res. Int.*, vol. 2014, 1-13, 2014.
- [5] P. R. Bouchard, R. M. Hutabarat, and K. M. Thompson, "Discovery and Development of Therapeutic Aptamers," *Annu. Rev. Pharmacol. Toxicol.*, vol. 50, no. 1, pp. 237–257, 2010.
- [6] V. Viglasky and T. Hianik, "Potential uses of G-quadruplex-forming aptamers," *Gen. Physiol. Biophys.*, vol. 32, pp. 149–172, 2013.
- [7] S. Burge, G. N. Parkinson, P. Hazel, A. K. Todd, and S. Neidle, "Quadruplex DNA: Sequence, topology and structure," *Nucleic Acids Res.*, vol. 34, no. 19, pp. 5402–5415, 2006.
- [8] M. L. Bochman, K. Paeschke, and V.A.Zakian "DNA secondary structures: stability and function of G- quadruplex structures," *Nat.Rev.Genet.*, vol. 13, no. 11, pp. 770–780, 2012.
- [9] D. Bhattacharyya, G. Mirihana Arachchilage, and S. Basu, "Metal Cations in G-Quadruplex Folding and Stability," *Front. Chem.*, vol. 4, no. 38, pp. 1–14, 2016.
- [10] V. Esposito, A. Galeone, L. Mayol, G. Oliviero, and A. Virgilio, "A topological classification of G-quadruplex structures," *Nucleosides, Nucleotides and Nucleic Acids*, vol. 26, no. 8–9, pp. 1155–1159, 2007.
- [11] A. N. Lane, J. B. Chaires, R. D. Gray, and J. O. Trent, "Stability and kinetics of G-quadruplex structures.," *Nucleic Acids Res.*, vol. 36, no. 17, pp. 5482–5515, 2008.
- [12] C. C. Hardin, T. Watson, M. Corregan, and C. Bailey, "Cation-Dependent Transition between the Quadruplex and Watson-Crick Hairpin Forms of d(CGCG3GCG)," *Biochemistry*, vol. 31, no. 3, pp. 833–841, 1992.
- [13] T. Miura, J. M. Benevides, and G. J. Thomas, "A phase diagram for sodium and potassium ion control of polymorphism in telomeric DNA.," *J. Mol. Biol.*, vol. 248, no. 2, pp. 233–8, 1995.
- [14] T. M. Bryan and P. Baumann, "G-quadruplexes: From guanine gels to chemotherapeutics," *Mol. Biotechnol.*, vol. 49, no. 2, pp. 198–208, 2011.
- [15] S. Neidle and M. A. Read, "G-Quadruplexes as Therapeutic Targets," *Biopolym.*, vol. 56, pp. 195–208, 2001.
- [16] W. I. Sundquist and A. Klug, "Telomeric DNA dimerizes by formation of guanine tetrads between hairpin loops," *Nature*, vol. 342, pp. 825–829, 1989.
- [17] D. Yang and K. Okamoto, "Structural insights into G-quadruplexes: towards new anticancer drugs," *Futur. Med. Chem.*, vol. 2, no. 4, pp. 619–646, 2010.
- [18] M. Read *et al.*, "Structure-based design of selective and potent G quadruplex-mediated telomerase inhibitors.," *Proc. Natl. Acad. Sci. U. S. A.*, vol. 98, no. 9, pp. 4844–9, 2001.
- [19] A. De Clan *et al.*, "Reevaluation of telomerase inhibition by quadruplex ligands and their mechanisms of action.," *Proc. Natl. Acad. Sci. U. S. A.*, vol. 104, no. 44, pp. 17347–52, 2007.
- [20] R. T. Wheelhouse, D. Sun, H. Han, F. X. Han, and L. H. Hurley, "Cationic porphyrins as telomerase inhibitors: The interaction of tetra- (N-methyl-4-pyridyl)porphine with quadruplex DNA [1]," *J. Am. Chem. Soc.*, vol. 120, no. 13, pp. 3261–3262, 1998.
- [21] T. Lemarteleur, D. Gomez, R. Paterski, E. Mandine, P. Mailliet, and J. F. Riou, "Stabilization

- of the c-myc gene promoter quadruplex by specific ligands' inhibitors of telomerase," *Biochem. Biophys. Res. Commun.*, vol. 323, no. 3, pp. 802–808, 2004.
- [22] P. Phatak *et al.*, "Telomere uncapping by the G-quadruplex ligand RHPS4 inhibits clonogenic tumour cell growth in vitro and in vivo consistent with a cancer stem cell targeting mechanism.," *Br. J. Cancer*, vol. 96, no. 8, pp. 1223–33, 2007.
- [23] M. Y. Kim, W. Duan, M. Gleason-Guzman, and L. H. Hurley, "Design, synthesis, and biological evaluation of a series of fluoroquinoanthroxazines with contrasting dual mechanisms of action against topoisomerase II and G-quadruplexes," *J. Med. Chem.*, vol. 46, no. 4, pp. 571–583, 2003.
- [24] N. Maizels, "Dynamic roles for G4 DNA in the biology of eukaryotic cells," *Nat. Struct. Mol. Biol.*, vol. 13, no. 12, pp. 1055–1059, 2006.
- [25] P. J. Bates, J. B. Kahlon, S. D. Thomas, J. O. Trent, and D. M. Miller, "Antiproliferative activity of G-rich oligonucleotides correlates with protein binding," *J. Biol. Chem.*, vol. 274, no. 37, pp. 26369–26377, 1999.
- [26] H. Qi *et al.*, "G-quadruplexes induce apoptosis in tumor cells," *Cancer Res*, vol. 66, no. 24, pp. 11808–11816, 2006.
- [27] V. Dapić, P. J. Bates, J. O. Trent, A. Rodger, S. D. Thomas, and D. M. Miller, "Antiproliferative activity of G-quartet-forming oligonucleotides with backbone and sugar modifications," *Biochemistry*, vol. 41, no. 11, pp. 3676–3685, 2002.
- [28] X. Xu *et al.*, "Inhibition of DNA Replication and Induction of S Phase Cell Cycle Arrest by G-rich Oligonucleotides," *J. Biol. Chem.*, vol. 276, no. 46, pp. 43221–43230, 2001.
- [29] A. C. Girvan *et al.*, "AGRO100 inhibits activation of nuclear factor-kB (NF-kB) by forming a complex with NF-kB essential modulator (NEMO) and nucleolin," *Mol. Cancer Ther.*, vol. 5, no. 7, pp. 1790–1799, 2006.
- [30] S. Soundararajan, W. Chen, E. K. Spicer, N. Courtenay-Luck, and D. J. Fernandes, "The nucleolin targeting aptamer AS1411 destabilizes Bcl-2 messenger RNA in human breast cancer cells," *Cancer Res.*, vol. 68, no. 7, pp. 2358–2365, 2008.
- [31] T. Chang *et al.*, "General Cell-Binding Activity of Intramolecular G-Quadruplexes with Parallel Structure," *PLoS One*, vol. 8, no. 4, pp. 1–10, 2013.
- [32] R. Tuteja and N. Tuteja, "Nucleolin: a multifunctional major nucleolar phosphoprotein", *Critical reviews in biochemistry and molecular biology*, vol. 33, no. 6, pp. 407–436, 1998.
- [33] A. G. Hovanessian *et al.*, "The Cell-Surface-Expressed Nucleolin Is Associated with the Actin Cytoskeleton," *Exp. Cell Res.*, vol. 261, no. 2, pp. 312–328, 2000.
- [34] E. M. Reyes-Reyes, F. R. Šalipur, M. Shams, M. K. Forsthoefel, and P. J. Bates, "Mechanistic studies of anticancer aptamer AS1411 reveal a novel role for nucleolin in regulating Rac1 activation," *Mol. Oncol.*, vol. 9, no. 7, pp. 1392–1405, 2015.
- [35] E. W. Choi, L. V. Nayak, and P. J. Bates, "Cancer-selective antiproliferative activity is a general property of some G-rich oligodeoxynucleotides," *Nucleic Acids Res.*, vol. 38, no. 5, pp. 1623–1635, 2010.
- [36] N. Zhang *et al.*, "Cytotoxicity of guanine-based degradation products contributes to the antiproliferative activity of guanine-rich oligonucleotides," *Chem. Sci.*, vol. 6, no. 7, pp. 3831–3838, 2015.
- [37] H. T. Le, W. L. Dean, R. Buscaglia, J. B. Chaires, and J. O. Trent, "An Investigation of G-Quadruplex Structural Polymorphism in the Human Telomere Using a Combined Approach of Hydrodynamic Bead Modeling and Molecular Dynamics Simulation," *J. Phys. Chem. B*, vol. 118, pp. 5390–5405, 2014.
- [38] A. Goodchild, A. King, M. M. Gozar, T. Passioura, C. Tucker, and L. Rivory, "Cytotoxic G-rich oligodeoxynucleotides: Putative protein targets and required sequence motif," *Nucleic Acids Res.*, vol. 35, no. 13, pp. 4562–4572, 2007.
- [39] M. M. Dailey, M. Clarke Miller, P. J. Bates, A. N. Lane, and J. O. Trent, "Resolution and characterization of the structural polymorphism of a single quadruplex-forming sequence,"

- Nucleic Acids Res.*, vol. 38, no. 14, pp. 4877–4888, 2010.
- [40] R. F. Macaya, P. Schultze, F. W. Smith, J. a Roe, and J. Feigon, “Thrombin-binding DNA aptamer forms a unimolecular quadruplex structure in solution,” *Proc. Natl. Acad. Sci. U. S. A.*, vol. 90, no. 8, pp. 3745–3749, 1993.
- [41] K. Y. Wang, P. H. Bolton, S. McCurdy, R. G. Shea, and S. Swaminathan, “A DNA Aptamer Which Binds to and Inhibits Thrombin Exhibits a New Structural Motif for DNA,” *Biochemistry*, vol. 32, no. 8, pp. 11285–92, 1993.
- [42] I. Russo Krauss, A. Merlino, A. Randazzo, E. Novellino, L. Mazzarella, and F. Sica, “High-resolution structures of two complexes between thrombin and thrombin-binding aptamer shed light on the role of cations in the aptamer inhibitory activity,” *Nucleic Acids Res.*, vol. 40, no. 16, pp. 8119–8128, 2012.
- [43] V. Dapić *et al.*, “Biophysical and biological properties of quadruplex oligodeoxyribonucleotides,” *Nucleic Acids Res.*, vol. 31, no. 8, pp. 2097–2107, 2003.
- [44] D. M. Tasset, M. F. Kubik, and W. Steiner, “Oligonucleotide inhibitors of human thrombin that bind distinct epitopes,” *J. Mol. Biol.*, vol. 272, no. 5, pp. 688–698, 1997.
- [45] T. Y. Tseng, Z. F. Wang, C. H. Chien, and T. C. Chang, “In-cell optical imaging of exogenous G-quadruplex DNA by fluorogenic ligands,” *Nucleic Acids Res.*, vol. 41, no. 22, pp. 10605–10618, 2013.
- [46] P. H. Wanrooij, J. P. Uhler, T. Simonsson, M. Falkenberg, and C. M. Gustafsson, “G-quadruplex structures in RNA stimulate mitochondrial transcription termination and primer formation,” *Proc. Natl. Acad. Sci.*, vol. 107, no. 37, pp. 16072–16077, 2010.
- [47] N. Al-Furoukh, S. Goffart, M. Szibor, S. Wanrooij, and T. Braun, “Binding to G-quadruplex RNA activates the mitochondrial GTPase NOA1,” *Biochim. Biophys. Acta - Mol. Cell Res.*, vol. 1833, no. 12, pp. 2933–2942, 2013.
- [48] T. Tang *et al.*, “hNOA1 interacts with complex I and DAP3 and regulates mitochondrial respiration and apoptosis,” *J. Biol. Chem.*, vol. 284, no. 8, pp. 5414–5424, 2009.
- [49] N. Al-Furoukh, S. Goffart, M. Szibor, S. Wanrooij, and T. Braun, “Binding to G-quadruplex RNA activates the mitochondrial GTPase NOA1,” *Biochim. Biophys. Acta - Mol. Cell Res.*, vol. 1833, no. 12, pp. 2933–2942, 2013.
- [50] C. A. Kretz, A. R. Stafford, J. C. Fredenburgh, and J. I. Weitz, “HD1, a thrombin-directed aptamer, binds exosite 1 on prothrombin with high affinity and inhibits its activation by prothrombinase,” *J. Biol. Chem.*, vol. 281, no. 49, pp. 37477–37485, 2006.
- [51] M. C. R. Buff *et al.*, “Dependence of aptamer activity on opposed terminal extensions: Improvement of light-regulation efficiency,” *Nucleic Acids Res.*, vol. 38, no. 6, pp. 2111–2118, 2009.
- [52] L. Bonifacio, F. C. Church, and M. B. Jarstfer, “Effect of locked-nucleic acid on a biologically active G-quadruplex. A structure-activity relationship of the thrombin aptamer,” *Int. J. Mol. Sci.*, vol. 9, no. 3, pp. 422–433, 2008.
- [53] N. Borbone *et al.*, “Investigating the role of T7 and T12 residues on the biological properties of thrombin-binding aptamer: Enhancement of anticoagulant activity by a single nucleobase modification,” *J. Med. Chem.*, vol. 55, no. 23, pp. 10716–10728, 2012.
- [54] S. Roy and M. Caruthers, “Synthesis of DNA/RNA and their analogs via phosphoramidite and H-phosphonate chemistries,” *Molecules*, vol. 18, no. 11, pp. 14268–14284, 2013.
- [55] J. Kypr, I. Kejnovská, D. Renčiuk, and M. Vorlíčková, “Circular dichroism and conformational polymorphism of DNA,” *Nucleic Acids Res.*, vol. 37, no. 6, pp. 1713–1725, 2009.
- [56] D. M. Gray, J.-D. Wen, C. W. Gray, R. Repges, C. Repges, G. Raabe and J. Fleischhauer, “Measured and Calculated CD Spectra of G-Quartets Stacked with the Same or Opposite Polarities,” *Chirality*, vol. 20, pp. 431–440, 2008.
- [57] C. M. Olsen, H. T. Lee, and L. A. Marky, “Unfolding thermodynamics of intramolecular G-quadruplexes: Base sequence contributions of the loops,” *J. Phys. Chem. B*, vol. 113, no. 9,

pp. 2587–2595, 2009.

- [58] M. Scuto et al., “Outstanding effects on antithrombin activity of modified TBA diastereomers containing an optically pure acyclic nucleotide analogue,” *Org. Biomol. Chem.*, vol. 12, no. July, pp. 5235–42, 2014.
- [59] R. De Cristofaro and E. Di Cera, “Phenomenological analysis of the clotting curve,” *J. Protein Chem.*, vol. 10, no. 5, pp. 455–468, 1991.
- [60] T. Coppola et al., “Synthesis, structural studies and biological properties of new TBA analogues containing an acyclic nucleotide,” *Bioorg. Med. Chem.*, vol. 16, no. 17, pp. 8244–8253, 2008.
- [61] M. Kolanczyk et al., “NOA1 is an essential GTPase required for mitochondrial protein synthesis,” *Mol. Biol. Cell*, vol. 22, no. 1, pp. 1–11, 2011.
- [62] J. Downward, “Targeting RAS signalling pathways in cancer therapy,” *Nat. Rev. Cancer*, vol. 3, no. 1, pp. 11–22, 2003.
- [63] B. Vogelstein and K. W. Kinzler, “Cancer genes and the pathways they control,” *Nat. Med.*, vol. 10, no. 8, pp. 789–799, 2004.
- [64] W. A. Kibbe, “OligoCalc: An online oligonucleotide properties calculator,” *Nucleic Acids Res.*, vol. 35, no. SUPPL.2, pp. 43–46, 2007.
- [65] K. Qian, S. L. Morris-Natschke and K.H. Lee, “HIV Entry Inhibitors and Their Potential in HIV Therapy” *Med. Res. Rev.*, vol. 29, no. 2, pp. 369–393, 2009.
- [66] R. Parker, D. J. Stein, and J. Jelsma, “Pain in people living with HIV/AIDS: A systematic review,” *J. Int. AIDS Soc.*, vol. 17, 2014.
- [67] P. Idele et al., “Epidemiology of HIV and AIDS Among Adolescents,” *JAIDS J. Acquir. Immune Defic. Syndr.*, vol. 66, pp. S144–S153, 2014.
- [68] A. Engelman and P. Cherepanov, “The structural biology of HIV-1: mechanistic and therapeutic insights,” *Nat. Rev. Microbiol.*, vol. 10, no. 4, pp. 279–290, 2009.
- [69] D. Musumeci, C. Riccardi and D. Montesarchio, “G-Quadruplex Forming Oligonucleotides as Anti-HIV Agents”, *Molecules*, vol. 20, no. 9, 17511-17532, 2015.
- [70] P. Cherepanov et al., “Mode of interaction of G-quartets with the integrase of human immunodeficiency virus type 1,” *Mol Pharmacol*, vol. 52, no. 5, pp. 771–780, 1997.
- [71] J. A. Este et al., “Human immunodeficiency virus gp120 as the primary target of action of AR177 (Zintevir),” *Molecular pharmacology*, vol. 53, pp. 340–345, 1998.
- [72] N. Jing, C. Marchand, J. Liu, R. Mitra, M. E. Hogan, and Y. Pommier, “Mechanism of inhibition of HIV-1 integrase by G-tetrad-forming oligonucleotides in vitro,” *J. Biol. Chem.*, vol. 275, no. 28, pp. 21460–21467, 2000.
- [73] N. Jing et al., “Stability-activity relationships of a family of G-tetrad forming oligonucleotides as potent HIV inhibitors. A basis for anti-HIV drug design,” *J. Biol. Chem.*, vol. 275, no. 5, pp. 3421–3430, 2000.
- [74] N. Q. Do, K. W. Lim, M. H. Teo, B. Heddi, and A. T. Phan, “Stacking of G-quadruplexes: NMR structure of a G-rich oligonucleotide with potential anti-HIV and anticancer activity,” *Nucleic Acids Res.*, vol. 39, no. 21, pp. 9448–9457, 2011.
- [75] V. T. Mukundan, N. Q. Do, and A. T. Phan, “HIV-1 integrase inhibitor T30177 forms a stacked dimeric G-quadruplex structure containing bulges,” *Nucleic Acids Res.*, vol. 39, no. 20, pp. 8984–8991, 2011.
- [76] L. Feng, R. C. Larue, A. Slaughter, J. J. Kessler, and M. Kvaratskhelia, “HIV-1 Integrase Multimerization as a Therapeutic Target,” *Curr Top Microbiol Immunol.*, vol. 389, no. 4, pp. 93–119, 2015.
- [77] T. Masuda, “Non-enzymatic functions of retroviral integrase: The next target for novel anti-HIV drug development,” *Front. Microbiol.*, vol. 2, no. OCT, pp. 1–5, 2011.
- [78] M. Sgobba, O. Olubiyi, S. Ke, and S. Haider, “Molecular dynamics of HIV-1 Integrase in complex with 93del-A structural perspective on the mechanism of inhibition,” *J. Biomol. Struct. Dyn.*, vol. 29, no. 5, pp. 863–877, 2012.

- [79] V. R. De Soultrait, P. Y. Lozach, R. Altmeyer, L. Tarrago-Litvak, S. Litvak, and M. L. Andréola, "DNA aptamers derived from HIV-1 RNase H inhibitors are strong anti-integrase agents," *J. Mol. Biol.*, vol. 324, no. 2, pp. 195–203, 2002.
- [80] A. T. Phan, V. Kuryavyi, J.-B. Ma, A. Faure, M.-L. Andréola, and D. J. Patel, "An interlocked dimeric parallel-stranded DNA quadruplex: a potent inhibitor of HIV-1 integrase.," *Proc. Natl. Acad. Sci. U. S. A.*, vol. 102, no. 3, pp. 634–9, 2005.
- [81] A. Mazumder, N. Neamati, J. O. Ojwang, S. Sunder, R. F. Rando, and Y. Pommier, "Inhibition of the human immunodeficiency virus type 1 integrase by guanosine quartet structures," *Biochemistry*, vol. 35, no. 43, pp. 13762–13771, 1996.
- [82] M. Vorlíčková *et al.*, "Circular dichroism and guanine quadruplexes," *Methods*, vol. 57, no. 1, pp. 64–75, 2012.
- [83] N. Jing and M. E. Hogan, "Structure-activity of tetrad-forming oligonucleotides as a potent anti- HIV therapeutic drug," *J. Biol. Chem.*, vol. 273, no. 52, pp. 34992–34999, 1998.
- [84] P. A. Rachwal and K. R. Fox, "Quadruplex melting," *Methods*, vol. 43, no. 4, pp. 291–301, 2007.
- [85] P. Schultze, N. V. Hud, F. W. Smith, and J. Feigon, "The effect of sodium, potassium and ammonium ions on the conformation of the dimeric quadruplex formed by the *Oxytricha nova* telomere repeat oligonucleotide d(G4T4G4)," *Nucleic Acids Res.*, vol. 27, no. 15, pp. 3018–3028, 1999.
- [86] M. P. Horvath and S. C. Schultz, "DNA G-quartets in a 1.86 Å resolution structure of an *Oxytricha nova* telomeric protein-DNA complex1," *J. Mol. Biol.*, vol. 310, no. 2, pp. 367–377, 2001.
- [87] M. Adrian, B. Heddi, and A. T. Phan, "NMR spectroscopy of G-quadruplexes," *Methods*, vol. 57, no. 1, pp. 11–24, 2012.
- [88] N. Jing, X. Gao, R. F. Rando, and M. E. Hogan, "Potassium-induced loop conformational transition of a potent anti-hiv oligonucleotide," *J. Biomol. Struct. Dyn.*, vol. 15, no. 3, pp. 573–585, 1997.
- [89] N. Q. Do and A. T. Phan, "Monomer-dimer equilibrium for the 5'-5' stacking of propeller-type parallel-stranded g-quadruplexes: NMR structural study," *Chem. Eur. J.*, vol. 18, no. 46, pp. 14752–14759, 2012.
- [90] F. Rosu, V. Gabelica, H. Poncelet, and E. De Pauw, "Tetramolecular G-quadruplex formation pathways studied by electrospray mass spectrometry," *Nucleic Acids Res.*, vol. 38, no. 15, pp. 5217–5225, 2010.
- [91] R. Ferreira, A. Marchand, and V. Gabelica, "Mass spectrometry and ion mobility spectrometry of G-quadruplexes. A study of solvent effects on dimer formation and structural transitions in the telomeric DNA sequence d(TAGGGTTAGGGT)," *Methods*, vol. 57, no. 1, pp. 56–63, 2012.
- [92] C. L. Mazzitelli, J. Wang, S. I. Smith, and J. S. Brodbelt, "Gas-Phase Stability of G-quadruplex DNA Determined by Electrospray Ionization Tandem Mass Spectrometry and Molecular Dynamics Simulations," *J. Am. Soc. Mass Spectrom.*, vol. 18, no. 10, pp. 1760–1773, 2007.
- [93] M. Rueda, S. G. Kalko, F. J. Luque, and M. Orozco, "The structure and dynamics of DNA in the gas phase.," *J. Am. Chem. Soc.*, vol. 125, no. 26, pp. 8007–14, 2003.
- [94] N. Nagesh and D. Chatterji, "Ammonium ion at low concentration stabilizes the G-quadruplex formation by telomeric sequence," *J. Biochem. Biophys. Methods*, vol. 30, no. 1, pp. 1–8, 1995.
- [95] L. Feng *et al.*, "The A128T resistance mutation reveals aberrant protein multimerization as the primary mechanism of action of allosteric HIV-1 integrase inhibitors," *J. Biol. Chem.*, vol. 288, no. 22, pp. 15813–15820, 2013.
- [96] N. Jing, R. F. Rando, Y. Pommier, and M. E. Hogan, "Ion selective Folding of loop domains in a potent anti-HIV oligonucleotide," *Biochemistry*, vol. 36, no. 41, pp. 12498–12505, 1997.

- [97] C. J. McKee, J. J. Kessl, N. Shkriabai, M. J. Dar, A. Engelman, and M. Kvaratskhelia, “Dynamic modulation of HIV-1 integrase structure and function by cellular lens epithelium-derived growth factor (LEDGF) protein,” *J. Biol. Chem.*, vol. 283, no. 46, pp. 31802–31812, 2008.
- [98] J. J. Kessl *et al.*, “FRET analysis reveals distinct conformations of in tetramers in the presence of viral DNA or LEDGF/p75,” *Nucleic Acids Res.*, vol. 39, no. 20, pp. 9009–9022, 2011.
- [99] P. Cherepanov, “LEDGF/p75 interacts with divergent lentiviral integrases and modulates their enzymatic activity in vitro,” *Nucleic Acids Res.*, vol. 35, no. 1, pp. 113–124, 2007.

Part II

1. Introduction

1.1. Azobenzenes as molecular photoswitchers

Nowadays, molecular switchers attract great interest in view of the fascinating challenge to reach the spatial and temporal control of chemical and/or biological processes. Light is the ideal external reagent trigger for *in situ* chemical and biological processes, because: i) it provides high selectivity and does not cause the sample contamination; ii) it is generally non-invasive within specific wavelength; iii) it can be regulated qualitatively and quantitatively, adjusting its wavelength and intensity, and iv) it can be delivered with very high spatial and temporal precision [1]. Photoresponsive molecules (“Photoswitchers”) exhibit two forms, differing from each other for their chemical-physical properties. Upon irradiation with a light tuned on specific wavelengths, the stable form may reversibly convert into metastable one. One of the most attractive application of photoswitchers concerns the dynamic photocontrol of drug activity. Indeed, being the pharmacodynamic and pharmacokinetic properties of drugs directly related to their molecular structure, exploiting photoinducible structural changes, the therapeutic action of photoresponsive agents should be finely controlled.

The most common photoswitchers are: azobenzenes and stilbenes, which undergo *cis-trans* isomerisation; diarylethenes and spiropyrans which interconvert between open and closed forms (Figure 1).

The largest and most investigated class of photoswitchers are the azobenzenes, which present two aromatic rings linked by azo group (N=N) and can exist in two isomeric states, *trans* and *cis*, with the former being ~10 kcal/mol more stable than the latter. The readily isomerization of the N=N double bond by a light source and the easiness of synthesis of many derivatives make azobenzenes good candidates for various applications from materials science to neurobiology. Originally, azo

compounds were used as synthetic colouring agents in the dye industry, their discovery dates back to 1800 [2][3]; a high number of chemical-physical studies have been performed in order to evaluate the fluctuation of photoresponsive properties in different sets of variously functionalized azobenzenes, including the introduction of multiple diazo moieties, the use of diverse aromatic rings and/or diverse substituents on aromatic rings [3][4][5].

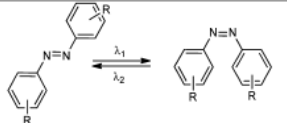
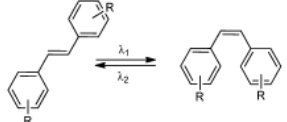
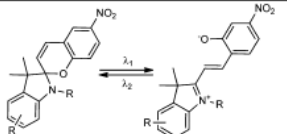
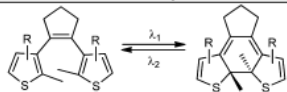
| | Photoswitches | Isomerization | λ_1/λ_2 | polarity change |
|----------|---------------|---|---------------------------------------|-------------------------------------|
| A | Azobenzenes |  | UV/VIS (ΔT) | medium ($\Delta\mu = \sim 3$ D) |
| B | Stilbenes |  | UV/UV | small |
| C | Spiropyrans |  | UV/VIS (ΔT) or VIS/UV | large ($\Delta\mu = 8-15$ D) |
| D | Diarylethenes |  | UV/VIS | small |

Figure 1. Molecular Structures of Photoswitchers.

The *trans* azobenzene is 10–12 kcal mol⁻¹ more stable than the *cis* isomer, accordingly, in the dark, at equilibrium, *trans* is the dominant isomer (>99.99%). The *trans* and *cis* azobenzenes differ from each other in polarity, molecular geometry and absorption spectrum. The *trans* isomer is almost planar and has a dipole moment near to zero, in contrast the *cis* isomer is twisted $\approx 55^\circ$ out of the plane and has a dipole moment of 3 Debye (Figure 2).

The *cis-trans* azobenzene isomerization process also causes the decrease of distance, from 9.0 Å to 5.5 Å between the two carbons in para positions.

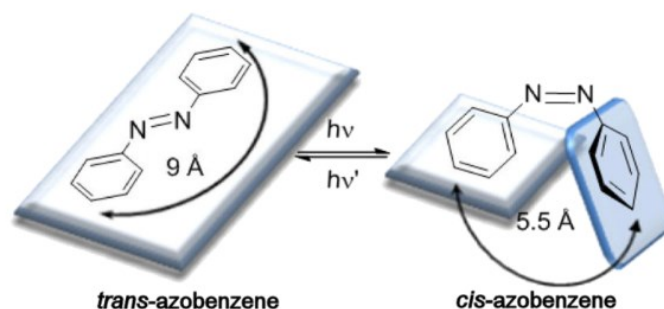


Figure 2. Photoisomerization process of azobenzene [from *Beilstein J. Org. Chem.*, vol. 8, pp. 1071–1090, 2012].

The UV–vis spectra of *cis/trans* azobenzene differ from each other [3] (Figure 3). *Trans*-Azobenzene shows a weak $n \rightarrow \pi^*$ band around 440 nm and a more intense $\pi \rightarrow \pi^*$ band near 320 nm; whereas the UV spectrum of the *cis*-azobenzene shows a more intense $n \rightarrow \pi^*$ band than that of the *trans* form, and other absorption bands at 280 nm and 250 nm. The transition $\pi \rightarrow \pi^*$ is usually in the near UV region, while the electronic transition $n \rightarrow \pi^*$ is usually located in the visible region and is due to the presence of unshared electron pairs of nitrogen atoms [6].

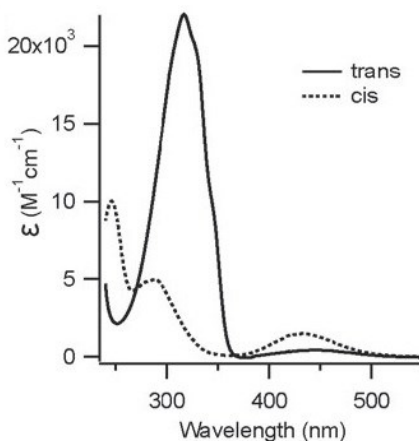


Figure 3 The UV-vis spectra of the *trans* and *cis* isomers of azobenzene [from *Chem. Soc. Rev.*, vol. 40, no. 8, pp. 4422–4437, 2011].

Thanks to the differences of the *cis/trans* adsorption bands, the irradiation with a light tuned on a specific wavelength allows the *cis/trans* photochemical conversion. The wavelength suitable to the conversion is dependent on both the nature and the position of the substituents of the aryl groups [3][7].

The *trans*-azobenzene easily isomerizes to the *cis* isomer by irradiation with a light tuned on 320–350 nm. The *trans* isomer is renovated reversibly irradiating the *cis* isomer with a light tuned on 400–450 nm, or spontaneously in the dark. The *cis/trans* photoisomerization of many azobenzenes occurs on the scale of picoseconds, while in other cases the thermal relaxation of the *cis* isomer to the *trans* isomer is slower (from milliseconds to days) [3].

The mechanism of photoisomerization of *trans* azobenzene has attracted interest for many years and is today still under investigation [8][9][10].

In the UV-visible spectra of the molecule the two major absorption bands correspond to $n \rightarrow \pi^*$ electronic transition ($S_0 \rightarrow S_1$) with the maximum intensity near 440 nm and to $\pi \rightarrow \pi^*$ electronic transition ($S_0 \rightarrow S_2$) with the maximum intensity near 320 nm.

Excitation of these two electronic states imply two different isomerization mechanisms; visible excitation to the $S_1(n, \pi^*)$ state leads to the isomerisation via inversion around one nitrogen atom in the same molecular plane, whereas UV excitation to the $S_2(\pi, \pi^*)$ state leads to the isomerisation via the rotation around the NN double bond (Figure 4) [11][12].

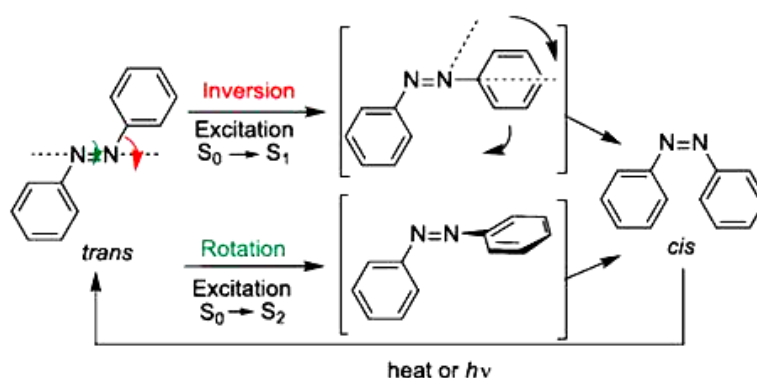


Figure 4. Inversion and Rotation Mechanisms of *trans*-azobenzene.

1.2. Modulating Azobenzenes photoisomerization for *in vivo* use

Pharmacotherapy aims to treat diseases and alleviate symptoms through the administration of drugs; however, poor drug selectivity can induce side effects and drug resistance. These restrictions should be predictable considering the affinity of drugs for more than one biological targets, being, the latter, involved at different stage of complex signalling and metabolic pathways. A possible solution to these problems could be the control of drug action in time and in space by light [13][14], achievable through the design and the synthesis of photopharmacological agents, whose pharmacodynamic and pharmacokinetic properties can be modified through photoinduced changes in the structure. In order to develop optically controlled drugs azo compounds are good candidates in view of their easy, quantitative and reversible *cis-trans* photoisomerization.

Very recently, some azobenzene derivatives have been reported as potential anti-cancer agents. Indeed, the main aim of the cancer research is the finding of selective and specific inhibitors of cancer cells growth, leading to a drastic reduction of systemic side effects. Being the pharmacological action of these azocompounds "*photoregulated*", the spatial-temporal control of their biological action can be triggered by light. The second part of my research activity has been performed in this fascinating field and such preliminary results are reported in the next two chapters.

2. Azobenzene Photoswitchers as anti-cancer tools

2.1. Photo-control of cancer cell growth by N-substituted pyrrole azo-derivatives

Currently, among the most clinically used chemotherapeutics are Microtubules (MTs) inhibitors, such as Taxol and the Vinca alkaloids. Microtubules are involved in several cellular processes, including intracellular transport, cell motility, and mitosis, therefore treatment with microtubule directed drugs often leads to serious systemic side-effects, such as cardiotoxicity and neurotoxicity. Mostly, it has been discovered that PSTs (Figure 5) could be an efficient alternative to colchicines and combretastatins, as tubulin and MTs directed drugs, since, being their action controlled by local and specific irradiation, the side effects associated with MTs depolymerization in normal cells can be, potentially, avoided. [15][16]. PSTs were designed as Combretastatin A-4 analogs only changing a double C bond in to a double N bond. Their affinities towards MTs colchicine binding site were turned on by irradiation of the stable *trans* isomers into the corresponding *cis*.

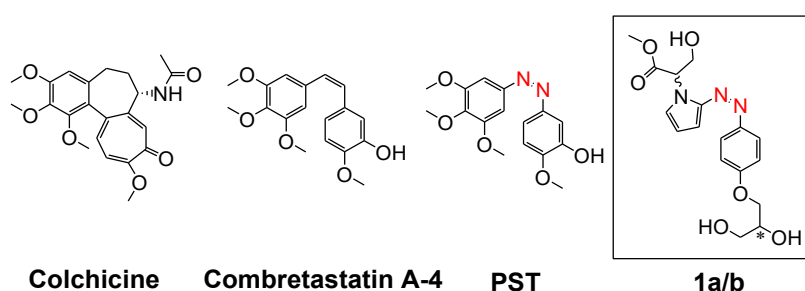


Figure 5. Natural ligands of MTs and AzD analogs.

In this frame, the large number of Combretastatin A-4 analogs discovered in the last years [17][18], modified at phenyl rings and/or at double carbon bond, suggest that the exploration of different typology of AzB analogs as potential photo-activable inhibitors of cancer cell growth should be achievable. Literature data highlight that etheroarene diazo derivatives showed interesting optical properties, in view of their ability to switch from the *trans* to the *cis* form by irradiation with low light intensity having red-shifted wavelengths, respect to that occurring for un-substituted AzB [19]. Furthermore, the regioselective reactivity at carbon 1 of N-substituted pyrrole derivatives in reaction

with azonium salts, should increase both the number of synthesizable Azo dyes, obtainable by replacing the substituent at nitrogen atom of pyrrole ring, and the yields of the coupling reaction, avoiding the formation of different regioisomers [17].

In order to explore the potentiality of azo-heteroarene typology as cancer cell growth inhibitors, we synthesized the **1a/1b** molecules (Figure 5), that were successively studied for their physical and biological properties. Based on the promising photo-activable antiproliferative action on HCT p53^{-/-} cancer cells (see below) the mixture **1a** was successively reproduced as pure stereomers **1RR** and **1RS**.

2.2. Results

Synthesis of **1a**, **1b** and **1RR**, **1RS**.

The four synthetic steps were performed starting from 4-nitrophenol (Figure 6), which was coupled with R or S glycidol in presence of catalytic amount of KOH, to obtain the intermediates **2** [20]. Reduction of **2**, as R or S stereomer, with H₂/Pd (C) and successive conversion of the amino- to the diazonium-group gave rise to **4R** or **4S**, each of them was finally coupled with racemic methyl 3-hydroxy-2-(1H-pyrrol-1-yl)propanoate **5**. The best yields of the coupling step were obtained quenching the reactions after 1h from the mixture.

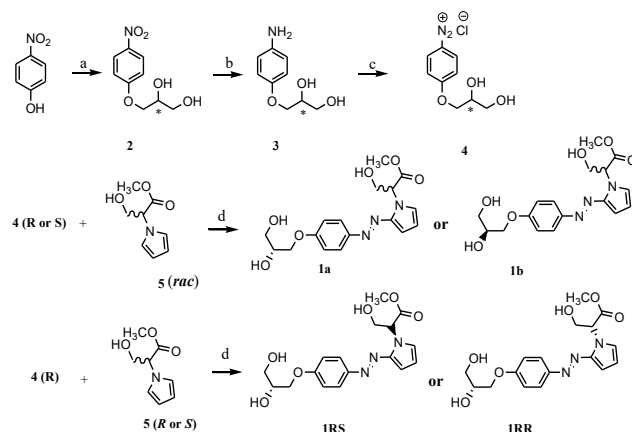


Figure 6. a) 4-nitrophenol, (0.500 g, 3,6 mmol), KOH (1 mg, $1,8 \times 10^{-2}$ mmol), dry toluene (2 mL) 30 min under reflux. 287 μ L of R or S glycidol (0,320 g, 4,3 mmol) was added at r.t., then heated at 90°C for 24h. b) 2 (R or S, 0,560 g, 2,6 mmol), Pd/C (28 mg), 25 mL di EtOH (90%, HPLC grade) were stirred 2 h in a Parr apparatus under H₂ (P= 400 psi). c) a mixture of 3 (0,400 g, 2,2 mmol), 205 μ L fluoroboric acid (water solution, 48%, 3,3 mmol), EtOH (4 mL) was cooled at -15°C under argon, 224 μ L of isoamyl nitrite (0,258 g, 2,2 mmol) were added and the reaction was kept at r.t. 12h. d) 4 (0,360 g, 1,8 mmol), 10 mL of acetic acid (14 g, 232 mmol), sodium acetate (4,0 g, 511mmol) and 5 (rac or R or S) (254 μ L, 0,270 g, 2,2 mmol) were kept 1 h at r.t., under slow stirring to give **1a**, or **1b**, or **1RR** or **1SS** (yields 58-59%).

The final diastereomeric mixtures **1a** and **1b**, as well as the pure **1RR** and **1RS**, and/or intermediates were characterized by mono- and bi-dimensional HRMS, NMR, and UV.

UV-Vis spectroscopy

UV spectra of the thermodynamically stable *trans* **1a** and **1b** were performed in three different solvents, MeOH, H₂O and Phosphate Buffer Solution (PBS). In order to obtain data related to the *trans* isomer, the cuvette (0.1 o.l. Vol. 400 μ L) containing 40 or 80 μ M of **1a** or **1b** in MeOH was taken in dark at r.t. for about 12 h

In all examined conditions the UV profiles (Figure 7A) of both species were almost superimposable, showing, in H₂O and Phosphate Buffer Solution (PBS), two major broad bands, with similar intensity, centered at 391 and 430 nm whereas in MeOH the relative intensity of the same two bands was appreciably different. After light exposition (435 nm), the UV profiles of *trans* **1a** and **1b** strongly changed to give rise to the *cis* **1a** and **1b** UV spectra, showing a significant decreasing of the band intensities in the range 350-460 nm, the occurrence of a new band centered at about 340 nm (Figure 7B, line blue) and a broad absorption band that extended over than 475 nm.

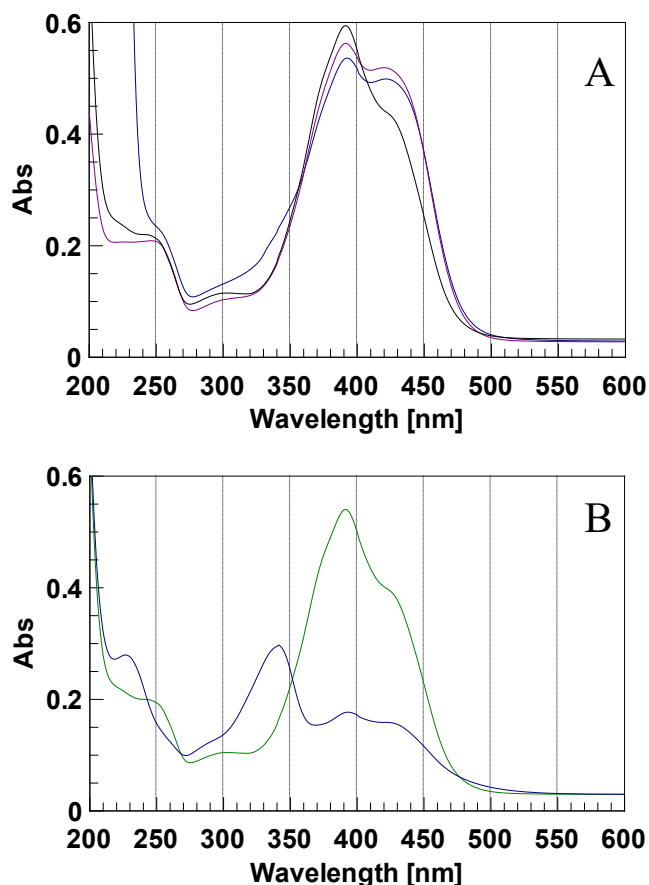


Figure 7. Panel A: UV spectra of **1a** in MeOH (black), PBS (blue) and H₂O (violet). Panel B: UV spectra of **1a** in MeOH before (green) and after (blue) irradiation at 435 nm.

The *cis* **1a/b** thermal decay was monitored by further sequential acquisition of spectra until the UV profile rises to that of the initial *trans* isomer (Figure 8). In order to obtain $t_{1/2}$ of *cis* isomer, after the sample irradiation with light at 435 nm, UV time course measurement experiments were performed monitoring the absorbance values at 340, 390, 425, 400 and 505 nm, number of cycle 100-180, cycle time 60 sec (Figure 9-10-11-12).

In both type of experiments, the intensity of UV band at 390 nm were almost restored into about 40 or 10 min in the case of **1a** and 80 or 10 min for **1b**, depending on the solvent conditions (MeOH or PBS, respectively). All the collected UV data strongly suggested that irradiation of samples with violet light induced the conversion of the thermodynamically stable *trans* **1a/b** to the corresponding metastable *cis*, and that *cis* to *trans* reversion occurred in dark.

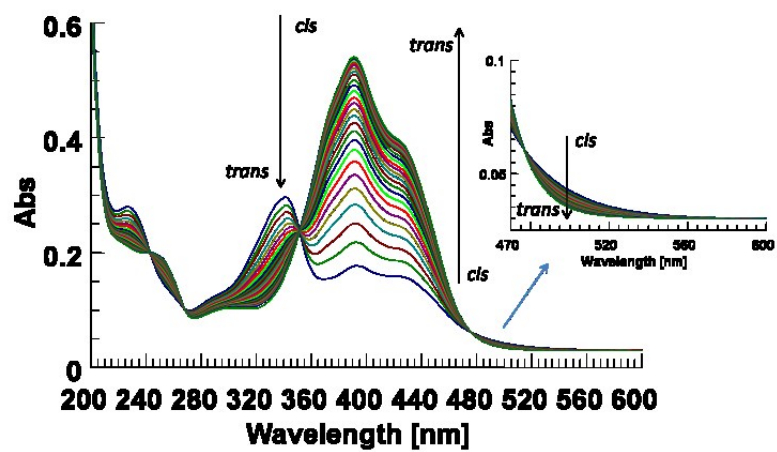
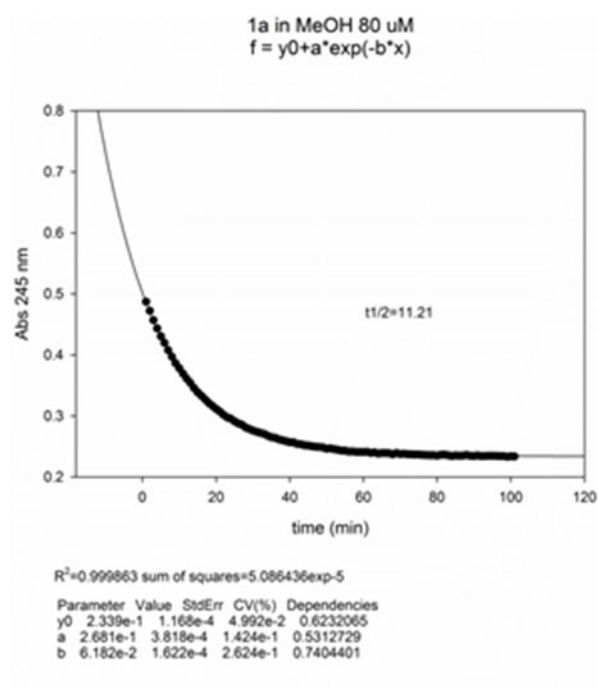
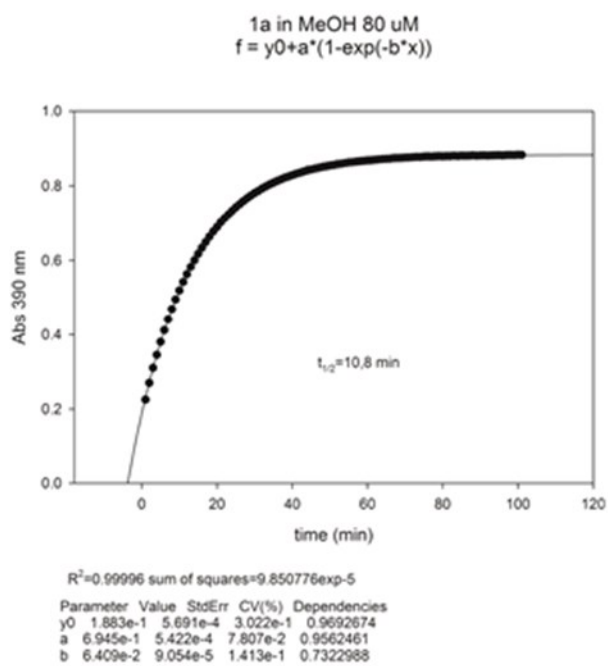


Figure 8. Time-dependent UV spectra of 1a (2 min) after irradiation at 435 nm.

Panel A



Panel B

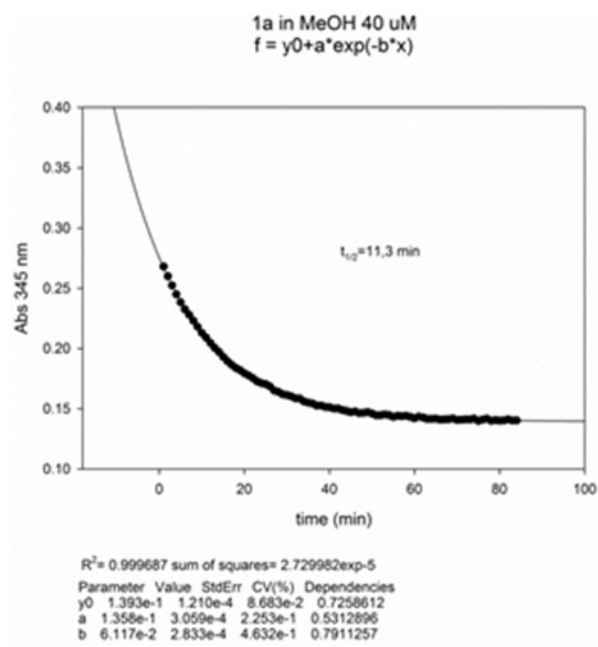
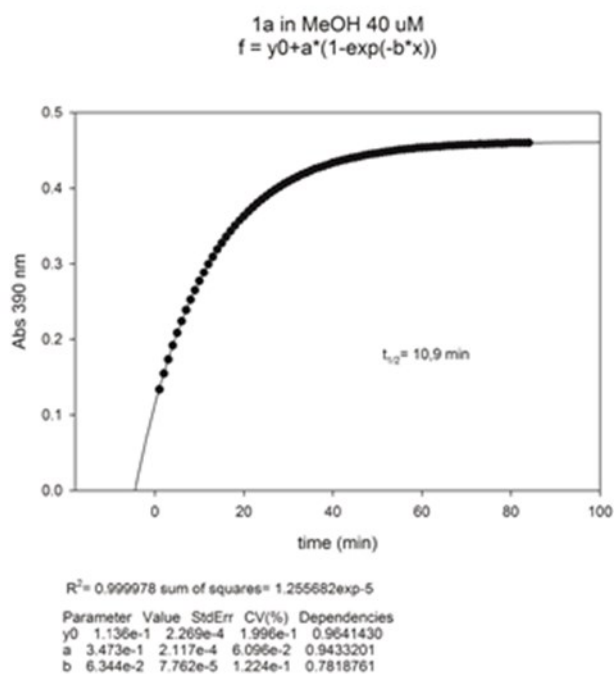
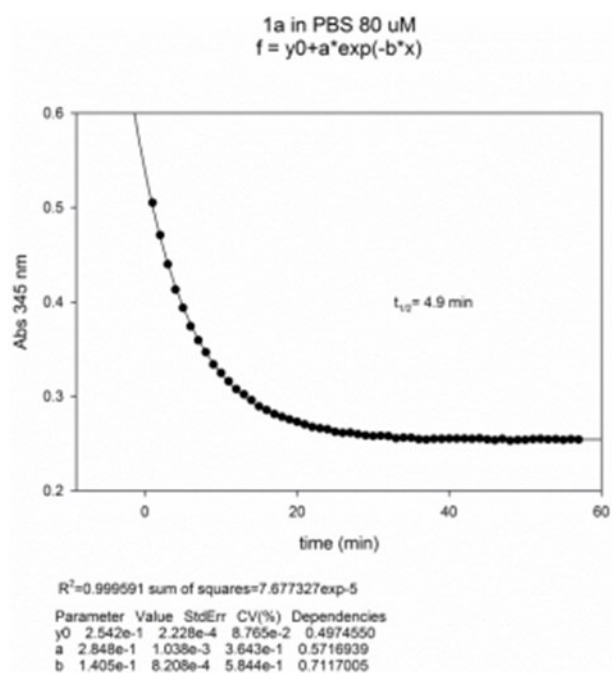
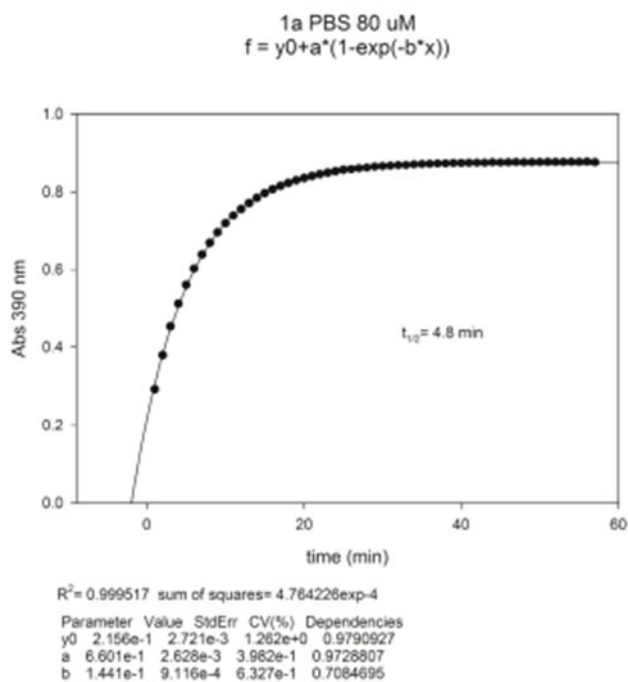


Figure 9. Time-dependent absorption after irradiation of **1a** measured in MeOH at 390 and 345 nm. Panel A [**1a**] = 80 μ M; panel B [**1a**] = 40 μ M

Panel C



Panel D

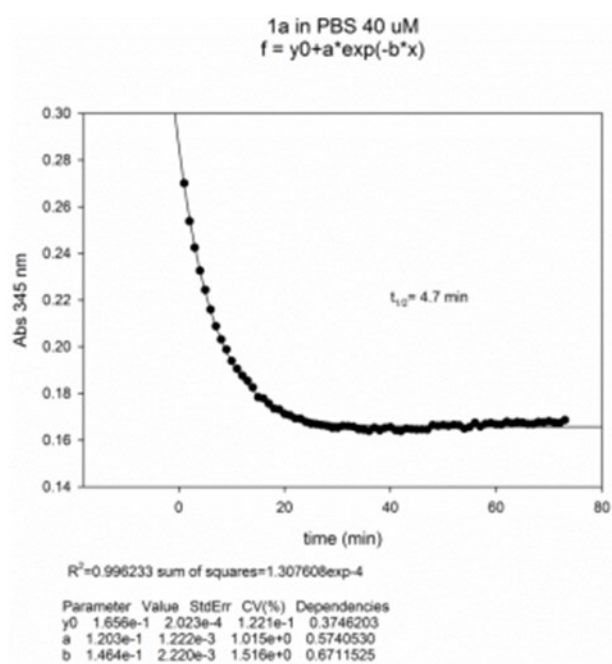
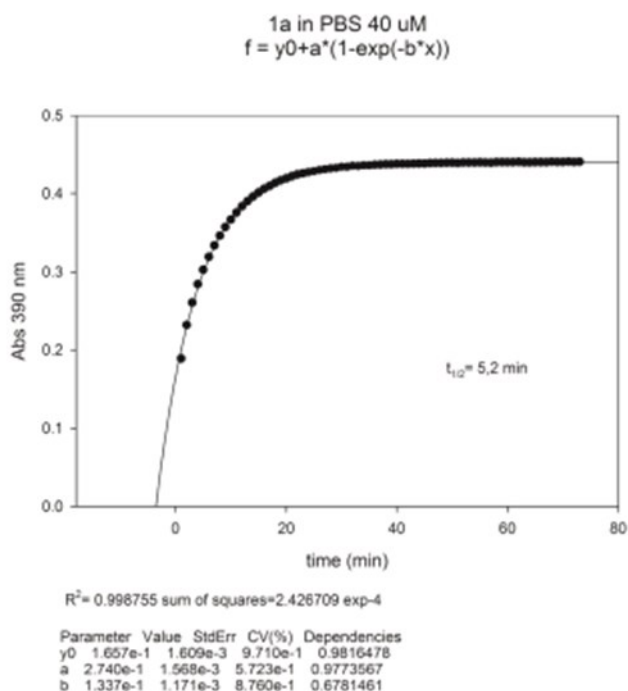
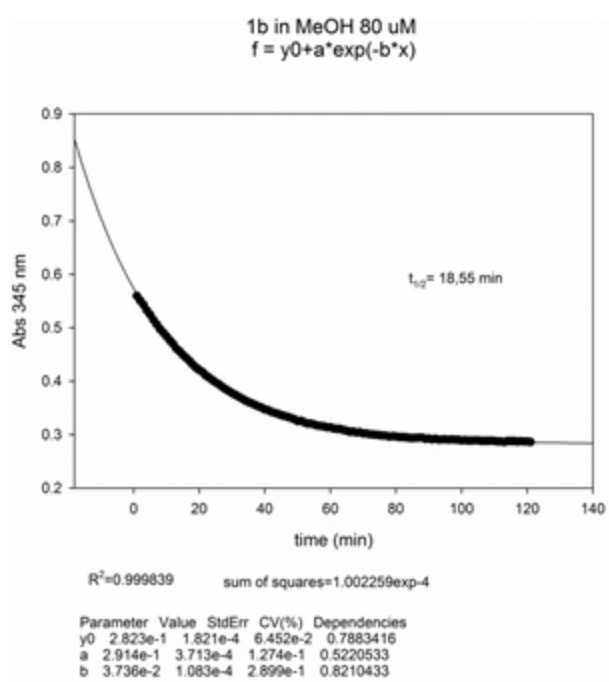
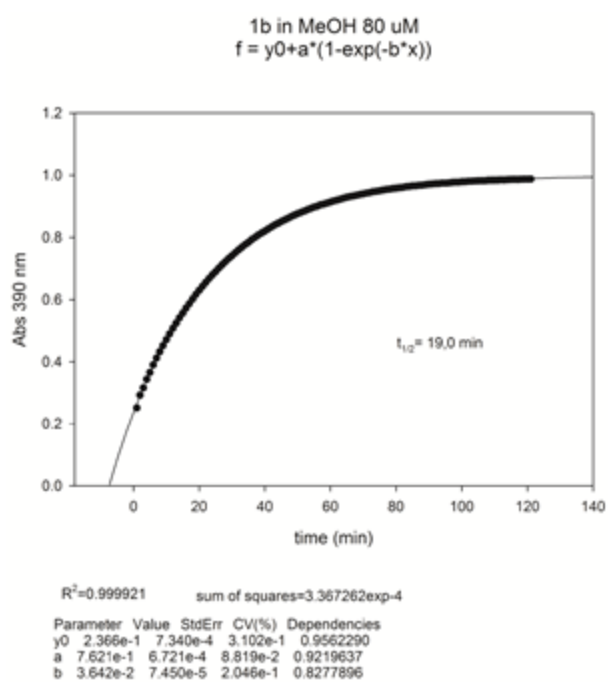


Figure 10. Time-dependent absorption after irradiation of **1a** measured in PBS at 390 and 345 nm. Panel C [1a] = 80 μ M; panel D [1a] = 40 μ M

Panel A



Panel B

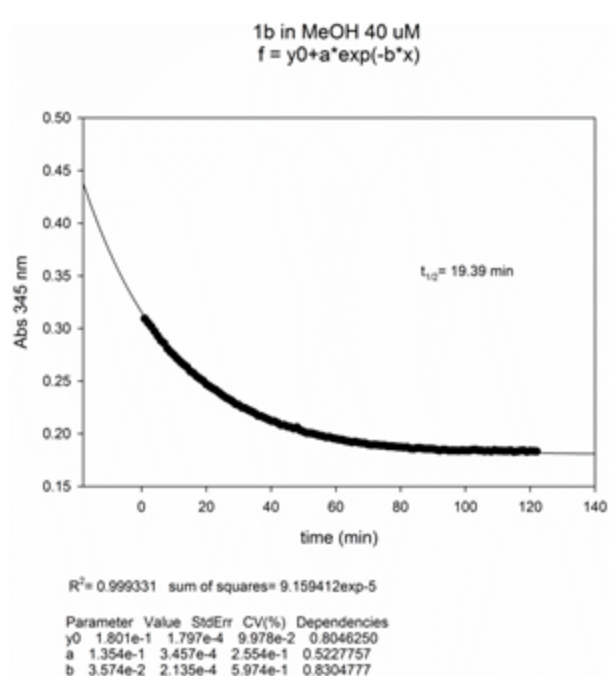
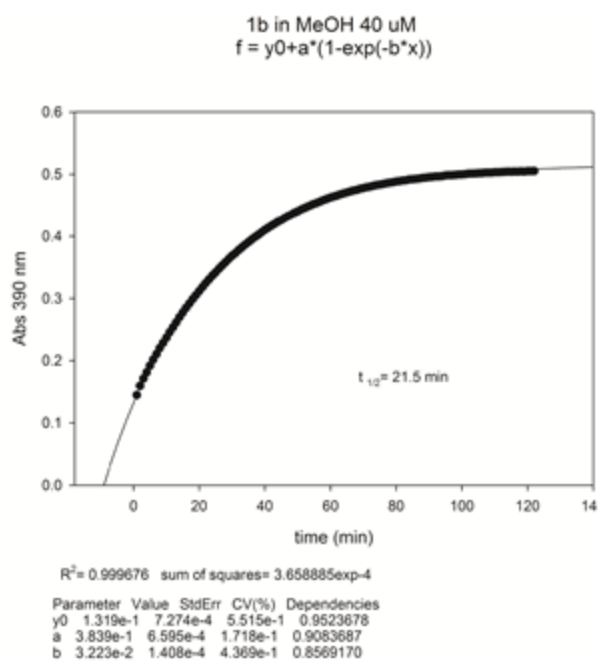
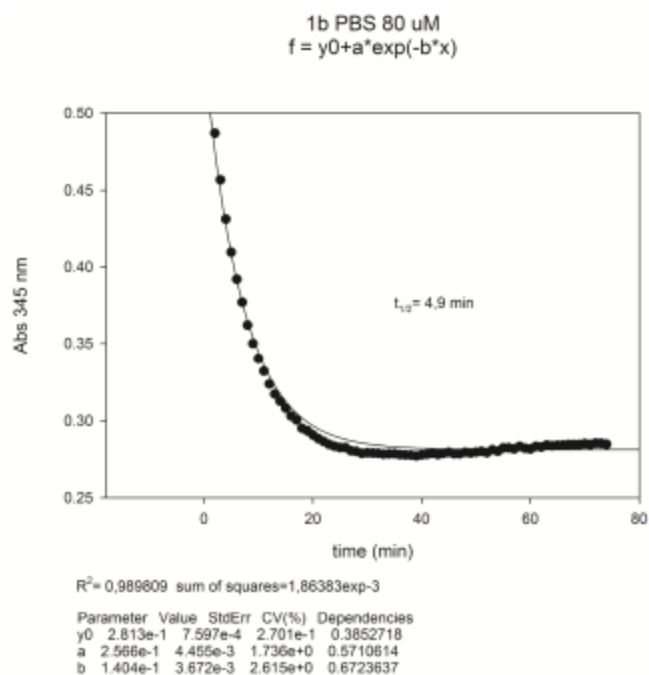
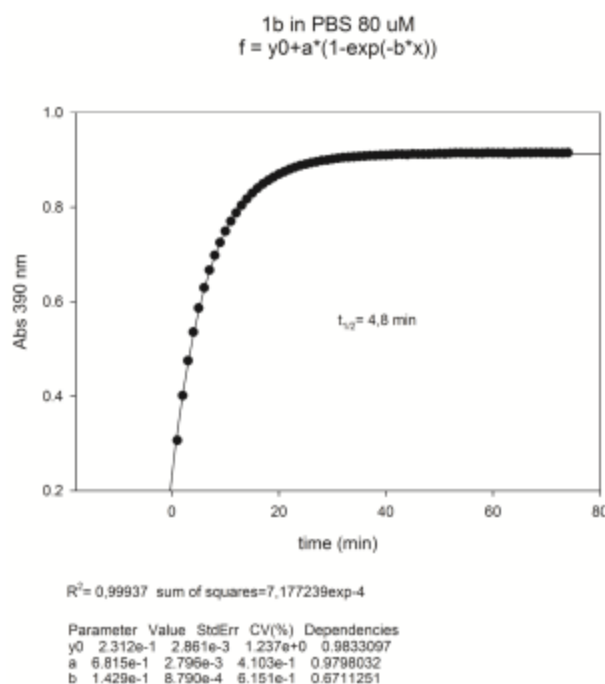


Figure 11. Time-dependent absorption after irradiation of **1b** measured in MeOH at 390 and 345 nm. Panel A [**1b**] = 80 μ M; panel B [**1b**] = 40 μ M

Panel C



Panel D PBS 40 μ M

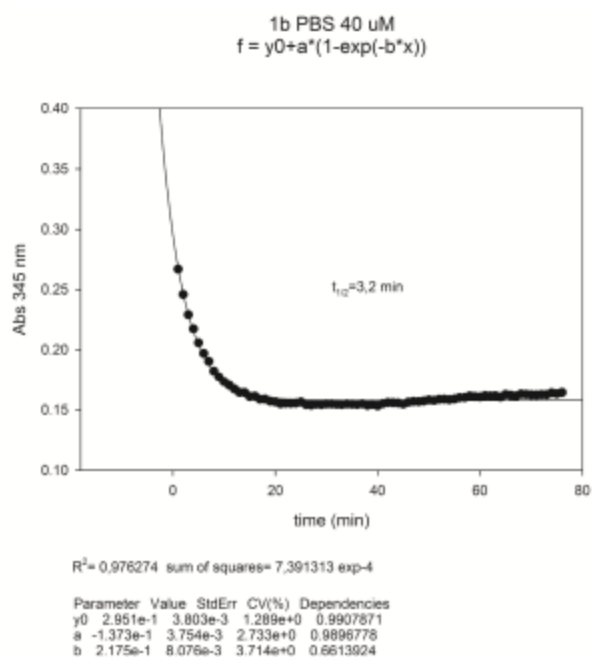
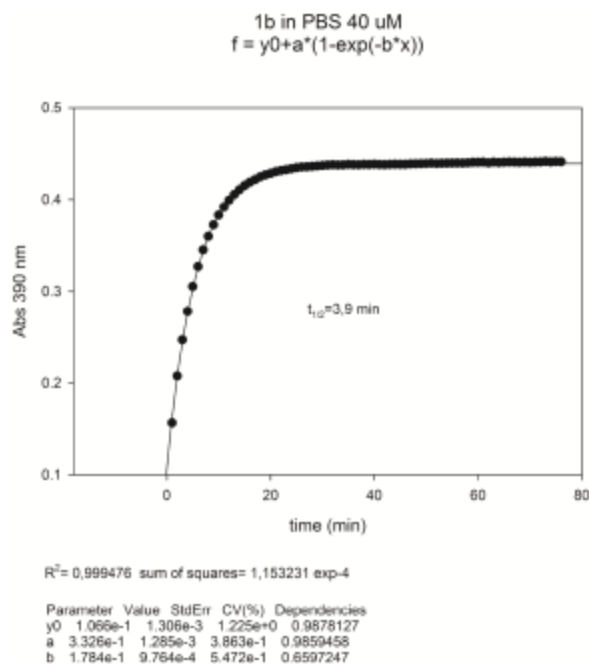


Figure 12. Time-dependent absorption after irradiation of **1b** measured in PBS at 390 and 345 nm. Panel C [**1b**] = 80 μ M; panel D [**1b**] = 40 μ M.

¹H NMR experiments

To gain further insight about the photo-conversion properties of **1a**, we also analysed the proceeding of *cis* to *trans* conversion by acquiring ¹H NMR spectra in dark and at different times from the irradiation at 435 nm. In dark, the ¹H NMR spectrum of **1a** (Figure 13) in the range of 7,6-5.5 ppm showed five aromatic proton resonances at 7,70, 7,28, 7,04, 6,67, 6,32 ppm and the proton on α -C of methyl-ester at 5,62 ppm.

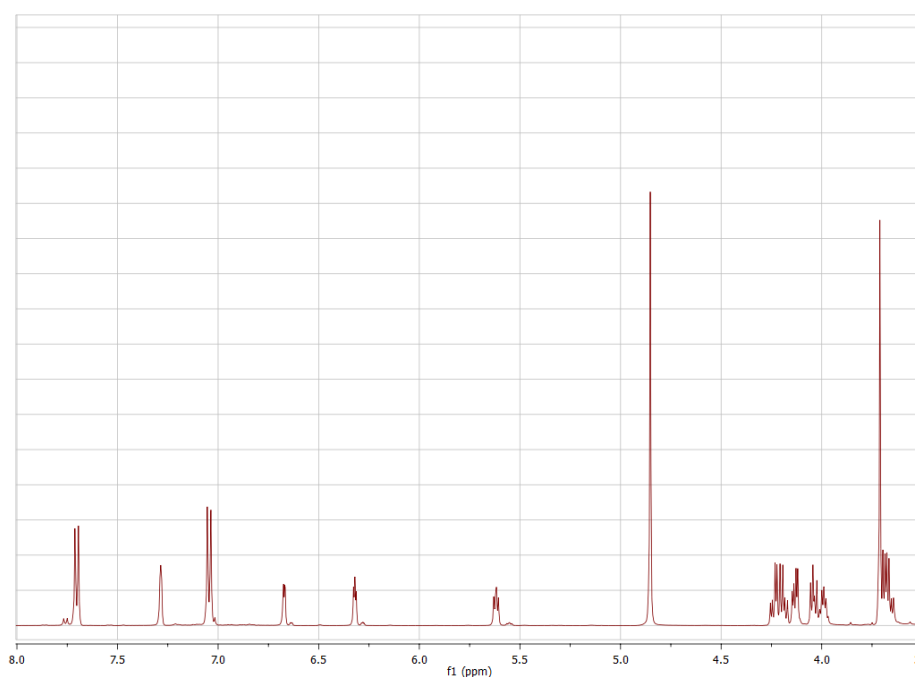


Figure 13. ¹H NMR spectrum of **1a** in CD₃OD

After light exposition of the sample, beside the proton resonances attributed to the *trans* **1a** (Figure 13), a new set of five signals appeared in the same region of the spectrum (Figure 14). Over time, the intensities of the new signals strongly decreased, and the ¹H NMR spectrum evolved towards that obtained for **1a** kept in dark. Therefore, the transient proton signals can be related to the metastable *cis* **1a**, activated by led light at 435 nm.

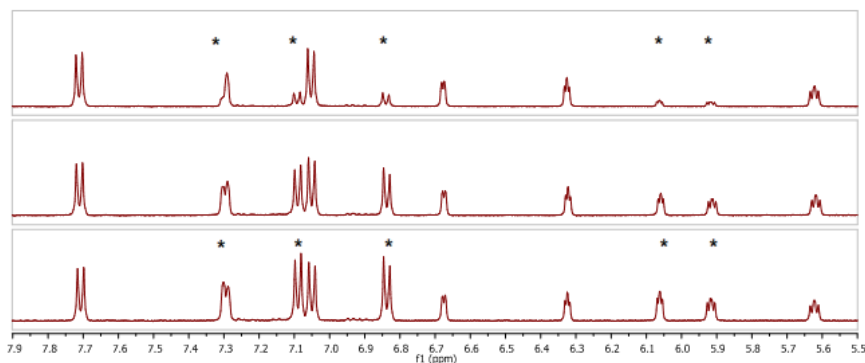


Figure 14. ^1H NMR spectra of **1a** in the range of 7.9-5.5 ppm, sequentially acquired after irradiation at 435 nm. Transient resonances signed by an asterisks were produced by the protons of the metastable *cis* **1a**.

Possible methyl ester hydrolysis

We tested the occurrence of the hydrolysis of methyl ester group of **1a/b** dissolved in PBS at r.t. During the first 2 days, nor hydrolyzed or degraded product was observed by TLC plate. After 5 days from dissolution, a mass spectrum corresponding to the hydrolyzed products (**6a/b**, figure 15) we recovered (see experimental section).

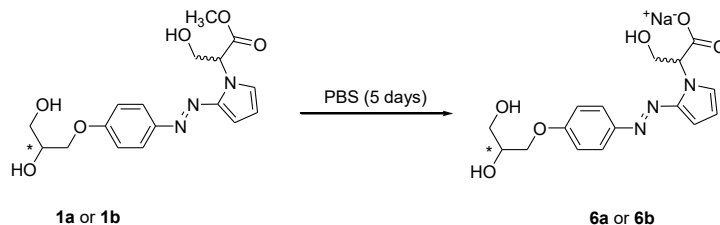


Figure 15. Schematic representation of the hydrolysis of **1a**.

UV spectra performed before and after irradiation of **6a/b** in PBS showed a substantial decreasing in the half life time of the corresponding metastable *cis* forms. Indeed, UV spectra measured after irradiation, showed only slightly difference with that measured in dark. In order to quantify the half life time of *cis* **6a/b** stereomers, in collaboration with professor C. Altucci (Department of Physic, University of Studies Federico II, Naples), we performed kinetic measurements for photo-conversion of the *trans* **6a/b** (in PBS and H_2O) and **1a/b** (in methanol) to the *cis* isomers, and for the thermal relaxation in dark by UV fast spectroscopy (Figure 16). An exponential decay model is used to fit on the measured data and the half-life times ($t_{1/2}$) for *trans* **1a**, **1b**, **6a** and **6b** to their *cis*

forms, moreover also the reverse *cis* to *trans* conversion are deduced, and reported (Figure 16B). Samples are made by dissolving **1a/b** molecules in different solvents: Methanol, H₂O and PBS. **6a** and **6b** are produced as a result of hydrolysis of the **1a/b** in water-based solutions. After five days from dissolution, the measured half-life time of *cis* **1a/b** in methanol had similar values than that measured by UV spectroscopy (Figure 16A and B). In contrast, in PBS solutions *cis* **6a/b** showed a decreasing in $t_{1/2}$ of about 4-7-fold respect to that of *cis* **1a/b**.

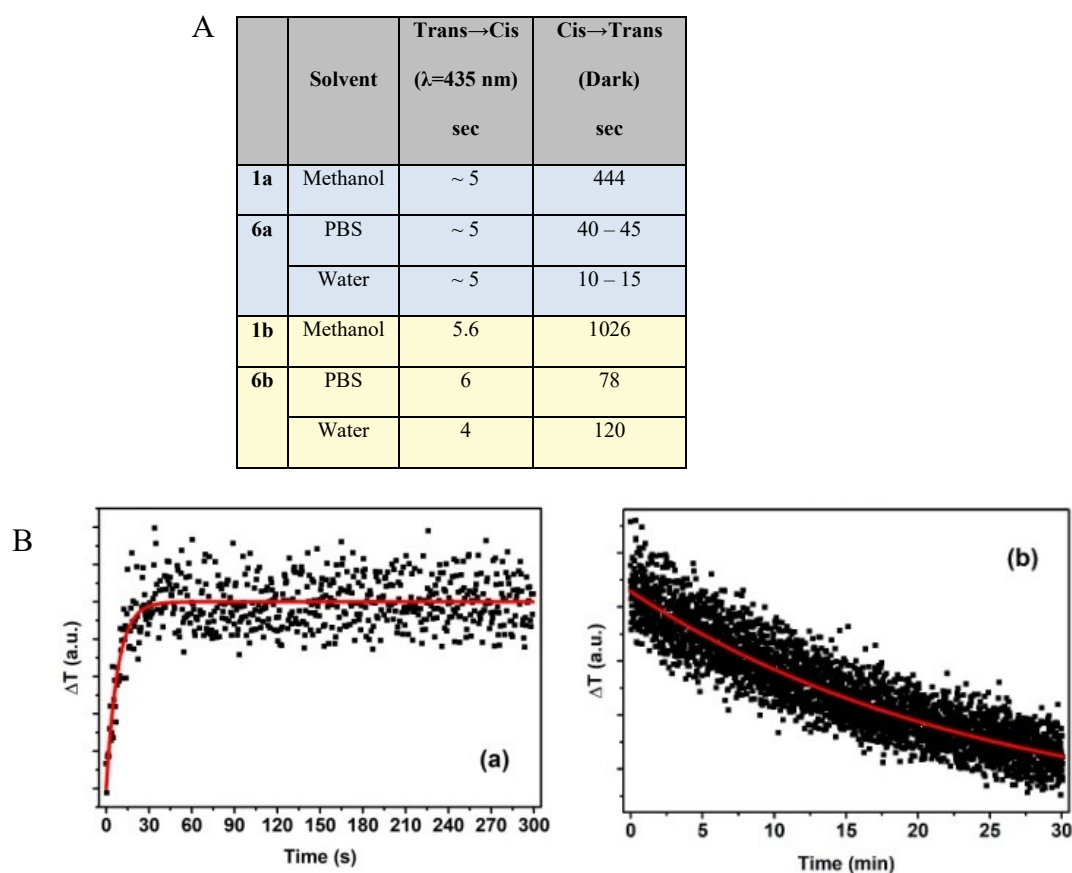


Figure 16. Panel A. Table showing half-life times of **1a/b** and their hydrolyzed derivatives **6a/b** measured with fast UV spectroscopy. **Panel B.** An example of 404-nm probe intensity changes: passing through **1b** in methanol solution as a function of time; **(a)** *trans* to *cis* conversion [when laser is on and the sample is being irradiated with 10 mW, 435 nm laser beam], and **(b)** *cis* to *trans* conversion [in dark].

Samples are made by dissolving **1a** and **1b** molecules in different solvents: Methanol, H₂O, and PBS. **6a** and **6b** are produced as a result of hydrolysis of the **1a/b** in water-based solutions.

Then, 2 mL of the sample is hold in a quartz cuvette, stirred by a magnetic stirrer; and transmission percentage at 404 nm in 10 mm optical path is monitored. A sketch of the optical setup for this experiment is shown in figure 17. A Mercury-Argon lamp is used as the light source of 404.6 nm.

Several optical filters are used to filter out other wavelengths and reduce 404 nm average power, preventing any perturbation of the sample with the probe light. A couple of UV-grade convex lenses are used to collimate diverging output light of the lamp and finally couple it to an optical fiber that conveys the light to the detector. The cuvette is kept between the two lenses and collimated 404 nm light is passing through the sample. The detector is a spectrograph combined with an intensified CCD (ICCD), which is recording the transmitted light at a repetition rate of 2 Hz.

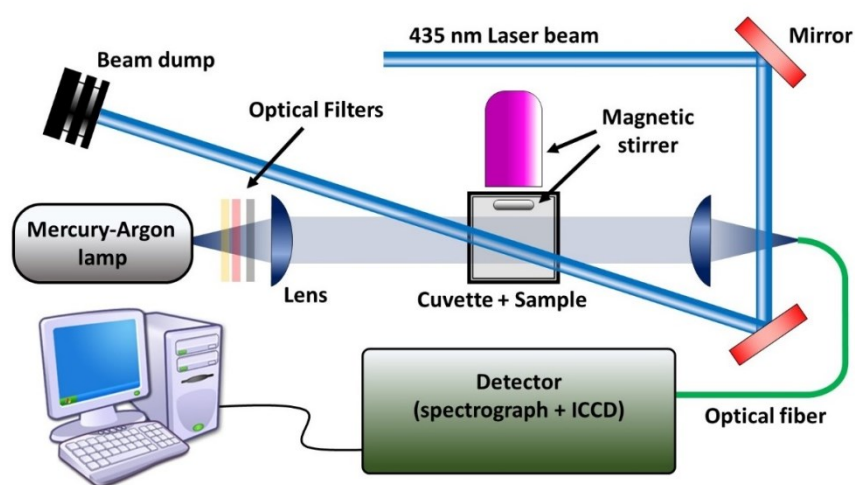


Figure 17. The optical setup for the UV fast spectroscopy.

435 nm laser beam is used to induce *trans* to *cis* reactions. This 435-nm laser beam is generated by an ORPHEUS optical parametric amplifier that is pumped by 1030-nm fundamental pulses emitted at 2 kHz repetition rate by a custom version of a PHAROS laser source. PHAROS output power is about 1.7 W and leads to ~ 10 mW laser beam at 435 nm generated in ORPHEUS. This laser beam is then passing through the sample with a small angle with the 404-nm probe. Transmitted 404-nm power is registered during the 435-nm irradiation to deduce *trans* to *cis* half-life time. In the next step the 435-nm laser is turned off to monitor the reverse reaction in dark (Figure 17).

Light-dependent cytotoxicity

The light-dependent **1a** and **1b** cytotoxicity was evaluated by MTT test on the HCT p53^{-/-} cell line. Keeping **1a/b** in the dark regime, the cytotoxic effects of *trans* **1a/b** were assayed, while applying short illumination impulses (50 ms ON/1 min OFF of 435 nm LED light) by a hand-built LED lighting system (Figure 18), the cytotoxic effects of *cis* **1a/b** were assayed.

Taking as a reference the LED lighting system built by Borowiak and co-workers [15], also we hand-built it to illuminate separately the 96-well cell culture plates with independent wavelengths.

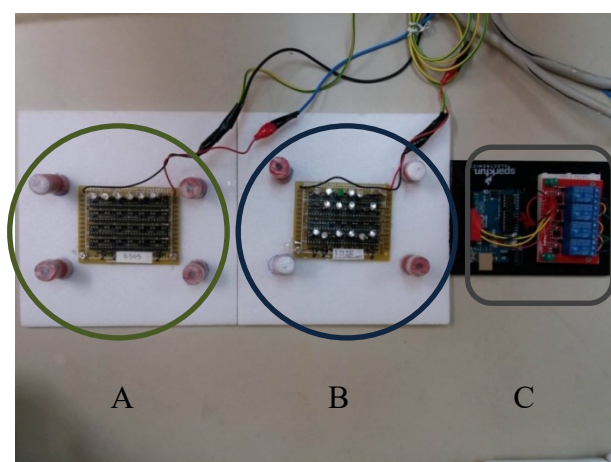


Figure 18. Led lighting system. A) Array with LED at 505nm, B) Array with LED at 435nm, C) Arduino

Specifically, the LED lighting system consists of arrays of LEDs at specific wavelength (435nm and 505nm) and connected in parallel (Figure 18). Each array irradiated a 96-well cell culture plate separately during the cell viability experiments (MTT test) and at same time was kept in incubator (37°C and 5% CO₂) (Figure 19).

The LED lighting system uses a programmed microcomputer (Arduino) to operate timing impulse patterns (50 ms ON/1 min OFF of 435 and 505 nm LED light) of LEDs arrays.

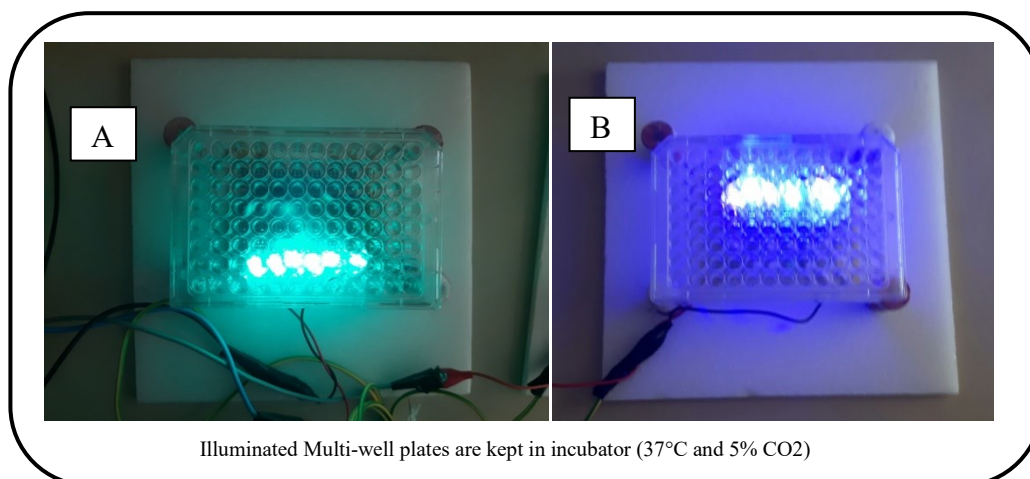


Figure 19. Irradiated 96-well cell culture plates at 505nm (A), and at 435nm (B).

In collaboration with prof. Giulia Russo of the University of Naples Federico II, MTT test of **1a** and **1b** was performed on the HCT p53^{-/-} cell line (Human Colon Carcinoma cell line) at two concentrations (1 and 10 μ M) (Figure 20).

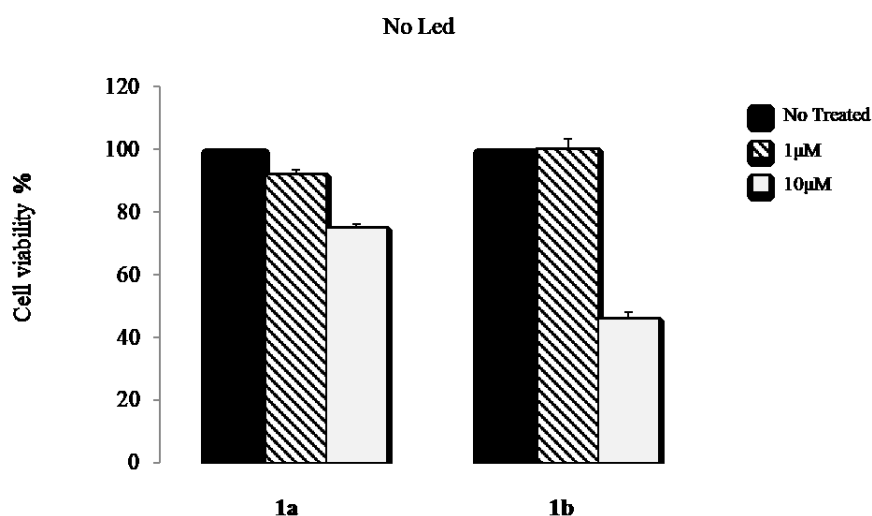


Figure 20. Cytotoxic effect on HCT p53^{-/-} cell line of **1a** and **1b** in dark regime at 1 and 10 μ M.

The HCT p53^{-/-} cell growth differently responded to the treatment with the two diastereomeric mixtures **1a** or **1b** both in dark and under led irradiations. Indeed, in dark (Figure 20), at concentration of 1 μ M, both **1a/b** resulted almost ineffective on cell growth. Used at 10 μ M, the antiproliferative activity showed by **1b** was considerably higher than that of **1a**. Furthermore, cells were treated with **1a** or **1b** undergoing irradiation at 435 or 505 nm during 12h. Based on half-lives

of **1a/b** and **6a/b** in PBS (Figures 10-12) we used a pulse-program 50 ms-ON/ 1,0 min-OFF by means of a Led light system. Led irradiation at used wavelengths resulted almost ineffective on viability of untreated cells. However, we observed a four-fold higher antiproliferative efficiency of **1a** in the presence of light at 435 nm, respect to the treated control in dark, at both used concentrations (Figure 21). Under the same wavelength irradiation, the cells treated with **1b** at 1 μM showed a growth decreasing of about 20%, whereas at 10 μM , **1b** caused almost the same cell growth inhibition than in the dark. Irradiation at 505 nm only slightly effected cell growth treated with **1a** but caused a complete reversion of the antiproliferative effect of **1b** in dark. Therefore, **1a** showed a significant photo-induced increasing of the potency of its antiproliferative action only under irradiation at 435 nm.

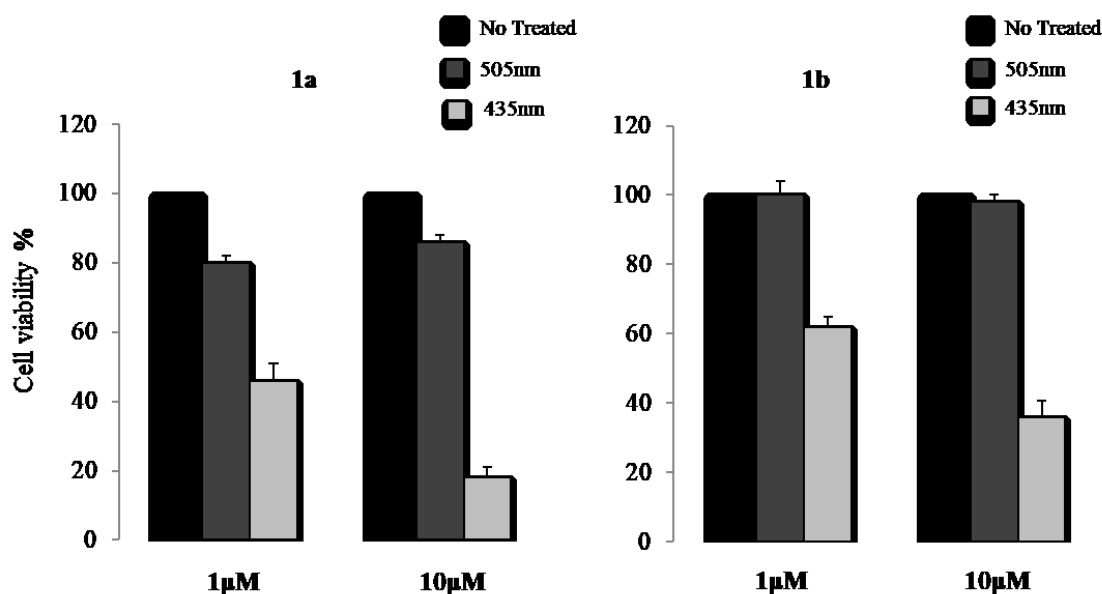


Figure 21. Cytotoxic effect on HCT p53^{-/-} cell line of **1a** and **1b** at 1 and 10 μM illuminating at 435 and 505 nm. **No Treated** = cells no treated and illuminated at 435 and 505nm separately. **505nm** = cells treated and illuminated at 505nm compared to the cells no treated and illuminated 505nm. **435nm** = cells treated and illuminated at 435nm compared to the cells no treated and illuminated 435nm.

In view of their promising photo-responsive antiproliferative activity, the stereospecific synthesis of the two stereomers forming **1a**, was performed (Figure 6). Time-dependent UV experiments revealed that the half-lives of *cis* **1RR** and *cis* **1RS** in PBS were slightly diverse (5,8 and 4,2 min, respectively, figure 22), whereas the average of the two values corresponded to that of **1a** (Figure

10). **1RR** and **1RS** also differed in their CD profiles, both showing a Cotton effect centered at about 400 nm but having almost opposite signature (Figure 23), and could be separated on chiral column by HPLC (Figure 24). However, the two diastereomers showed the same ^1H and ^{13}C NMRs.

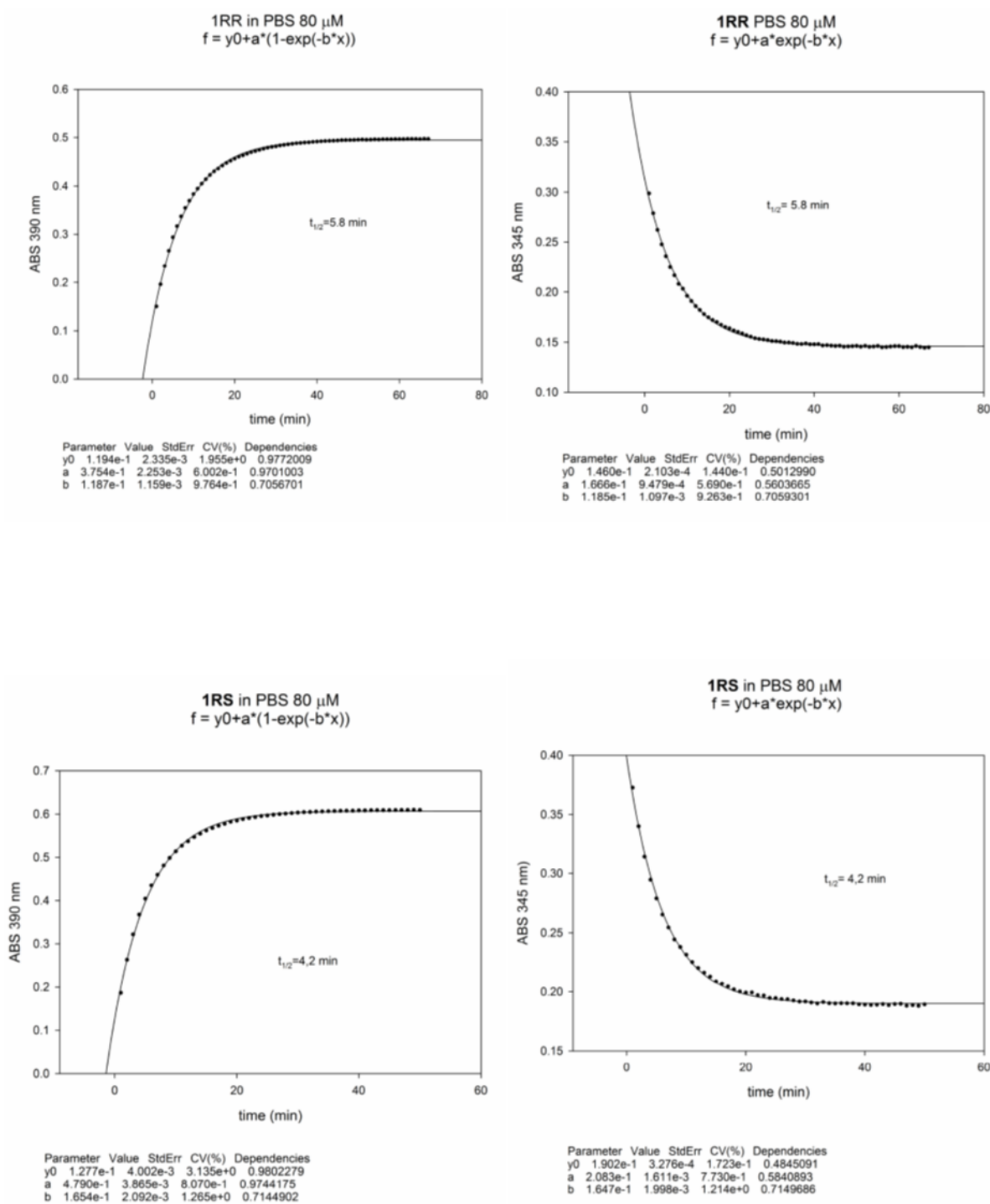


Figure 22. Time-dependent absorption of **1RR** and **1RS** in PBS after irradiation. Data were collected at 390 (absorption of the *trans* form) and 345 (absorption of *cis* form) nm. Panel A [**1RR**] = 80 μM ; panel B [**1RS**] = 80 μM .

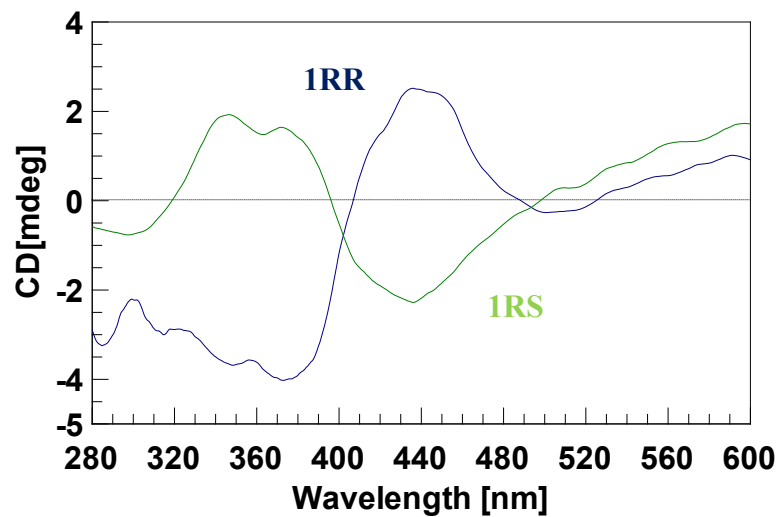


Figure 23. CD spectra of **1RR** (blue line) and **1RS** (green line) measured in MeOH. o.l. 0.5 cm, Vol= 1400 μ L. each compound was used at final concentration of 80 μ M.

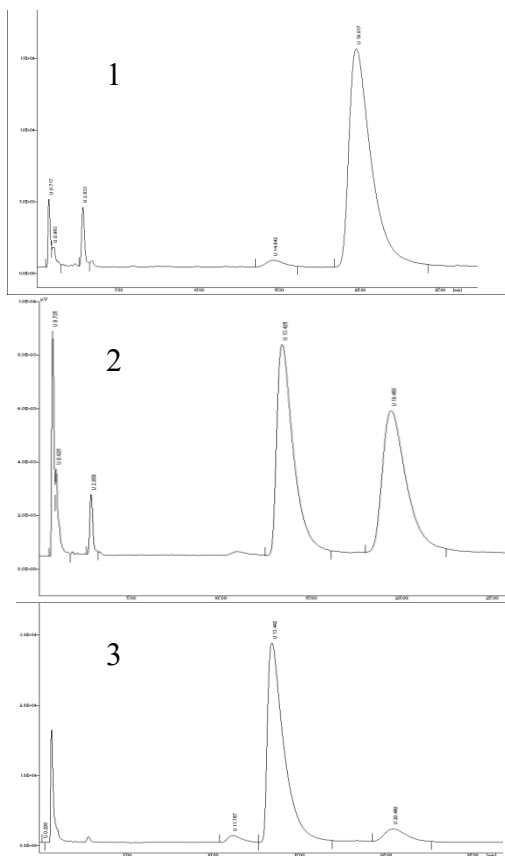


Figure 24. HPLC chromatograms of **1RR** and **1RS** on chiral column Lux 3u Cellulose-3 eluted with n-hexane:propan-2-ol (80:20) Flow: 1.0. **1.** mixture of the two diastereomers **1a**; **2.** **1RR**; **3.** **1RS**.

2.3. Experimental section

General procedure

Chemicals and anhydrous solvents were purchased from Fluka-Sigma-Aldrich. TLCs were run on Merck silica gel 60 F254 plates. Silica gel chromatography was performed using Merck silica gel 60 (0.063–0.200 mm). HPLC purifications and analyses were carried out using a JASCO PU-2089 Plus HPLC pump equipped with a JASCO BS-997-01 UV detector. CD experiments were performed on a JASCO 715 spectropolarimeter equipped with a PTC-348 temperature controller. UV experiments were performed on a JASCO V-530 spectrophotometer, equipped with a PTC-348 temperature controller. High-resolution ESI-MS analyses were performed on a Thermo LTQ Orbitrap XL mass spectrometer (Thermo-Fisher, San José, CA, USA). The spectra were recorded by infusion into the ESI (Thermo-Fisher, San José, CA, USA) source using MeOH as solvent. ^1H (500 MHz and 400 MHz) and ^{13}C (125 MHz) NMR spectra were recorded on a Agilent INOVA spectrometer (Agilent Technology, Cernusco sul Naviglio, Italy); chemical shifts were referenced to the residual solvent signal (CHD_2OD : $\delta_{\text{H}} = 3.31$, $\delta_{\text{C}} = 49.0$; $\text{C}_6\text{D}_5\text{N}$: $\delta_{\text{H}} = 7.19$, 7.55 and 8.71 ppm). For an accurate measurement of the coupling constants, the one-dimensional ^1H NMR spectra were transformed at 64 K points (digital resolution: 0.09 Hz). ^1H connectivities were determined by COSY and TOCSY (mixing time 100 ms) experiments. Through-space ^1H connectivities were evidenced using a ROESY experiment with a mixing time of 500 ms. Two and three bond ^1H - ^{13}C connectivities were determined by gradient 2D HMBC experiments optimized for a 2,3 J of 8 Hz. $^3J_{\text{H-H}}$ values were extracted from 1D ^1H NMR.

Synthesis of 1a, 1b, 1RR e 1RS

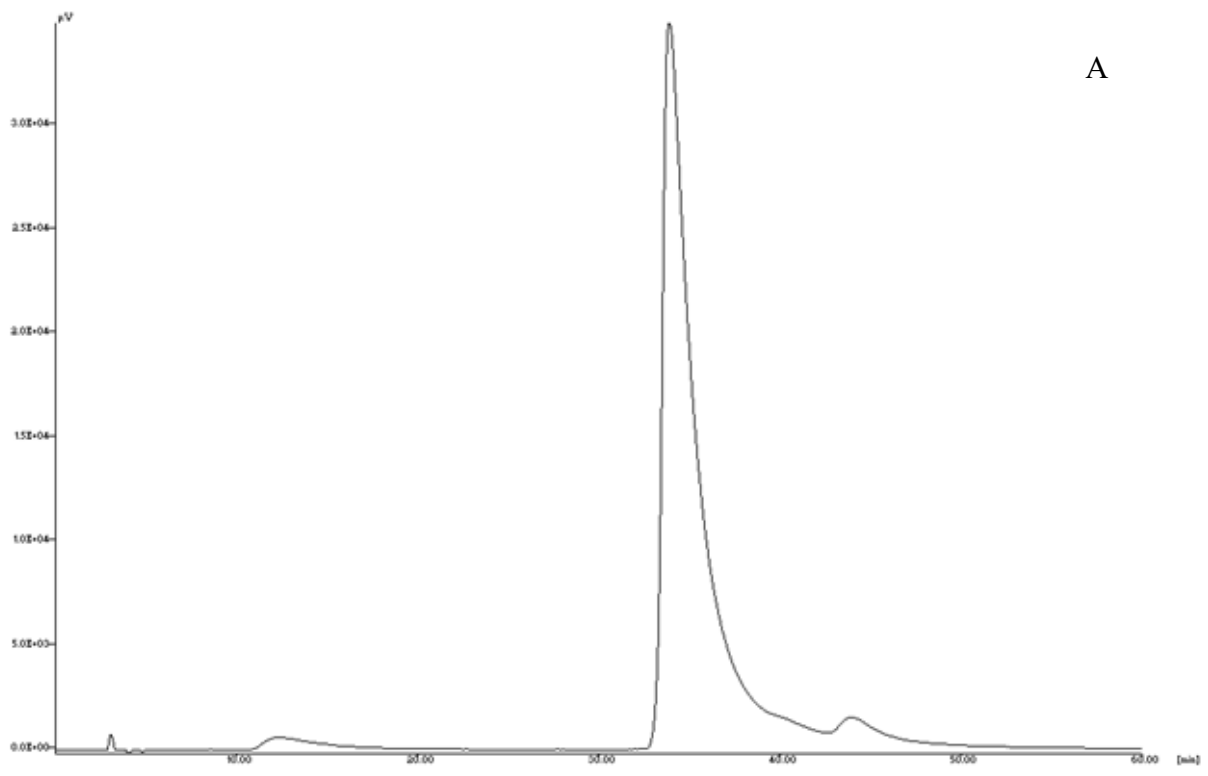
R or S 3-(4-nitrophenoxy)propane-1,2-diol (2). A mixture of 1, (0.500 g, 3,6 mmol), KOH (1 mg, $1,8 \times 10^{-2}$ mmol, dissolved in 50 μL of EtOH) and dry toluene (2 mL) was stirred under reflux in a double neck flask. After 30 min, the mixture was cooled to r.t. and 287 μL of R or S glycidol (0,320

g, 4,3 mmol) were slowly added by a syringe. The mixture was further stirred at 90 °C for 24 h. The solvent was then evaporated under vacuo and the residue re-dissolved in MeOH. The obtained solution was embedded on silica and then rotary evaporated to dryness. The resulting powder was applied on a Ethyl acetate: Acetone 70:30 (v/v) packed silica gel column and then eluted using isocratic conditions. The fractions containing the desired product were dried under vacuo to give 0,58 g of 2 as R or S stereomer as a yellow gel (yields 85%). TLC plate R_f 0,73 (Ethyl acetate: Acetone 70:30 (v/v)).

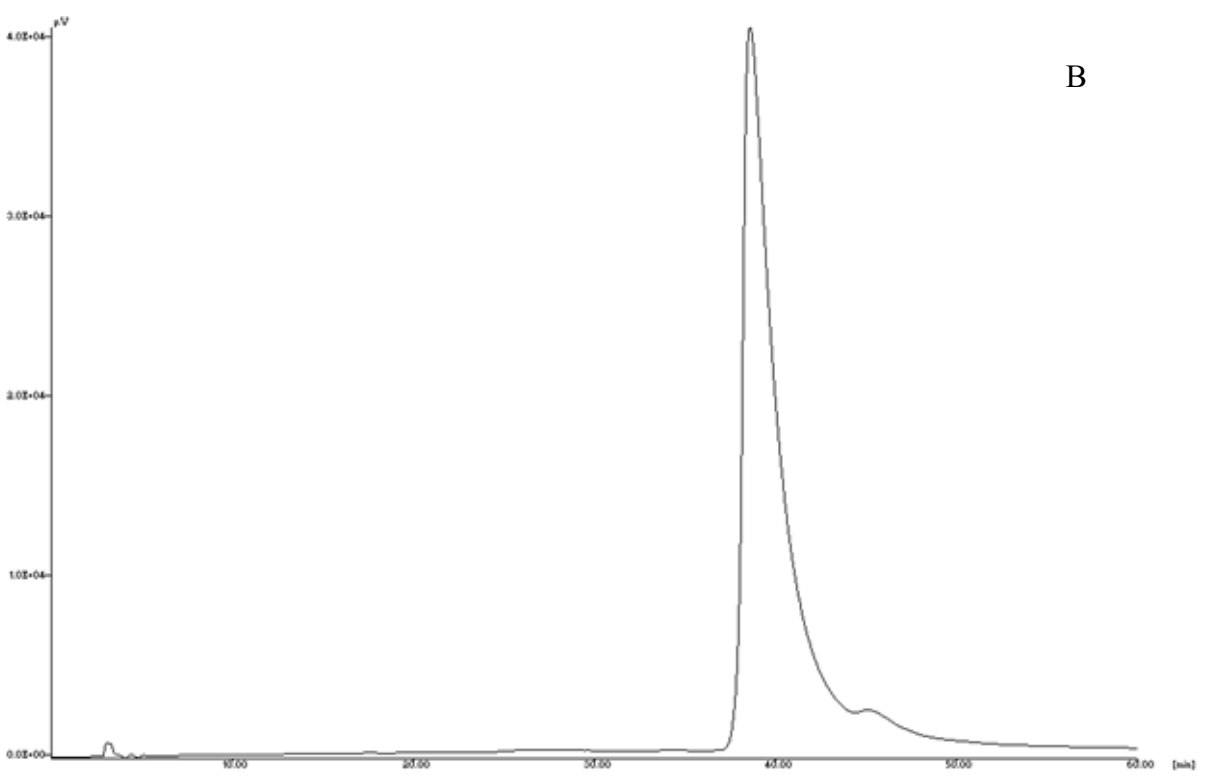
¹H NMR (CD₃OD) δ: 3.64–3.73 (m, 2H, CH₂OH), 3.97–4.05 (m, 1H, CHOH), 4.09 (dd, J = 6.1, 9.8 Hz, 1H, OCH₂), 4.18 (dd, J = 4.1, 9.8 Hz, 1H, OCH₂), 7.05–7.10 (m, 2H, C^{2,6}_{Ar}H), 8.14–8.20 (m, 2H, C^{3,5}_{Ar}H). ¹³C NMR (CD₃OD) δ: 63.9 (CH₂OH), 71.2 (CHO), 71.4 (CH₂O), 115.8 (C^{2,6}_{Ar}), 126.8 (C^{3,5}_{Ar}), 142.8 (C⁴_{Ar}), 165.5 (C¹_{Ar}). HRESIMS (positive ion mode, CH₃OH) m/z 236.0533 [M+Na]⁺ (calcd for C₉H₁₁NO₅Na, 236.0529).

[α]²⁵ R= -17.8 [c= 12.4 mg/mL; EtOH] S=+16.9 [c=19.2 mg/mL; EtOH]

In order to quantify the stereo specificity of the reaction, HPLC chromatography on chiral column was performed. On the basis of previous reported data [20] we analyzed each single R or S 3-(4-nitrophenoxy)propane-1,2-diol and a mixture of both species on HPLC by means of ChiralpaK 1A column (4,6x 250 mm, particle size: 5 micron) eluted with 90:10 n-exane:propan-2-ol. R- 3-(4-nitrophenoxy)propane-1,2-diol R_T=33,85 min and S 3-(4-nitrophenoxy)propane-1,2-diol 38.55 min. The obtained chromatograms were reported in figure 25.



A



B

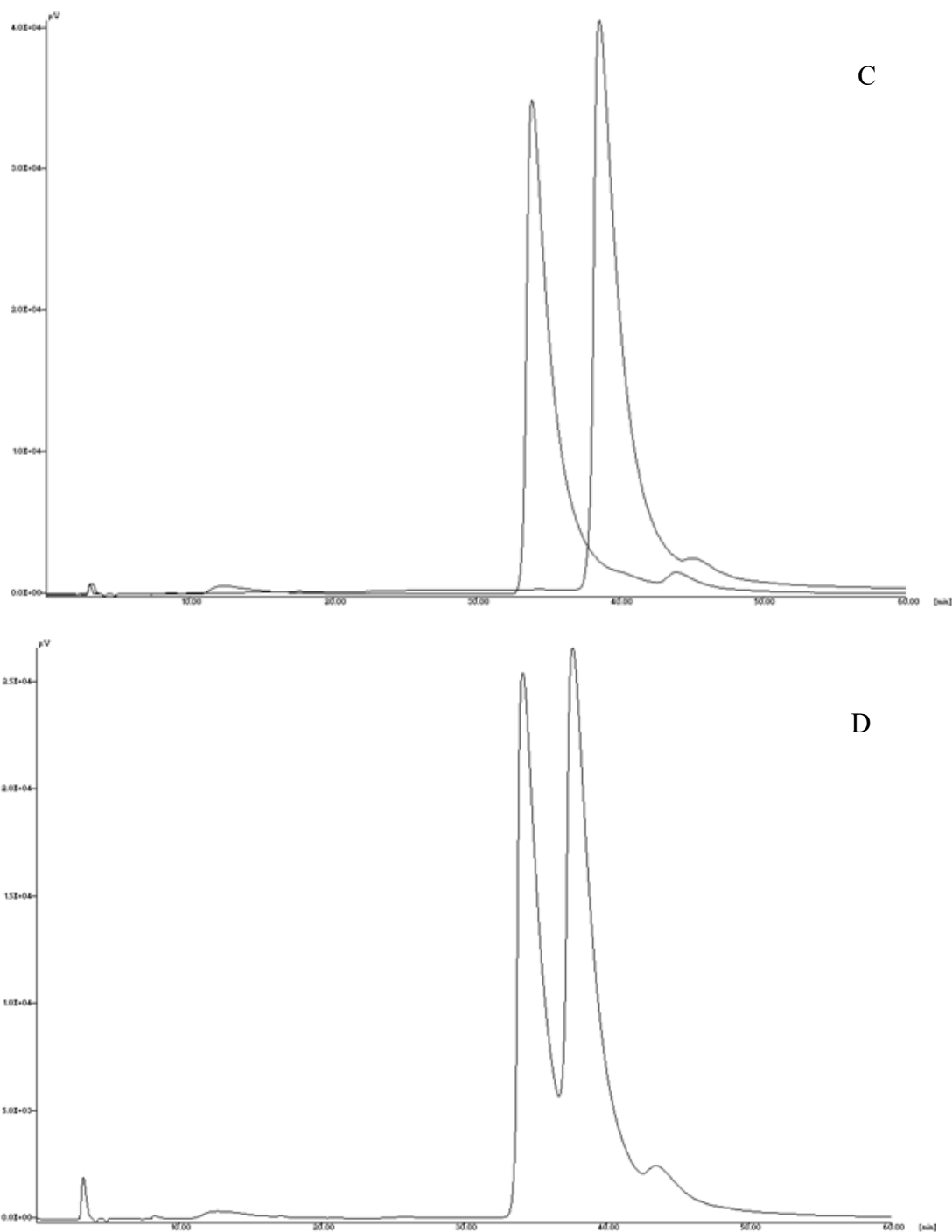


Figure 25. A and B. HPLC chromatograms of (R) - and (S) 3-(4-nitrophenoxy)propane-1,2-diol (**2**) on chiral column Chiralpak IA eluted with n-hexane:propan-2-ol. C. Overlay of the two chromatograms. D. Mixture of the two stereoisomers.

S or R 3-(4-aminophenoxy)propane-1,2-diol (3**).** A mixture of **2** (R or S, 0, 560 g, 2,6 mmol), Pd/C (5% w/w respect to **2**, 28 mg) and 25 mL di EtOH (90%, HPLC grade) was stirred in a Parr apparatus under hydrogen atmosphere ($P = 400$ psi). After 1.5 -2.0 h the reaction was monitored by disappearance of UV band of **2** on TLC plate (R_f 0.73, Ethyl acetate: Acetone 70:30 (v/v) and the

appearance of an UV band also strongly sensitive to ninhydrin (R_f 0.46). The mixture was filtered on paper, and the eluted solution dried on vacuo, to obtain **3** as brick-red solid. **3** was further purified by crystallization from DCM:MeOH 7:3 (0,440 g, yields 93%)

NMR (CD_3OD) δ : 3.62 (dd, $J = 5.4, 11.2$ Hz, 1H, CH_2OH), 3.67 (dd, $J = 4.8, 11.2$ Hz, 1H, CH_2OH), 3.89–3.84 (m, 1H, $CHOH$), 3.91 (dd, $J = 5.1, 9.8$ Hz, 1H, OCH_2), 3.95 (dd, $J = 4.1, 9.8$ Hz, 1H, OCH_2), 6.70 (d, $J = 8.8$ Hz, 2H, $C^{2,6}_{Ar}H$), 6.76 (d, $J = 8.8$ Hz, 2H, $C^{3,5}_{Ar}H$). ^{13}C NMR (CD_3OD) δ : 64.3 (CH_2OH), 71.1 (CHO), 71.9 (CH_2O), 118.1 ($C^{2,6}_{Ar}$), 116.6 ($C^{3,5}_{Ar}$), 141.8 (C^4_{Ar}), 153.6 (C^1_{Ar}). HRESIMS (positive ion mode, CH_3OH) m/z 184.0980 [$M+H$] $^+$ (calcd for $C_9H_{14}NO_3$, 184.0974).

1a, 1b, 1RR and 1RS.

A mixture of **3** (0,400 g, 2,2 mmol), 205 μ L fluoroboric acid (water solution, 48%, 3,3 mmol) 4 mL of EtOH was cooled to $-15^\circ C$ under argon and then 224 μ L of isoamyl nitrite (0,258 g, 2,2 mmol) were added. After 12h under stirring, the produced diazonium salt was first precipitated diluting the mixture with n-hexane, and then further washed with n-hexane (three times). The solid residue was dried under vacuo to give **4**, which was used in the next step without further treatment. **4** (0,360 g, 1,8 mmol) was dissolved in 10 mL of acetic acid (14g, 232 mmol), under stirring. Sodium acetate (4,0 g, 51 mmol) and rac-**5** or **5R** or **S** (254 μ L, 0,270 g, 2,2 mmol) were added, consecutively, to the solution. After 15 min at r.t., the formation of a gel-like mixture was observed. The reaction time was further prolonged up to 1 h, under slow stirring. The final mixture was diluted with water and extracted with DCM (4-5 times). The collected organic layers were dried under vacuo and the residue re-dissolved in MeOH. The obtained solution was embedded on silica and then rotary evaporated to dryness. The resulting powder was applied on a DCM: propan-2-ol 90:10 (v/v) packed silica gel column and then chromatographed using isocratic conditions. The collected fractions, dried under *vacuo* (TLC 90:10 DCM:MeOH, v/v, $R_f=0.6$) was further purified on HPLC RP-18 column (water:acetonitrile, 80:20, v/v, $RT=12$ min), to get 0.185 of **1b** (yields 51%), 0.210 g

of **1a** (yields 58%), 0.214 g of **1RR** or **1RS** (yields 59%). In view of the equivalence in proton and carbon resonances of the four species, the following NMR are one time reported, whereas the NMR spectra of each species are attached at the end of section.

¹H NMR: NMR (CD₃OD) δ: 3.66 (m, 2H, CH₂OH), 3.67 (s, 3H, OCH₃), 3.99 (m, 1H, CHOH), 4.13 (dd, J = 4.2, 9.6 Hz, 1H, OCH₂), 4.19 (dd, J = 6.8, 11.7 Hz, 1H, CH₂OH), 4.24 (dd, J = 4.7, 11.7 Hz, 1H, CH₂OH_{pyr}), 4.24 (dd, J = 6.0, 9.6 Hz, 1H, OCH₂), 5.62 (dd, J = 4.8, 6.6 Hz, 1H, CHCOCH₃), 6.32 (dd, J = 3.0, 3.38 Hz, 1H, C⁴_{pyr}), 6.67 (dd, J = 1.2, 3.9 Hz, 1H, C³_{pyr}), 7.04 (d, J = 8.9 Hz, 2H, C^{2,6}_{Ar}H), 7.28 (s, 1H, C⁵_{pyr}), 7.70 (d, J = 8.9 Hz, 2H, C^{3,5}_{Ar}H). ¹³C NMR (CD₃OD) δ: 51.8 (OCH₃), 60.2 (CHCOCH₃), 62.8 (CH₂OH), 70.5 (CHOH), 69.5 (OCH₂), 69.4 (CH₂OH), 99.9 (C³_{pyr}), 110.0 (C⁴_{pyr}), 126.2 (C⁵_{pyr}), 147.8 (C²_{pyr}), 114.7 (C^{2,6}_{Ar}), 123.4 (C^{3,5}_{Ar}), 145.5 (C⁴_{Ar}), 160.7 (C¹_{Ar}), 170.2 (COCH₃).

HRESIMS (positive ion mode, CH₃OH) **1a** m/z 364.1510 [M+H]⁺; **1b** m/z 364.1498 [M+H]⁺; **1RR** m/z 364.1498 [M+H]⁺ **1RS** m/z 364.1498 [M+H]⁺ (calcd for C₁₇H₂₂N₃O₆, 364.1503).

UV experiments

In order to obtain data related to the *trans* isomer, the cuvette (0.1 o.l. Vol. 400 μL) containing 40 or 80 μM of **1a** or **1b** in MeOH was taken in dark at r.t. for about 12 h. UV spectra of the *cis* isomers were acquired after irradiation of the samples with light at 400 or 435 nm (1 min, 1 LED 400 or 435, Roithner Lasertechnik). The *cis* thermal decay was monitored by further sequential acquisition of spectra until the UV profile rise to that of the initial *trans* isomer. In order to obtain t_{1/2} of *cis* isomer, after the sample irradiation with light at 400 or 435 nm, UV time course measurement experiments were performed monitoring the absorbance values at 340, 390, 425, 400 and 505 nm, number of cycle 100-180, cycle time 60 sec.

The spectra showing the *cis* → *trans* photo-conversion were obtained after irradiation with green light (1 min, 1 LED 505 nm). Finally, the stability of **1a** or **1b** under the used light conditions, were verified acquiring spectra after 12 h of irradiations using the same pulse-program than that programmed for biological assay. In particular, the UV cuvette containing **1a** or **1b** at 40 mM was

exposed to led lamps at 435 or 505 nm. Leds were managed by an Arduino module (50 ms-ON/ 1.0 min-OFF).

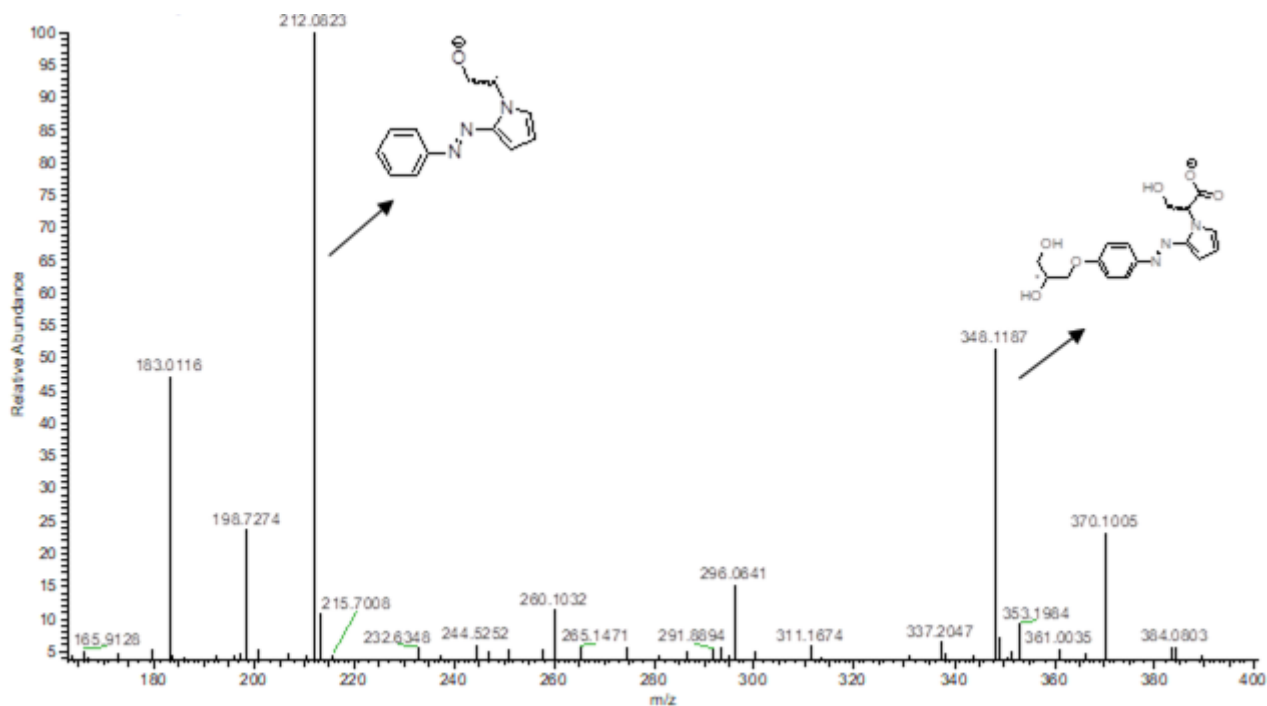
Cell cultures and treatments

HCT 116p53^{-/-} cells were cultured in Dulbecco's Modified Eagle's Medium (DMEM), supplemented with 10% fetal bovine serum (FBS) (Euroclone S.p.A), 2 mM L-glutamine and 50 U/ml penicillin-streptomycin, under humidified atmosphere of 5% CO₂ at 37°C. Treatments of cells were performed replacing the culture medium with those containing indicated compounds at final concentration of 1 and 10 µM per well. Cells were subsequently exposed to light irradiation at 400, 435 or 515 nm for 12h and analyzed by MTT assay.

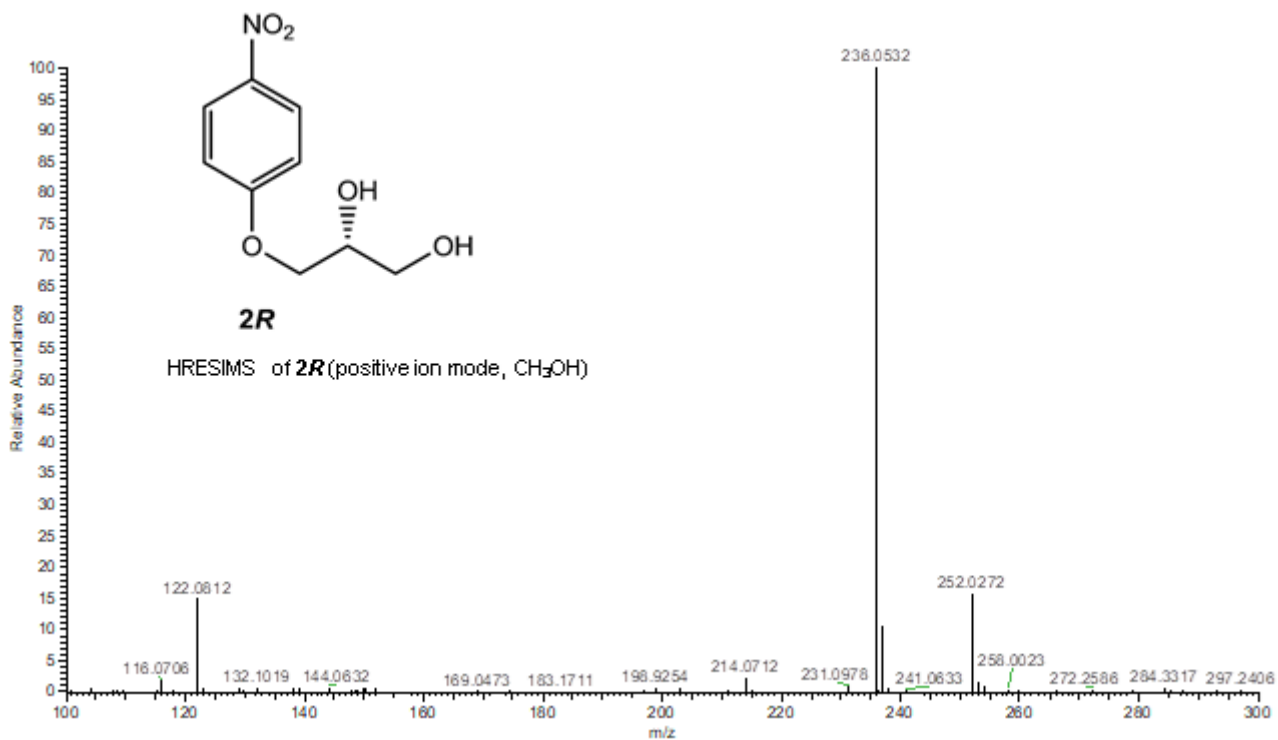
MTT assay

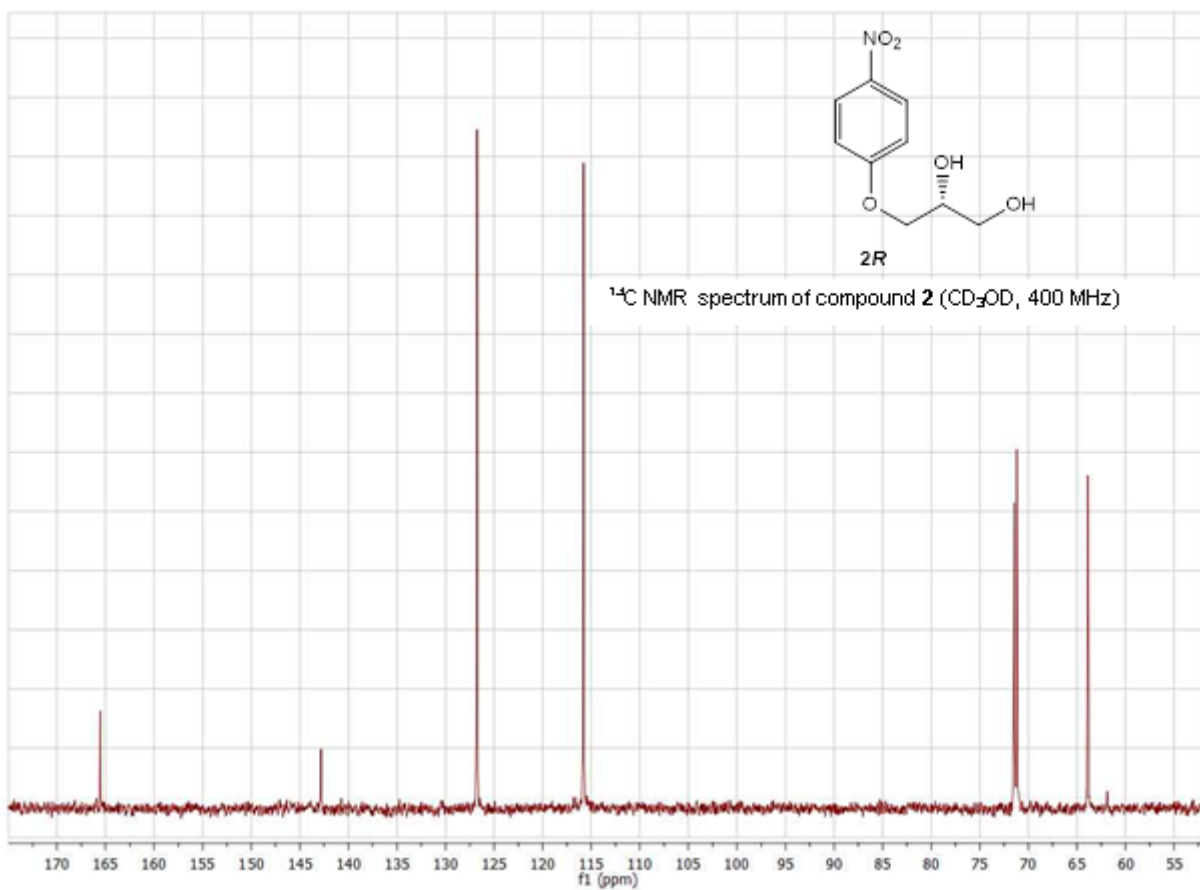
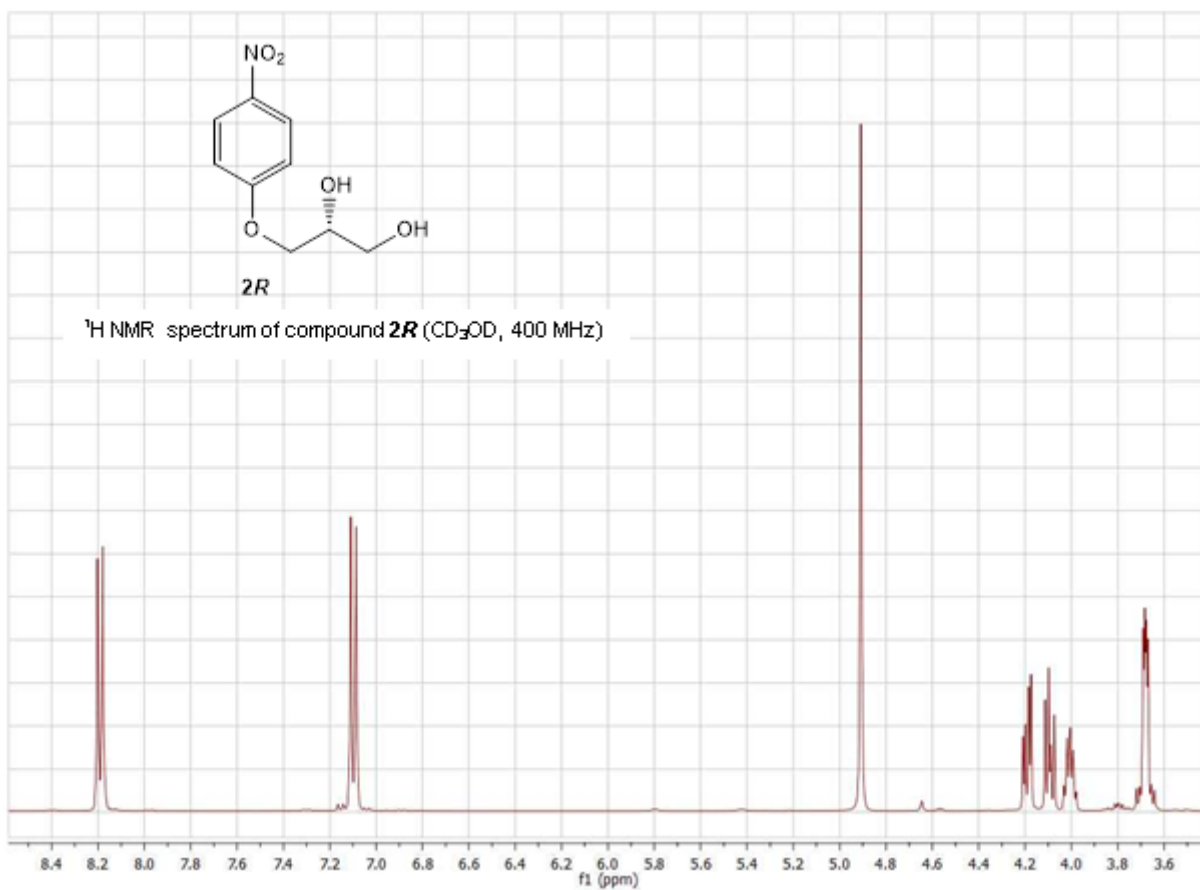
HCT 116p53^{-/-} cells were seeded onto 96-well plates at density of 2 x 10⁴ cells/well. Cell viability was evaluated using the MTT assay procedure, which measures the level of mitochondrial dehydrogenase activity of living cells using the yellow 3-(4,5-dimethyl-2-thiazolyl)-2,5-diphenyl-2H-tetrazolium bromide (MTT) as substrate. The absorbance was measured at 540 nm using a microplate reader (Labsystems Multiskan). A pool of three different sets of experiments were performed. Error bars represent mean ± SEM from n=3 biological replicates. Statistical analysis was performed as previously described.

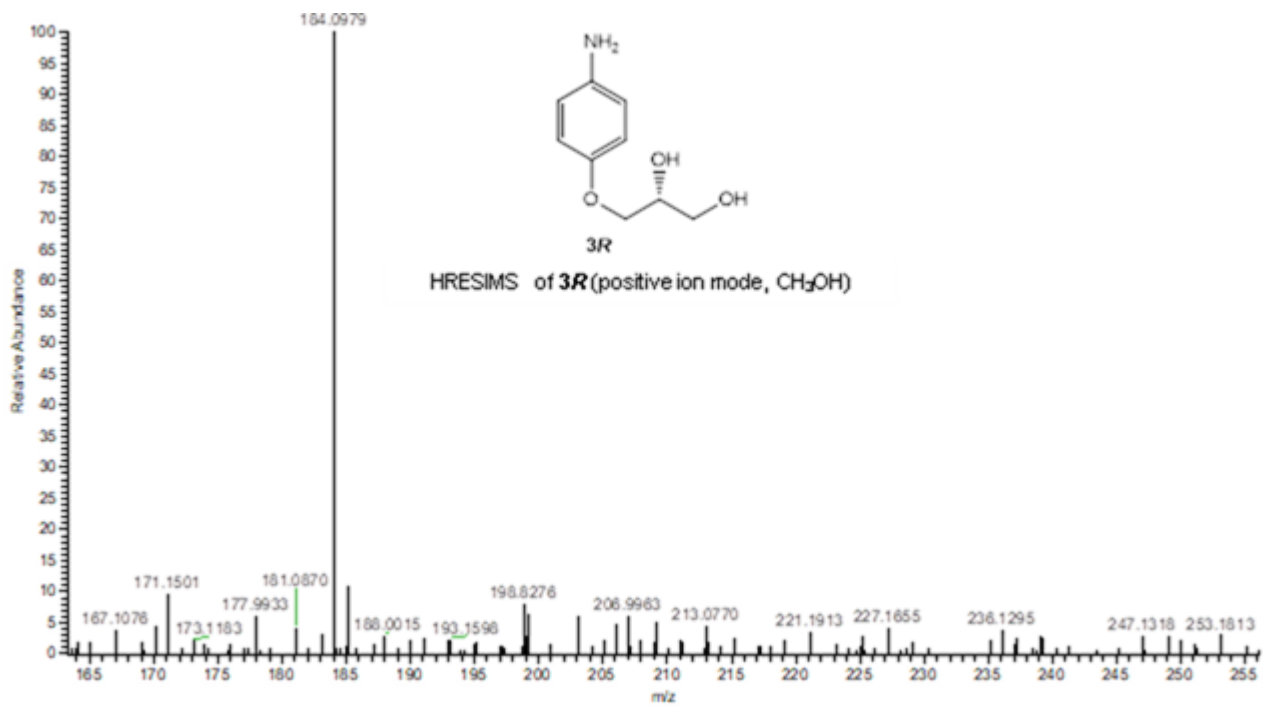
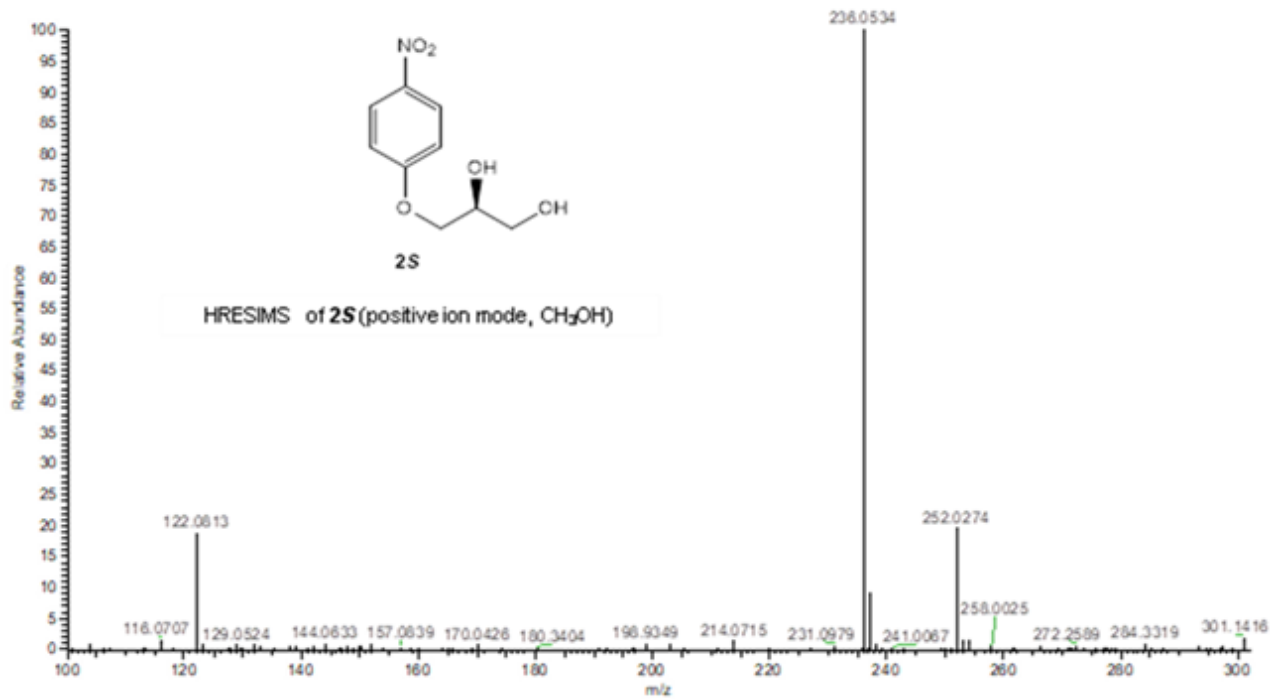
HRESIMS of **1a** after 5 days from dissolution in PBS (negative ion mode, CH₃OH)

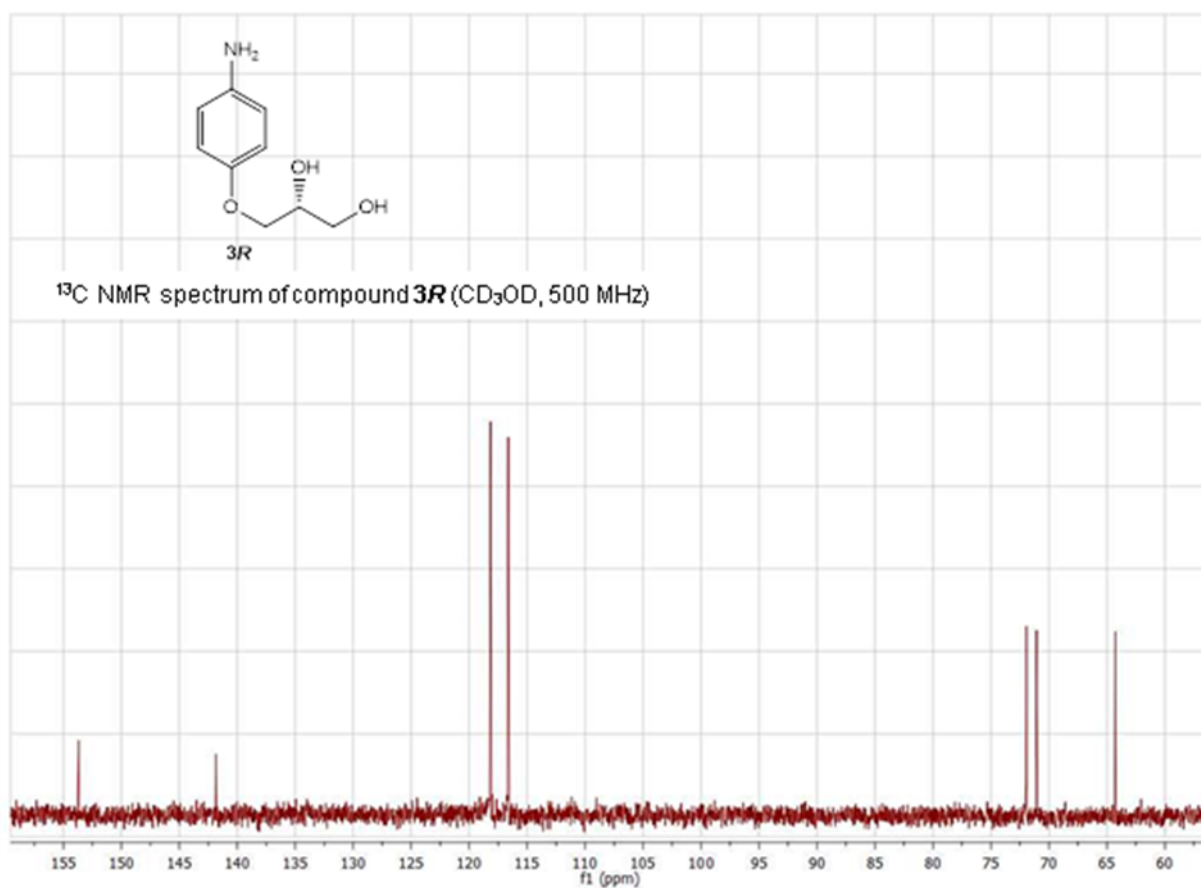
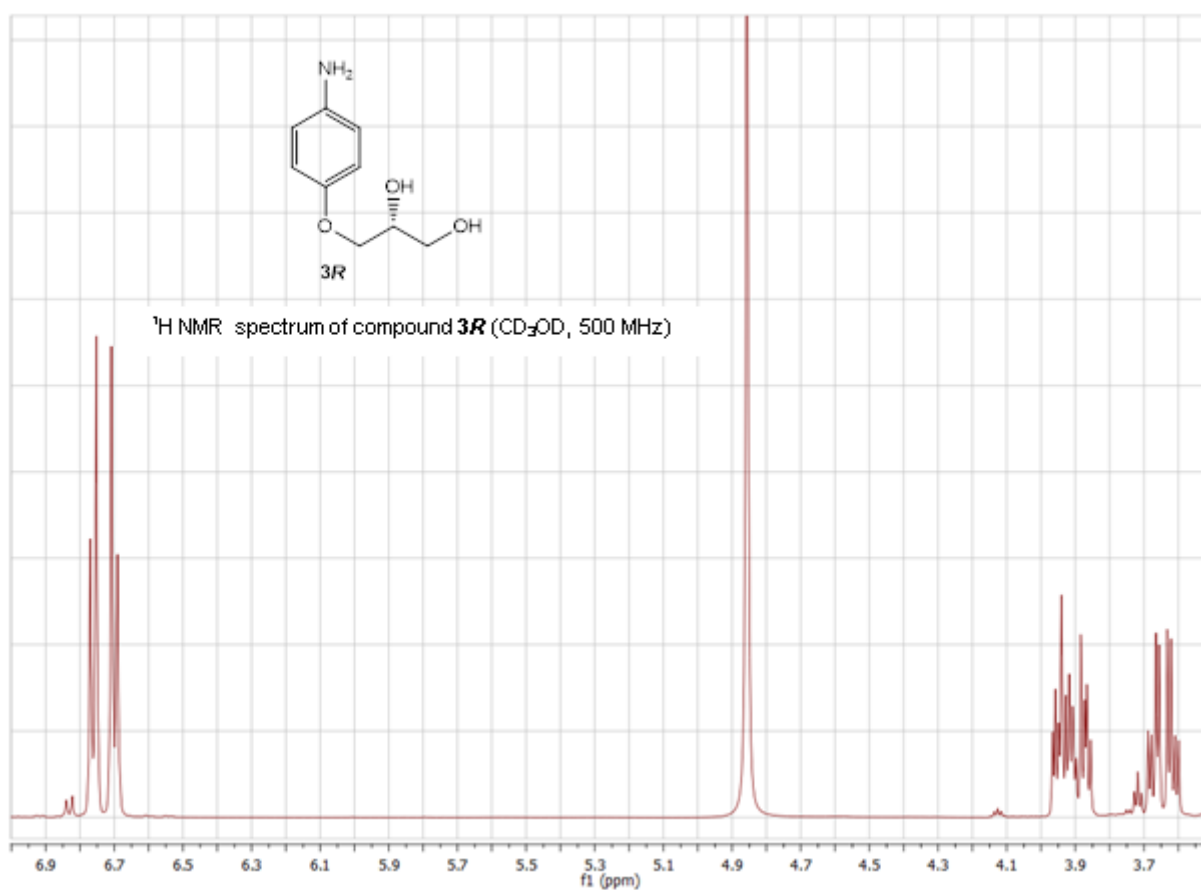


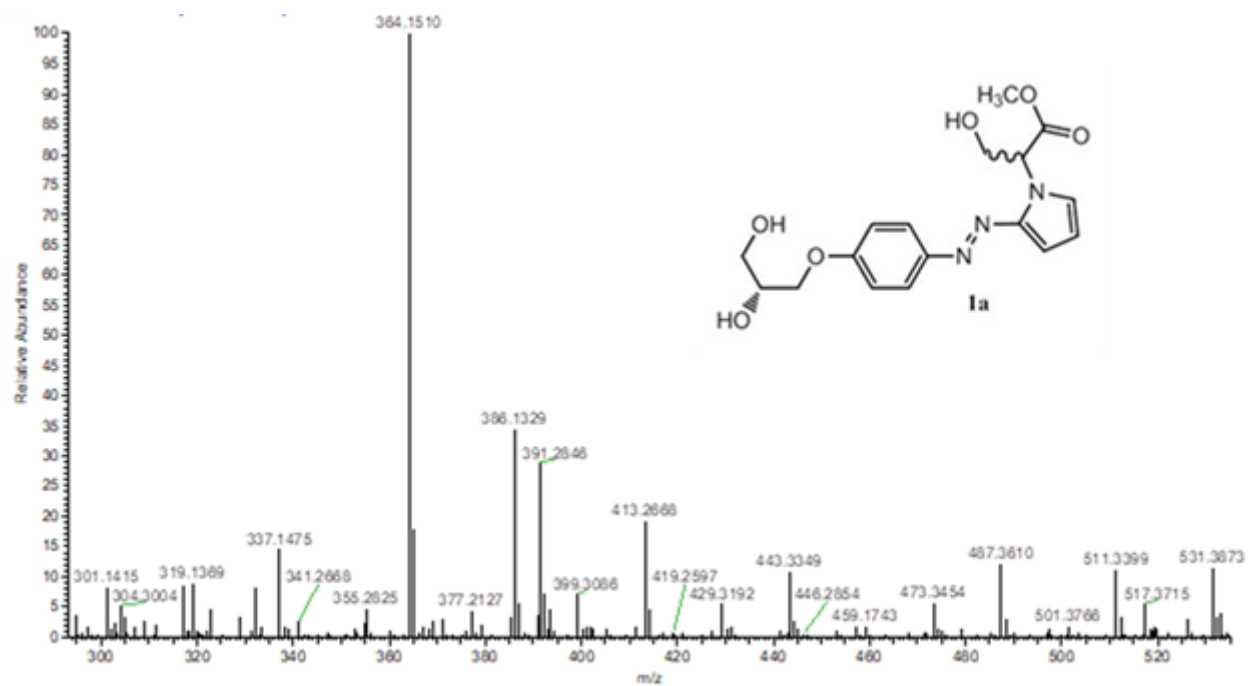
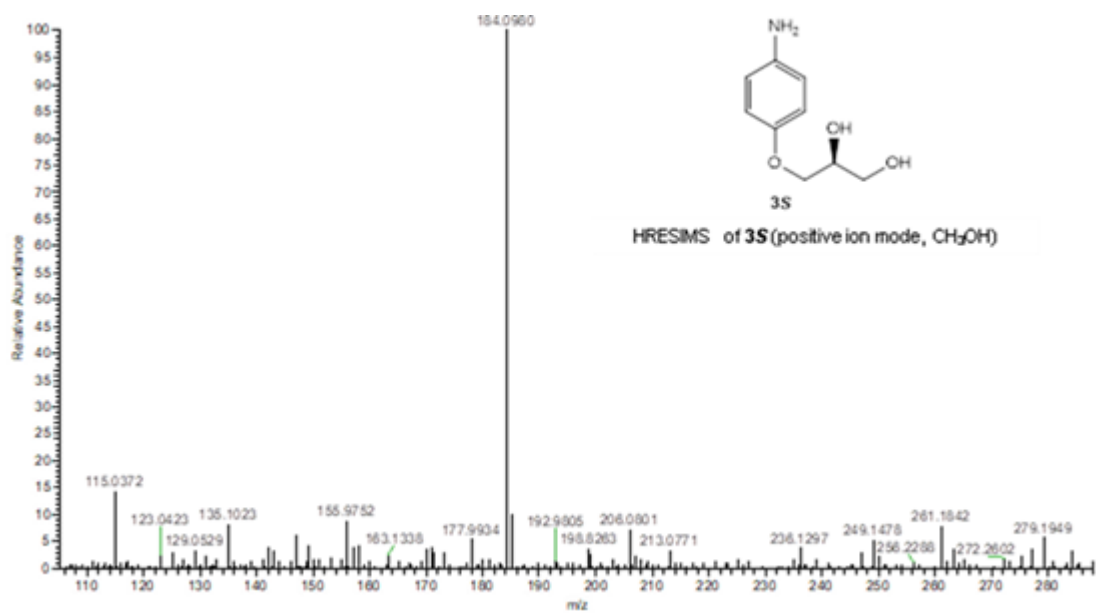
HRESIMS of **1a** after 5 days from dissolution in PBS. The spectrum was acquired in negative mode. [C₁₆H₁₈N₃O₆⁻] calculated 348.1201 uma experimental 348.1187 uma; [C₁₆H₁₇N₃NaO₆⁻] calculated 370.1021 uma experimental 370.1005; mass fragment [C₁₂H₁₀N₃O⁻] calculated 212.0829 experimental 212.0823 uma.

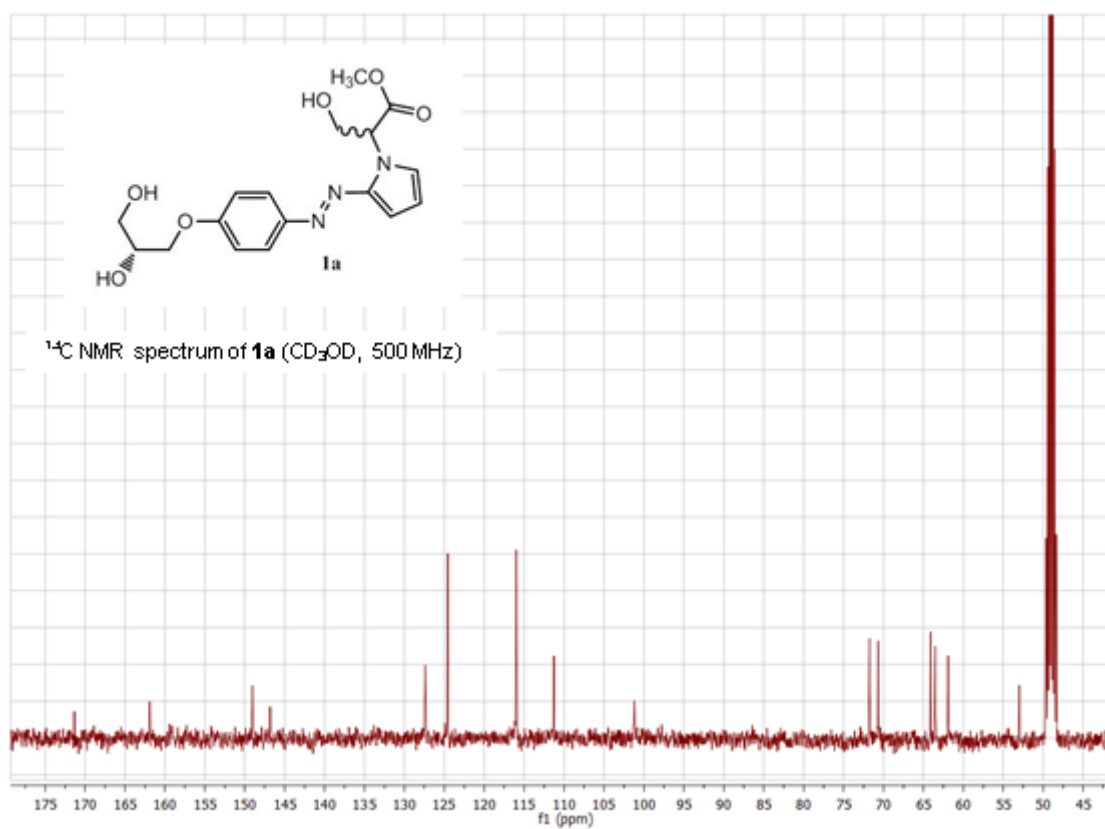
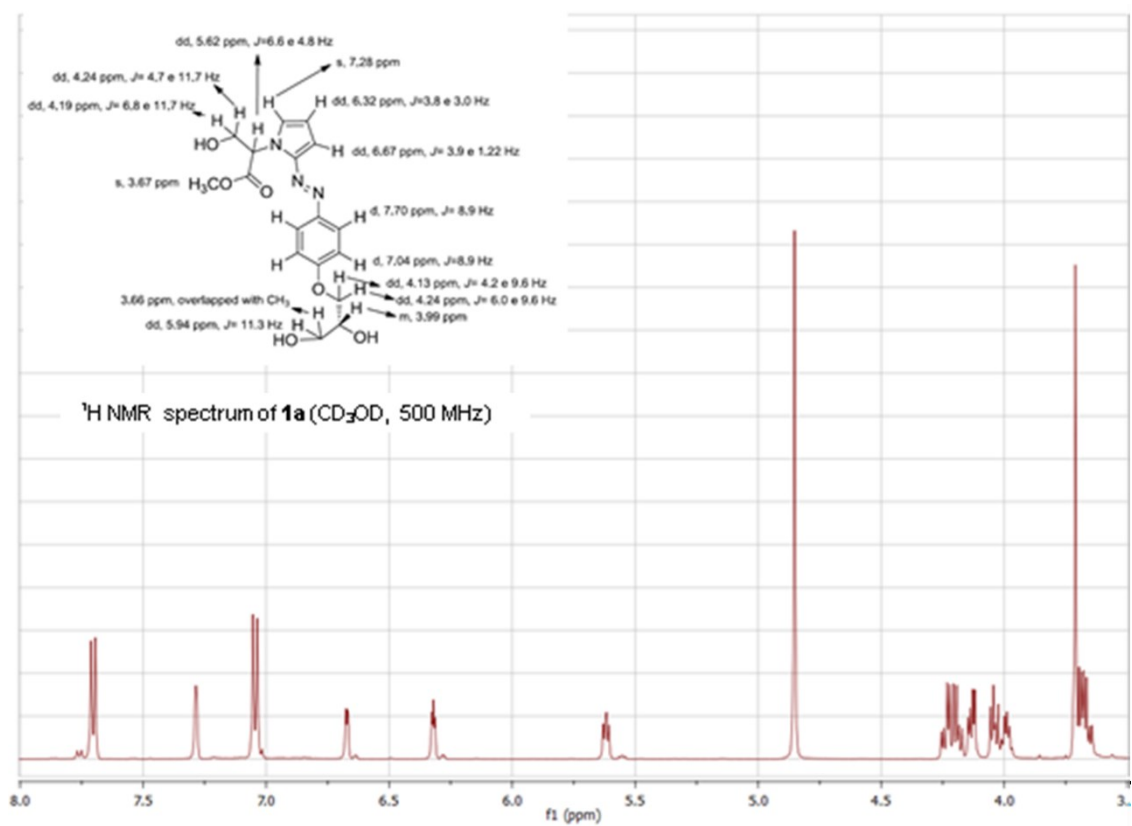


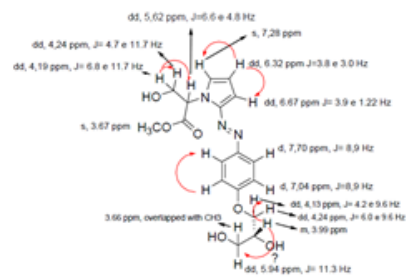




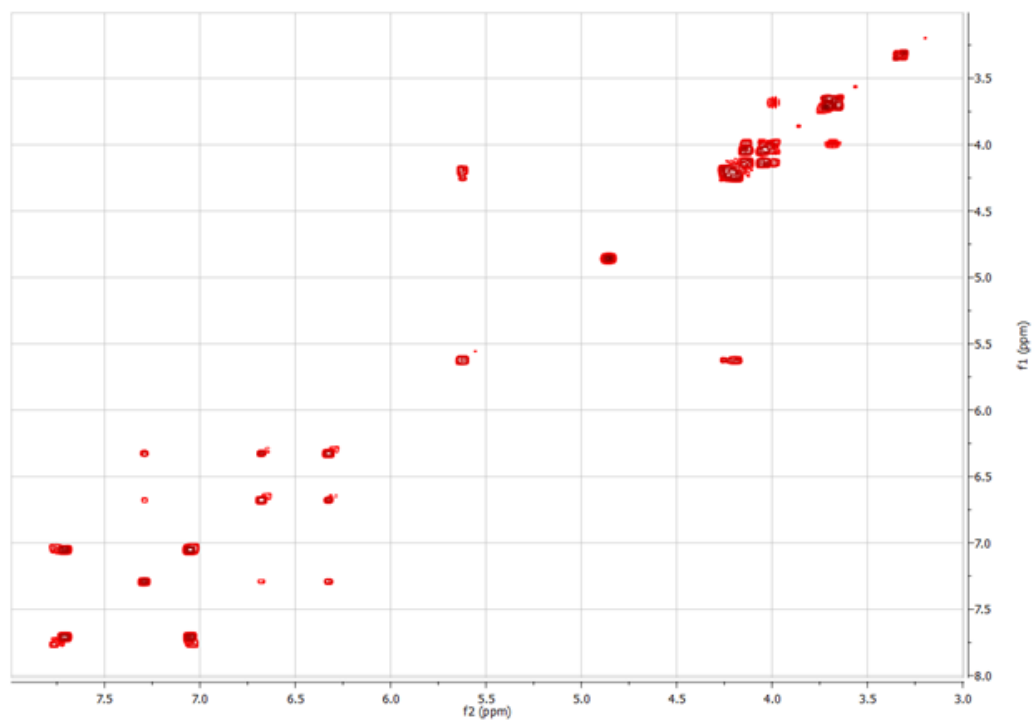


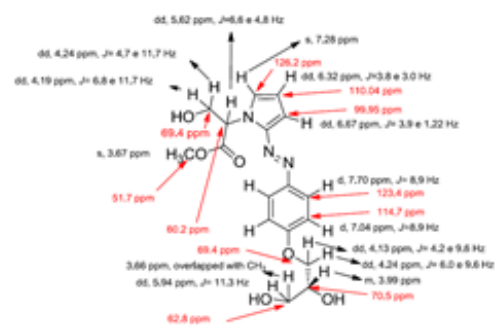




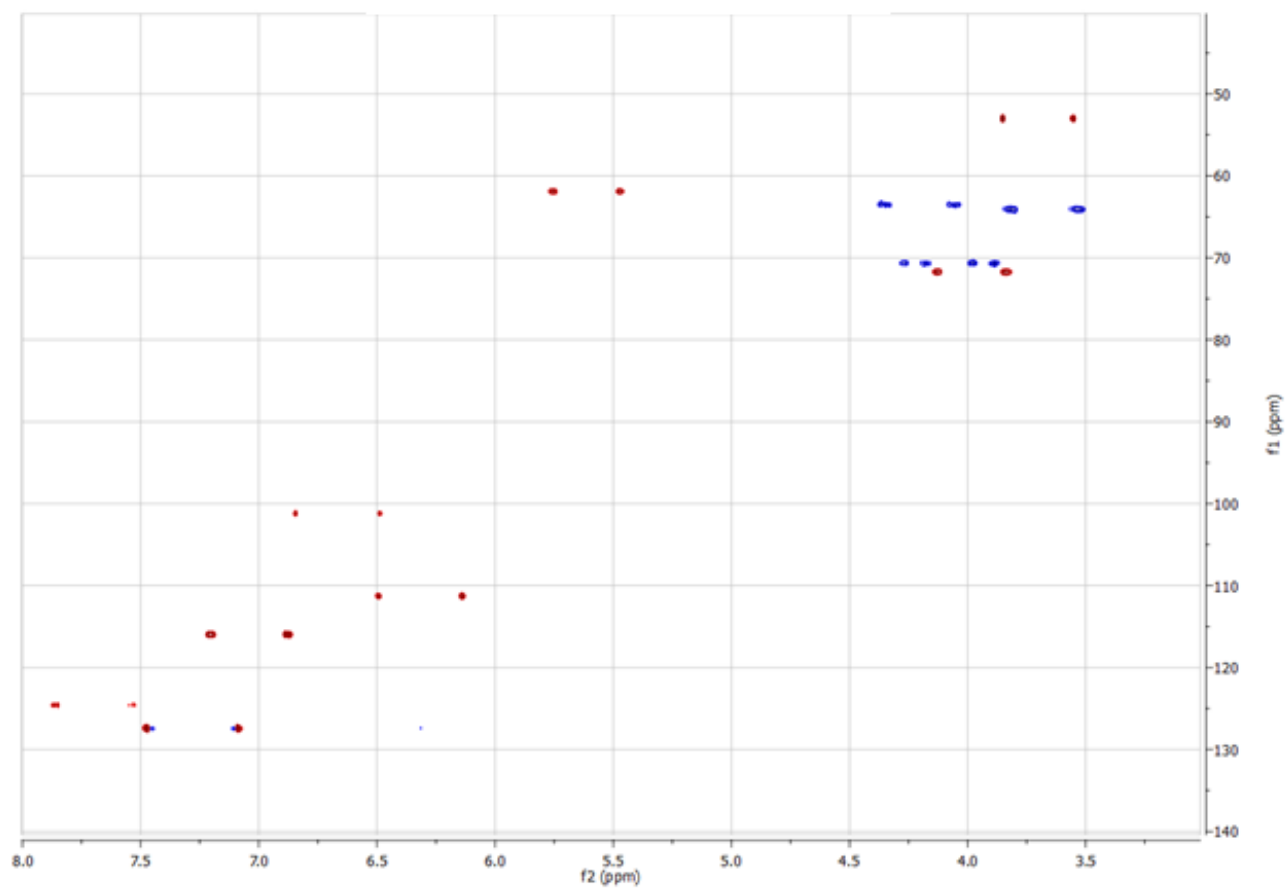


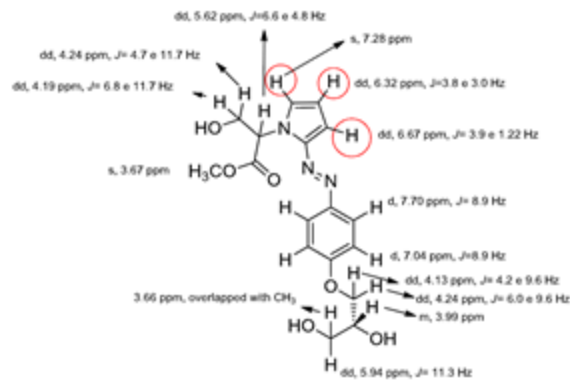
COSY NMR spectrum of **1a** (CD_2OD , 500 MHz)



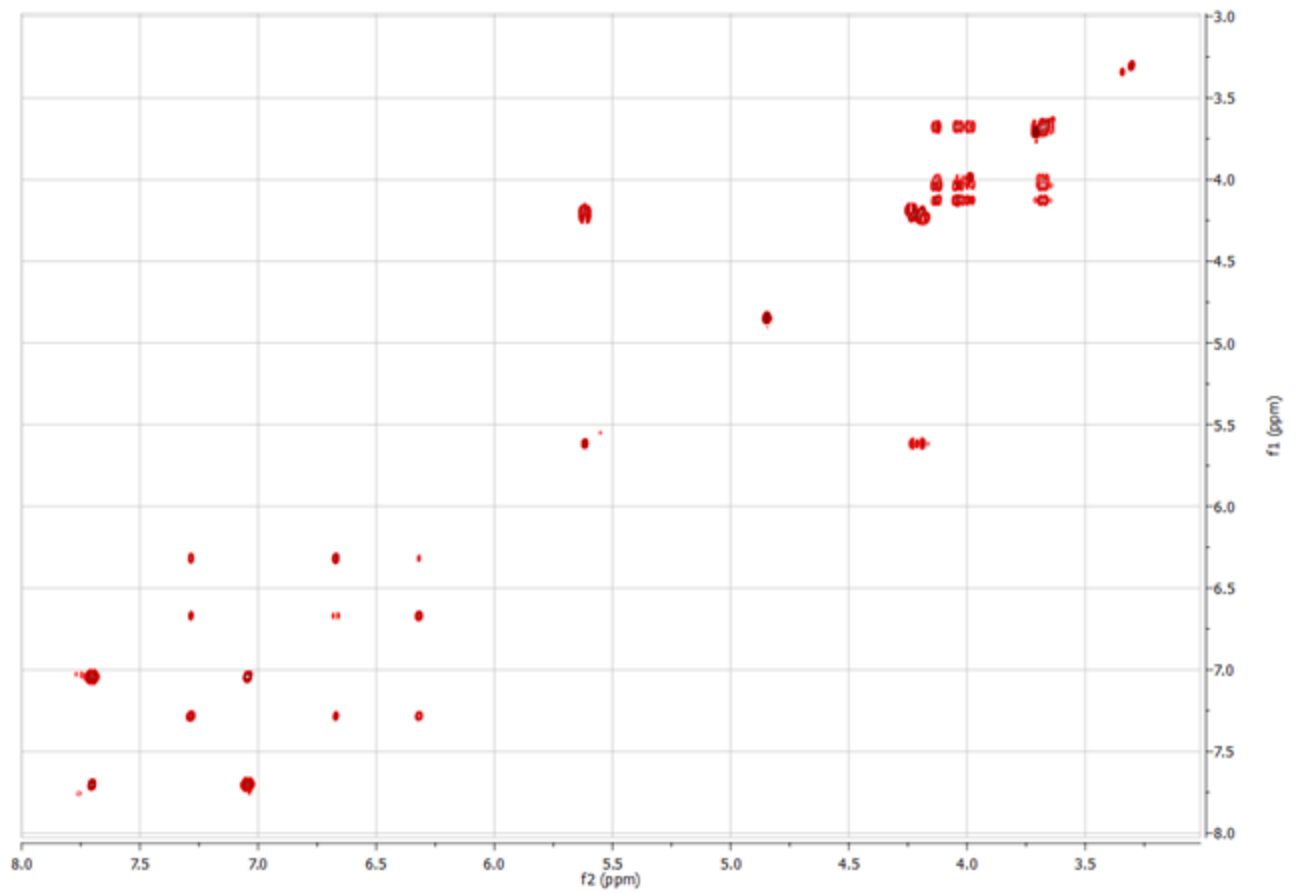


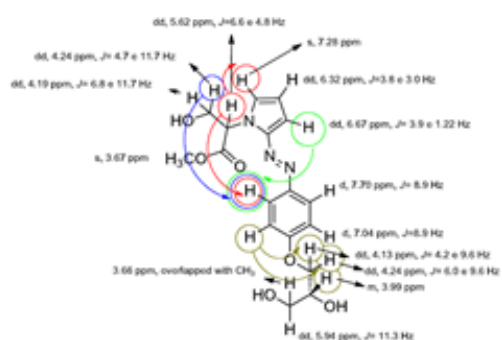
gHSQC NMR spectrum of **1a** (CD_3OD , 500 MHz)



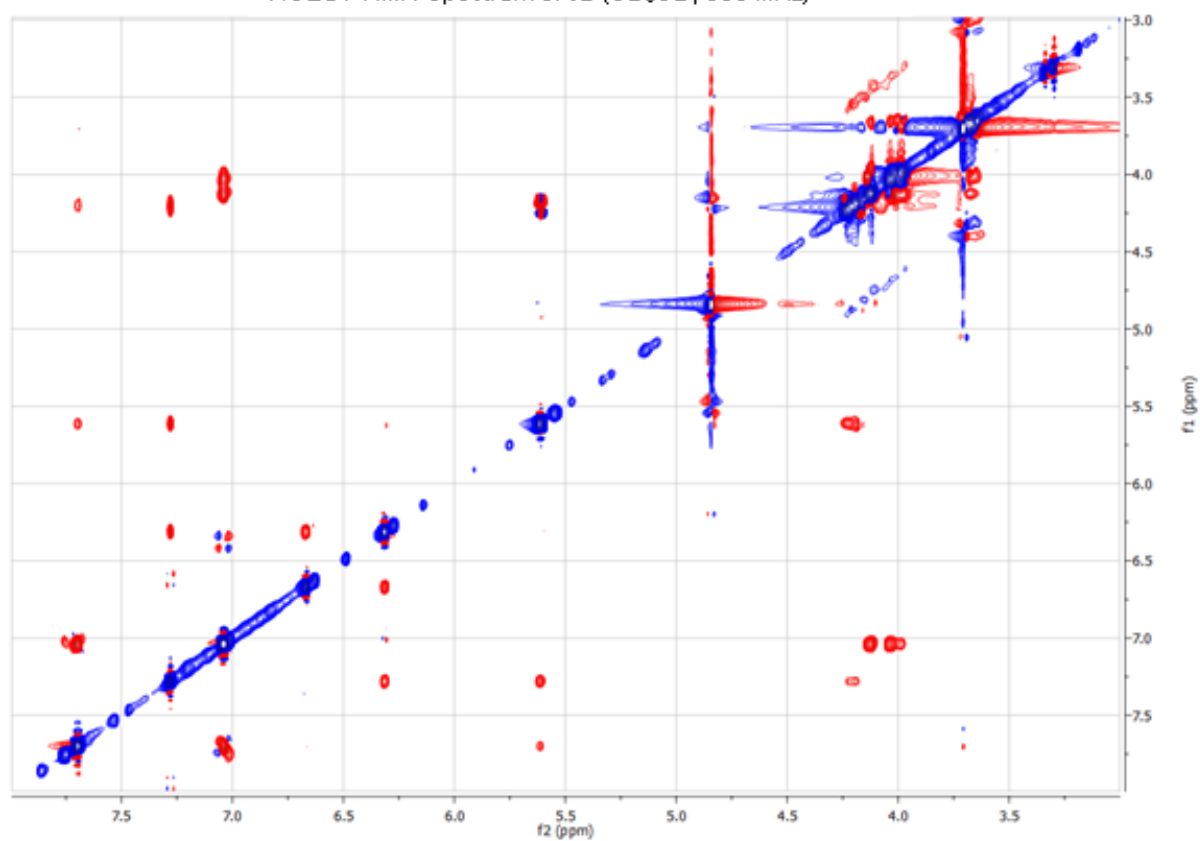


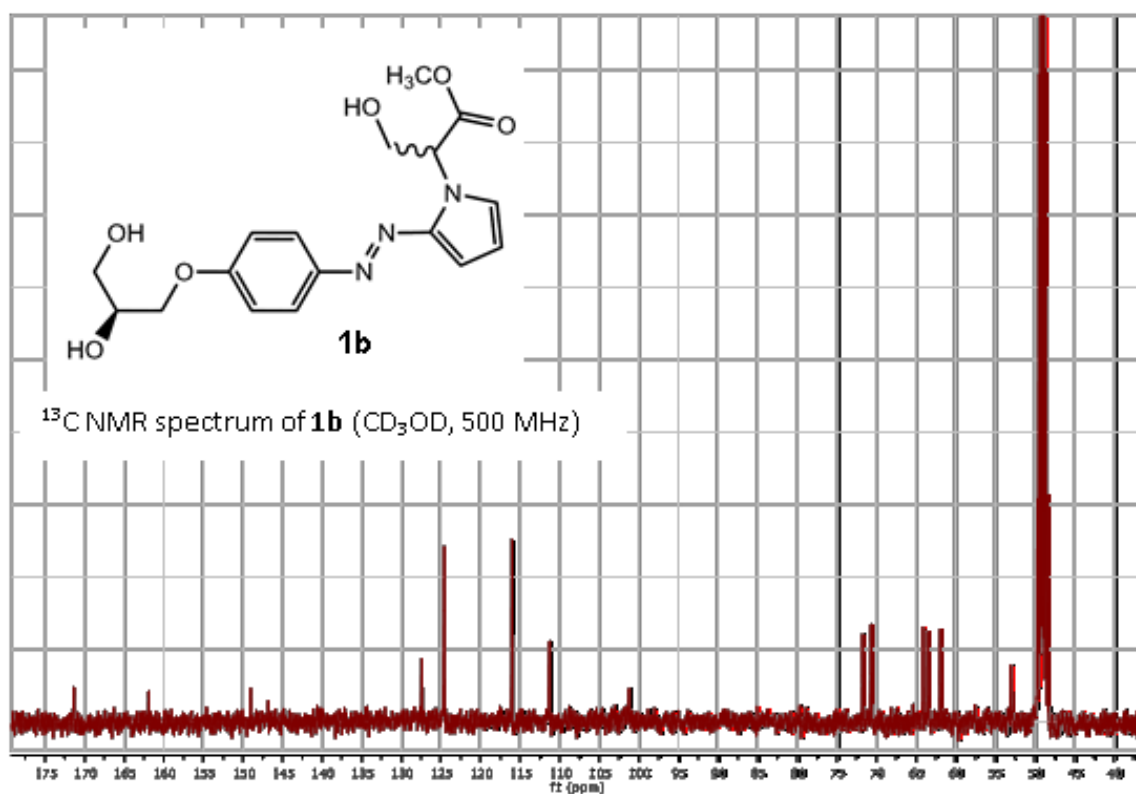
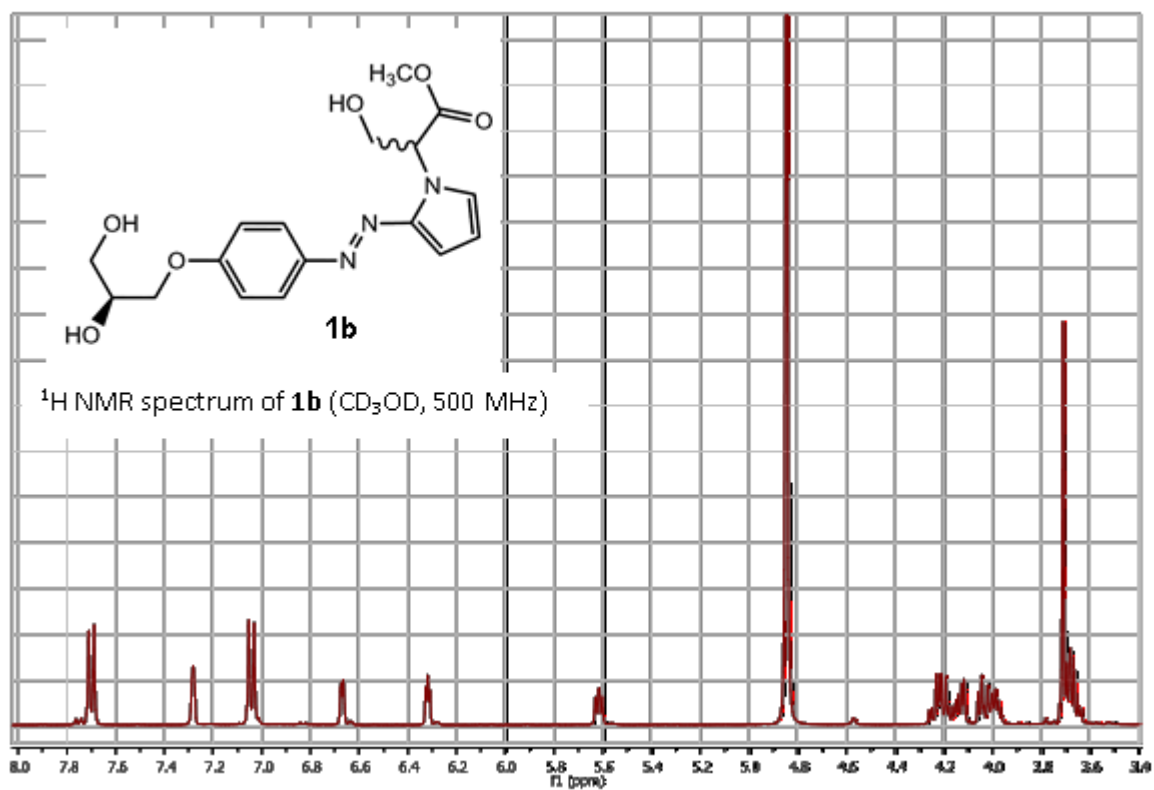
TOCOSY NMR spectrum of **1a** (CD_3OD , 500 MHz)

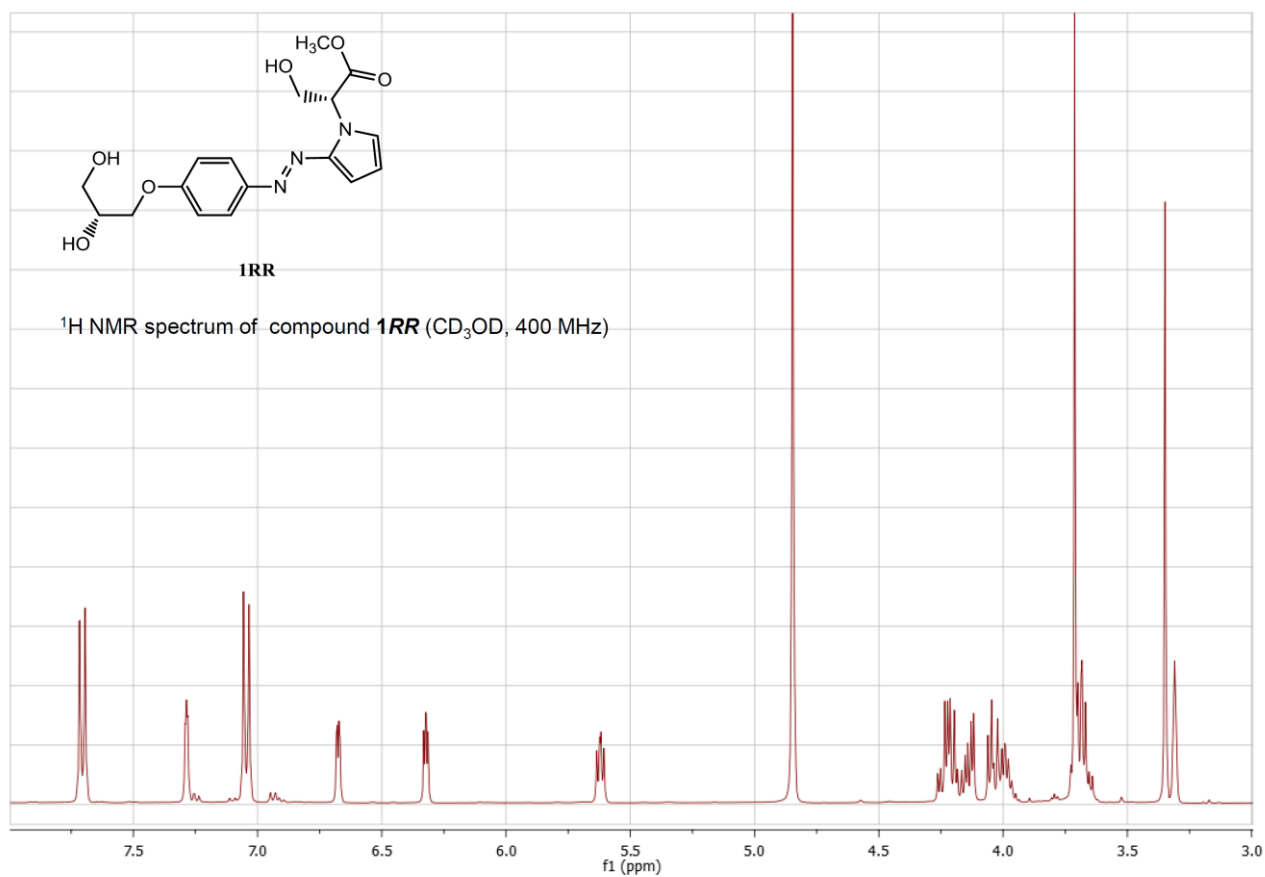
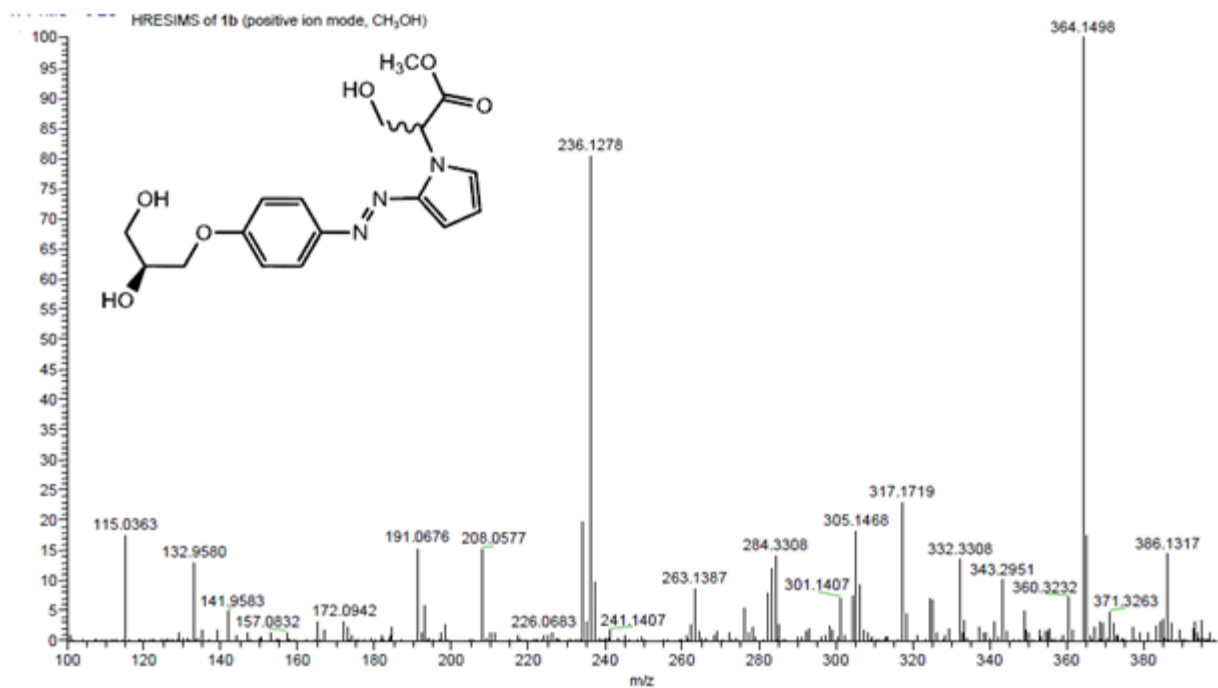


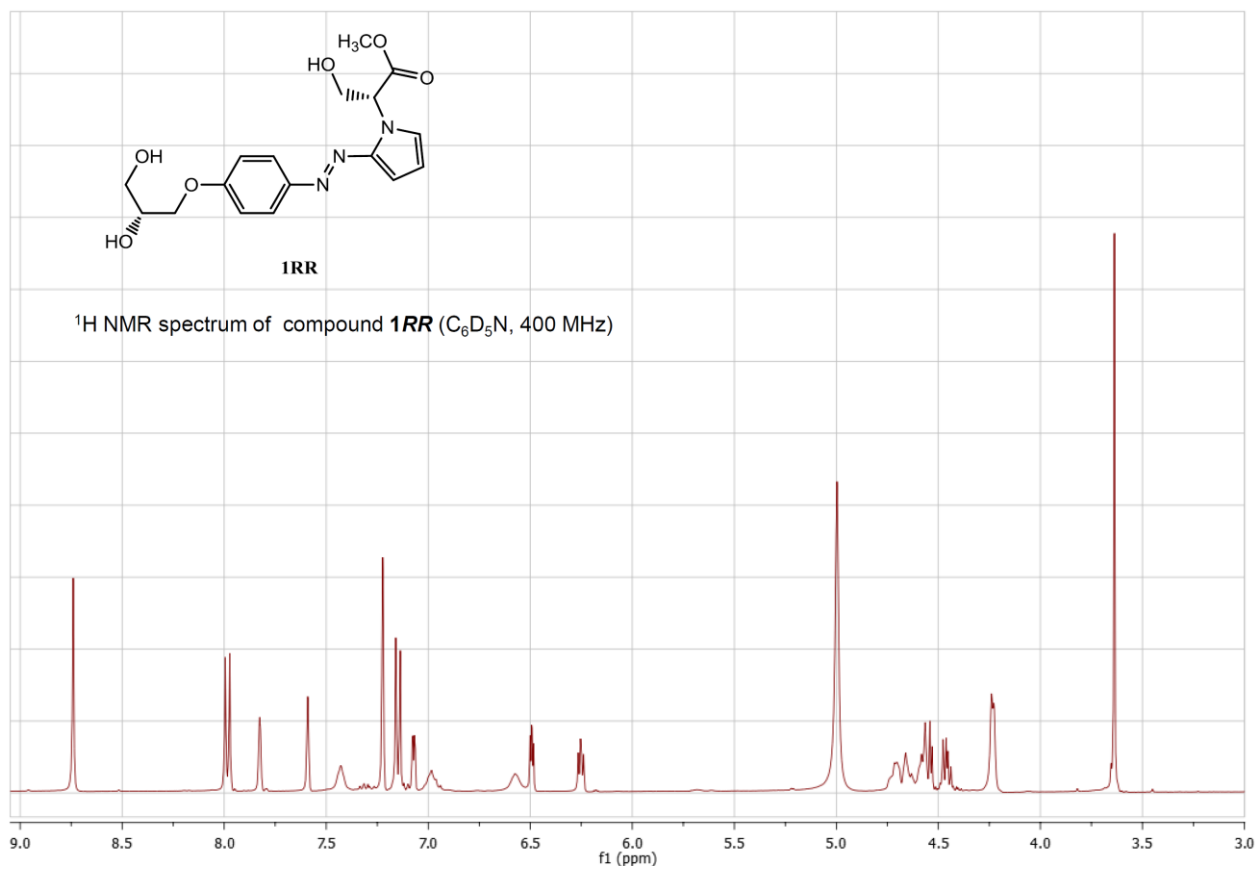
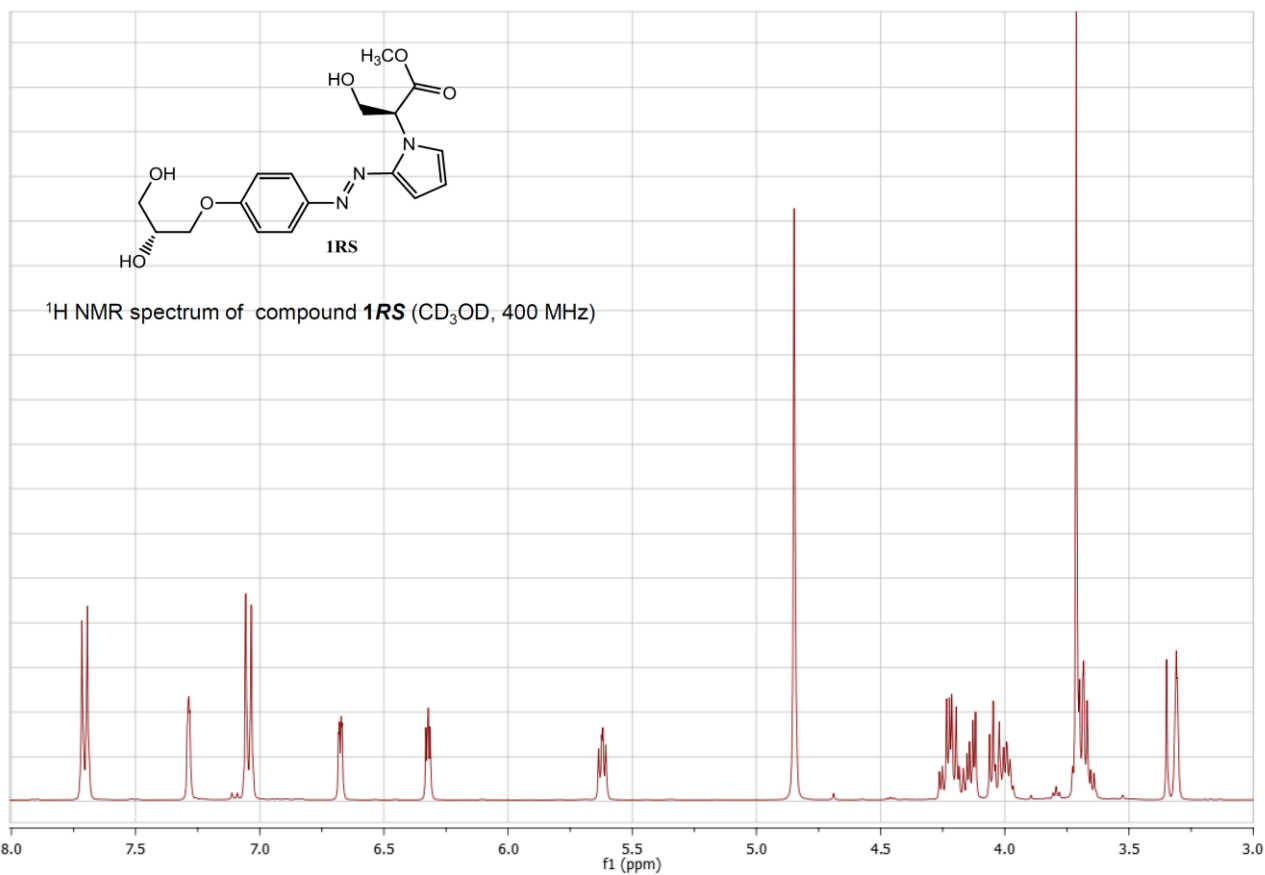


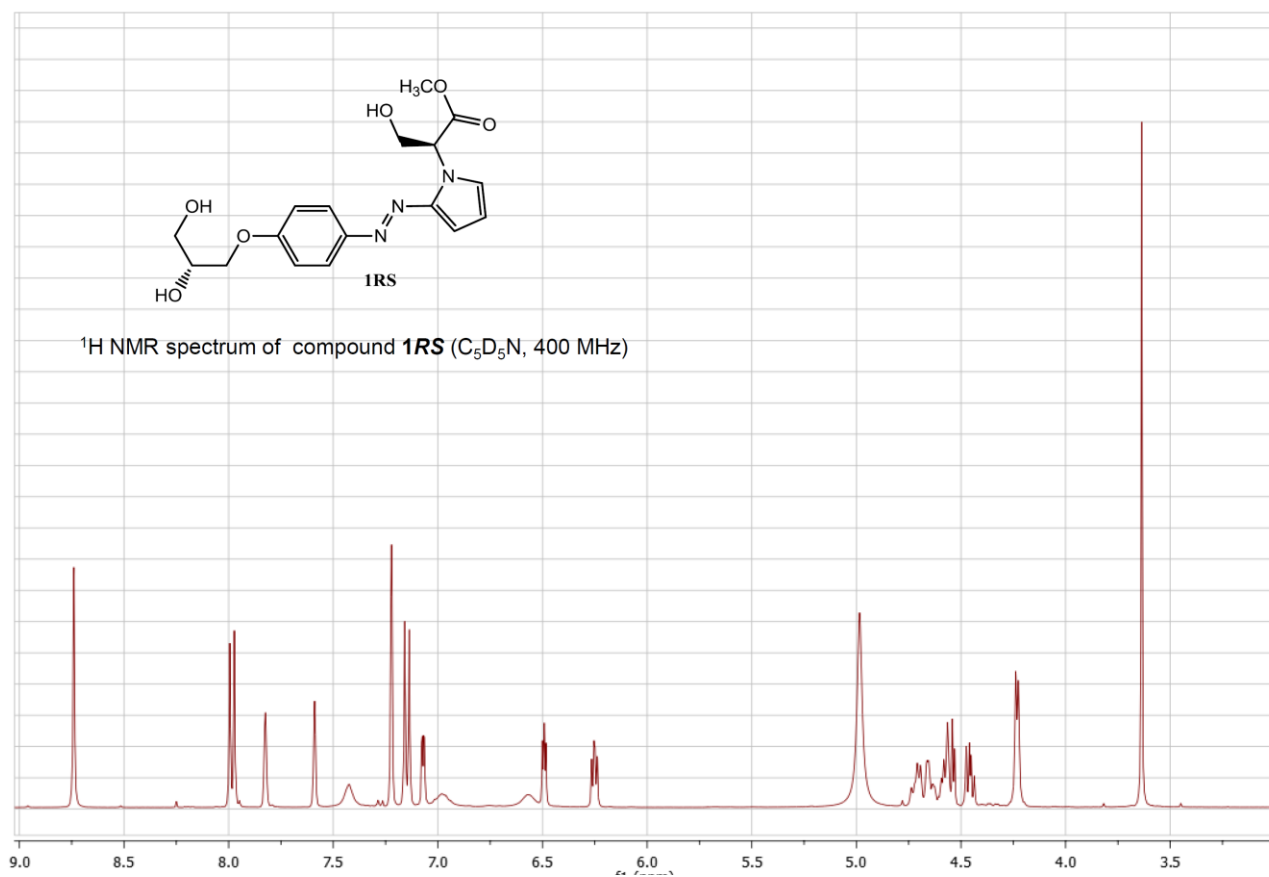
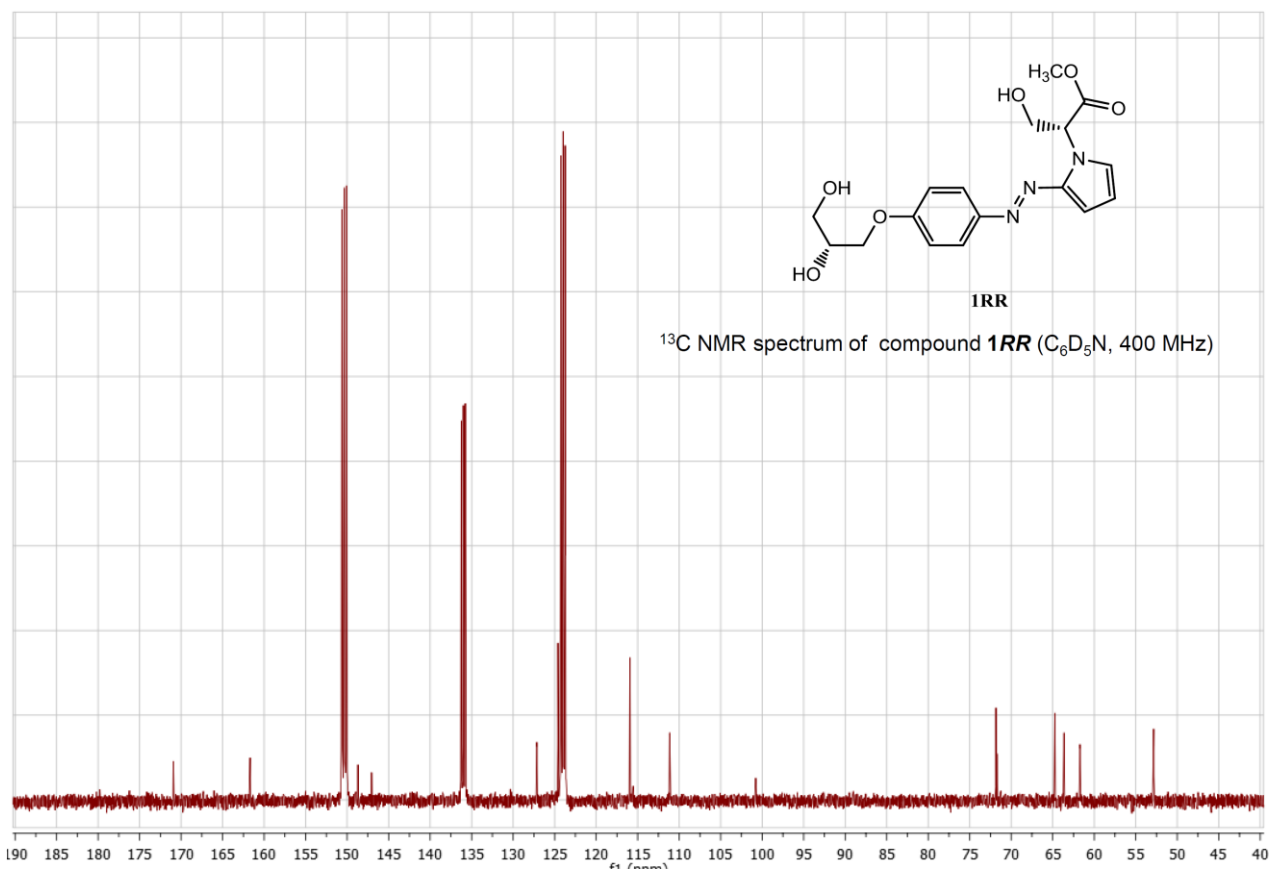
ROESY NMR spectrum of **1a** (CD₃OD, 500 MHz)

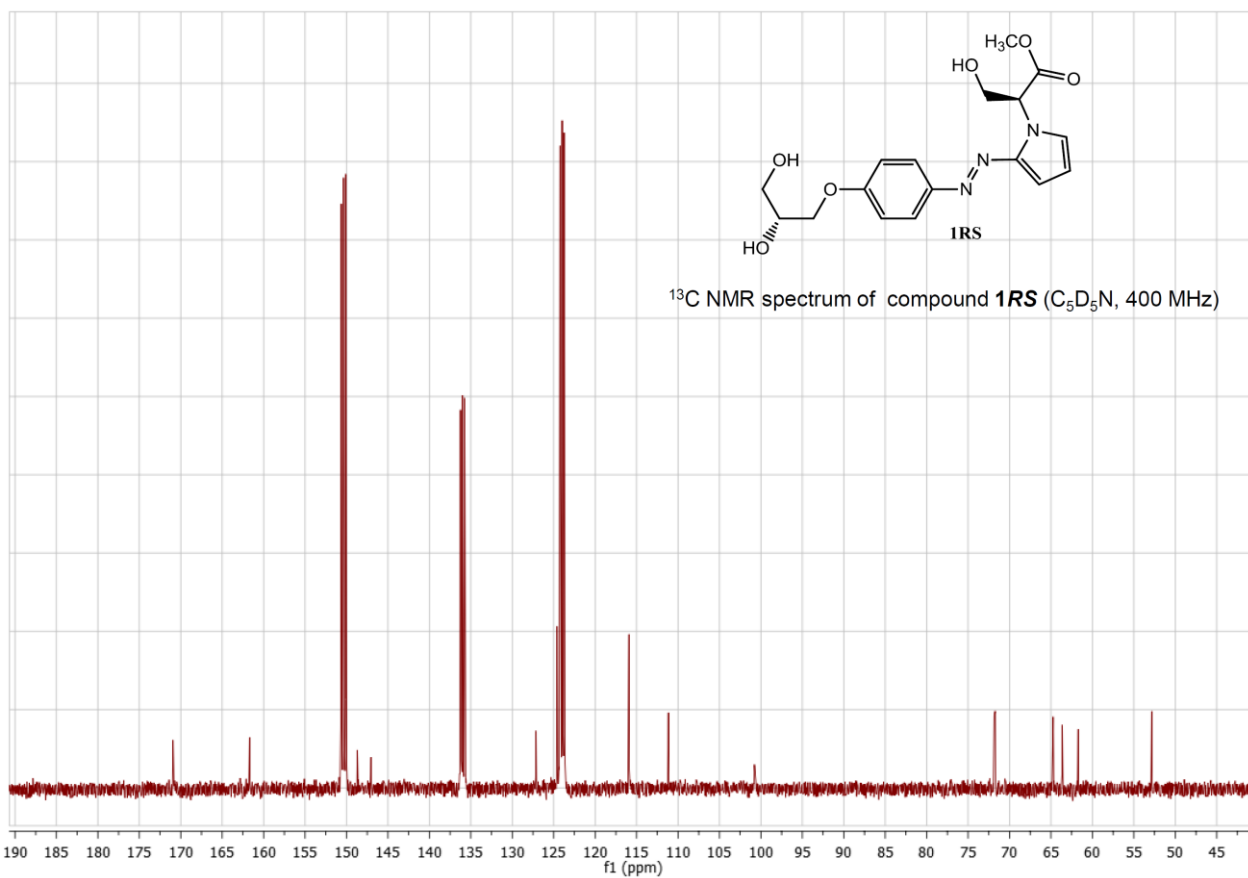












3. Incorporation of a 4-(dimethylamino)azobenzene moiety into G-quadruplex aptamers

3.1. Introduction

A molecular nano-machine may be described as a molecular nanostructure, performed by the self-assembly of monomers, that, upon external stimuli, undergoes some structural changes amounted to mechanical movements (temperature, pH value, electrical-field strength, molecular recognition, etc.) [21]. Stimulation by light is the most promising compared to chemical (or electrochemical) stimuli [22]. Indeed, as above discussed, modulating either the wavelength or the intensity of light high level of spatiotemporal control can be achieved.

Structured DNA is a good candidate as molecular-level machine in view of its self-assembly properties [23]. Moreover, DNA is characterized by high structural polymorphism allowing to potentially expand the number of achievable nano-machines [24]. Among the possible DNA structures, G-Quadruplexes (GQ) are of great interest because of their well-defined and stable conformations.

Pioneering work about a G-quadruplex nano-machine was reported by Mergny and co-workers [25]. Starting from a single 21-base oligonucleotide, folded into a G-quadruplex, the sequential addition of two complementary single stranded oligonucleotides generated a quadruplex–duplex reversible equilibrium that released a DNA duplex as side product. Recently, Ogasawara and Maeda [26] described for the first time a method for the reversible photo-regulation of G quadruplex structures. In particular, 8-fluorenylvinyl-2'-deoxyguanosine (^{8FV}G, figure 26), was incorporated in the G-quadruplex. After irradiation ^{8FV}G undergoes to *trans*→*cis* photo-isomerization causing the reversible disruption of the G-quadruplex.

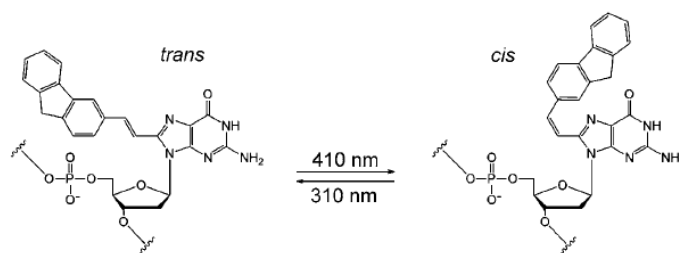


Figure 26. Photo-induced *cis*–*trans* isomerization of 8-fluorenylvinyl-2'-deoxyguanosine (^{8FV}G)[from *Angew. Chemie-Int. Ed.*, vol. 48, no. 36, pp. 6671–6674, 2009].

Furthermore, Wang and co-workers through the use of azobenzene derivative reported in figure 27 provoked, by photo-irradiation, the reversible stretching and folding of the d-(TTAGGG)₄ G-Q. The *trans* azobenzene moiety induced the folding of the sequence into GQ, whereas the *cis* azobenzene moiety caused the disruption of the folded GQ (Figure 27) [27].

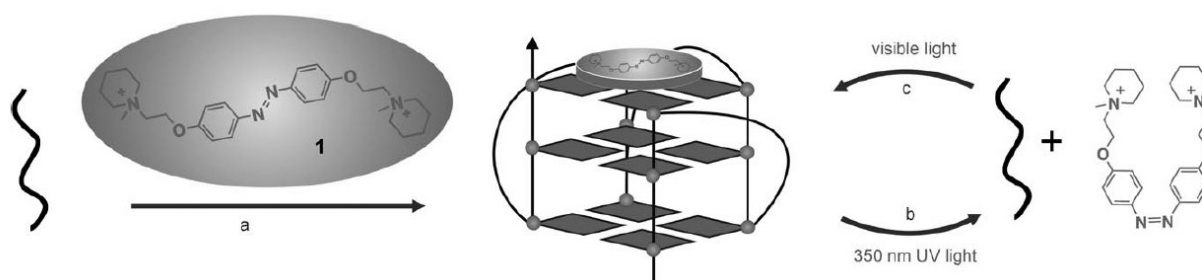
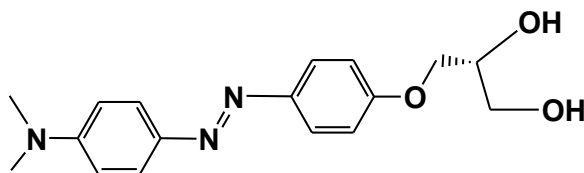


Figure 27. Reversible folding and stretching of the d-(TTAGGG)₄G quadruplex through the *trans*–*cis* photoisomerization of the azobenzene moiety [from *Angew. Chem. Int. Ed.* 2010, 49, 5305–5309].

In this frame, the photo-control of GQ forming aptamers, endowed with pharmacological activities, should be of interest. Given that specific conformations of the folded GQ are the key elements for the binding of aptamers to their targets, the photo-regulation of the aptamer GQ conformations could be used both to control their biological action and to develop new potential nano-machines.

In this frame, recently I started a research project concerning the synthesis and the structural characterization of azobenzene-conjugated GQs. In order to reach this goal, firstly I synthesized the 4-(dimethylamino)azobenzene derivative (4-DMAzo R) reported in figure 28. *Trans*–*cis* photoisomerisation of 4-(dimethylamino)azobenzene (4-DMAzo R) can be induced by violet light, suitable to be used on DNA systems. Furthermore, the two hydroxyl groups of the glycerol linker inserted on one benzene ring are useful to convert the azobenzene derivative into the appropriate

phosphoramidite building block. The latter molecule was used to obtain, by means of automated DNA synthesizer, TBA and T30695 GQs conjugated at 5'end with 4-DMAzo R.



5

Figure 28. (R)-3-(4-((4-(dimethylamino)phenyl)diazanyl)phenoxy)propane-1,2-diol (4-DMAzo R).

First of all, I started to evaluate the photo-responsive properties of the new 4-DMAzo-R, which are particularly distinctive compared to other azobenzene compounds, as previously reported in literature [28][29]. Starting from these results, I explored the behaviour of the free 4-DMAzo R (Figure 28) and of 5'-DMAzo-TBA or 5'-DMAzo-T30695 (Table 1) in different solvent condition.

3.2. Results and discussion

Synthesis of Phosphoramidite Monomer 7R

The synthesis the 4-DMAzo moiety is shown in Figure 29.

The four synthetic steps were performed starting from 4-nitrophenol (Figure 29), which was coupled with R glycidol in presence of catalytic amount of KOH, to obtain the intermediates 2 [20]. Reduction of 2, as R stereomer, with H₂/Pd (C) and successive conversion of the amino- to the diazonium-group gave rise to 4R, which was finally coupled with N,N-dimethylaniline 5. According to the above reported synthesis of **1a** (see page 83), the best yields of the coupling step were obtained quenching the reactions after 1h from the mixture gelification.

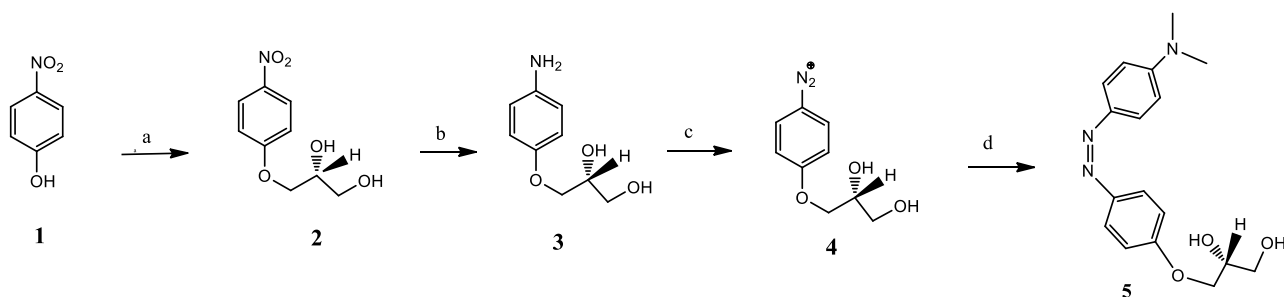


Figure 29. Synthesis of 4-DMAzo R moiety. a) **1**, (0.500 g, 3,6 mmol), KOH (1 mg, $1,8 \times 10^{-2}$ mmol) and dry toluene (2 mL); b) **2** (R, 0, 560 g, 2,6 mmol), Pd/C (5% w/w respect to **2**, 28 mg) and 25 mL di EtOH; c) **3** (0,400 g, 2,2 mmol), 205 μ L fluoroboric acid (water solution, 48%, 3,3 mmol) 4 mL of EtOH (-15°C), isoamyl nitrite (0,258 g, 2,2 mmol); d) **4** (0,360 g, 1,8 mmol) was dissolved in 10 mL of acetic acid (14g, 232 mmol), sodium acetate (4,0 g, 51 mmol) and N,N-dimethylaniline (254 μ L, 0,270 g, 2,2 mmol). Percentage yield: 59%

The synthesis of phosphoramidite monomer **7R** (Figure 30) started from the 4-(dimethylamino)azobenzene moiety (**5R**) that was subjected to the standard protection of one alcoholic function with 4,4'-dimethoxytrityl group. The protected product **6R** was then reacted with β -cyanoethyl-N,N'-diisopropyl-chloro-phosphoramidite to obtain **7R**. This monomer was used to automatically synthesize the modified ONs reported in Table 1 using the standard phosphoramidite protocol (see part I). The yields of coupling were similar to those obtained using the standard phosphoramidite building blocks.

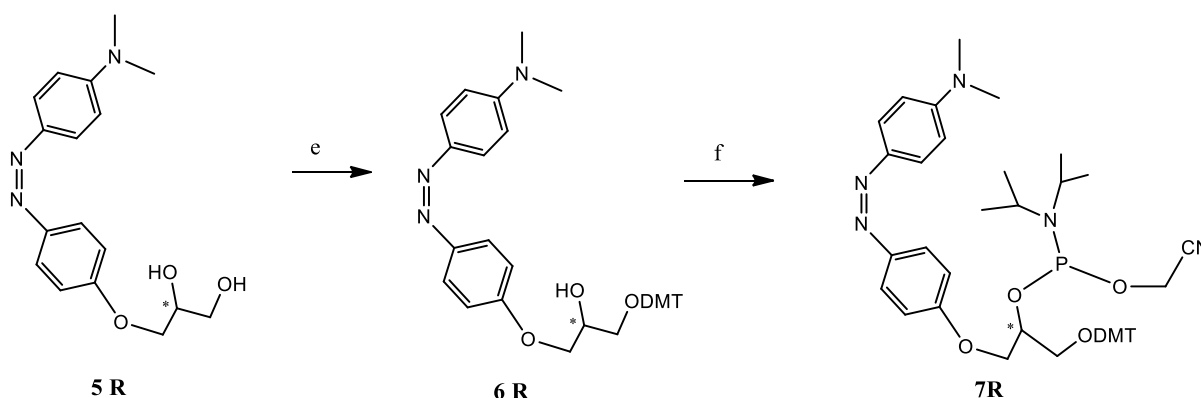


Figure 30. Synthesis of phosphoramidite monomer **7R**. e) **5R** (0.400 g, 1.3 mmol), 4,4-dimethoxytrityl chloride (0.430 g, 1.3 mmol), 4-dimethylaminopyridine (0.0076 g, 0.062 mmol) dry Py (6.35 ml), 2.5 h, yields 44%; f) **6R** (0.350 g, 0.57 mmol), β -cyanoethyl-N,N'-diisopropyl-chloro-phosphoramidite (0.190 ml, 0.85 mmol), DIPEA (0.296 ml, 1.7 mmol), dry DCM (3 ml), 1.0 h. 70%.

Table 1.

| ON | Sequence |
|------------------|--------------------------------|
| T30695 | 5'-GGGTGGGTGGGTGGGT-3' |
| 5'-DMAzoR-T30695 | 5'-DMAzo R-GGGTGGGTGGGTGGGT-3' |
| TBA | 5'-GGTTGGTGTGGTTGG-3' |
| 5'-DMAzoR-TBA | 5'-DMAzo R-GGTTGGTGTGGTTGG-3' |

UV/Vis spectra of 5R

The rate of thermal relaxation of the *cis*-4-DMAzo is strongly dependent on solvent polarity and on the pH of the solutions. Indeed, *cis* to *trans* thermal decay of 4-DMAzo compounds increases with the increasing of either the solvent polarity or the proton concentration in the solution [28][29]. Sanchez and co-workers reported the dependence of the rate of *cis* → *trans* conversion from the concentration of hydroxide ions in the solution. Similarly, the *cis-trans* isomerization can be accelerated by small traces of acids [30].

Successive studies suggested a plausible mechanism concerning the pH influence on the half-life of certain functionalized 4-DMAzo *cis* isomers (Figure 31) [31].

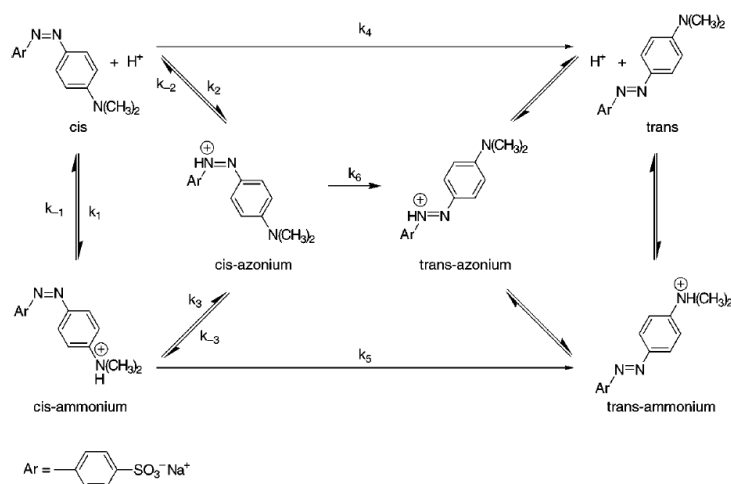


Figure 31. Schematic representation of *cis-trans* equilibria. The constants rate k_4 and k_5 are lower than k_6 , consequently the conversion rate is mainly dependent on the thermal conversion of the *cis*-azonium [from *J. Org. Chem.*, vol. 64, no. 17, pp. 1604–1609, 1999].

In the opinion of those authors, the acid/base-assisted tautomerization of *cis* ammonium ions into *cis*-azonium ions could cause the catalytic effect on thermal decay of the *cis* form. Indeed, *cis*-

azonium ions could easily isomerize via rotation around the $-N=N-$ bond as a result of the concomitant decrease in the double bond character. In addition, the solvent can also affect the thermal conversion rates of the *cis* amino-benzene derivatives, indeed this *cis* to *trans* conversion could be accelerated in protic solvents [32].

Confirming these findings, the UV spectra of *cis* 5R obtained using water or methanol, or different H_2O/ACN mixtures, could not be evidenced by means of a conventional UV-Vis spectrophotometer, in view of the extremely fast *cis*→*trans* conversion (Figure 32). These results evidenced that the presence of glycerol linker on one benzene ring of 5R did not significantly affect the general behaviour of the 4-DMAzo.

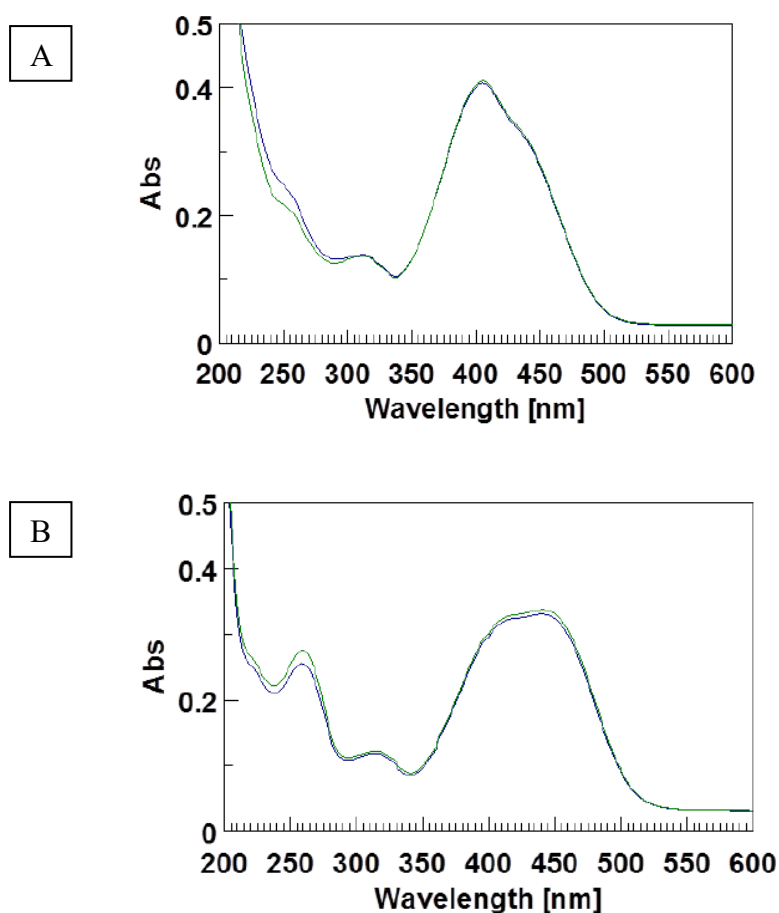


Figure 32. UV spectra of the 5R before (green) and after (blue) irradiation with 400 or 435 nm led, in CH_3OH (A) and in H_2O/ACN (B).

In order to decrease the *cis*→*trans* thermal decay, UV-Vis spectroscopy experiments of 5R (131 μM) were carried out in H₂O/ACN solution 60:40 (v:v) in the presence of growing concentrations of an organic base, triethylamine (TEA) (Table 2).

Table 2

| 5R (μM) | TEA (μM) | Ratio (5R/TEA) |
|------------|---------------------|-------------------|
| 131 | 131 | 1:1 |
| 131 | 1310 | 1:10 |
| 131 | 1965 | 1:15 |
| 131 | 3275 | 1:25 |
| 131 | 6550 | 1:50 |
| 131 | 13100 | 1:100 |
| 131 | 32750 | 1:250 |
| 131 | 65500 | 1:500 |
| 131 | 98250 | 1:750 |
| 131 | 131x10 ³ | 1:1000 |
| 131 | 131x10 ⁴ | 1:10000 |

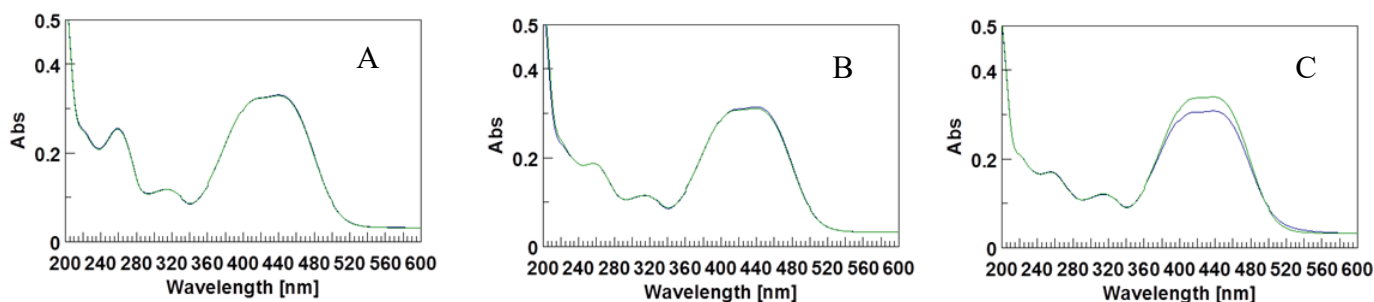
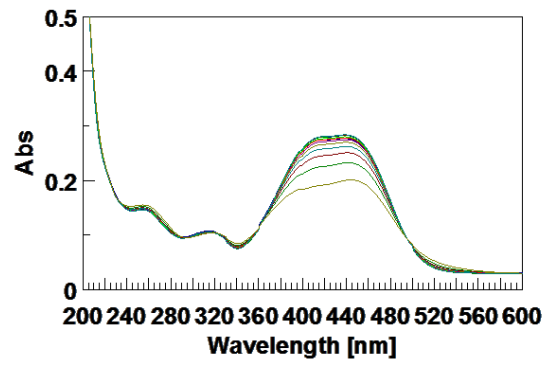
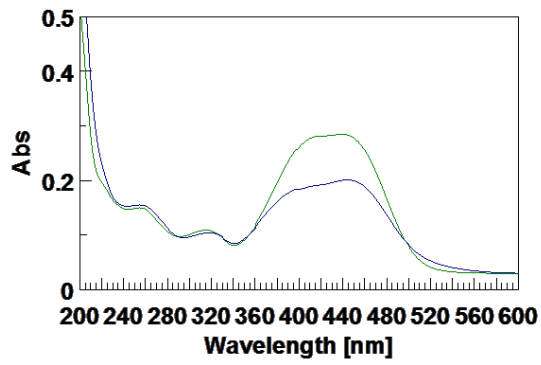


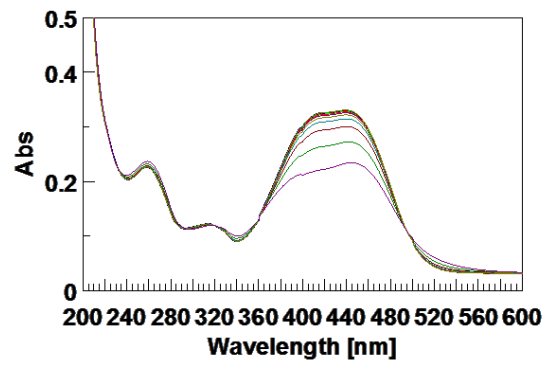
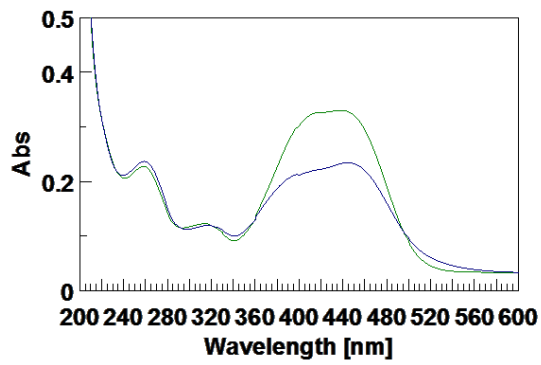
Figure 33. UV-Vis spectra of 5R (131 μM) in H₂O/ACN 60:40 (v:v); A) 5R:TEA (1:1), B) 5R:TEA (1:10), C) 5R:TEA (1:15).

A slight decrease of the *cis*-*trans* conversion rate was observed at the ratio 5R:TEA (1:15) (Figure 33 C), increasing the TEA concentration a significant decreasing in the rate of *cis*→*trans* thermal decay was obtained. In particular, starting from the ratio 5R:TEA (1:25) it was possible to monitor the thermal decay by sequential acquisition of spectra until reaching the initial *trans* isomer UV profile (Figure 34 1-8).

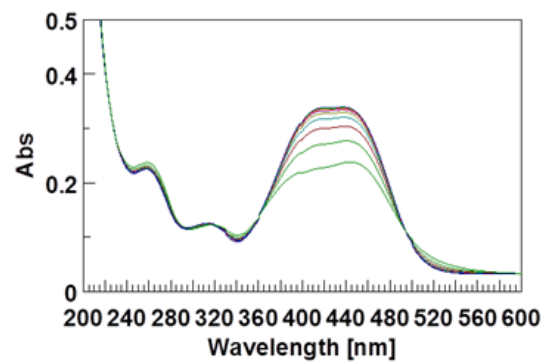
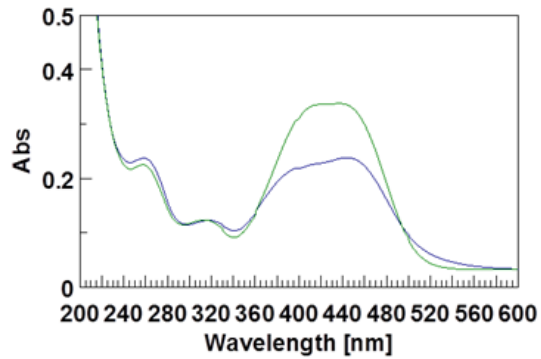
1) 5R : TEA=1:25 in H₂O:Acn (6:4)



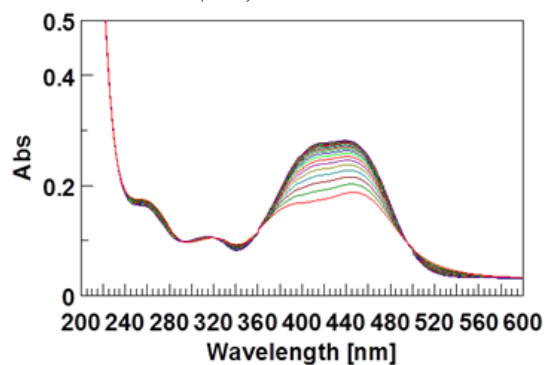
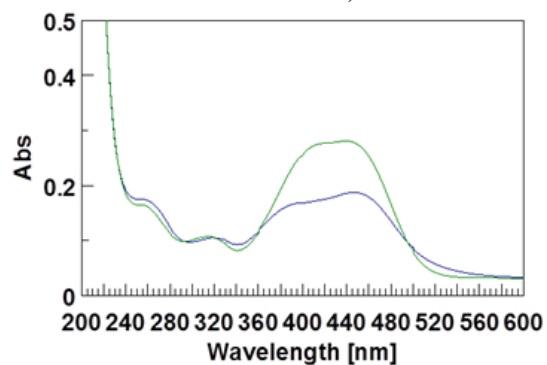
2) 5R : TEA=1:50 in H₂O:Acn (6:4)



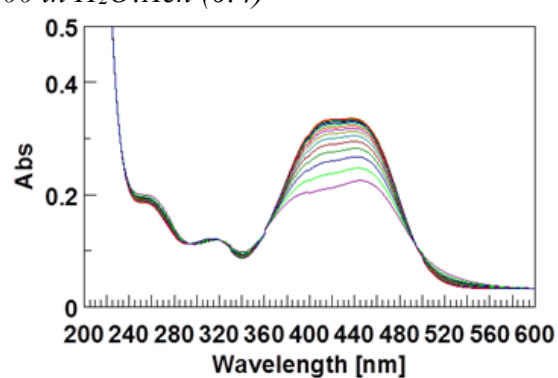
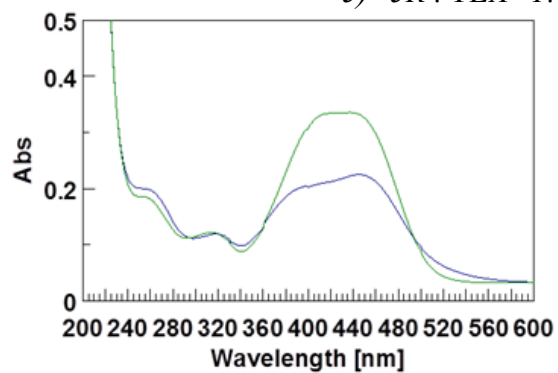
3) 5R : TEA=1:100 in H₂O:Acn (6:4)



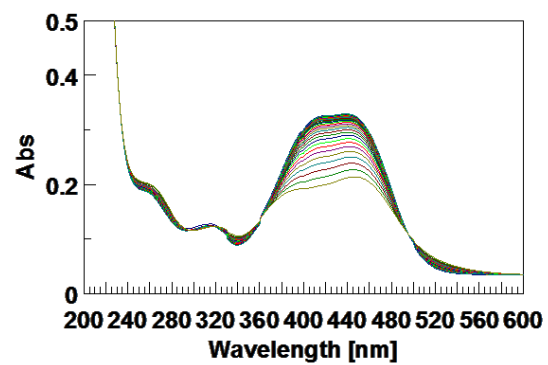
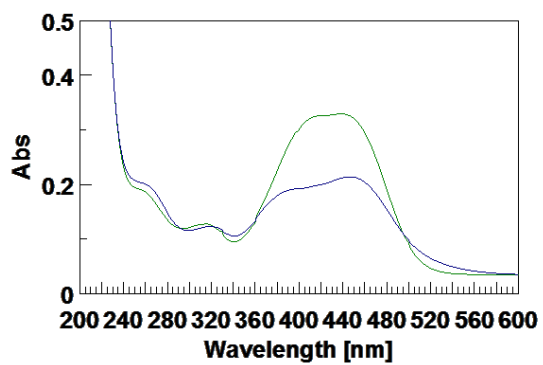
4) 5R : TEA=1:250 in H₂O:Acn (6:4)



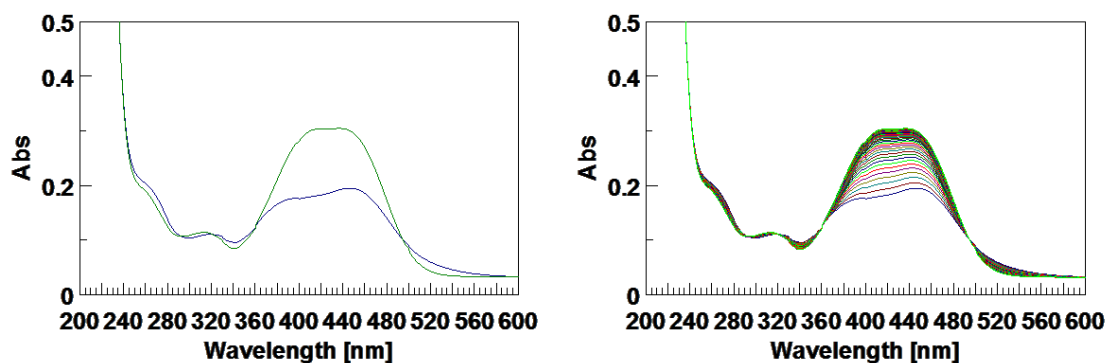
5) 5R : TEA=1:500 in H₂O:Acn (6:4)



6) 5R : TEA=1:750 in H₂O:Acn (6:4)



7) 5R : TEA=1:1000 in H₂O:Acn (6:4)



8) 5R : TEA=1:10000 in H₂O:Acn (6:4)

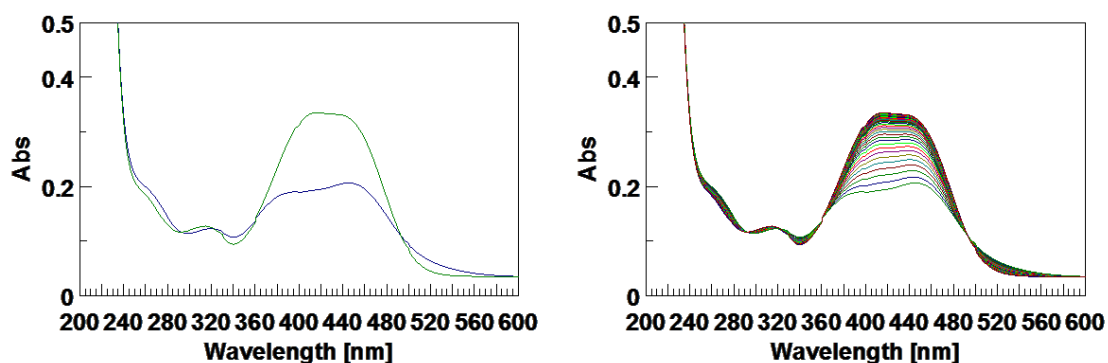


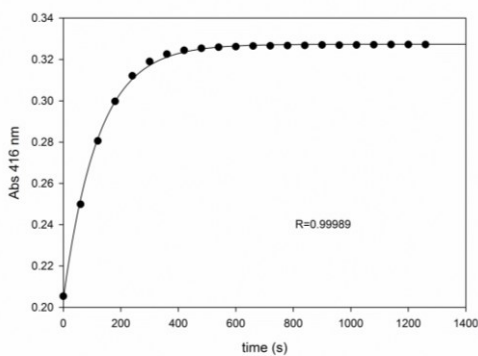
Figure 34. UV spectra of *trans* (green) and *cis* (blue) 5R in H₂O / ACN (6:4) at different ratio 5R:TEA (1:25, 1:50, 1: 100, 1: 250, 1: 500 , 1: 750, 1: 1000, 1: 10000). In all these conditions, the thermal decay was monitored by sequential acquisition of spectra until the UV profile rises to that of the initial *trans* isomer. Cell length: 0.1 cm.

In order to measure the $t_{1/2}$ of metastable *cis* isomer, obtained after irradiation at 435 nm, UV time course measurement experiments were performed monitoring the absorbance values at 416, 448, 525, 260 nm (number of cycle 100-180, cycle time 60 sec). In figure 35 the kinetics were all reported at 416 nm. The $t_{1/2}$ values were calculated from the resulting calibration curve fit equation, these results are shown in Table 3.

Table 3. $t_{1/2}$ values of *cis* 4-DMAzo R (5R,131 μ M) at different ratio of TEA.

| 5R:TEA | $t_{1/2}$ (s) \pm standard error |
|---------|------------------------------------|
| 1:15 | $<75 \pm 15$ |
| 1:50 | 74 ± 14 |
| 1:100 | 84 ± 6 |
| 1:250 | 219 ± 34 |
| 1.500 | $200,5 \pm 4,5$ |
| 1:750 | 294 ± 7 |
| 1:1000 | 555 ± 145 |
| 1.10000 | 467 ± 50 |

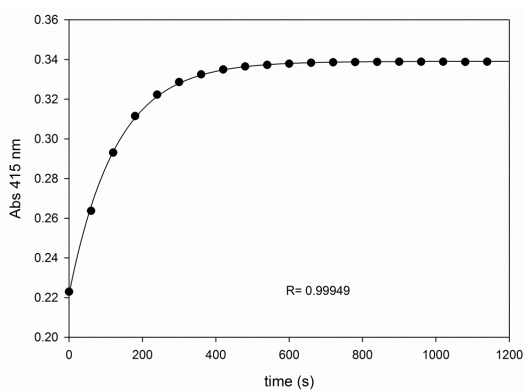
5R:TEA=1:50 in H₂O:Acn (6:4)



$$y = y_0 + a \cdot (1 - \exp(-b \cdot x))$$

| Parameter | Value | StdErr | CV(%) | Dependencies |
|-----------|----------|----------|----------|--------------|
| y0 | 2.040e-1 | 9.528e-4 | 4.671e-1 | 0.9479342 |
| a | 1.234e-1 | 9.631e-4 | 7.806e-1 | 0.9393374 |
| b | 8.286e-3 | 1.290e-4 | 1.557e+0 | 0.4373805 |

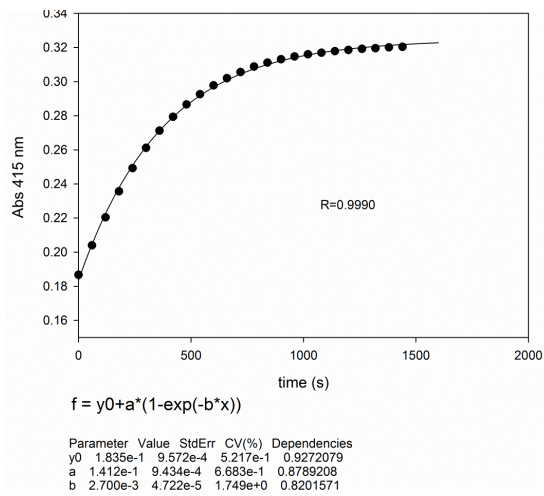
5R:TEA=1:100 in H₂O:Acn (6:4)



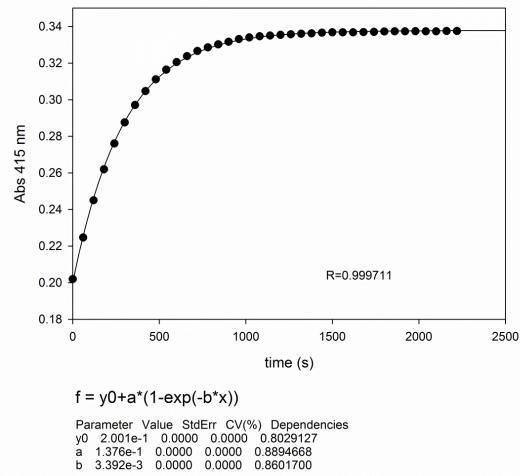
$$y = y_0 + a \cdot (1 - \exp(-b \cdot x))$$

| Parameter | Value | StdErr | CV(%) | Dependencies |
|-----------|----------|----------|----------|--------------|
| y0 | 2.218e-1 | 6.700e-4 | 3.021e-1 | 0.9419772 |
| a | 1.173e-1 | 6.776e-4 | 5.777e-1 | 0.9304882 |
| b | 7.864e-3 | 9.213e-5 | 1.172e+0 | 0.4776581 |

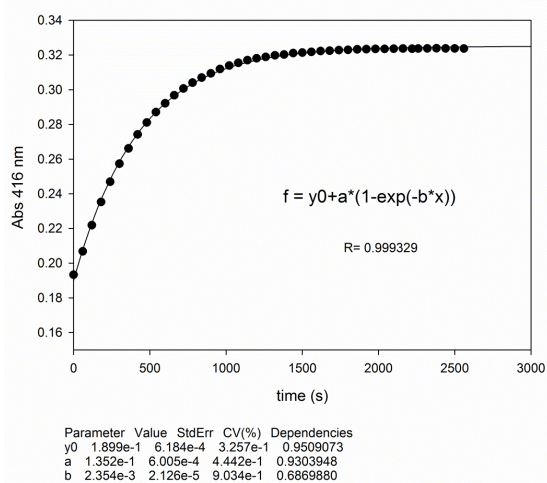
5R:TEA=1:250 in H₂O:Acn (6:4)



5R:TEA=1:500 in H₂O:Acn (6:4)



5R:TEA=1:750 in H₂O:Acn (6:4)



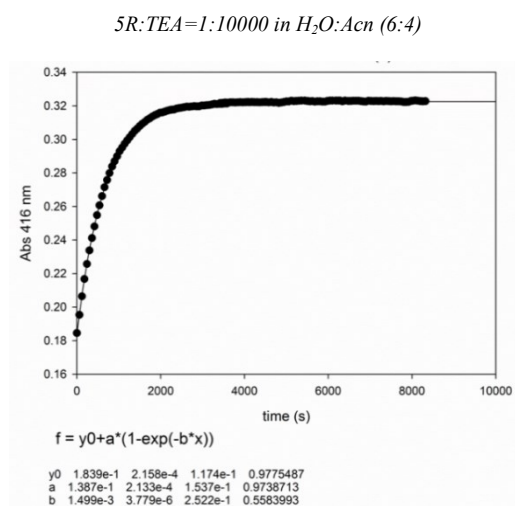
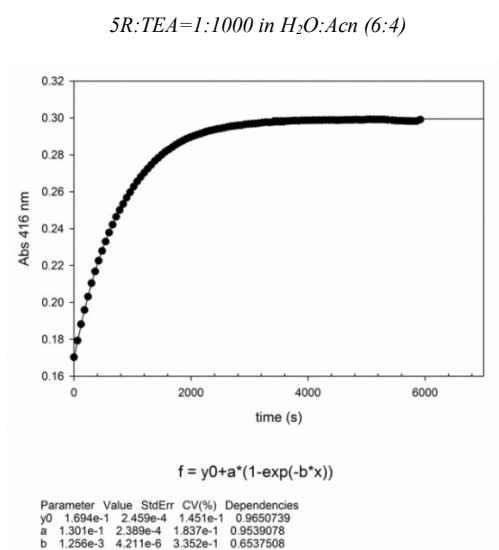


Figure 35. Time-dependent absorption of 5R after irradiation in H₂O / ACN (6:4) at wavelength 416 nm in presence of different equivalents of TEA (5R:TEA= 1:50; 1: 100; 1: 250; 1: 500; 1: 750; 1: 1000; 1:10000). All curves were obtained by using the "fixed wavelength" application.

From these results it appears that TEA can extend the *cis* half-life. Particularly, increasing the concentration of TEA from 100 to 750 equivalents (respect to 1 equivalent of 5R) a strong decreasing of the rate of *cis* 5R thermal relaxation decay was observed. The highest half-life value was obtained for a ratio 5R: TEA of 1: 1000 (Table 3). Further increasing of the base concentration did not change the $t_{1/2}$ of *cis* to *trans* conversion (Figure 36).

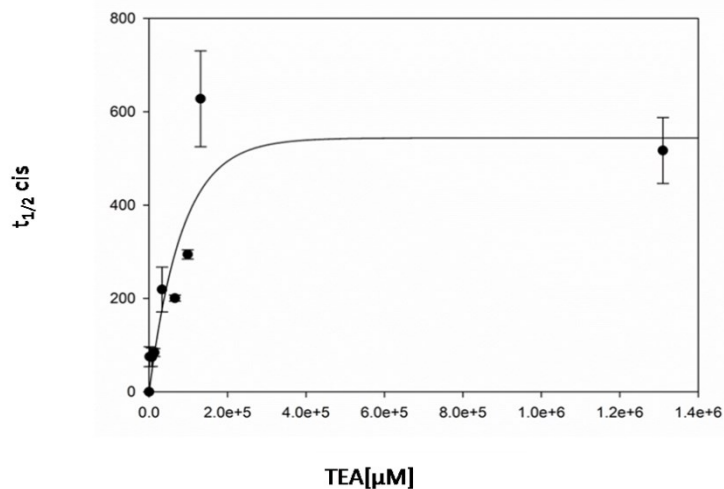


Figure 36. *Cis* half-life dependent on base concentration (TEA).

Considering the highest *cis* half-life obtained with 1:1000 (5R: TEA), I also evaluated the effect of DIPEA on the *cis-trans* isomerization rate at the same concentration. As showed in figure 37, also the DIPEA was able to decrease the rate of the *cis* 5R thermal relaxation.

5R : DIPEA = 1:1000 in H₂O:Acn (6:4)

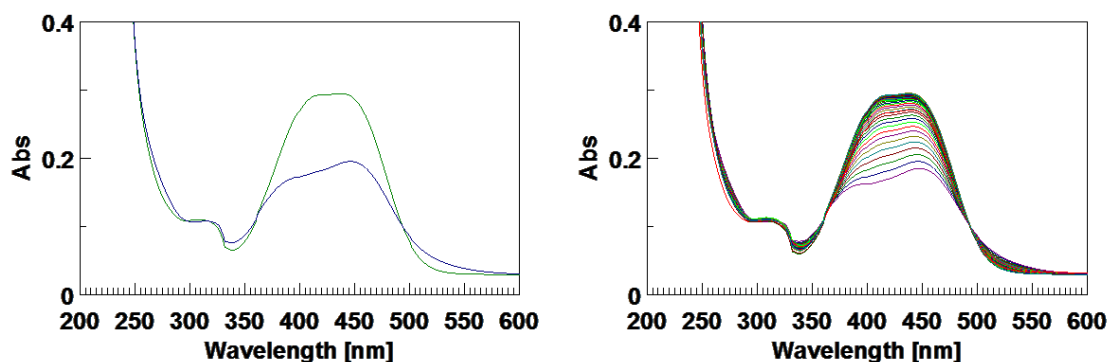


Figure 37. UV spectra of *trans* (green) and *cis* (blue) 5R in H₂O/ACN (6: 4) at a ratio 5R:DIPEA (1: 1000). The thermal decay was monitored by sequential acquisition of spectra until the UV profile rises to that of the initial *trans* isomer.

Finally, I considered also the effect of an inorganic base, NaOH, on *cis-trans* thermal relaxation rate of 5R. Once again, the base was able to increase the half-life of the *cis* form (Figure 38).

5R: NaOH = (1:1000) in H₂O/ACN (7:3)

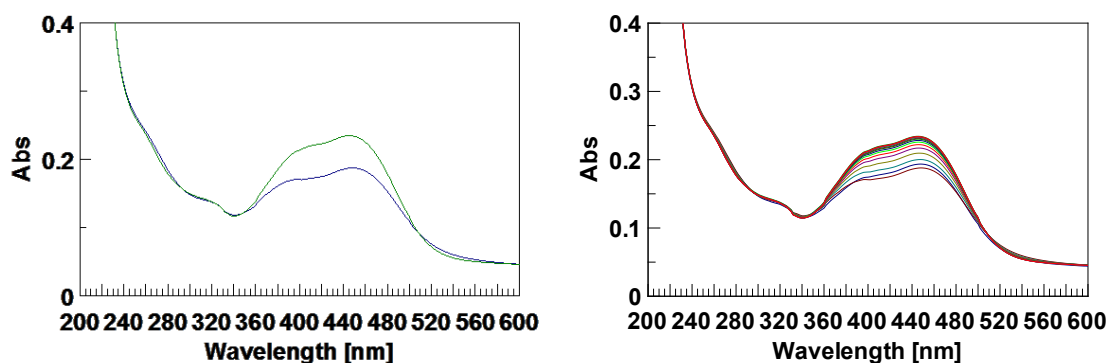


Figure 38. UV spectra of *trans* (green) and *cis* (blue) 5R in H₂O / ACN (7:3) at a ratio 5R: NaOH (1:1000). The *cis* thermal decay was monitored by sequential acquisition of spectra until the UV profile raised that of the initial *trans* isomer.

Owing to the poor solubility of 5R in the used solvents, I performed UV absorbance measurements at different concentrations of 5R (Figure 39).

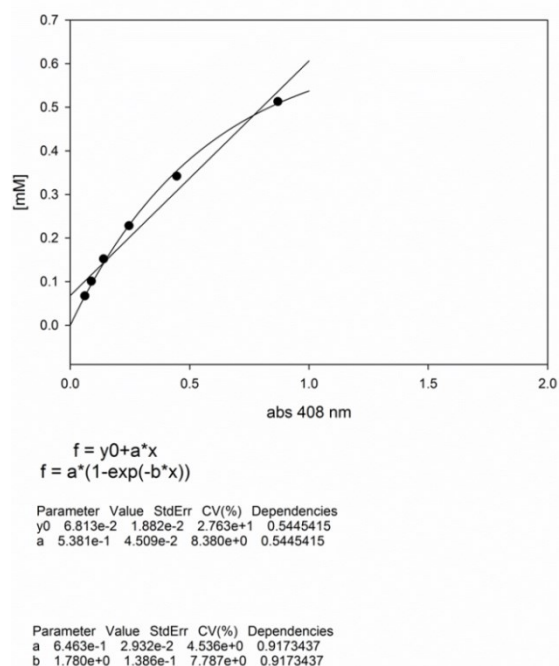


Figure 39. Dependence of UV absorbance measured at 408nm on 5R concentration in H₂O:ACN (6:4).

As shown in the figure 39, using the mixture H₂O:ACN (6:4) as solvent, a linear dependence of the absorbance measured at 408 nm on 5R concentration was observed only in the range of 0.05-0.2 mM. The most significant deviation from linearity were obtained increasing the concentration over than 0.35 mM. This value was strongly similar (131 μM) to that used in our experiments to evaluate

the rate of thermal decay of *cis* 5R. In view of these results, specific phenomena associated with molecular aggregation on the half-life time of *cis* 5R could be excluded.

Fast spectroscopy experiments

In order to quantify the fast thermal relaxation rate in dark of *cis* isomer in methanol, UV fast spectroscopy experiments were conducted in collaboration with Professor Carlo Altucci (Department of Physics, University of Studies Federico II, Naples) (for the description see paragraph 2.2) 5R was dissolved in methanol and was irradiated with a laser beam focused at different wavelengths; at the same time fluorescence measurements of the sample were performed. In these experiments a weak fluorescence, whose decay was in the range of nanoseconds, was observed when the solution was irradiated at 312 nm with fluorescence bands in emission of 342 and 372 nm (Figure 40). Therefore, in methanol *cis-trans* conversion of 5R proceeds with relaxation times in the range of nanoseconds, confirming our previous observation on the basis of the UV measurements.

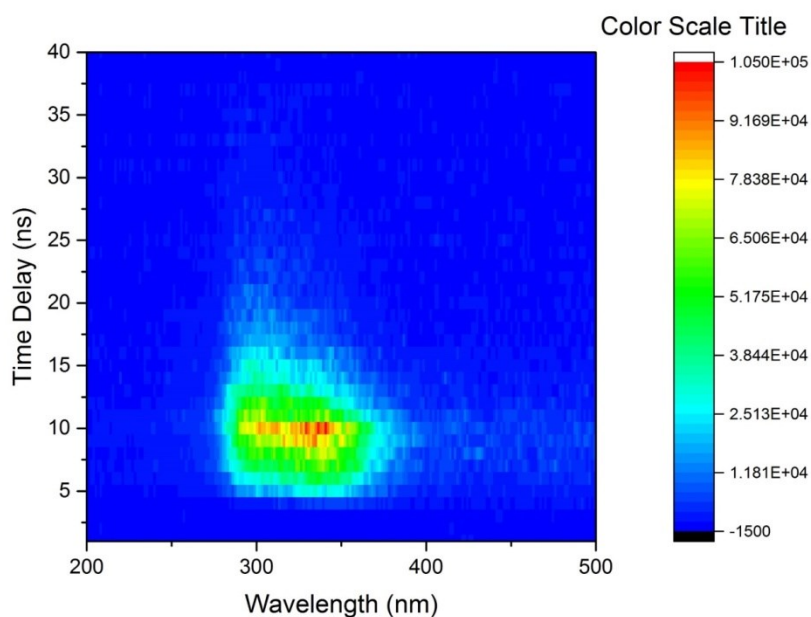


Figure 40. Fluorescence intensity dependence on time, after irradiation at 312 nm.

Structural characterization of conjugated oligonucleotides (5'-DMAzo-T30695 and 5'-DMAzo-TBA)

UV-vis spectra

UV-vis spectra of conjugated oligonucleotides (5'-DMAzo-T30695 and 5'-DMAzo-TBA) showed two bands, at 258 and 450 nm (Figures 41 and 42). The first one is centred at 258 nm and corresponded to the DNA absorption band. The latter, that was absent in the UV spectrum of the unmodified sequences should correspond to that of conjugated chromophore.

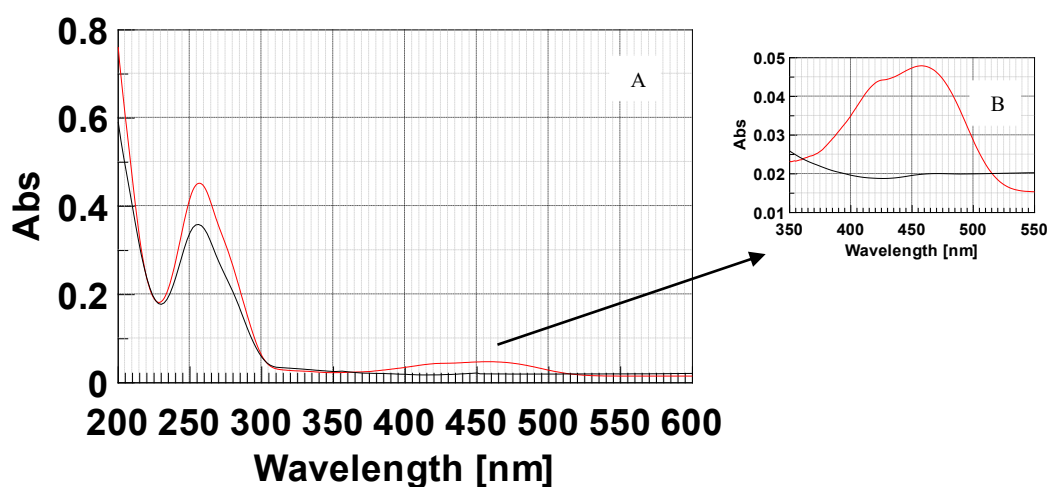


Figure 41. (A) T30695 (black) and 5'-DMAzo-T30695 (red) 20 μ M in K⁺ buffer (10 mM potassium phosphate, 10 mM KCl, pH=7.4). Cell length 0.5 cm (B) Enlargement of the range 350-550 nm.

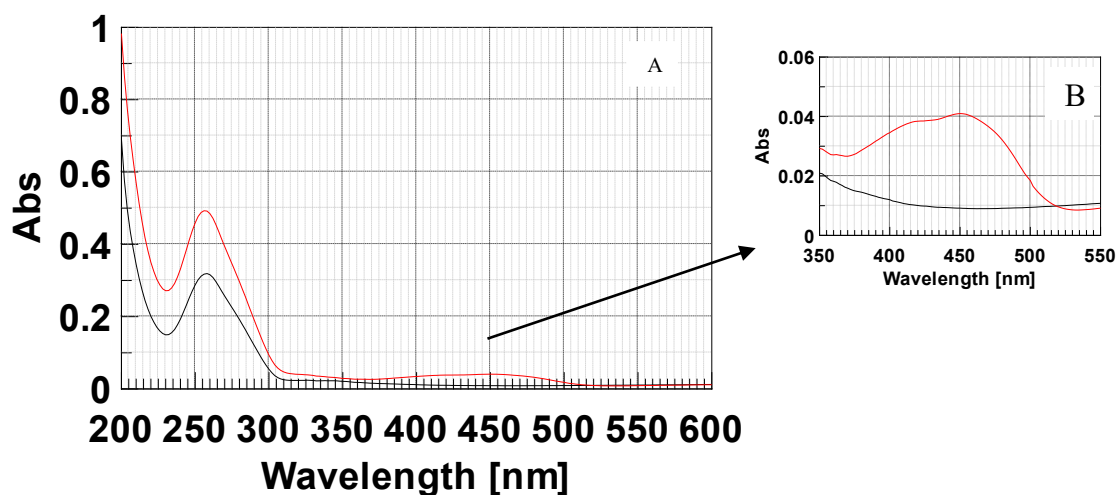


Figure 42. (A) UV spectra of TBA (black) and 5'-DMAzo-TBA (red) 20 μ M in K⁺ buffer (10 mM potassium phosphate, 90 mM KCl, pH=7.4). Cell length 0.5 cm. (B) Enlargement of the range 350-550nm.

CD and CD melting

In order to evaluate the effects of the 4-(dimethylamino)azobenzene on the ability of the conjugated sequences to fold into G-quadruplexes, I performed CD spectra in K^+ buffer (Figure 43 A-B) From the collected data it appeared that 5'-DMAzo-TBA and 5'-DMAzo-T30695 are able to fold into G-quadruplex structures very similar to the corresponding unmodified oligonucleotides. Indeed, similarly to the unmodified TBA, the CD profile of 5'-DMAzo-TBA is characterized by three positive bands at 212, 247 and 295 nm and a negative band around 270 nm that can be attributed to the presence in the solutions of an antiparallel G-quadruplex (Figure 43A). Correspondingly, also the CD profiles of T30695 and of 5'-DMAzo-T30695 are characterized by three positive CD bands at about 209, 262 and 303 nm and one negative CD band at 242 nm, thus suggesting that the conjugated sequence preserved the same ability of T30695 to fold into parallel a G4 structure. (Figure 43B).

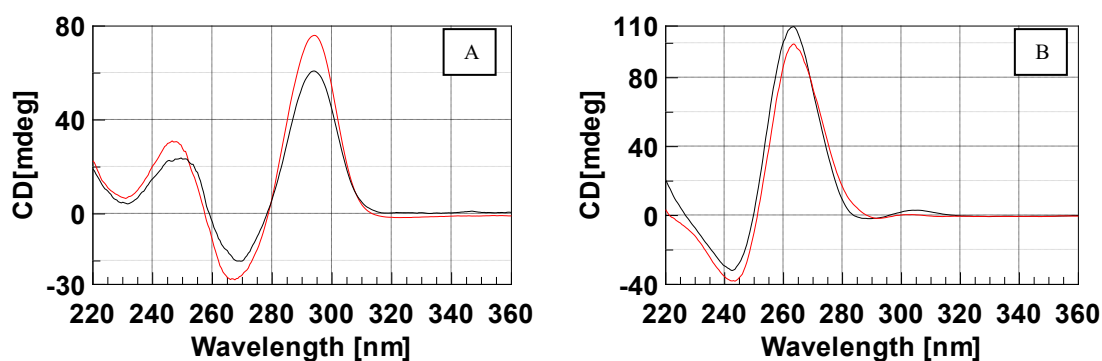


Figure 43. (A) CD profiles of TBA (black) and 5'-DMAzo-TBA (red) 20 μ M in K^+ buffer (10 mM potassium phosphate, 10 mM KCl, pH=7.4); (B) CD profiles of T30695 (black) and 5'-DMAzo-T30695 (red) 20 μ M in K^+ buffer (10 mM potassium phosphate, 90 mM KCl, pH=7.4). Cell length: 0.5 cm.

CD melting studies were also performed in order to evaluate the effects of the conjugated azocompound on GQs stabilities (Figures 44-45).

The melting curve of 5'-DMAzo-TBA was registered monitoring the change of the intensity of the band at 295 nm increasing the temperature from 10°C to 90°C in K^+ buffer. Figure 44 shows the two obtained CD melting profiles for TBA (black) and for 5'-DMAzo TBA (red). It appears

that the conjugation with the azobenzene moiety significantly reduced the thermal stability of TBA G4 structure ($\Delta T_m \sim 6^\circ\text{C}$).

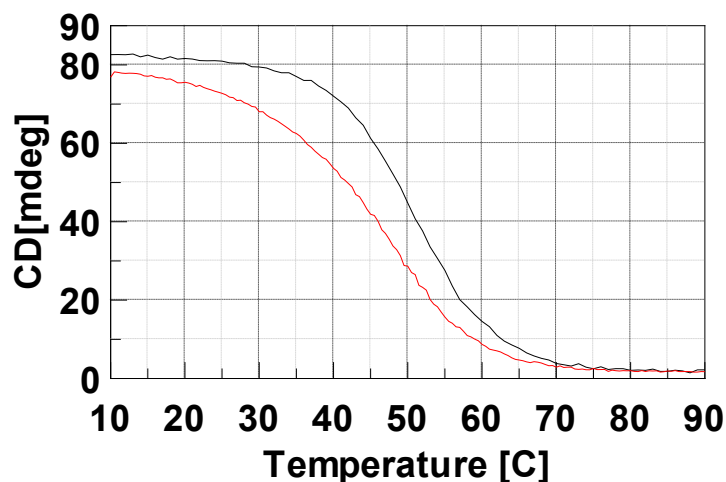


Figure 44. CD melting profiles of TBA (black) and 5'-DMazo-TBA (red). Fixed wavelength 295 nm. [ON] of 2.0×10^{-5} M. in K^+ buffer (10 mM potassium phosphate, 10 mM KCl, pH=7.4). Temperature scan speed $0.2^\circ\text{C}/\text{min}$. Cell length 0.5 cm.

Two CD melting profiles for the 5'-DMAzo-T30695 were obtained, using two different buffered solutions, containing K^+ or Na^+ cations. In both cases the experiments were performed monitoring the change of the intensity of the band at 263 nm increasing the temperature from 10°C to 100°C . Similarly to T30695 (see also part I paragraph 3.2), the CD melting curve of 5'-DMAzo-T30695 showed two inflection points suggesting that two unfolding events (5'-5' end-to-end stacked dimeric GQs \rightarrow GQs monomers \rightarrow unfolded single strands) occurred in the solutions (Figure 45 A-B). Although 5'-DMAzo-T30695 showed a thermal stability higher than T30695 both in Na^+ and in K^+ buffer, the two profiles were quite different; particularly in K^+ buffer the monitored CD band appeared to persist also at 100°C , thus suggesting that the corresponding G-quadruplex should yet be in the solution at the highest explored temperature.

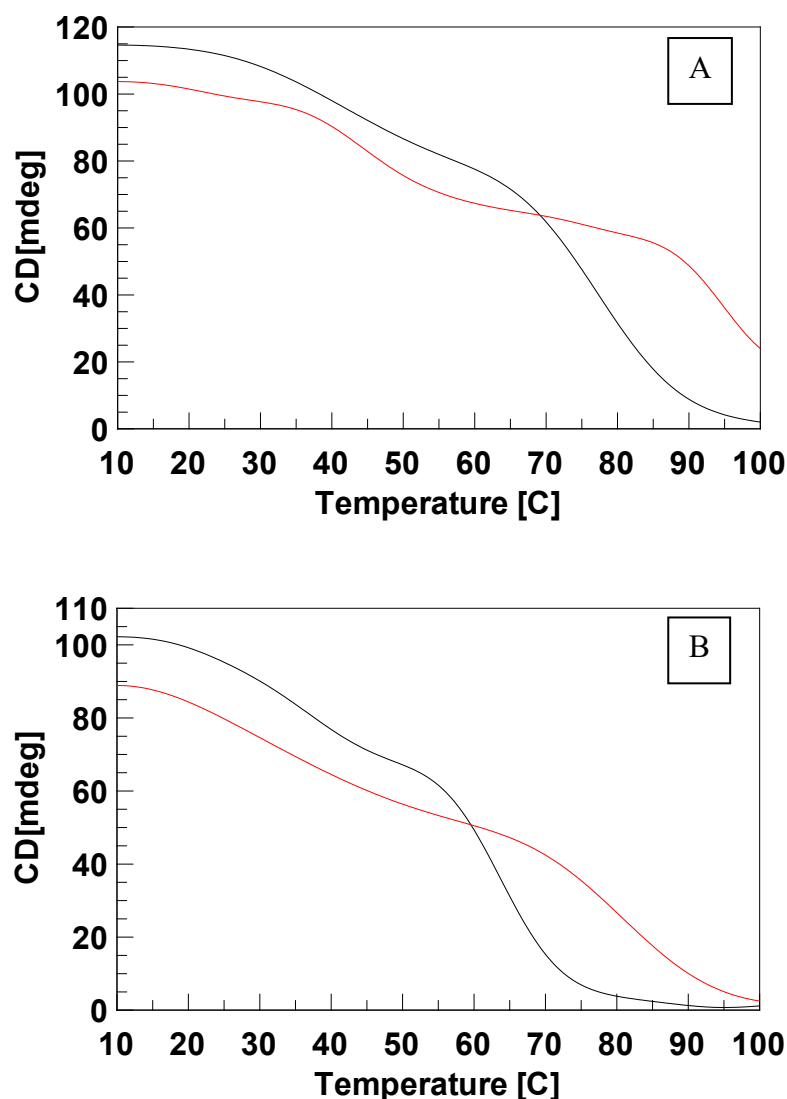


Figure 45. CD melting profiles of T30695 (black) and 5'-DMazo-T30695 (red). Fixed wavelength 263 nm. [ON] of 2.0×10^{-5} M. Cell length 0.5 cm. Temperature scan speed $0.2^\circ\text{C}/\text{min}$. (A) K^+ buffer (10 mM potassium phosphate, 90 mM KCl, pH=7.4); (B) Na^+ buffer (10 mM sodium phosphate buffer, 60 mM NaCl, pH=7.4).

Photo-responsivity of 4-(dimethylamino) azobenzene derivative conjugated to TBA and T30695

In order to verify the effect of the *cis-trans* photoisomerisation of the 4-(dimethylamino) azobenzene moiety on the 5'-end of TBA and of T30695 G-quadruplex structures, it was appropriate to investigate the right conditions both to enable a slow *cis* to *trans* thermal relaxation time of *cis* form, and to preserve the oligonucleotides integrity. As described above, the *cis* 5R half-life could be increased by a certain concentration of triethylamine, starting from the ratio 5R: TEA (1:25) a substantial *cis* half-life increasing was obtained by allowing to monitor the thermal decay

by a conventional UV-Vis spectrophotometer. In view of this fact, I chose the minimum concentration of TEA with the aim of reducing substantially the *cis* thermal relaxation rate without affecting the oligonucleotides stability.

Due to the poor solubility of the triethylamine in the aqueous solutions suited for the oligonucleotides, it was necessary to add an organic solvent. Literature data showed that ethanol should stabilize the G-quadruplex structure [33]. On this basis, I chose to explore the behavior of 5R in a mixture H₂O:EtOH (1:1).

First of all, I verified that 5R proceeded to photo-isomerization in these conditions: H₂O:EtOH=1:1, 5R:TEA 1:25 and 20mM KCl; $t_{1/2}$:0.72 (Figures 46-47)

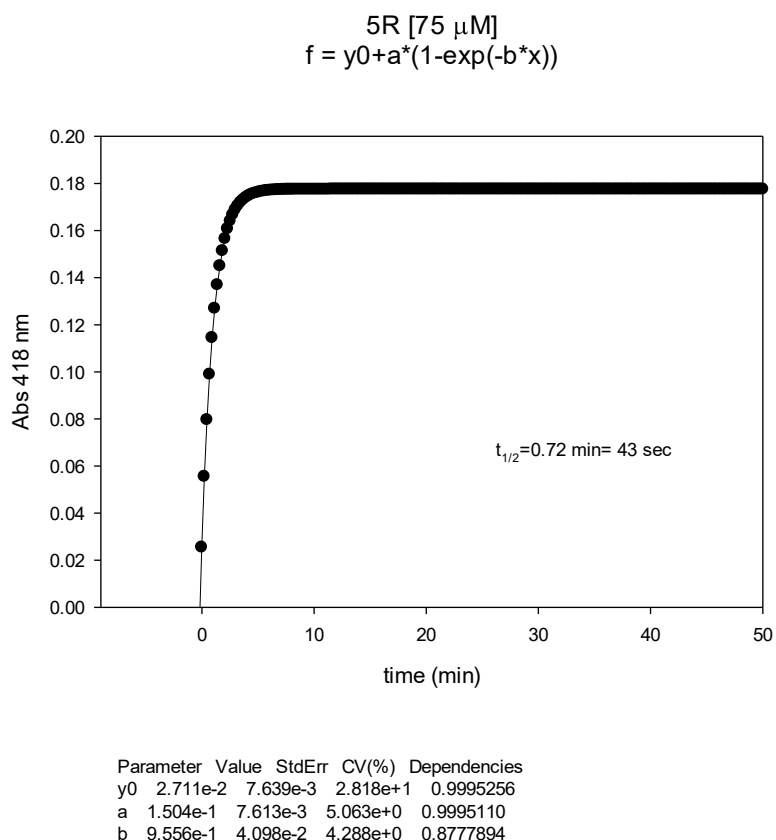


Figure 46. Time-dependent absorption of 5R after irradiation in H₂O/EtOH (1:1) at wavelength 416 nm in presence of TEA (5R:TEA= 1:25).

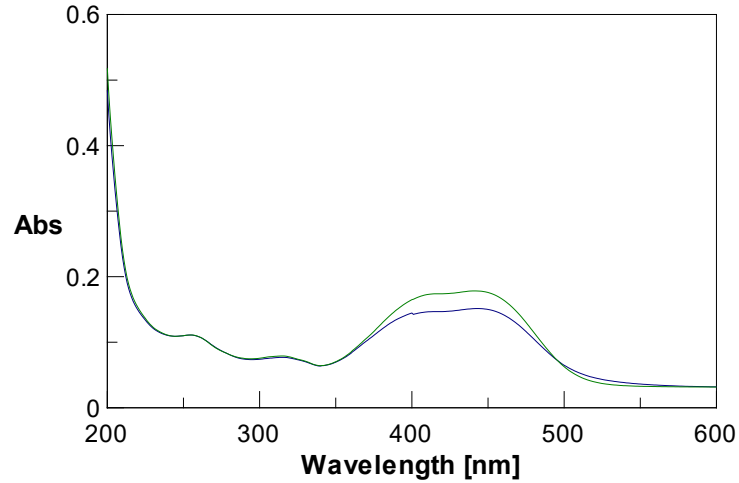


Figure 47. UV spectra of *trans* (green) and *cis* (blue) 5R in H₂O/EtOH (1:1) at a ratio 5R:TEA (1:25), 20mM KCl. Cell length: 0.1 cm.

In addition, CD and CD melting data showed that 5'-DMAzo-TBA and 5'-DMAzo-T30695 preserved the G-quadruplex structures in the used conditions.

The CD spectra in H₂O : EtOH (1:1) and with a ratio of oligonucleotides: TEA (1:25) kept the same profiles compared to that obtained in K⁺ buffer, above reported (Figure 43).

To better compare the two different conditions for each oligonucleotide, the CD spectra were reported in molar ellipticity (Figure 48).

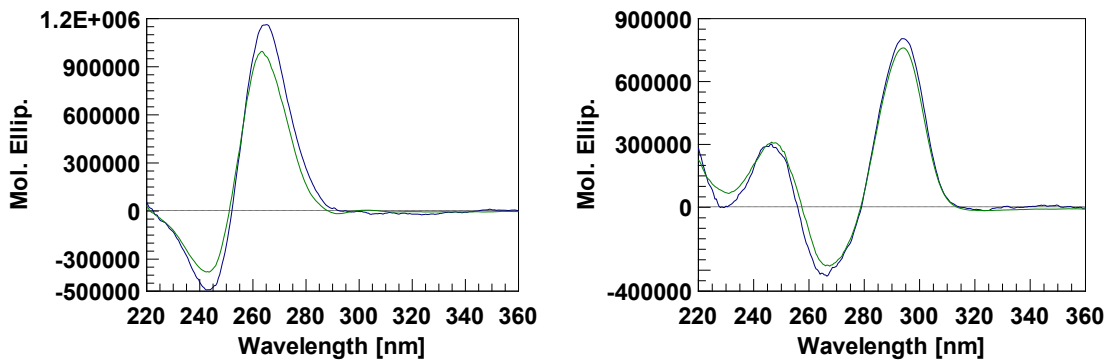


Figure 48. CD profiles: (A) 20 μ M of 5'-DMAzo-T30695 (green) in K⁺ buffer (10 mM potassium phosphate, 90 mM KCl, pH=7.4), cell length 0.5 cm; 3.5 μ M of 5'-DMAzo-T30695 (blue) in H₂O / EtOH (1: 1), ON:TEA (1:25), 20mM KCl, cell length 0.5 cm. (B) 20 μ M of 5'-DMAzo-TBA (green) in K⁺ buffer (10 mM potassium phosphate, 90 mM KCl, pH=7.4), cell length 0.5 cm; 3.5 μ M of 5'-DMAzo-TBA (blue) in H₂O / EtOH (1: 1), ON : TEA (1:25), 20mM KCl, cell length 0.5 cm.

As concerning the CD melting curves, the G4 structure of 5'-DMAzo-TBA and 5'-DMAzo-T30695 preserved also a certain stability (T_m 5'-DMAzo-TBA $\sim 57^\circ\text{C}$, T_m of 5'-DMAzo-T30695 was not detectable in view of the persistence of the CD band at 263 nm also at the highest explored temperature) (Figures 49-50).

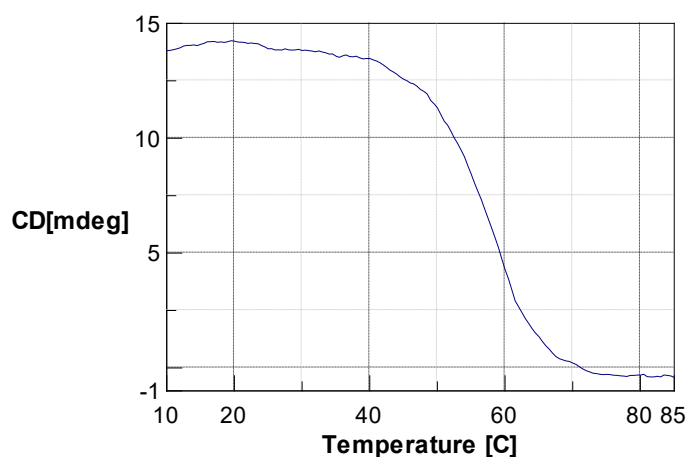


Figure 49. CD melting curve of 5'-DMAzoTBA in $\text{H}_2\text{O} / \text{EtOH}$ (1: 1), $[\text{ON}] = 3.5 \times 10^{-6}\text{M}$; ON : TEA (1:25), 20mM KCl. Cell length 0.5 cm. Scan speed= $0.2^\circ\text{C}/\text{min}$.

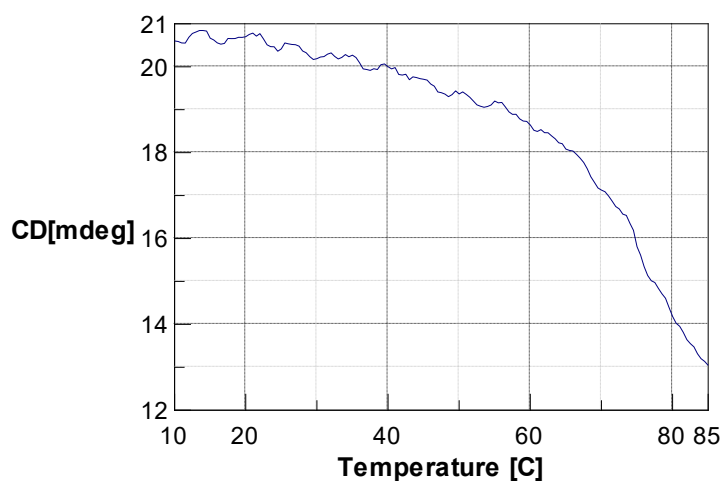


Figure 50. CD melting curve of 5'-DMAzo T30695 in $\text{H}_2\text{O} / \text{EtOH}$ (1: 1), $[\text{ON}] = 3.5 \times 10^{-6}\text{M}$; ON : TEA (1:25), 20mM KCl. Cell length 0.5 cm. Scan speed= $0.2^\circ\text{C}/\text{min}$.

Based on the described results it should be considered that the solvent conditions used for the experiments and the presence of the organic base in the solutions did not affect the ability of 5'-DMAzo-T30695 and 5'-DMAzo-TBA to fold into G4. In order to study the effects of the photo-

isomerization of the conjugated chromophore on the stability and/or typology of the TBA- or T30695-G4 structures these solutions were successively irradiated at 435 nm.

UV-Vis spectra of 5'-DMAzo-TBA and 5'-DMAzo-T30695 were performed before and after irradiation by LED light at 435 nm (Figures 51-52).

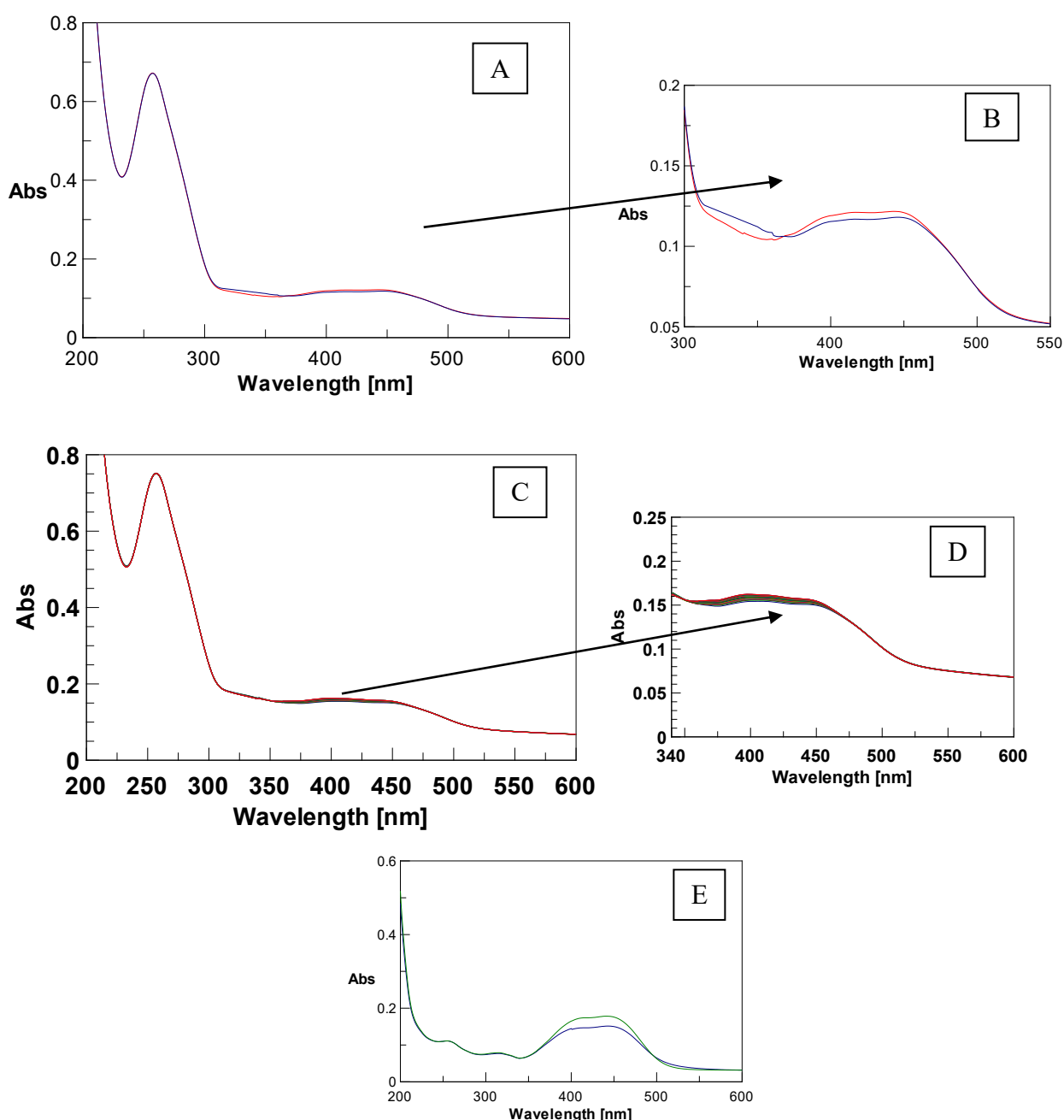


Figure 51. UV spectra of 5'-DMAzo-TBA before irradiation at 435 nm RED, after irradiation at 435nm BLUE, in H₂O/EtOH (1:1), [ON] = 3.5x10⁻⁶M; ON : TEA (1:25), 20mM KCl. Cell length 0.5cm. (A) Full spectrum (B) Enlargement 300-550 nm corresponding the absorption band of the 5'-DMAzo moiety. Before and after irradiation a slight changing of this portion of the UV spectrum occurred (Figure B). Time-dependent UV spectra of 5'-DMAzo-TBA after irradiation at 435 nm, UV band of the 5'-DMAzo moiety changes during time (C) Full spectrum (D) Enlargement 340-600 nm corresponding the absorption band of the 5'-DMAzo moiety. (E) UV spectra of *trans* (green) and *cis* (blue) 5R in H₂O / EtOH (1: 1) at a ratio 5R:TEA (1:25), 20mM KCl. Cell length: 0.1 cm.

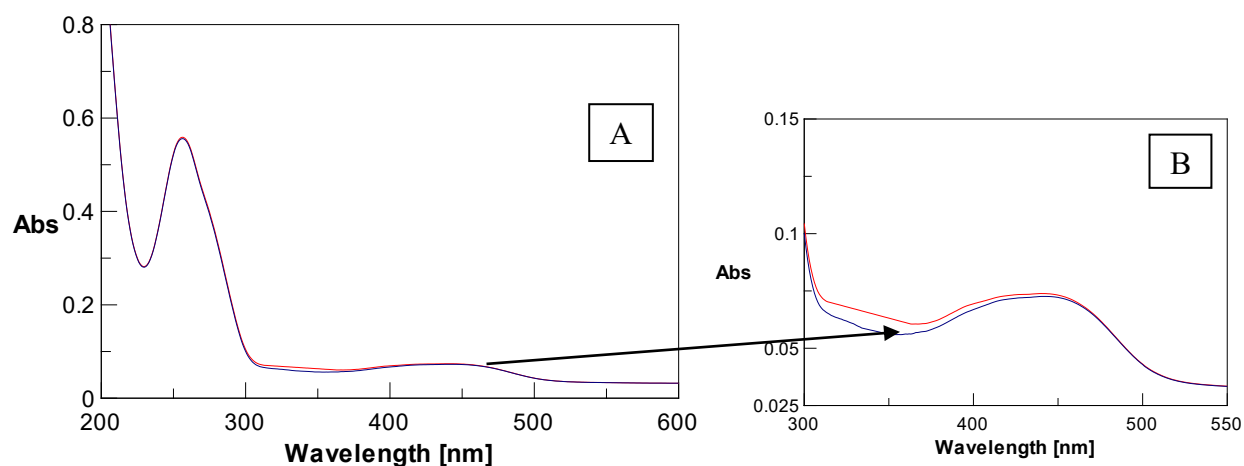


Figure 52. UV spectra of 5'-DMAzo-T30695 before irradiation at 435nm (red) and after irradiation at 435nm (Blue), in H₂O/EtOH (1:1), [ON] = 3.5x10⁻⁶M; ON : TEA (1:25), 20mM KCl. Cell length 0.5cm. (A) Full spectrum (B) Enlargement 300-550 nm corresponding the absorption band of the conjugated 5'-DMAzo moiety.

UV spectra of 5'-DMAzo-T30695 after irradiation did not show substantial changes of the absorption band connected to 5'-DMAzo moiety. Slight differences in the region 350-500 nm of the UV spectra before and after irradiation were found in the case of 5'-DMAzo-TBA.

Our results are in contrast with previous results reported by Kamei and co-workers concerning the *cis* to *trans* photoisomerization of an analogue of 4-DMAzo conjugated at DNA double helices. In that case, the use of aqueous basic solution stabilized the *cis* form of azobenzene analogue conjugated at DNA [30].

In order to further explore the effect of the *trans* → *cis* photo-isomerization on the G4 structures, CD experiments conducted before and after irradiation were also performed.

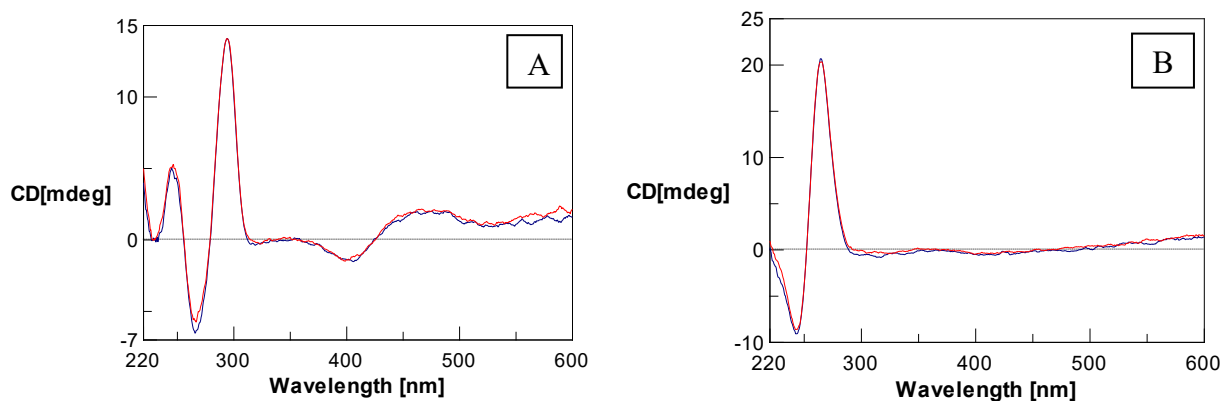


Figure 53. CD spectra: **(A)** 5'-DMAzo-TBA before irradiation at 435nm RED, after irradiation at 435nm BLUE, in H₂O/EtOH (1:1), [ON] = 3.5x10⁻⁶M; ON : TEA (1:25), 20mM KCl. **(B)** 5'-DMAzo-T30695 before irradiation at 435nm RED, after irradiation at 435nm BLUE, in H₂O/EtOH (1: 1), [ON] = 3.5x10⁻⁶M; ON : TEA (1:25), 20mM KCl. Cell length 0.5 cm.

The CD profiles of the two modified sequences did not undergo significant variations after irradiation (Figure 53). However, considerable differences in the region 350-500 of the CD spectra acquired for 5'-DMAzo-TBA and 5'-DMAzo-T30695 were observed. CD bands in this region should be attributable to the conjugated chromophore. A Cotton effect centered at 435 nm appeared only in the CD profiles of 5'-DMAzo-TBA, thus suggesting that the 5'-conjugated chromophore could have different spatial orientation respect to the TBA or T30695 G-quadruplex.

3.3. Conclusion

In this work we focused on the synthesis of the new azobenzene derivative named 4-DMAzo R (Figure 28) and its conjugation at the 5' end of two G-quadruplex forming oligonucleotides, TBA and T30695 (Table 1). Firstly, we studied the photo-responsive properties of the 4-DMAzo R after irradiation with a LED light at 435 nm in different solvent conditions. From the obtained results, it can be deduced that the relaxation thermal rate of *cis* 4-DMAzo R strongly depends on the polarity of the solvent and on protonation of the azo-group, in particular it increases with increasing of

either the solvent polarity or the proton concentration in the solution. In basic conditions obtained by adding small quantity of TEA, using H₂O:EtOH (1:1) as solvent, the *cis* → *trans* 4-DMAzo R thermal relaxation occurred in the time scale of minutes, that is suitable to be registered by a conventional UV-Vis spectrophotometer. However, the photo-responsive properties of 4-DMAzo-conjugated oligonucleotides, 5'-DMAzo-TBA and 5'-DMAzo-T30695, significantly differ from that of free 4-DMAzo R, measured in the same solvent conditions. Notably, also adding TEA to the sample, irradiation at 435 nm does not produce changes in the shape and in the intensity of the UV bands of 5'-DMAzo-T30695; while slight changes of the adsorption band associated to the 4-DMAzo moiety are observed in the UV spectra of 5'-DMAzo-TBA. Probably, the 5'-conjugated moiety could interact with the folded TBA- or T30695-G-quadruplex structures in different way, from which different effects on thermal relaxation rate could be provoked. This hypothesis is, at least in part, corroborated by the CD heating experiments that show significant increasing of the thermal stability of the 5'-DMAzo-T30695 G-quadruplex, compared to that of T30695; contrarily, it appears that the conjugation at 5'-end of TBA negatively affects the thermal stability of the corresponding TBA-G-quadruplex. On the basis of these results, in collaboration with the Prof. C. Altucci (Department of Physic, University of Studies Federico II, Naples), further studies by means of UV fast spectroscopy will be performed, in order to characterize the kinetic of the *trans* to *cis* 5'-DMAzo-TBA and 5'-DMAzo-T30695 photo-conversion. Moreover, we are now synthesizing the right quantity of the conjugated oligonucleotides in order to perform 1D and 2D NMR experiments useful for the structural characterization of the folded G-quadruplex structures.

3.4. Experimental section

General procedure

General procedure is already described at pages 35, 67, 100.

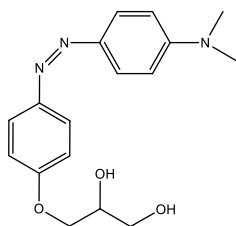
Synthesis of 5R

The synthesis of 5R is very similar to that reported for 1a, 1b, 1RR e 1RS (see paragraph 2.3 page 100), but at the final step N,N-dimethylaniline (254 μ L, 0,270 g, 2,2 mmol) was added instead of the pyrrole derivative.

^1H NMR (CD_3OD) δ : 3.06 (s, 6H, $\text{N}(\text{CH}_3)_2$), 3.67 (m, 2H, CH_2OH), 4.00 (m, 1H, CHOH), 4.04 (dd, $J = 4.2, 9.6$ Hz, 1H, OCH_2), 4.14 (dd, $J = 6.0, 9.6$ Hz, 1H, OCH_2), 6.82 (d, $J = 9.1$ Hz, 2H, $\text{C}^{3,5}_{\text{ArH}}$), 7.06 (d, $J = 8.9$ Hz, 2H, $\text{C}^{2,6}_{\text{ArH}}$), 7.77 (d, $J = 9.1$ Hz, 2H, $\text{C}^{2,6}_{\text{ArH}}$), 7.77 (d, $J = 8.9$ Hz, 2H, $\text{C}^{3,5}_{\text{ArH}}$).

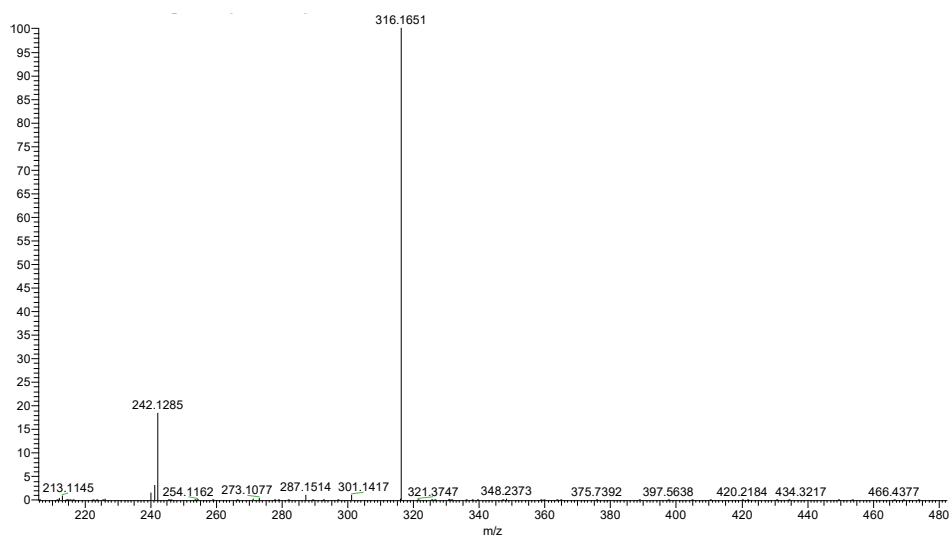
^{13}C NMR (CD_3OD) δ : 39.3 ($\text{N}(\text{CH}_3)_2$), 62.9 (CH_2OH), 70.6 (CHOH), 69.4 (OCH_2), 111.5 ($\text{C}^{3,5}_{\text{Ar}}$), 114.6 ($\text{C}^{2,6}_{\text{Ar}}$), 123.8 ($\text{C}^{3,5}_{\text{Ar}}$), 124.3 ($\text{C}^{2,6}_{\text{Ar}}$), 143.7 (C^1_{Ar}), 147.7 (C^4_{Ar}), 152.5 (C^4_{Ar}), 160.7 (C^1_{Ar}).

HRESIMS (modalità positiva, CH_3OH) m/z massa trovata 316.1651 $[\text{M}+\text{H}]^+$ (calcd for $\text{C}_{17}\text{H}_{22}\text{N}_3\text{O}_3$, 316.1656).

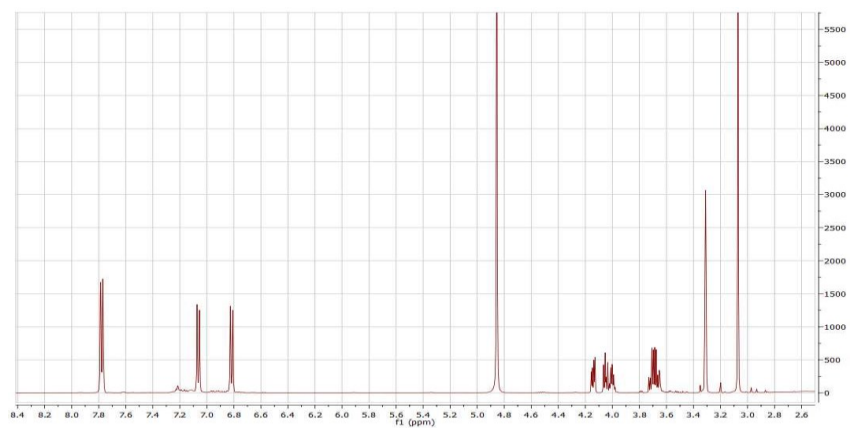


R (*E*)-3-(4-((4-(dimethylamino)phenyl)diazenyl)phenoxy)propane-1,2-diol (5R)

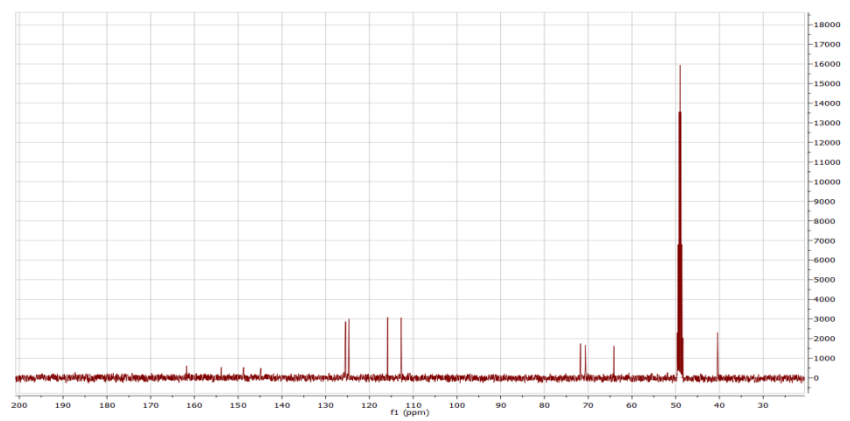
HRMS (ESI+)



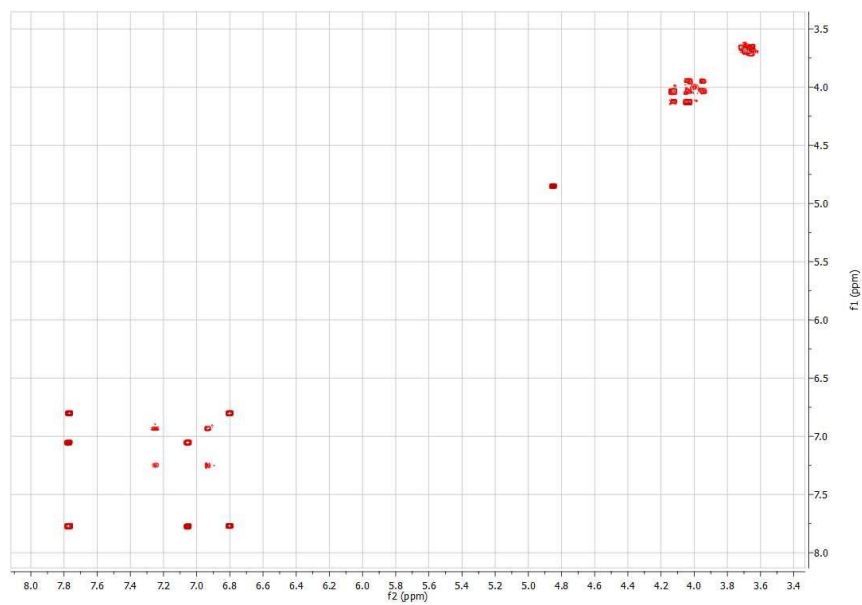
$^1\text{H-NMR}$



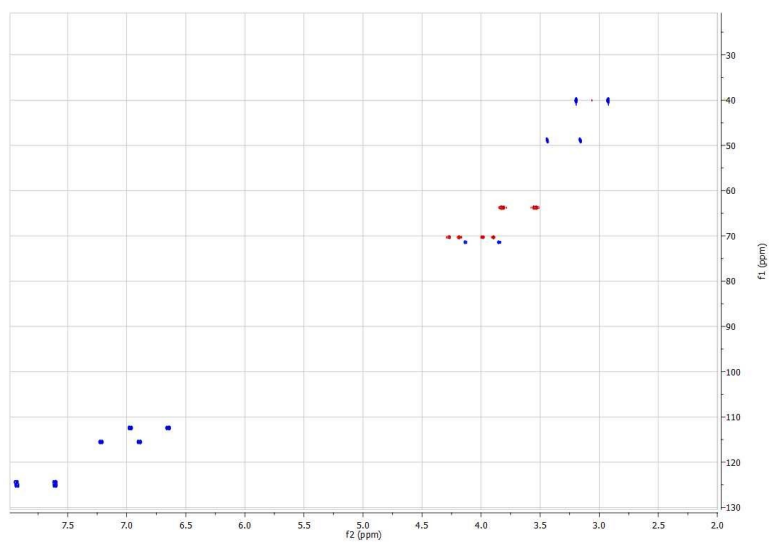
$^{13}\text{C-NMR}$



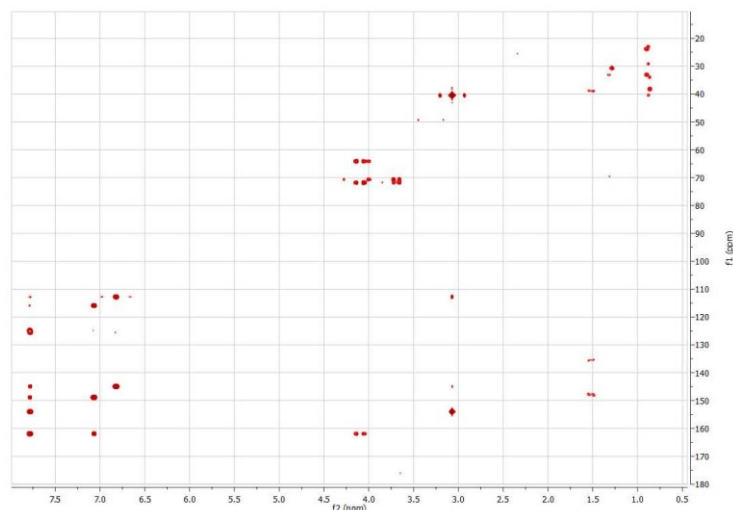
COSY



HSQC



HSQC



Synthesis of monomer phosphoramidite building block **7R**

5R (0.400 g, 1.3 mmol), 4,4-dimethoxytrityl chloride (0.430 g, 1.3 mmol), 4-dimethylaminopyridine (0.0076 g, 0.062 mmol) were dissolved in dry Pyridine (6.35 ml). The resulting solution was stirred at room temperature (r.t.) under argon for 3 h. The solution was concentrated under reduced pressure and the residue purified by column chromatography on silica gel (eluted with 50:50:0.1 N hexane/ethyl acetate /Et₃N) to give monodimethoxytritylated **6R** as a clear orange solid (yields 44%). **6R** (0.350 g, 0.57 mmol), β-cyanoethyl-N,N'-diisopropyl-chlorophosphoramidite (0.190 ml, 0.85 mmol), DIPEA (0.296 ml, 1.7 mmol) were dissolved in dry DCM (3 ml), 1.0 h. 70%.

After 60 min, the reaction was diluted with ethyl acetate (15 ml), and finally washed with 10% sodium carbonate solution (15 ml) and brine (15 ml). The organic layer was dried on magnesium sulphate and concentrated *in vacuo*. The residue was purified by silica gel chromatography eluted with hexane/ethyl acetate and triethylamine (80:10:10). The fractions containing the product were collected and concentrated under vacuum, yielding **7R** as orange foam (85% yield).

Synthesis of oligomers

5'-DMAzo-TBA and 5'-DMAzo-T30695 were synthesized using the standard solid phase DNA chemistry similarly to the oligonucleotides reported in the part I adding a coupling stage with the 7R phosphoramidite building block at the end of the synthesis of the TBA and T30695 sequences, and extending the times of the two coupling steps from 2 to 15 minutes.

Bibliography

- [1] G. Mayer and A. Hechel, "Biologically active molecules with a 'light switch'" *Angew. Chemie Int. Ed.*, vol. 45, no. 30, pp. 4900–4921, 2006.
- [2] J. Griffiths, "Photochemistry of azobenzene and its derivatives," *Chem. Soc. Rev.*, vol. 1, no. 4, p. 481–493, 1972.
- [3] A. A. Beharry and G. A. Woolley, "Azobenzene photoswitches for biomolecules," *Chem. Soc. Rev.*, vol. 40, no. 8, pp. 4422–4437, 2011.
- [4] S. Samanta *et al.*, "Photoswitching Azo compounds in vivo with red light," *J. Am. Chem. Soc.*, vol. 135, no. 26, pp. 9777–9784, 2013.
- [5] J. García-Amorós and D. Velasco, "Recent advances towards azobenzene-based lightdriven real-time information-transmitting materials," *Beilstein J. Org. Chem.*, vol. 8, pp. 1003–1017, 2012.
- [6] E. Merino and M. Ribagorda, "Control over molecular motion using the cis-trans photoisomerization of the azo group," *Beilstein J. Org. Chem.*, vol. 8, pp. 1071–1090, 2012.
- [7] M. Dong, A. Babalhavaeji, S. Samanta, A. A. Beharry, and G. A. Woolley, "Red-Shifting Azobenzene Photoswitches for in Vivo Use," *Acc. Chem. Res.*, vol. 48, no. 10, pp. 2662–2670, 2015.
- [8] C. W. Chang, Y. C. Lu, T. Te Wang, and E. W. G. Diau, "Photoisomerization dynamics of azobenzene in solution with S1 excitation: A femtosecond fluorescence anisotropy study," *J. Am. Chem. Soc.*, vol. 126, no. 32, pp. 10109–10118, 2004.
- [9] Eric Wei-guang Diau, "A New Trans-to-Cis Photoisomerization Mechanism of Azobenzene on the S1(n,π*) Surface," *J. Phys. Chem. A*, vol. 108, pp. 950–956, 2004.
- [10] T. Asano, T. Yano, and T. Okada, "Mechanistic Study of Thermal Z-E Isomerization of Azobenzenes by High-Pressure Kinetics," *J. Am. Chem. Soc.*, vol. 104, no. 18, pp. 4900–4904, 1982.
- [11] G. Zimmerman, L. yung Chow, and U. jin Paik, "The Photochemical Isomerization of Azobenzene," *J. Am. Chem. Soc.*, vol. 80, no. 14, pp. 3528–3531, 1958.
- [12] Y. Dou, Y. Hu, S. Yuan, W. Wu, and H. Tang, "Detailed mechanism of trans-cis photoisomerization of azobenzene studied by semiclassical dynamics simulation," *Mol. Phys.*, vol. 107, no. 2, pp. 181–190, 2009.
- [13] W. A. Velema, W. Szymanski, and B. L. Feringa, "Photopharmacology: beyond proof of principle," *J. Am. Chem. Soc.*, vol. 136, p. 2178–2191, 2014.
- [14] M. M. Lerch, M. J. Hansen, G. M. van Dam, W. Szymanski, and B. L. Feringa, "Emerging Targets in Photopharmacology," *Angew. Chemie - Int. Ed.*, vol. 55, no. 37, pp. 10978–10999, 2016.
- [15] M. Borowiak *et al.*, "Photoswitchable Inhibitors of Microtubule Dynamics Optically Control Mitosis and Cell Death," *Cell*, vol. 162, no. 2, pp. 402–411, 2015.
- [16] J. E. Sheldon, M. M. Dcona, C. E. Lyons, J. C. Hackett, and M. C. T. Hartman, "Photoswitchable anticancer activity via trans–cis isomerization of a combretastatin A-4 analog," *Org. Biomol. Chem.*, vol. 14, no. 1, pp. 40–49, 2016.
- [17] P. Zhou *et al.*, "Potent Antitumor Activities and Structure Basis of the Chiral β-Lactam Bridged Analogue of Combretastatin A-4 Binding to Tubulin," *J. Med. Chem.*, vol. 59, no. 22, pp. 10329–10334, 2016.
- [18] S. Zheng *et al.*, "Design, synthesis, and biological evaluation of novel pyridine-bridged analogues of combretastatin-A4 as anticancer agents," *J. Med. Chem.*, vol. 57, no. 8, pp. 3369–3381, 2014.
- [19] J. Garcia-Amorós, M. Cidália, R. Castro, P. Coelho, M. M. M. Raposo, and D. Velasco, "New heterocyclic systems to afford microsecond green-light isomerisable azo dyes and their use as fast molecular photochromic switches" *Chem. Commun.*, vol. 49, pp. 11427–11429, 2013,
- [20] Z. A. Bredikhina, A. V. Kurenkov, O. A. Antonovich, A. V. Pashagin, and A. A. Bredikhin "A

- rare case of facial selectivity inversion for Sharpless asymmetric dihydroxylation in a series of structurally homogeneous substrates: synthesis of non-racemic 3-(nitrophenoxy)-propane-1,2-diols,” *Tetrahedron: Asymmetry*, vol. 25, pp. 1015–1021, 2014.
- [21] V. Balzani, A. Credi, and M. Venturi, “Controlled disassembling of self-assembling systems: Toward artificial molecular-level devices and machines,” *Proc. Natl. Acad. Sci.*, vol. 99, no. 8, pp. 4814–4817, 2002.
- [22] T. Muraoka, K. Kinbara, and T. Aida, “Mechanical twisting of a guest by a photoresponsive host,” *Nature*, vol. 440, no. 7083, pp. 512–515, 2006.
- [23] C. Mao, W. Sun, Z. Shen, and N. C. Seeman, “A nanomechanical device based on the B-Z transition of DNA,” *Nature*, vol. 397, no. 6715, pp. 144–6, 1999.
- [24] Rich, A., “DNA comes in many forms,” *Gene*, vol. 135, pp. 99–109, 1993.
- [25] X. Xing *et al.*, “Light-driven conformational regulation of human telomeric G-quadruplex DNA in physiological conditions,” *Org. Biomol. Chem.*, vol. 9, no. 19, pp. 6639–6645, 2011.
- [26] S. Ogasawara and M. Maeda, “Reversible photoswitching of a G-quadruplex,” *Angew. Chemie - Int. Ed.*, vol. 48, no. 36, pp. 6671–6674, 2009.
- [27] X. Wang *et al.*, “Conformational switching of G-quadruplex DNA by photoregulation,” *Angew. Chemie - Int. Ed.*, vol. 49, no. 31, pp. 5305–5309, 2010.
- [28] A. Sanchez and R. H. Derossi, “Strong Inhibition of Cis Trans Isomerization of Azo-Compounds by Hydroxide Ion,” *J. Org. Chem.*, vol. 58, no. 8, pp. 2094–2096, 1993.
- [29] A. M. Sanchez and R. H. de Rossi, “Effect of Hydroxide Ion on the Cis–Trans Thermal Isomerization of Azobenzene Derivatives,” *J. Org. Chem.*, vol. 60, no. 10, pp. 2974–2976, 1995.
- [30] T. Kamei *et al.*, “Visible-light photoresponsivity of a 4-(dimethylamino)azobenzene unit incorporated into single-stranded DNA: Demonstration of a large spectral change accompanying isomerization in DMSO and detection of rapid (Z)-to-(E) isomerization in aqueous solution,” *European J. Org. Chem.*, no. 11, pp. 1846–1853, 2007.
- [31] A. M. Sanchez, M. Barra and R. H. De Rossi, “On the Mechanism of the Acid / Base-Catalyzed Thermal Cis - Trans Isomerization of Methyl Orange,” *J. Org. Chem.*, vol. 64, no. 17, pp. 1604–1609, 1999.
- [32] K.S. Schanze, T.F. Mattox, D.G. Whitten, “Solvent Effects upon the Thermal Cis-Trans Isomerization and Charge-Transfer Absorption of 4-(Diethylamino)-4'-nitroazobenzene,” vol. 48, no. 7, pp. 2808–2813, 1983.
- [33] A.V. Doghaei, M.R.Housaindokht, M.R. Bozorgmehr “Molecular crowding effects on conformation and stability of G-quadruplex DNA structure: Insights from molecular dynamics simulation” *Journal of Theoretical Biology*, 364, 103–112, 2015.